EXPERIMENTAL STUDY AND NUMERICAL MODELING OF THE PERFORMANCE OF FLUE GAS DESULFURIZATION (FGD) BRINE/COAL FLY ASH CO-DISPOSAL

by

Rui He

A dissertation submitted to the faculty of
The University of North Carolina at Charlotte
in partial fulfillment of the requirements
for the degree of Doctor of Philosophy in
Civil Engineering

Charlotte

2022

Approved by:

_____
Dr. Vincent O. Ogunro,

_____
Dr. John L. Daniels

_____
Dr. Simon M. Hsiang

_____
Dr. Alireza Tabarraei

_____
Dr. Anton Pujol

ABSTRACT

RUI HE. Experimental Study and Numerical Modeling of the Performance of Flue Gas Desulfurization (FGD) Brine/Coal Fly Ash Co-Disposal. (Under the direction of DR. VINCENT O. OGUNRO)

The coal-fired steam electricity plants are interested in finding efficient ways to manage by-products from the combustion process out of environmental and regulatory considerations. As one of the major solid by-products, the coal fly ash (CFA) is required by the Coal Combustion Residuals (CCRs) rules to be disposed of in an engineered landfill to protect groundwater. While the disposal of the CFA in the landfill needs water for moisture conditioning and dust control measures, it is convenient to use liquid by-products as alternative moisture sources. The concentrates (brines) generated from the volume reduction of the flue gas desulfurization (FGD) wastewater, such as reverses osmosis and evaporation treatment, can be an alternative liquid source to achieve zero-liquid-discharge (ZLD) for its economic benefit and environmental responsibility considerations. In this study, chloride was the dominant anion with a significant presence of sulfate and bromide in the hypersaline FGD brine, and the cations were mainly calcium and magnesium. The class F CFA used in this study was acquired from an electric plant in the southeast U.S. and did not possess cementitious properties needed for stabilization/solidification (S/S) of co-disposal material. Methods investigated were the co-disposal through (1) compaction and (2) paste encapsulation technology. Instrumented testbeds with leachate and runoff collection systems for each co-disposal method were used to study their field behaviors under the weather conditions of Charlotte, North Carolina.

The chemical analysis of leachate and runoff samples from the compacted testbed found that the method released 79.1% of chloride and 88.6% of bromide in added FGD brine due to the

absence of solidification/stabilization of the material. While the electrical conductivity (EC) was used as an indicator of the pore solution's salinity, the chemical compositions of the fluid could vary as observed in the shifting of dominant anion from chloride to sulfate in the leachate. This study established a set of empirical equations to translate the permittivity to volumetric water content (VWC) for the pore solution's of a known EC (salinity). The low intensity, high-frequency precipitation provided high infiltration during the winter, resulting leachate generation by the testbed with a little amount of runoff. In contrast, the summer's high intensity, low-frequency rains resulted in a high runoff with little infiltration, coupled with extensive evaporation, causing a pause in leachate generation.

Compared to the compacted method, the paste encapsulation method successfully sequestered the halides mainly through the solidification process of the material, as indicated by the leaching test. Further analysis of the chemical composition of inner and annulus leachate coupled with the low hydraulic conductivity (1.44×10^{-8}) of parallelly tested laboratory samples and the negligible leachate volume collected from the inner section of the leachate collection system suggests the leachate collected in the annulus section originated from side leakage. The chemical analysis of leachate and runoff showed on average 80% of retention of chloride and bromide during the experiment period and 97% retention if the side leakage could have been eliminated. The relatively impermeable paste suggests storm management of a paste landfill should expect runoff quantity approximately equivalent to the local precipitation. The surface temperature of the paste was elevated by solar radiation during the summer, which indicated the paste landfill could serve as a heat source that could impact the local microclimate. The mineralogy study of different samples showed the formation of poorly structured minerals which caused interpretation challenges of XRD results. The anticipated halide stabilization pathway through the precipitation

of Friedel's salt and Kuzel's salt was complicated by the significant presence of magnesium in the brine.

Although the compacted method failed to retain halides under current weather conditions (Charlotte, NC, US), it does not necessarily disqualify its use in different environments. Therefore, a physics-based COMSOL-MATLAB (CM) model was established to simulate the field behaviors of the compacted co-disposal material, which was validated with the field data. The CM model consisted of three main components: heat transfer (HT), unsaturated flow (UF), and solute transport (ST) processes. The model also simulated the runoff, evaporation, and solar heating at the surface of the testbed. The CM model could appropriately reproduce the field leachate/runoff generation pattern, moisture content variation, temperature profile, and the change of chloride and bromide concentrations in the leachate during the washoff stage. The accuracy of simulation results could be improved with a better estimation of the conditions on the testbed surface.

While the validated physics-based model could be used to explore potential management methods for the compacted landfill and its behaviors under different weather conditions, the abundance of data spurred the interest in developing data-driven models. Since the bulk dielectric permittivity, which could be translated into VWC, was the measured property, a data-driven model simulating the change of permittivity in the compacted testbed was developed. The data-driven model was structured as three layers of material stacked in spatial order to address the standard operation of implementing new layers on top of old materials during landfill operation. With a forecast interval of 24 hours, the prediction over time of three years had an average R^2 of 97.6% with the data-driven model trained with the first-year data, and R^2 of 99.5% if two years of data were used in the training. The scenario studies showed that the data-driven model could only accurately predict permittivity values included in the training dataset, which indicates that a failure

to predict could happen when unprecedented values occurred. Further investigation showed the data-driven model could simulate processes that would have conventionally required additional physics-related information through unique pattern recognition in the training dataset.

DEDICATION

To my dad and mom, you've shown me the value of hard-working and taking responsibility, and you have given me the trust and support in my pursuit of higher education. Thank you all, love you!

ACKNOWLEDGEMENTS

Along this journey, I have a lot of people to appreciate, the first of all is my advisor, Dr. Vincent O. Ogunro, who mentored me to be a better researcher and guided me through this complex project. His encouragements had supported me through tough times, and his keen insights had contributed so much to my works. I want to thank members of my dissertation committee, Dr. John. L. Daniels, Dr. Simon M. Hsiang, Dr. Alireza Tabarraei, and Dr. Anton Pujol for their services, valuable contributions to the research, and extraordinary patients and supports through this challenging time. I would like to acknowledge Dr. Milind V. Khire for his service on my qualifying exam committee and for sharing the weather station. I am also grateful for the chance to work with Dr. William L. Saunders, JR., it's been a great experience. Special thanks to Dr. William Langley for your great support and service on my qualifying exam committee. I would like to express my appreciation for EPRI and Duke Energy for their partial funding of this project and Mr. Kirk Ellison for his help along the process. I would like to thank Mr. Mike Moss for his experiences and insights. I would like to express my gratitude to the CEE and INES program at UNC Charlotte for supporting my research and providing a friendly and resourceful research environment.

My life these years in this new city had never been lonely as my friends in the graduate student community in the INES and CEE programs had been so welcoming. My special thanks go to Dr. Abhisek V. Manikonda, Dr. Livingstone Dumenu, and Akpovona Ojaruega, you've given me supports in so many ways, in both academic and personal life, thank you so much! Then to Dr. Vivek Francis, Babatunde Adeyeye, Manohar Seetharamu, I hold dearly to your friendships and supports through all these years. To my office mate Dr. Sol Park, it's been a great pleasure to share an office with you, and thank you for the bakeries and snacks that cheered me up. A special salute

to Cheng Yang, an old friend who shares my interests and world view deserves my sincere appreciation. Mike, Adeola, Dr. Saulick, Emmanuel, Weina, Liu, and name goes on and on, thank you, my friends, thank you all!

Dad and mom, thank you for your support and understanding, and there are no words to adequately express my gratitude and love for you, thank you, and I love you!

TABLE OF CONTENTS

LIST OF TABLES

LIST OF FIGURES

LIST OF ABBREVIATIONS

ACAA	American coal ash association
ASTM	American society for testing and materials
CAH	Calcium aluminate hydrate
Ca-LDH	Calcium based layered double hydrates
CASH	Calcium aluminate silicate hydrate
CCPs	Coal combustion products
CFA	Coal fly ash
CH	Calcium hydroxide
CM	COMSOL-MATLAB
CSH	Calcium silicate hydrates
DAS	Data acquisition system
DD	Data-driven
DI	Deionized watere
DSC	Differential scanning calorimetry analysis
DTG	Differential thermogravimetric analysis
EC	Electric conductivity
ELGs	Effluent limitations guidelines
FGD	Flue gas desulfurization
FI	Forecast interval
FS	Friedel's salts
FTIR	Fourier-transform infrared spectroscopy
HDPE	High-density polyethylene
HELP	Hydrologic evaluation of landfill performance
HT	Heat trasnfer
IC	Ion chromatography
ICP-OES	Inductively coupled plasma-optical emission spectrometry
L/S	leachate to CFA ratio

LCS	Leachate collection system
Ldc	Decarbonation
Ldh	Dehydration
LDHs	Layered double hydroxides
Ldx	Dehydroxylation
LOI	Loss-on-ignition
MAE	Mean absolute error
Mg-LDH	Magnesium based layered double hydrates
MSE	Mean squared error
MSH	Magnesium silicate hydrates
M-W effect	Maxwell-Wagner effect
NN	Neural Network
OMC	Optimum moisture content
P/O	Percolation to overburden thickness
POC	Primary oxide contents
RMSE	Root mean squared error
S/S	Solidification/stabilization
SCMs	Supplementary cementing materials
SEM	Scanning electron microscopy
SEM-EDS	Scanning electron microscopy with energy dispersive X-ray spectroscopy
SL	Simulated location
SRCS	Surface runoff collection system
ST	Solute transport
TDS	Total dissolved solids
TGA	Thermogravimetric analysis
TS	Total solids
TSS	Total suspended solids
TxDOT	Texas department of transportation
U.S. EIA	Energy Information Administration of the United States

U.S. EPA	Environmental Protection Agency of the United States
UF	Unsaturated flow
UNSAT-H	Unsaturated soil water and heat flow
UV	Ultraviolet
VWC	Volumetric water content
VWCDI	Volumetric water content of deionized water
VWCs	Volumetric water content of solution
XRD	X-ray diffraction
ZLD	Zero liquid discharge

CHAPTER 1 INTRODUCTION

Coal fly ash (CFA) is a major coal combustion by-product (CCP) composed mostly of fine particles in the silt size range, regulated by the U.S. EPA coal combustion residuals (CCRs) rule (U.S. EPA 2015a). Studies have shown that coal fly ash, when in contact with water, has the potential to release constituents of concerns (COCs) such as chromium (Cr), cadmium (Cd), lead (Pb), and selenium (Se) (Dudas 1981; Harris and Silberman 1983; Izquierdo and Querol 2012). According to American Coal Ash Association (ACAA), 64.5% of the annual production of coal fly ash was beneficially used in 2020, leaving 8.53 million tons of the material requiring proper storage or disposal (ACAA 2021). Flue gas desulfurization (FGD) wastewater is another by-product of the coal fire plant generated through air emission control, also regulated by the US EPA's Effluent Limitation Guidelines (ELGs) (U.S. EPA 2015, U.S. EPA 2020). The chemical compositions of FGD scrubber wastewater purges reported by the steam power plants indicate that the total dissolved solids (TDS) ranged from 6,500 to 26,000 mg/L with the chloride concentration in the range of 1,100 to 13,000 mg/L (U.S. EPA 2009). More details of the FGD scrubber purge is presented in Table 1.1.

Table 1.1: Influent to FGD wastewater treatment system FGD scrubber purge (U.S. EPA 2009).

Analyte	Number of Plants	Number of Samples	Minimum Concentration	Maximum Concentration	Units
Total Metals					
Aluminum	1	38	8,200	333,000	µg/L
Antimony	1	38	4.1	23	µg/L
Arsenic	4	99	58	5,070	µg/L
Barium	1	38	110	2,050	µg/L
Beryllium	1	38	ND (0.7)	113	µg/L
Boron	3	95	7,410	250,000	µg/L
Cadmium	2	51	ND (0.5)	302	µg/L
Chromium	2	51	1.7	350	µg/L

Cobalt	1	38	6.4	148	µg/L
Copper	2	43	12.8	456	µg/L
Iron	3	79	1,100	300,000	µg/L
Lead	1	38	14.7	252	µg/L
Magnesium	1	13	1,200,000	1,800,000	µg/L
Manganese	1	38	339	5,460	µg/L
Mercury	4	132	ND (0.1)	872	µg/L
Molybdenum	1	38	ND (2)	250	µg/L
Nickel	3	67	23.4	710	µg/L
Selenium	4	158	400	21,700	µg/L
Silver	3	44	ND (0.2)	65	µg/L
Thallium	2	46	ND (4)	746	µg/L
Vanadium	1	38	14.2	14,800	µg/L
Zinc	4	72	33.1	1,060	µg/L
Dissolved Metals					
Mercury	1	17	60	440	µg/L
Selenium	2	33	130	3,000	µg/L
Classicals					
BOD5	1	8	3.4	21	mg/L
COD	2	49	140	1,100	mg/L
Total suspended solids	2	111	24	14,000	mg/L
Total dissolved solids	3	106	6,500	26,000	mg/L
Sulfate	4	85	780	4,100	mg/L
Chloride	4	104	1,100	13,000	mg/L
Bromide	1	28	43	96	mg/L
Fluoride	1	37	6.8	57	mg/L
Nitrate/nitrite	2	76	ND (10.0)	270	mg/L
Total Kjeldahl nitrogen	2	37	2.8	24	mg/L
Total phosphorus	1	1	4	4	mg/L

* The maximum concentration presented is the maximum detected value in the data set, unless all the results in the data set were not detected for the analyte.

FGD wastewater is treated at the plants using a combination of several technologies, including biological, zero-valent iron, membrane filtration, thermal evaporation, and other innovative pilot-scale tested technologies. These treatment processes inevitably produce downstream wastes such as biological sludge and FGD rejects/concentrates, which require additional treatments or special disposal operations. Therefore, additional management steps beyond the current practice are necessary to achieve a closed-loop or zero liquid discharge (ZLD) operation.

Motivated by the obvious operational benefits and environmental impact of reducing FGD wastewater discharge, onsite co-disposal of the CFA and FGD brine is the preferred management practice by some power plants as the CCRs rule requires the dry disposal of coal fly ash in an engineered landfill (U.S. EPA 2009). The co-disposal approach can potentially serve as the final step for the closed-loop ash and liquid management operation. However, for plants using FGD brine as the conditioning and molding liquid of dry ash, the compacted ash-brine mixture is likely to produce a structurally and hydraulically unstable material that may be susceptible to high water infiltration and result in the generation of a large quantity of contaminated fluids/leachate. The required additional treatment of the leachate generated from the mixture may result in a significant increase in the operational expenses of the engineered landfill. Thus, this research focuses on evaluating some performance aspects of the co-disposal practices where FGD brine is used to condition the CFA in an engineered landfill vis-à-vis an innovative paste encapsulation technology implemented in a paste landfill. This innovative alternative paste encapsulation technology has been shown in lab experiments to produce a structurally stable material that generates little to no leachate, thereby minimizing the potential contamination of groundwater.

1.1. Chemical Properties of CFA

1.1.1. Chemical compositions of CFA

The chemical compositions of coal fly ash depend on various factors such as the source of coal, the method of combustion, and the co-combustion additives (Chou 2012; Daood et al. 2014; Ramezanianpour 2014; Tharaniyil 2004). In general, the primary oxide compositions (POC) of a CFA are constituted of oxygen (O), silicon (Si), calcium (Ca), aluminum (Al), iron (Fe) with minority elements such as magnesium (Mg), sodium (Na), potassium (K), titanium (Ti), manganese (Mn), sulfur (S), phosphorus (P) (Blissett and Rowson 2012; Ramezanianpour 2014). Research also found the presence of rare earth elements (REEs) such as yttrium (Y) and scandium (Sc) with heavy metals such as lead (Pb) and cobalt (Co) and trace elements Arsenic (Ar), chromium (Cr), Cadmium (Cd), Selenium (Se) in coal fly ash (Fernández-Turiel et al. 1994; Furr et al. 1977; Garavaglia and Caramuscio 1994; Izquierdo and Querol 2012; Kashiwakura et al. 2013; da Silva 2017; Tolhurst 2015). The unburnt carbon and organic compounds in coal fly ash are reported as loss-on-ignition (LOI) (ASTM 2012; Külaots et al. 2004; Rubio et al. 2007). The summary of the ranges of chemical compositions in coal fly ash from different regions is presented in Table 1.2.

Table 1.2: Summary of coal fly ash composition ranges in different regions (Bhatt et al. 2019)

Weight %	United States	China	South Africa	India	Australia	Europe	Canada
SiO2	34.9-58.5	35.6-57.2	46.3-67	50.2-59.7	31.1-68.6	28.5-59.7	35.5-62.1
Al2O3	19.1-28.6	18.8-55	21.3-27	14-32.4	17-33	12.5-35.6	12.5-23.2
Fe2O3	3.2-25.5	2.3-19.3	2.4-4.7	2.7-16.6	1-27.1	2.6-21.2	3-44.7

CaO	0.7-22.4	1.1-7	6.4-9.8	0.6-9	0.1-5.3	0.5-28.9	1.2-13.3
K2O	0.9-2.9	0.8-0.9	0.5-1	0.2-4.7	0.1-2.9	0.4-4	0.5-3.2
MgO	0.5-4.8	0.7-4.8	1.9-2.7	0.1-2.3	0-2	0.6-3.8	0.4-3.1
SO3	0.1-2.1	1-2.9	na	na	0-0.6	0.1-12.7	0.2-7.8
TiO2	1-1.6	0.2-0.7	1.2-1.6	0.3-2.7	1.2-3.7	0.5-2.6	0.4-1
Na2O	0.2-1.8	0.6-1.3	0-1.3	0.2-1.2	0-1.5	0.1-1.9	0.1-7.3
P2O5	0.1-1.3	1.1-1.5	0.3-0.9	na	0-3.9	0.1-1.7	0.1-1.5
MnO	na	nd	0-0.5	na	nd	0-0.2	na
LOI	0.2-20.5	nd	na	0.5-7.2	na	0.8-32.8	0.3-9.7

* nd = Not detected, na = Not available

1.1.2. Classification of CFA

The widely used ASTM C618 standard classifies the CFA into class F and C based on the percentages of their primary oxide contents (POC) (ASTM International 2017), and primarily as supplementary cementing materials (SCMs) for pozzolanic activity in concrete. The chemical and physical requirements used to classify CFA are presented in tables 1.3 and 1.4, respectively. The interpretation of chemical requirements by the Texas Department of Transportation (TxDOT) suggests the sum of SiO_2, Al_2O_3, and Fe_2O_3 for class C ash should be greater than 50 and less than 70 (Lianxiang et al. 2013). The class C coal fly ash typically has higher calcium content than class F, which gives class C ash cementitious properties in addition to the pozzolanic properties that both classes possess. Further classification of CFA based on the calcium content was developed by Shehata et al. (2000) that categorizes ash as type F, CI, and CH for its gravimetric calcium content of $< 8\% \pm 1\%$, $>8\%$ and $\leq 20\% \pm 2\%$, and $>20\%$, respectively. Owning to the high calcium contents in class C fly ash, it is a self-cementing material that may not require an additional hydraulic binder for a cementitious matrix as opposed to class F fly ash, which requires a hydraulic

binder to form a cementitious matrix and initiate the pozzolanic process. Loss on ignition (LOI) is an index parameter to estimate the level of unburnt carbon in the fly ash. Other fly ash materials not meeting the classification in Table 1.3 are generally referred to as off-specification fly ash and are not used in concrete.

Table 1.3: Chemical requirements for CFA classification (ASTM International 2017)

	Class F	Class C
Silicon dioxide (SiO2) plus aluminum oxide (Al2O3) plus iron oxide (Fe2O3), min, %	70	50
Sulfur trioxide (SO3), max, %	5	5
Moisture content, max, %	3	3
Loss on ignition, max, %	6*	6

* The use of Class F pozzolan containing up to 12.0 % loss on ignition may be approved by the user if either acceptable performance records or laboratory test results are made available.

Table 1.4: Physical requirements for CFA classification (ASTM International 2017)

	Class F	Class C
Fineness:		
Amount retained when wet-sieved on 45 μm (No. 325) sieve, max, %	34	34
Strength activity index:		
With Portland cement, at 7 days, min, percent of control	75	75
With Portland cement, at 28 days, min, percent of control	75	75
Water requirement, max, percent of control	105	105
Soundness:		
Autoclave expansion or contraction, max, %	0.8	0.8

Uniformity requirements:		
Density, max variation from average, %	5	5
Percent retained on 45-μm (No. 325), max variation, percentage points from average	5	5

1.1.3. Morphology and mineralogy of CFA

Despite the homogeneous appearance of the coal fly ash, it is a mixture of unburned carbon, inorganic solid spheres, inorganic irregular particles, inorganic hollow spheres, and the debris of the hollow spheres (Blissett and Rowson 2012; Fisher et al. 1978; Külaots et al. 2004; Ranjbar and Kuenzel 2017). The formation mechanism of these particles is shown in Figure 1.1. The hollow spheres in the coal fly ash are known as the cenosphere and the plerosphere, which means a hollow sphere and a hollow sphere packed with spheres (Fisher et al. 1976). However, cenosphere is often referred to as the fraction of the coal fly ash particle that has a density lower than that of water, which is misleading since such a structure is also typically observed in denser particles (Fisher et al. 1978; Ghosal and Self 1995; Hulett and Weinberger 1980; Ranjbar and Kuenzel 2017). The external gas infiltration and the internal gas generation are two theories proposed for the hollow sphere formation (Dudas and Warren 1987; Fisher et al. 1976; Ghosal and Self 1995; Li et al. 2013; Ranjbar and Kuenzel 2017; Sarofim et al. 1977).

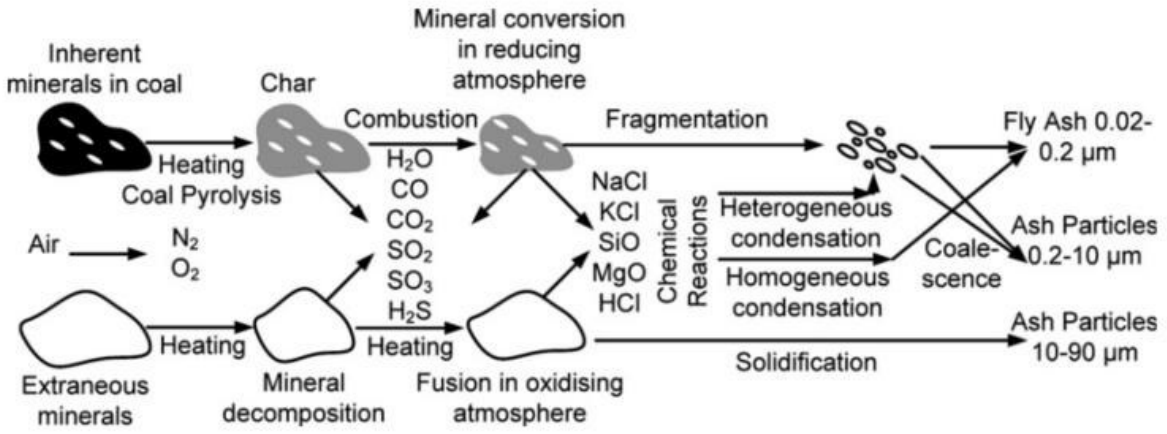

Figure 1.1: Simplified mechanism of CFA formation from pulverized fuel combustion (Blissett and Rowson 2012).

Dudas et al. (1987) identified a more reactive glass hull than the interior matrix in the solid particles, suggesting the particle is ready for reactions (Figure 1.2). Typical minerals in class F coal fly ash are mullite, quartz, magnetite, hematite, and amorphous phase (Bhagath Singh and Subramaniam 2017a; Hulett and Weinberger 1980; Towler et al. 2002). The general structure of class F coal fly ash particles in terms of mineralogy can be described as an amorphous aluminosilicate glass body embedded with mullite skeleton and coated with metal oxides deposits of crystalline phases on the exterior (Dudas and Warren 1987; Hansen and Fisher 1980; Hulett and Weinberger 1980; Ranjbar and Kuenzel 2017). The X-ray diffraction (XRD) analysis is the most widely used method for mineralogy determination for the coal fly ash particles. The XRD-Rietveld method can quantitatively analyze each mineral phase (Bhagath Singh and Subramaniam 2017b; Davis et al. 1977). The relative quantity of the amorphous phase in coal fly ash is used as an indicator for various reactions such as aluminum extraction and hydration since the crystalline is chemically stable (Bhagath Singh and Subramaniam 2016, 2017b; Guo et al. 2017; Luo et al. 2016).

Therefore, the quantitative analysis of the mineralogy of the CFA, especially on the amorphous phase, provides essential information on the potential reactivity of the ash.

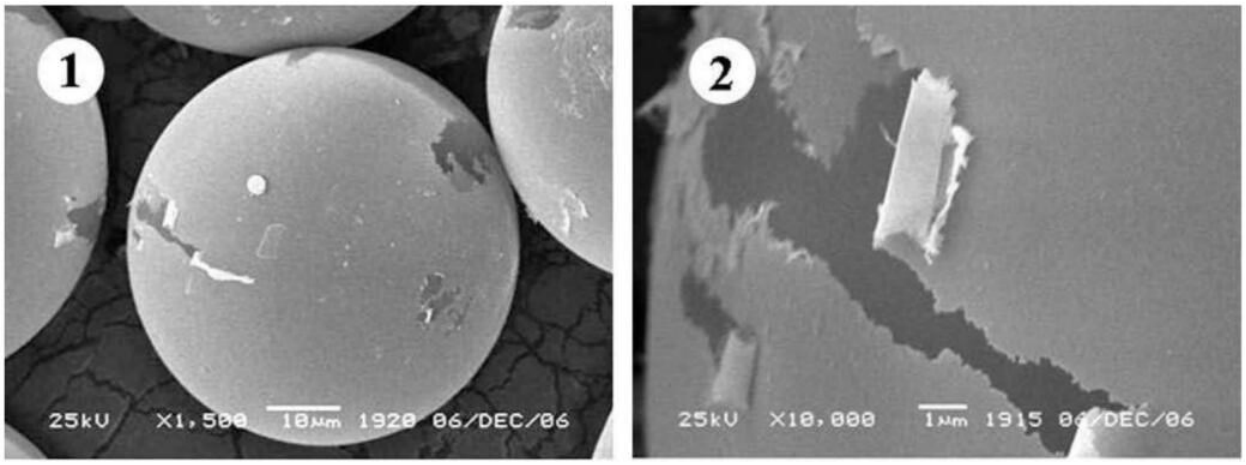

Figure 1.2: Scanning electron microscopy (SEM) image of thin film on the surface of fly ash particles (Anshits et al. 2010).

1.1.4. Dissolution of CFA in the alkaline environment

The dissolution of the amorphous phase of CFA in an alkaline environment is widely studied for beneficial uses such as cement replacement, geopolymer synthesis, desilication for aluminum and titanium extraction, and mullite synthesis (Blissett and Rowson 2012; Paul et al. 2007; Robl et al. 2017; Somna et al. 2011; Su et al. 2011; Tanaka et al. 2004). The dissolution process in an alkaline environment can be described as the balance between the dissolution of silicate and the precipitation of metal-silicate complex (Gallup 1997, 1998; Oelkers et al. 1994; Snellings 2013, 2015). The dissolution process in the hyperalkaline environment (pH≥11) is studied for cement replacement, where calcium hydroxide is the provider of alkalinity and calcium for cementitious reactions (Arulrajah et al. 2017; Bhatt et al. 2019; Robl et al. 2017; Snellings 2013). However,

these studies typically use sodium hydroxide and potassium hydroxide to create the alkaline environment, which can lead to overestimation of dissolution rate attributed to these alkaline metals by complexation and charge balance (Criscenti et al. 2005; Davidovits 2008; Gasteiger et al. 1992; La Plante et al. 2019). The aluminum released from the dissolution of the amorphous aluminosilicate also serves as an inhibitor by the absorption of $Al(OH)_4^-$ and the precipitation of aluminum silicate precipitates (Gabelich et al. 2005; Gallup 1997, 1998; Pokrovski et al. 1996; Snellings 2013, 2015). The aluminum silicate precipitation is confirmed in the study done by Lee et al. (2002), which showed the secondary precipitation on the ash particles by using SEM imagining.

Interestingly, a lower dissolution rate of aluminum than silicate in alkaline leaching of a class F coal fly ash was observed in the same study. In contrast, the addition of soluble silicate at lower concentrations enhanced both the rate and the final concentration of aqueous aluminum (Lee and van Deventer 2002). Since the dissolution of aluminosilicate is the only source of aluminum, the increase of aqueous aluminum indicates the increased glassy phase dissolution. The phenomenon can be explained by the removal of aqueous aluminum from the surface of glass particles by precipitation of aluminum silicate in bulk solution, which is similar to the self-sustained hydration process by the formation of precipitates described by Snellings (2015) and the promotion of aluminum dissolution by increase stirring speed (Tanaka and Fujii 2009). The calcium and iron tend to precipitate during the alkaline dissolution of the amorphous phase and can inhibit the dissolution process (Izquierdo and Querol 2012; Lee and van Deventer 2002; Snellings 2015). The release of metals from the amorphous phase results in a surface enriched in unstable silica, which is susceptible to alkaline dissolution (Snellings 2013, 2015). The dissolved silicate from the surface layer is then diffused into the bulk solution and forms new precipitates with dissolved metals,

reproducing the concentration gradient of silicate and metals that promotes further dissolution (Crundwell 2014; Snellings 2013). Evidence of the existence of the diffusion layer has been provided using SEM imaging showing the apparent presence of spherical fly ash particles and the mullite skeleton separated from the surrounding solid matrix by a clear gap after curing in both hyperalkaline environment and geopolymerization environments (Bakharev 2005; Lee and van Deventer 2002).

1.1.5. Cementitious and pozzolanic reactions with CFA

The main chemical reactions involved in the solidification of waste material using lime and coal fly ash can be categorized as cementitious and pozzolanic reactions. The interactions between cementitious material and water generate a large amount of heat due to the exothermic hydration reaction or the exothermic dissolution process, which is often used for monitoring hydration kinetics by calorimetry (Bentz 2014; Malhotra and Mehta 1996; Scrivener et al. 2018; Xu et al. 2017; Yin et al. 2018). The gelation and precipitation of cementitious products such as calcium silicate hydrates (CSH), calcium aluminate hydrates (CAH), and calcium aluminate silicate hydrates (CASH) create networks that bond grains in the system and form a dense matrix (Königsberger et al. 2016; Scherer 1999). The formation of cementitious products by the reactions between calcium hydroxide (CH) and fine particulate silicate/aluminosilicate in the presence of water is referred to as the pozzolanic reaction (Marsh and Day 1988; Massazza 1998; Sargent 2015). The water consumption by the pozzolanic reaction depends on the final CSH product (Marsh and Day 1988; Shi and Day 2000). The kinetic controlling process in the pozzolanic reaction is the dissolution of the silicate material, resulting in a continuous reaction that can last as long as five years (Sargent 2015; Shi and Day 2000). The class F coal fly ash in the paste encapsulation technology only serves as the pozzolan while lime provides the cementitious

properties, which indicates the strength development of the mixture will significantly depend on the dissolution of amorphous aluminosilicate in CFA. The products of cementitious and pozzolanic processes then solidify and densify the matrix by occupying the initial pore volume. The stabilization of heavy metals in the cemented matrix is mainly achieved by substitution of calcium in cementitious products or precipitate, while the anions can be chemically bond by the formation of layered double hydrate (LDHs) such as Friedel's and Kuzel's salts (Birnin-Yauri and Glasser 1998; Huang et al. 2017; Manikonda 2020; Manikonda et al. 2019; Mesbah et al. 2011; Renew et al. 2016; Rose et al. 2000, 2001). Other stabilization mechanisms using cementitious mixture include sorption, chemical precipitation, and encapsulation through the formation of dense materials (Chen et al. 2009; Renew et al. 2016).

1.2. Co-disposal of CFA and FGD Brine in the Landfill

While the CFA is required to be disposed of in an engineered landfill by U.S. EPA (U.S. EPA 2015b), the co-disposal material is subject to the same requirement. The liquids produced during the operation of an engineered landfill are the surface runoff and the bottom leachate, which are regulated under the ELGs rules (U.S. EPA 2020). Considering the inorganic nature of most CFA and FGD brine, the salinity in the co-disposed mixture is likely to be released through the liquids generated from the landfill. In this case, the effectiveness of salinity retention of the co-disposed material can be evaluated by the release of dissolved solids within the runoff and leachates.

1.2.1. Co-disposal through compaction

The co-disposal of CFA with FGD brine by compaction is a convenient practice for some facilities, which used the brine as an alternative liquid source for CFA moisture conditioning and

dust control measures. Considering some ashes contain a certain amount of lime content that gives the material cementitious properties but have no commercial values, the compacted mixture of such CFA and FGD brine could experience S/S required to sequestrate salinity (Fatoba 2010).

While the CFA used in this study process has negligible cementitious properties, the S/S is unlikely to occur in the compacted co-disposal material without the addition of hydraulic binder(s). Therefore, the material is likely to behave like compacted fine-grain soil, and the release of salinity from FGD brine will be dominantly through the moisture flow within the material. The hydraulic performance of compacted solid materials in a landfill such as evaporation, infiltration, and leachate generation is highly dependent on the local weather conditions, which are often required site-specific studies. If the leachate and runoff generated from the landfill do not meet environmental discharge requirements, further treatments of these liquids may compromise the effort to achieve the ZLD strategy. Therefore, the sequestration effectiveness of salinity in a compacted CFA- FGD brine co-disposal material in a landfill requires a weather-specific study.

1.2.2. Paste encapsulation technology

The paste encapsulation technology, which involves mixing CFA, brine, and hydraulic binders(s) such as lime or cement, is characterized by the rheology of the fresh mixture and the stabilization/solidification (S/S) processes of its hydrated material. The mixing process produces a mixture of materials with the physical feature of a paste, which can be transported by pump to a paste landfill. The S/S process is an established technology and has been successfully used for more than 160 superfund sites, including 16 industrial/municipal landfills sites and 38 waste management/disposal sites (U.S. EPA 2000). The solidification process targets the reduction of water infiltration into the matrix, while the stabilization ensures the reduction of the mobility of contaminants with water (U.S. EPA 2000). The traditional S/S process requires the mixture to be

compacted to its maximum dry unit weight at or near the optimum moisture content, significantly limiting the maximum liquid-to-solid ratio in the blend. However, with paste technology, the overall operational expense will decrease since the liquid-to-solid ratio in the mixture increase. As a result, the paste encapsulation technology, which operates at a 30% or higher liquid-to-solid ratio, is gaining more acceptance by waste management operators at coal-fired power plants more so as U.S.EPA has evaluated the paste encapsulation as the least-cost nationally available alternative for brine disposal.

The conceptual diagram of the proposed closed-loop system with the implementation of paste encapsulation technology is shown in Figure 1.3. The red dash lines refer to the material flow if the paste encapsulation technology option is not implemented. The blue line refers to environmentally safe discharge from the system, and the green line represents the materials input from outside the system.

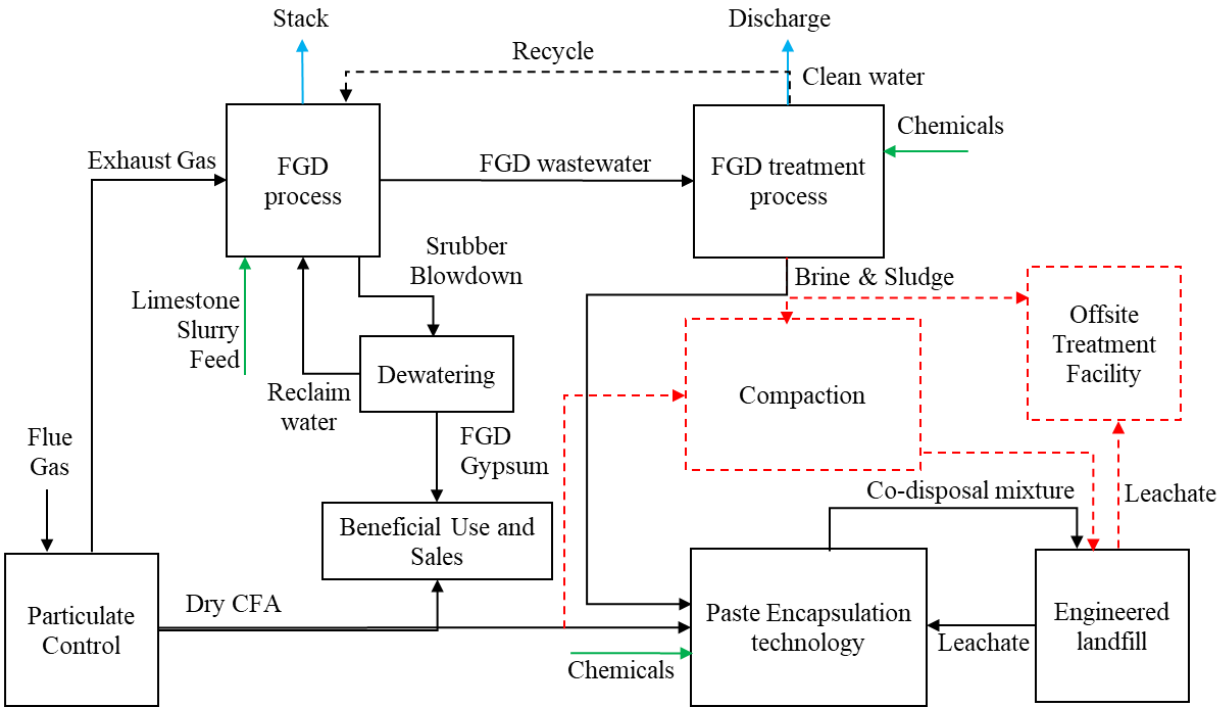

Figure 1.3. Conceptual diagram of the proposed closed-loop system with the implementation of paste encapsulation technology.

The main goal of the mixing process in the paste encapsulation technology is to produce a homogeneous paste mixture while providing kinetic energy for the initial dissolution of materials. The controlling factors for the mixing process are the duration and the rate of mixing, with circumstantial factors such as ambient temperature and humidity. The mixing rate determines the shear applied to the mixture by the stirrer, which controls the efficiency of energy transfer and effectiveness of stirring (Dickey and Fasano 2004). Considering the high cost of additional energy, the current process does not implement a temperature and humidity control system for the mixing chamber. The pilot mixing system does not monitor the pH and the electric conductivity of the mixture before the addition of the hydraulic reagent and before the deployment of the mixture. The quality control for each batch of mixtures focuses on the workability, which corresponds to the

pumpability of paste. The workability of the mixture is assessed through a slump test prior to deposition (ASTM 2018).

The paste encapsulation requires the addition of hydraulic binders such as cement or quick lime, FGD brine, and CFA (a material with pozzolanic properties). The properties of the raw materials result in the formation of a dense matrix with high resistance to water infiltration after curing. The mixture's ability to stabilize the target contaminants has been attributed to the formation of minerals or the adsorption process. The formation of halide binding minerals such as layered double hydroxides (LDHs) and the ability to retain heavy metal through sorption is the primary mechanism in the current application of paste technology for co-disposal CFA-FGD wastewater (Manikonda et al. 2019; Renew et al. 2016). Although the LDHs have proven to sequester chloride ions successfully, chloride retention's potential depends on the formation of LDHs in the paste. A recent lab-scale leaching test performed by Zhang et al. (2020) suggested that most of the chloride in the paste is likely to be removed from the matrix with low LDHs formation. Solidification becomes the critical aspect of paste mixtures with unfavorable LDHs formation conditions as it reduces or prevents water infiltration. Due to the subject's novelty, only a handful of conceptual studies are available from research partners (Ellison 2019; Ellison et al. 20s17; Oza et al. 2015; Zhang et al. 2020).

1.3. Dissertation Aims and Objectives

This dissertation research aims to provide a quantitative analysis of the co-disposed CFA - FGD brine material through compaction method and paste technology method in terms of halides sequestration and the hydraulic performances (leachate/runoff generation) under the field conditions. Two instrumented testbeds simulating the characteristics of the co-disposal methods

were constructed and monitored from 11/8/2018 at the Energy Production and Infrastructure Center (EPIC) courtyard in UNC Charlotte. The purpose of this research is:

1. Quantitatively evaluate the halide sequestration and hydraulic performance of CFA-FGD brine co-dispose by compaction method under a field environment.

The chemical properties of the CFA and the potential chemical reactions associated with the stabilization/solidification process have been discussed in detail in the previous sections. While the CFA used in this study does not possess the self-cementing ability, the retention of halides in the compacted CFA-FGD co-disposal material relies heavily on the local weather condition since the salinity is only expected to be released in the leachate and runoff. In this case, the leachate and runoff generated from the compacted material may require additional treatment if the liquids do not meet regulatory requirements for discharge. While the quantity and quality of the leachate and runoff are the keys to the design and operation of an engineered landfill, the moisture content profile will provide valuable information for designing leachate management strategies.

2. Quantitatively evaluate the halide sequestration and hydraulic performance of CFA-FGD brine co-dispose by paste encapsulation technology under a field environment.

Due to the novelty of applying paste encapsulation technology for co-disposal of CFA-FGD brine in an engineered landfill, the investigation in a testbed provides insight into the halide sequestration and hydraulic behaviors under natural environments. While leaching tests represent the worst-case scenario for halide release under continuous submerged conditions, the actual halide sequestration of the paste under a natural environment with discrete rainfalls and zero ponding conditions requires investigation. Information is also lacking on the

formation of layered double hydrates in paste material, which is the hypothesized halide sequestration pathway, under a field environment. The highly complex composition matrix in the CFA-FGD brine-quicklime mixture also interrogates the actual mineral formation in such a system.

3. Numerically simulate the heat transfer, moisture transfer, and solute transport processes in the compacted co-disposal material with a physics-based model.

While compaction is the most convenient method for CFA-FGD co-disposal, its performance under current weather conditions does not necessarily disqualify its use in other environments. Considering the hydraulic performance of the compacted co-disposal is highly dependent on the local weather condition, a site-specific study will be required to evaluate the applicability of such a method. As an alternative, a physics-based model simulating the moisture transfer, heat transfer, and solute transport validated with the field data in this experiment may provide a numerical template to explore the material's performances under different weather conditions and management strategies.

4. Numerically simulate the moisture movement in the compacted co-disposal material with a data-driven model.

The data acquisition system instrumented in testbeds collected an extensive quantity of data with good quality, which promoted the interest to develop a data-driven model to simulate the moisture flow in the material. The data-driven model provides the specified solution based on field observation without the need for extensive knowledge of physical processes. While the advancement of technology makes the use of large-scale in-situ, real-time sensor matrix in

the landfill feasible, the data-driven model may empower the facilities to make better decisions on daily operation and tackle extreme precipitation events.

The rest of this dissertation is structured into five chapters to systematically present the research and address the specific objectives presented above. Chapter 2 presents the preliminary results of the compacted test from the first year of the experiment, highlighting the rapid decrease of the EC in the leachate and the challenges associated with interpreting sensor measurement. Chapter 3 addresses the interpretation challenges observed in chapter 2 by developing a set of empirical equations to interpret the sensor measurements and presenting the quantitative chemical analysis on leachate and runoff to determine the effectiveness of halide retention. Further investigation on the correlation between hydraulic performance and weather conditions was performed to identify the potential leachate and runoff generation patterns, which was aided by the empirical equations and estimated EC profile. The temperature variation in the testbed and on the surface was also investigated to understand the heat transfer processes in the compacted material. Chapter 4 presents the analytical results for the halide sequestration and hydraulic performance of the paste testbeds. The chapter further investigated the mineralogy and leaching mechanisms of the paste material. Chapter 4 also investigated the temperature variation of the paste material under field conditions. Chapter 5 presented the development of a physics-based model simulating the compacted testbed, which allows the hourly simulation of the heat transfer, moisture transfer, and halide transport processes using COMSOL and MATLAB. The physics-based model was validated with the field data. With a large quantity of data, chapter 6 was dedicated to developing a data-driven model to simulate the change of moisture within the compacted material and explore potential challenges associated with the modeling. Considering the actual sensor measurement was the

bulk dielectric permittivity of the material, which could be translated into the volumetric water content, the data-driven model focused on simulating the permittivity to avoid bias from interpretation. Chapter 7 concludes the research findings and provides recommendations for facility operation and future research opportunities.

References

ACAA. (2021). *Coal Ash Recycling Rate Increases in 2020, Reversing Declines in Previous Two Years*.

Anshits, N. N., Mikhailova, O. A., Salanov, A. N., and Anshits, A. G. (2010). "Chemical composition and structure of the shell of fly ash non-perforated cenospheres produced from the combustion of the Kuznetsk coal (Russia)." *Fuel*, 89(8), 1849–1862.

Arulrajah, A., Mohammadinia, A., Horpibulsuk, S., Samingthong, W., and ArulArulrajahaAlirezaMohammadiniaaSuksunHorpibulsuk. (2017). "Influence of class F fly ash and curing temperature on strength development of fly ash-recycled concrete aggregate blends - ScienceDirect." *Construction and Building Materials*, Elsevier, 127, 743–750.

ASTM International. (2012). "D7348-13 Standard Test Methods for Loss on Ignition (LOI) of Solid Combustion Residues."

ASTM International. (2017). "ASTM C618-17a Standard Specification for Coal Fly Ash and Raw or Calcined Natural Pozzolan for Use in Concrete."

ASTM International. (2018). "Standard Test Method for Slump Flow of Self-Consolidating Concrete."

Bakharev, T. (2005). "Geopolymeric materials prepared using Class F fly ash and elevated temperature curing." *Cement and Concrete Research*, 35(6), 1224–1232.

Bentz, D. P. (2014). "Activation energies of high-volume fly ash ternary blends: hydration and setting." *Cement and Concrete Composites*, Elsevier, 53, 214–223.

Bhagath Singh, G. V. P., and Subramaniam, K. V. L. (2016). "Quantitative XRD study of amorphous phase in alkali activated low calcium siliceous fly ash." *Construction and Building Materials*, 124, 139–147.

Bhagath Singh, G. V. P., and Subramaniam, K. V. L. (2017a). "Direct decomposition X-ray diffraction method for amorphous phase quantification and glassy phase determination in binary blends of siliceous fly ash and hydrated cement." *Journal of Sustainable Cement-Based Materials*, 6(2), 111–125.

Bhagath Singh, G. V. P., and Subramaniam, K. V. L. (2017b). "Method for Direct Determination of Glassy Phase Dissolution in Hydrating Fly Ash-Cement System Using X-ray Diffraction."

Journal of the American Ceramic Society, 100(1), 403–412.

Bhatt, A., Priyadarshini, S., Acharath Mohanakrishnan, A., Abri, A., Sattler, M., and Techapaphawit, S. (2019). "Physical, chemical, and geotechnical properties of coal fly ash: A global review." *Case Studies in Construction Materials*, 11, e00263.

Birnin-Yauri, U. A., and Glasser, F. P. (1998). "Friedel's salt, Ca2Al(OH)6(Cl,OH)·2H2O: its solid solutions and their role in chloride binding." *Cement and Concrete Research*, 28(12), 1713–1723.

Blissett, R. S., and Rowson, N. A. (2012). "A review of the multi-component utilisation of coal fly ash." *Fuel*, 97, 1–23.

Chen, Q. Y., Tyrer, M., Hills, C. D., Yang, X. M., and Carey, P. (2009). "Immobilisation of heavy metal in cement-based solidification/stabilisation: a review." *Waste management*, Elsevier, 29(1), 390–403.

Chou, M.-I. M. (2012). "Encyclopedia of Sustainability Science and Technology." R. A. Meyers, ed., Springer New York, New York, NY, 3820–3843.

Criscenti, L. J., Brantley, S. L., Mueller, K. T., Tsomaia, N., and Kubicki, J. D. (2005). "Theoretical and 27Al CPMAS NMR investigation of aluminum coordination changes during aluminosilicate dissolution." *Geochimica et Cosmochimica Acta*, 69(9), 2205–2220.

Crundwell, F. K. (2014). "The mechanism of dissolution of minerals in acidic and alkaline solutions: Part II Application of a new theory to silicates, aluminosilicates and quartz." *Hydrometallurgy*, 149, 265–275.

Daood, S. S., Ord, G., Wilkinson, T., and Nimmo, W. (2014). "Fuel additive technology – NOx reduction, combustion efficiency and fly ash improvement for coal fired power stations." *Fuel*, 134, 293–306.

Davidovits, J. (2008). *Geopolymer Chemistry and Applications*. Geopolymer Institute.

Davis, J. A., Leckie, J., Anderson, M. A., Ferguson, J. F., Gavis, J., Pierce, M. L., and Moore, C. B. (1977). *Crystalline Components of Stack-Collected, Size-Fractionated Coal Fly Ash*. *J. Colloid Interface Sci*.

Dickey, D. S., and Fasano, J. B. (2004). "Mechanical design of mixing equipment." *Handbook of Industrial Mixing: Science and Practice*, Wiley Online Library, 1247–1332.

Dudas, M. J. (1981). "Long-term leachability of selected elements from fly ash." *Environmental*

Science and Technology, 15(7), 840–843.

Dudas, M. J., and Warren, C. J. (1987). "Submicroscopic model of fly ash particles." *Geoderma*, 40(1), 101–114.

Ellison, K. (2019). *Landfill Sequestration of Brine: Research Updates*. *World of Coal Ash*.

Ellison, K., Yeboah, N., and Pretorius, C. (2017). "Brine encapsulation bench and field testing recommendations." *2017 World of Coal Ash Conference (www. worldofcoalash. org)*.

Fatoba, O. O. (2010). "Chemical interactions and mobility of species infly ash-brine co-disposal systems." University of the Western Cape.

Fernández-Turiel, J. L., de Carvalho, W., Cabañas, M., Querol, X., and López-Soler, A. (1994). "Mobility of heavy metals from coal fly ash." *Environmental Geology*, 23(4), 264–270.

Fisher, G. L., Chang, D. P., and Brummer, M. (1976). "Fly ash collected from electrostatic precipitators: microcrystalline structures and the mystery of the spheres." *Science (New York, N.Y.)*, 192(4239), 553.

Fisher, G. L., Prentice, B. A., Silberman, D., Ondov, J. M., Biermann, A. H., Ragaini, R. C., and McFarland, A. R. (1978). "Physical and morphological studies of size-classified coal fly ash." *Environmental Science & Technology*, ACS Publications, 12(4), 447–451.

Furr, A., Parkinson, T., Hinrichs, R., Van, C., Bache, C., Gutenmann, W., and St, J. (1977). "National Survey of Elements and Radioactivity in Flyashes: Absorption of Elements by Cabbage Grown in Flyash-Soil Mixtures." *Environmental Science & Technology*, (Ak. Furr, ed.), 11(13), 1194.

Gabelich, C. J., Chen, W. R., Yun, T. I., Coffey, B. M., and "Mel" Suffet, I. H. (2005). "The role of dissolved aluminum in silica chemistry for membrane processes." *Desalination*, 180(1), 307–319.

Gallup, D. L. (1997). "Aluminum silicate scale formation and inhibition: Scale characterization and laboratory experiments." *Geothermics*, 26(4), 483–499.

Gallup, D. L. (1998). "Aluminum silicate scale formation and inhibition (2): scale solubilities and laboratory and field inhibition tests." *Geothermics*, 27(4), 485–501.

Garavaglia, R., and Caramuscio, P. (1994). "Coal Fly-Ash Leaching Behaviour and Solubility Controlling Solids." *Environmental Aspects of Construction with Waste Materials*, J. J. J. M. Goumans, H. A. van der Sloot, and T. G. B. T.-S. in E. S. Aalbers, eds., Elsevier, 87–102.

Gasteiger, H. A., Frederick, W. J., and Streisel, R. C. (1992). “Solubility of aluminosilicates in alkaline solutions and a thermodynamic equilibrium model.” *Industrial & engineering chemistry research*, ACS Publications, 31(4), 1183–1190.

Ghosal, S., and Self, S. A. (1995). “Particle size-density relation and cenosphere content of coal fly ash.” *Fuel*, 74(4), 522–529.

Guo, Y., Zhao, Z., Zhao, Q., and Cheng, F. (2017). “Novel process of alumina extraction from coal fly ash by pre-desilicating—Na2CO3 activation—Acid leaching technique.” *Hydrometallurgy*, Elsevier B.V., 169, 418–425.

Hansen, L. D., and Fisher, G. L. (1980). “Elemental distribution in coal fly ash particles.” *Environmental Science & Technology*, ACS Publications, 14(9), 1111–1117.

Harris, W. R., and Silberman, D. (1983). “Time-Dependent Leaching of Coal Fly Ash by Chelating Agents.” *Environ. Sci. Technol*, 17, 139–145.

Huang, C.-H., Renew, J. E., Engineering, C. and E., Burns, S., Yiacoumi, S., Chen, Y., and Tang, Y. (2017). “Immobilization of heavy metals in solidified/stabilized co-disposed bituminous coal fly ash and concentrated flue gas desulfurization wastewater.”

Hulett, L. D., and Weinberger, A. J. (1980). “Some etching studies of the microstructure and composition of large aluminosilicate particles in fly ash from coal-burning power plants.” *Environmental science & technology*, ACS Publications, 14(8), 965–970.

Izquierdo, M., and Querol, X. (2012). “Leaching behaviour of elements from coal combustion fly ash: An overview.” *International Journal of Coal Geology*, 94, 54–66.

Kashiwakura, S., Kumagai, Y., Kubo, H., and Wagatsuma, K. (2013). “Dissolution of Rare Earth Elements from Coal Fly Ash Particles in a Dilute H 2 SO 4 Solvent.” *Open Journal of Physical Chemistry*, 3, 69–75.

Königsberger, M., Hellmich, C., and Pichler, B. (2016). “Densification of CSH is mainly driven by available precipitation space, as quantified through an analytical cement hydration model based on NMR data.” *Cement and Concrete Research*, Elsevier, 88, 170–183.

Külaots, I., Hurt, R. H., and Suuberg, E. M. (2004). “Size distribution of unburned carbon in coal fly ash and its implications.” *Fuel*, 83(2), 223–230.

Lee, W. K. W., and van Deventer, J. S. J. (2002). “Structural reorganisation of class F fly ash in alkaline silicate solutions.” *Colloids and Surfaces A: Physicochemical and Engineering*

Aspects, 211(1), 49–66.

Li, Y., Gao, X., and Wu, H. (2013). "Further Investigation into the Formation Mechanism of Ash Cenospheres from an Australian Coal-Fired Power Station." *Energy & Fuels*, American Chemical Society, 27(2), 811–815.

Lianxiang, D., Elizabeth, L., and Andy, N. (2013). "Texas Department of Transportation Fly Ash Database and the Development of Chemical Composition–Based Fly Ash Alkali-Silica Reaction Durability Index." *Journal of Materials in Civil Engineering*, American Society of Civil Engineers, 25(1), 70–77.

Luo, Y. H., Zhu, D. Q., Pan, J., and Zhou, X. L. (2016). "Thermal decomposition behaviour and kinetics of Xinjiang siderite ore." *Mineral Processing and Extractive Metallurgy*, Taylor & Francis, 125(1), 17–25.

Malhotra, V. M., and Mehta, P. K. (1996). *Pozzolanic and cementitious materials*. Taylor & Francis.

Manikonda, A., Ogunro, V. O., Ellison, K. M., and Moo-Young, K. (2019). "Synthesis of Friedel's Salt for Application in Halide Sequestration Using Paste Encapsulation Technology." *Geo-Congress 2019: Geoenvironmental Engineering and Sustainability*, American Society of Civil Engineers Reston, VA, 167–176.

Marsh, B. K., and Day, R. L. (1988). "Pozzolanic and cementitious reactions of fly ash in blended cement pastes." *Cement and concrete research*, Elsevier, 18(2), 301–310.

Massazza, F. (1998). "Pozzolana and pozzolanic cements." *Lea's chemistry of cement and concrete*, Elsevier, London, 4, 471–631.

Mesbah, A., François, M., Cau-dit-Coumes, C., Frizon, F., Filinchuk, Y., Leroux, F., Ravaux, J., and Renaudin, G. (2011). "Crystal structure of Kuzel's salt 3CaO·Al2O3·1/2CaSO4·1/2CaCl2·11H2O determined by synchrotron powder diffraction." *Cement and Concrete Research*, 41(5), 504–509.

Oelkers, E. H., Schott, J., and Devidal, J.-L. (1994). "The effect of aluminum, pH, and chemical affinity on the rates of aluminosilicate dissolution reactions." *Geochimica et Cosmochimica Acta*, Elsevier Ltd, 58(9), 2011–2024.

Oza, S., Ogunro, V., Daniels, J., and Ellison, K. M. (2015). "Sequestration of Halides from FGD Wastewater through Lime Stabilization of Fly Ash." *2015 World of Coal Ash Conference.*

Retrieved from http://www. flyash. info/2015/064-ogunro-2015. pdf.

Paul, K., Satpathy, S., Manna, I., Chakraborty, K., and Nando, G. (2007). "Preparation and Characterization of Nano structured Materials from Fly Ash: A Waste from Thermal Power Stations, by High Energy Ball Milling." *Nanoscale Research Letters*, 2(8), 397–404.

La Plante, E. C., Oey, T., Hsiao, Y.-H., Perry, L., Bullard, J. W., and Sant, G. (2019). "Enhancing Silicate Dissolution Kinetics in Hyperalkaline Environments." *The Journal of Physical Chemistry C*, American Chemical Society, 123(6), 3687–3695.

Pokrovski, G. S., Schott, J., Harrichoury, J.-C., and Sergeyev, A. S. (1996). "The stability of aluminum silicate complexes in acidic solutions from 25 to 150°C." *Geochimica et Cosmochimica Acta*, 60(14), 2495–2501.

Ramezanianpour, A. A. (2014). *Cement Replacement Materials: Properties, Durability, Sustainability*. *Springer Geochemistry/Mineralogy*, Springer Berlin Heidelberg, Berlin, Heidelberg.

Ranjbar, N., and Kuenzel, C. (2017). "Cenospheres: A review." *Fuel*, 207, 1–12.

Renew, J. E., Huang, C.-H., Burns, S. E., Carrasquillo, M., Sun, W., and Ellison, K. M. (2016). "Immobilization of Heavy Metals by Solidification/Stabilization of Co-Disposed Flue Gas Desulfurization Brine and Coal Fly Ash." *Energy & Fuels*, 30(6), 5042–5051.

Robl, T., Oberlink, A., and Jones, R. (2017). *Coal Combustion Products (CCPs): Characteristics, Utilization and Beneficiation*. Woodhead Publishing.

Rose, J., Moulin, I., Hazemann, J.-L., Masion, A., Bertsch, P. M., Bottero, J.-Y., Mosnier, F. F., Haehnel, C., Wiesner, M. R., Bottero, J.-Y., Mosnier, F. F., and Haehnel, C. (2000). "X-ray absorption spectroscopy study of immobilization processes for heavy metals in calcium silicate hydrates. 2. Zinc." *Langmuir*, ACS Publications, 16(25), 9900–9906.

Rose, J., Moulin, I., Masion, A., Bertsch, P. M., Wiesner, M. R., Bottero, J.-Y., Mosnier, F., and Haehnel, C. (2001). "X-ray absorption spectroscopy study of immobilization processes for heavy metals in calcium silicate hydrates. 2. Zinc." *Langmuir*, ACS Publications, 17(12), 3658–3665.

Rubio, B., Izquierdo, M. T., Mayoral, M. C., Bona, M. T., and Andres, J. M. (2007). "Unburnt carbon from coal fly ashes as a precursor of activated carbon for nitric oxide removal." *Journal of Hazardous Materials*, 143(1), 561–566.

Sargent, P. (2015). “21 - The development of alkali-activated mixtures for soil stabilisation.” F. Pacheco-Torgal, J. A. Labrincha, C. Leonelli, A. Palomo, and P. B. T.-H. of A.-A. C. Chindaprasirt Mortars and Concretes, eds., Woodhead Publishing, Oxford, 555–604.

SAROFIM, A. F., HOWARD, J. B., and PADIA, A. S. (1977). “The Physical Transformation of the Mineral Matter in Pulverized Coal Under Simulated Combustion Conditions.” *Combustion Science and Technology*, Taylor & Francis, 16(3–6), 187–204.

Scherer, G. W. (1999). “Structure and properties of gels.” *Cement and Concrete Research*, Elsevier, 29(8), 1149–1157.

Scrivener, K., Snellings, R., and Lothenbach, B. (2018). *A practical guide to microstructural analysis of cementitious materials*. Crc Press.

Shehata, M. H., and Thomas, M. D. A. (2000). “The effect of fly ash composition on the expansion of concrete due to alkali–silica reaction.” *Cement and Concrete Research*, Elsevier, 30(7), 1063–1072.

Shi, C., and Day, R. L. (2000). “Pozzolanic reaction in the presence of chemical activators: Part II—Reaction products and mechanism.” *Cement and Concrete Research*, Elsevier, 30(4), 607–613.

da Silva, E. (2017). “Metal leachability from coal combustion residuals under different pHs and liquid solid ratios.” *Journal of Hazardous Materials*, 341, 66–74.

Snellings, R. (2013). “Solution-Controlled Dissolution of Supplementary Cementitious Material Glasses at pH 13: The Effect of Solution Composition on Glass Dissolution Rates.” *Journal of the American Ceramic Society*, 96(8), 2467–2475.

Snellings, R. (2015). “Surface chemistry of calcium aluminosilicate glasses.” *Journal of the American Ceramic Society*, Wiley Online Library, 98(1), 303–314.

Somna, K., Jaturapitakkul, C., Kajitvichyanukul, P., and Chindaprasirt, P. (2011). “NaOH-activated ground fly ash geopolymer cured at ambient temperature.” *Fuel*, 90(6), 2118–2124.

Su, S. Q., Yang, J., Ma, H. W., Jiang, F., Liu, Y. Q., and Li, G. (2011). “Preparation of Ultrafine Aluminum Hydroxide from Coal Fly Ash by Alkali Dissolution Process.” *Integrated Ferroelectrics*, Taylor & Francis Group, 128(1), 155–162.

Tanaka, H., and Fujii, A. (2009). “Effect of stirring on the dissolution of coal fly ash and synthesis of pure-form Na-A and -X zeolites by two-step process.” *Advanced Powder Technology*,

20(5), 473–479.

Tanaka, H., Matsumura, S., and Hino, R. (2004). “Formation process of Na-X zeolites from coal fly ash.” *Journal of Materials Science*, Kluwer Academic Publishers, Boston, 39(5), 1677–1682.

Tharaniyil, R.-. (2004). *We Energies Coal Combustion Products Utilization Handbook*.

Tolhurst, L. (2015). *Commercial Recovery of Metals from Coal Ash*. *World of Coal Ash*.

Towler, M. R., Stanton, K. T., Mooney, P., Hill, R. G., Moreno, N., and Querol, X. (2002). “Modelling of the glass phase in fly ashes using network connectivity theory.” *Journal of Chemical Technology & Biotechnology*, (M. Cox, ed.), John Wiley & Sons, Ltd., Chichester, UK, 77(3), 240–245.

U.S. EPA. (2000). *Solidification/Stabilization Use at Superfund Sites*.

U.S. EPA. (2009). *Steam Electric Power Generating Point Source Category: Final Detailed Study Report*. United States Environmental Protection Agency, Washington, D.C.].

U.S. EPA. (2015a). “Effluent Limitations Guidelines and Standards for the Steam Electric Power Generating Point Source Category; Final Rule 40 CFR Part 423 US E P Agency Federal Register.”

U.S. EPA. (2015b). “Hazardous and Solid Waste Management System; Disposal of Coal Combustion Residuals From Electric Utilities; Final Rule.” *The Federal Register*, Federal Information & News Dispatch, Inc., Washington.

U.S. EPA. (2020). “Steam Electric Reconsideration Rule.” 40 C.F.R. Part 423.

Xu, G., Tian, Q., Miao, J., and Liu, J. (2017). “Early-age hydration and mechanical properties of high volume slag and fly ash concrete at different curing temperatures.” *Construction and Building Materials*, Elsevier, 149, 367–377.

Yin, B., Kang, T., Kang, J., Chen, Y., Wu, L., and Du, M. (2018). “Investigation of the hydration kinetics and microstructure formation mechanism of fresh fly ash cemented filling materials based on hydration heat and volume resistivity characteristics.” *Applied Clay Science*, Elsevier B.V., 166, 146–158.

Zhang, W., Oswal, H., Renew, J. E., Gallagher, B., Ellison, K., and Huang, C.-H. (2020). “Solidification/stabilization of flue gas desulfurization brine and coal fly ash for heavy metals and chloride immobilization: Effects of S/S conditions and zero-valent-iron pretreatment.”

Journal of Hazardous Materials, 384, 121463.

CHAPTER 2 PRELIMINARY RESULTS OF COMPACTED COAL FLY ASH/FLUE GAS DESULFURIZATION BRINE CO-DISPOSAL IN AN INSTRUMENTED TESTBED

Rui He, M.S. S.M. ASCE[1], Vincent O. Ogunro, Ph.D. A.M. ASCE[2], Kirk M. Ellison, M.S.[3]

Citation

He, R., Ogunro, V. O., and Ellison, K. M. (2022). "Preliminary Results of Compacted Coal Fly Ash/Flue Gas Desulfurization Brine Co-disposal in an Instrumented Testbed." *Geo-Congress 2022:* State of the Art & Practice in *Geotechnical Engineering*, American Society of Civil Engineers Reston, VA

Abstract

This study presents the preliminary results of coal fly ash (CFA) - flue gas desulfurization (FGD) brine co-disposal by compaction as a method to achieve the zero liquid discharge (ZLD) strategy in coal-fired steam electric power plant operation. While the method utilizes the FGD brine to reduce water consumption for CFA landfilling, the compacted mixture serves as a reservoir to store brine salinity. To test the method under the field condition in Charlotte, NC area, a testbed instrumented with volumetric water content (VWC) and temperature sensors was used to investigate the leachate/runoff generation and variation of moisture and salinity storage of the co-disposal mixture. The results from 11/2018 to 12/2019 showed the total collected runoff and the leachate was 11% and 37% of total precipitation, respectively. The analysis of leachates suggested the majority of salinity from added brine was removed by 754 mm precipitation. The preliminary results from this ongoing research indicate that the co-disposal method fails to retain the stored brine salinity under the local weather conditions due to a lack of stabilization ability, which can

lead to an increase of the landfill operational cost and will thus necessitate additional leachate treatment.

2.1. Introduction and Background

The major by-products generated by the coal-fired steam electric power plant are coal combustion products (CCPs) and flue gas desulfurization (FGD) products. Coal fly ash (CFA) is the main component of the CCPs, and it is regulated by the U.S. EPA's Coal Combustion Residuals (CCRs) rule (U.S. EPA 2015). Contaminants such as mercury and arsenic released from improper management of the CFA can lead to surface water and groundwater contamination (U.S. EPA 2019). The CCRs final rule requires CFA to be disposed in an engineered landfill, which requires the landfill to have a leachate collection system and a composite liner for groundwater protection. According to the report prepared by American Coal Ash Association (ACAA) (2019), 10.5 out of 26.6 million metric tons of fly ash produced in 2019 requires storage and/or disposal. Another product of most environmental concern from the power plant operation is the FGD wastewater. The FGD wastewater is regulated by the Effluent Limitations Guidelines (ELGs) (U.S. EPA 2020a). The chemical compositions of FGD scrubber wastewater purges reported by the steam power plants indicate that the total dissolved solids (TDS) ranged from 6,500 to 26,000 mg/L with high halide concentrations (U.S. EPA 2009). The FGD wastewater also contains contaminants such as mercury, cadmium, and arsenic (U.S. EPA 2020b). Despite the recent amendments to the CCR and ELGs rules that ease some regulatory requirements and deadlines, coal power plants still face many difficult decisions on the optimal management option for the facilities.

One management option involves co-disposal of CFA and FGD brine, which is generated by the use of volume reduction technologies such as membranes or thermal evaporation in order

to produce a brine of a low enough volume to be amenable to combination with CFA in the engineered landfill to achieve zero-liquid-discharge (ZLD) because of economic benefit and environmental responsibility considerations. Although the ZLD strategy aims at eliminating any wastewater stream leaving the facility, the process can produce solid waste if the brine is managed with an evaporation pond or solid recovery processes (Tong and Elimelech 2016). The cost of energy, land use, and potential environmental risks associated with the evaporation and solid recovery processes reduce their likelihood of being used as sustainable ZLD strategies. Since CFA requires disposal in an engineered landfill, the use of FGD wastewater or concentrated brine as the moisture conditioner or dust control for the CFA compaction could become a practical option as a part of the ZLD process. In this case, the compacted CFA and FGD brine mixture is expected to retain or impede the release of the contaminants and the salinity from the material matrix. This co-disposal strategy had been used in South Africa and showed promising results with coal fly ash containing 5% or more lime content (Fatoba et al. 2011). However, for compacted mixtures with CFA having lower lime content (less than 10%) that lacks cementitious properties to solidify and stabilize the matrix, this co-disposal strategy has not yet been investigated. Studies show the CFA can serve as a sorbent of heavy metals due to the negatively charged particle surface in an alkaline environment (Apak et al. 1998; Cho et al. 2005; Mohan and Gandhimathi 2009). The surface charge mechanism also suggests that CFA cannot simultaneously provide adsorption capacity for negatively charged anions such as chloride and bromide. In addition, leachate generation is also influenced by the local weather conditions. Thus, the ability of the compacted CFA/brine co-disposal to retain halides, especially a class F CFA co-disposal with a high halide concentration brine (salinity of 130,000 ppm), needs thorough investigation. In this study, an instrumented small-scale testbed simulating an engineered landfill under a field scenario is used to investigate: (1) the

leachate/runoff generation, (2) variation of internal moisture and temperature profile, and (3) the salinity retention of the compacted CFA/FGD brine material.

2.2.Material Characterization

2.2.1. Coal fly ash (CFA)

CFA from a steam electric power generating facility in the southeast USA was used in this study. The particle size distribution of the CFA was measured using a Horiba LA-910 laser diffraction particle size analyzer. The specific gravity was measured following ASTM D854-14 (ASTM International 2014). The quantitative mineralogical analysis of the CFA was conducted with a PANalytical X'Pert Pro diffractometer and the Rietveld refinement X-Ray diffraction (XRD) method. The Cu-Kα radiation was used for XRD, with the 2θ angle in the range of 5-90°. The chemical composition analysis was performed following ASTM D6349 (ASTM International 2013). The digested solution was analyzed with an inductively coupled plasma atomic emission spectrometer (ICP-AES). The CFA is classified as class F with a specific gravity of 2.322 at 20°C. The CFA is classified as non-plastic silty material, with the particle size distribution of D_{10}, D_{50}, and D_{90} equal 4.78 µm, 17.37 µm, and 54.57 µm, respectively. The major chemical compositions and the mineralogy of the CFA are presented in Table 2.1.

Table 2.1. Major chemical composition and mineralogy of the CFA

Mineral			Chemical Composition		
Quartz	5.0%	w/w	Al_2O_3	26.9%	w/w
Mullite	16.0%	w/w	SiO_2	53.5%	w/w
Magnetite	2.0%	w/w	Fe_2O_3	8.7%	w/w
Amorphous	75.0%	w/w	CaO	0.9%	w/w

2.2.2. Flue gas desulfurization (FGD) brine

FGD brine from a steam electric power generating facility in the southeast USA was used in this study. The FGD brine has a total solids (TS) of 0.216 gram per gram brine. The value of total suspended solids (TSS) in the brine is 0.005 gram per gram brine, with a total dissolved solids (TDS) of 0.211 gram per gram brine. The pH and the electric conductivity (EC) of the FGD brine are 8.11 and 131,585 µS/cm, respectively. The EC is used as the indicator of the ionic concentration and salinity of the solution in this study. To capture the changes in the pore fluid of the testbed over time, the brine characteristics at different dilution levels were measured. The density of the FGD brine at room temperature is 1.103 g/cm^3, and the 100 times diluted brine solution has a density of 1.002 g/cm^3. The change of EC and pH with the dilution levels of the FGD brine is as shown in Figure 2.1. The dilution was prepared with FGD brine and ultrapure deionized water with a resistivity of 18.2 MΩ·cm. As expected, the density of FGD brine decreases as the dilution increases, from approximately 1.1 g/cm^3 of brine to approximately 1.0 g/cm^3 at 20 times dilution level.

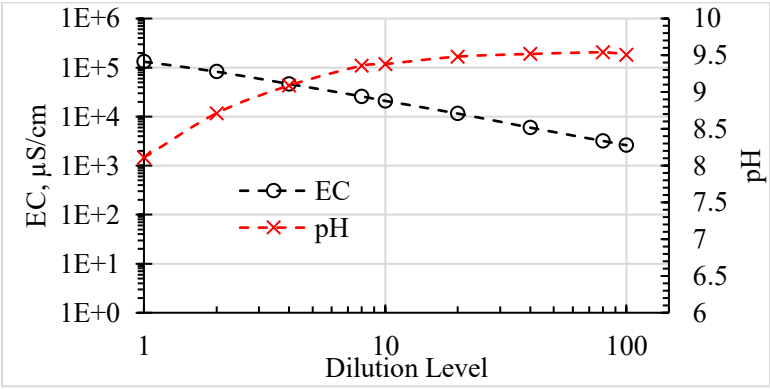

Figure 2.1. EC and pH of FGD brine at different dilution levels.

2.2.3. CFA-FGD brine mixture

The compaction test of the CFA was prepared according to ASTM D698 (ASTM International 2012) with deionized water (DI) and undiluted FGD brine using standard compaction energy of 600 kN-m/m^3. The maximum dry unit weights (γ_{max}) and optimum moisture contents (OMC) of CFA molded with DI and the FGD brine are 22.7%, 13.11 kN/m^3, and 22.0%, 13.55 kN/m^3, respectively. The dry unit weight of the CFA-FGD brine mixture accounted for the TS within the brine. The 95% maximum dry unit weight for CFA-FGD compaction is 12.17 kN/m^3. The mixture for the field test was prepared with a target moisture content of 22%. The compaction of the mixture was performed manually by tamping the mixture to the targeted volume. The interlayer surfaces were scarified before placing the next layer. The final average moisture content was 21.9%. Accounting for the TS of the brine, the dry unit weight of the mixture was 12.17 kN/m^3, which is equivalent to 11.62 kN/m^3 considering only the CFA solids. The volume fraction of CFA solids is 48.96%, with a potential maximum porosity of 51.04%. The saturated hydraulic conductivity of the CFA-DI mixture at the maximum dry unit weight was found to be 1×10^{-4} cm/s (Dumenu 2019), falling within a typical range of values of silty sand soils.

2.3.Instrumented Testbed

The body of the testbed is a High-Density Polyethylene (HDPE) tote with width, length, and height of 96.52 cm × 114.30 cm × 111.76 cm, respectively. The testbed is located at 35º18'33.3" N, 80 º44'31.9" W in Charlotte, NC. The external walls of the testbed are insulated with 15.88 cm thick R-19 fiberglass. The insulation is protected from precipitation and degradation by a layer of UV-resistant HDPE liner. The leachate collection system (LCS) is divided into the inner and annulus sections to investigate the potential influence of side leakage, as illustrated in Figure 2.2 a. The HDPE walls separating the two sections are 2.54 cm higher than the 17.78 cm

sand layer. The sand used in this study has a saturated hydraulic conductivity of 0.180 cm/s. The area of inner and annulus LCS are 1224.0 cm^2 and 9808.2 cm^2, respectively. The testbed is tilted at a 2% angle with the surface runoff collection system (SRCS) located at the lower end of the slope. The SRCS is an HDPE film lined trench filled with gravel, and the width, length, and depth of the SRCS are 7.62 cm, 96.52 cm, and 12.7 cm, respectively. The size range of gravel used in SRCS is 5 to 10 mm. Designated chemical resistant piping and HDPE are used to collect leachates and runoff. The exposed top surface of the testbeds routinely undergoes inspection and removal of any growth to eliminate potential evapotranspiration.

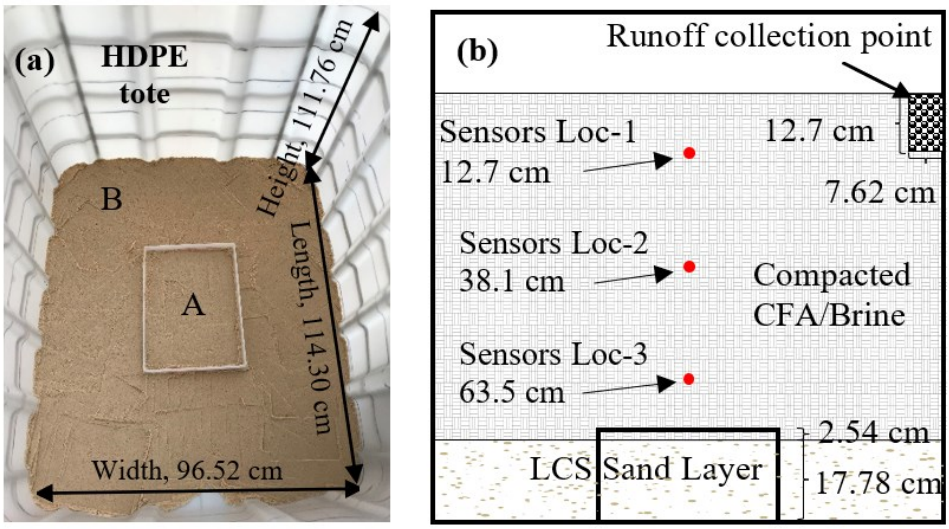

Figure 2.2. (a): Plan view of the (A) inner section and (B) annulus section of leachate collection system (LCS) in HDPE container, (b): Profile view schematic of the testbed.

An in-situ data collection system was implemented to investigate the spatial and temporal profile of both moisture and temperature of the testbed, as illustrated in Figure 2.2 (b). A set of one ML3 ThetaProbe volumetric water content (VWC) sensor and one T108 temperature sensor

was placed at each depth of 12.7 cm (Loc 1), 38.1 cm (Loc 2), and 63.5 cm (Loc 3) from the exposed surface. Dataloggers were programmed to collect hourly data from all sensors. The hourly local weather data are collected from a weather station located 5 meters from the testbed, and the data from the data collection system are collected and analyzed weekly.

2.4.Sensor Calibration for FGD Dilutions

The measurement of VWC by ML3 sensor was achieved by measuring the permittivity (Ɛ) of the mixture. As the pore solution predominantly contributes to the Ɛ of a soil mixture, a material-specific correlation can be used to translate the square root of permittivity ($Ɛ^{0.5}$) of the mixture to VWC (Topp et al. 1980). The $Ɛ^{0.5}$ of a porous medium depends on temperature, the solid properties, the VWC, and the salinity of the pore solutions (Chen and Or 2006a, 2006b). As with data reported by Rumble (2018), the influence of the temperature on $Ɛ^{0.5}$ was not considered in this study since the deviation of $Ɛ^{0.5}$ was only ±3% for the test temperature of 0 °C and 50 °C. While the influence of soil properties on the bulk $Ɛ^{0.5}$ also depends on the soil dry unit weight, this study only focused on the CFA matrix with a specific dry unit weight of 11.62 kN/m^3.

Consequently, the influence of pore solution's salinity on the $Ɛ^{0.5}$- VWC correlation was investigated with deionized water (DI) and FGD brine at different dilution levels (undiluted, 10- and 100-times dilution levels). The CFA and liquids were thoroughly mixed within a container and sealed for 24 hours to mellow (to achieve equilibrium), and then compacted in a 7.62 cm - diameter by 15.24 cm - height cylinder for testing. Three samples were prepared from each batch of the mixture, and the samples were oven-dried to determine the volumetric water content after measurement of the permittivity of the matrix. As shown in Figure 2.3, dilution significantly impacts the $Ɛ^{0.5}$- VWC correlation of the brine solutions. The data also suggests that at 100-times

dilution level of the brine, the correlation closely approaches that of the DI water. Therefore, selecting the appropriate correlation will be based on the dilution level that matches the EC value of the pore-solution.

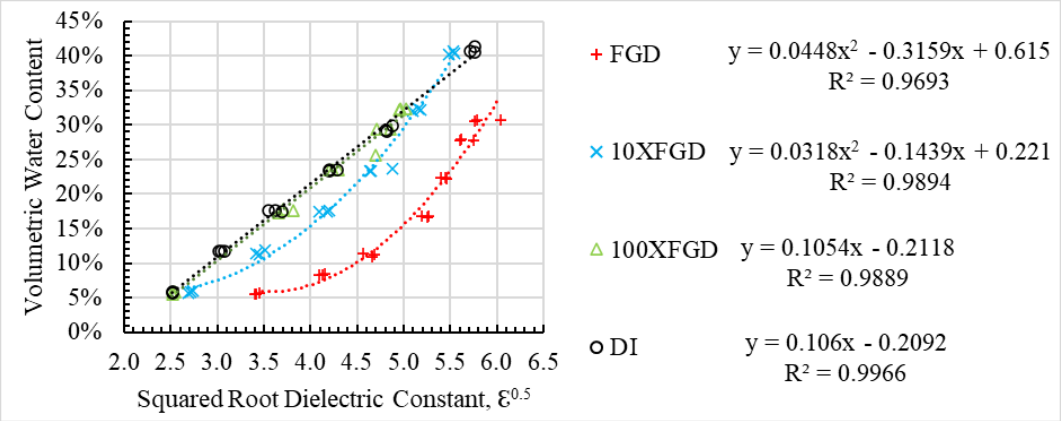

Figure 2.3. Permittivity – volumetric water content data with FGD brine dilutions and deionized water (DI).

2.5.Results and Discussion

2.5.1. Quantity and quality of runoffs and leachate

The area-normalized cumulative quantities of the leachates and runoff collected from the testbed between 11/6/2018 and 12/31/2019 are presented in Figure 4. With a total of 1625.6 mm precipitation received at the testbed location, the area normalized liquids collected from the runoff, inner drainage, and annulus drainage were 178.4 mm, 683.9 mm, and 594.6 mm, respectively. The initial moisture buildup in the testbed from precipitation events primarily occurred before 12/10/2018, when the first leachate was collected. Figure 2.4 also shows a noticeable pause in leachate generation between 4/19/2019 and 11/8/2019. Conversely, the runoff occurred mostly from April to September 2019 during the period of limited leachate generation. Furthermore, it can be deduced that frequent and low-intensity hourly precipitations during the winter and spring

seasons generate a larger amount of leachate with little runoff, while few but high-intensity hourly rainfalls in the summer and fall periods produce a large amount of runoff with little to no leachate.

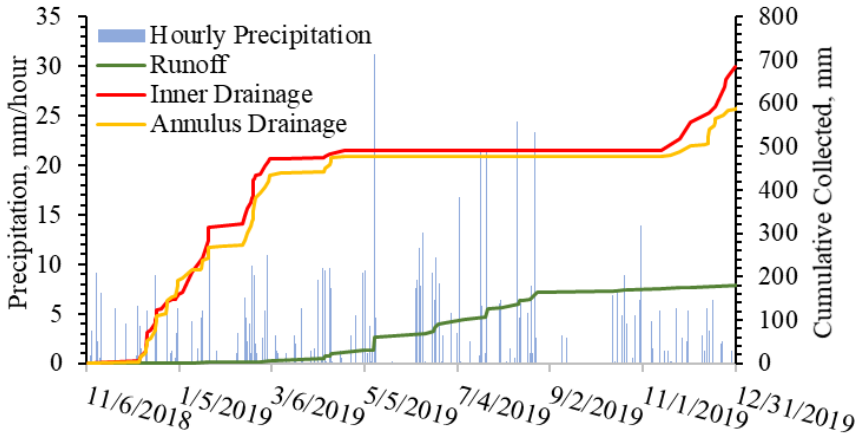

Figure 2.4. Area normalized cumulative leachate collected from annulus and inner sections, surface runoff, and hourly precipitation.

The EC and pH of leachates and runoffs collected during the study period are presented in Figure 2.5. The closely matched threads of quantity (Figure 2.4) and quality (Figure 2.5) of leachates collected from two LCS anecdotally indicate no significant preferential flow such as side leakage or fracture flow occurred during this study period. To simplify the analysis, the variation of pore solution salinity can be generally categorized into initial (undiluted) phase, transition (diluting) phase, and stable (diluted), corresponding to undiluted, 10-, and 100-times dilution levels of the brine (Figure 2.3) based on EC values. The redistribution of salinity before achieving the stable or diluted phase will lead to the spatial variation of pore fluid salinity in the compacted material. These processes include but not limited to wash off, leaching, advective flow, and diffusion. As diffusion most likely occurred against the direction of infiltration due to salinity

gradient, the selection of the $\varepsilon^{0.5}$ - VWC correlation during the initial (undiluted) and transition (diluting) phases is much more complex. The plateauing of EC at 3,000 µS/cm shown in Figure 2.5 as the leaching process continues was also observed in Figure 2.1 as the dilution level of FGD brine increases. The highly similar EC and pH variation trends during the leaching and diluting process support the use of $\varepsilon^{0.5}$ – VWC correlations established using different brine dilution levels.

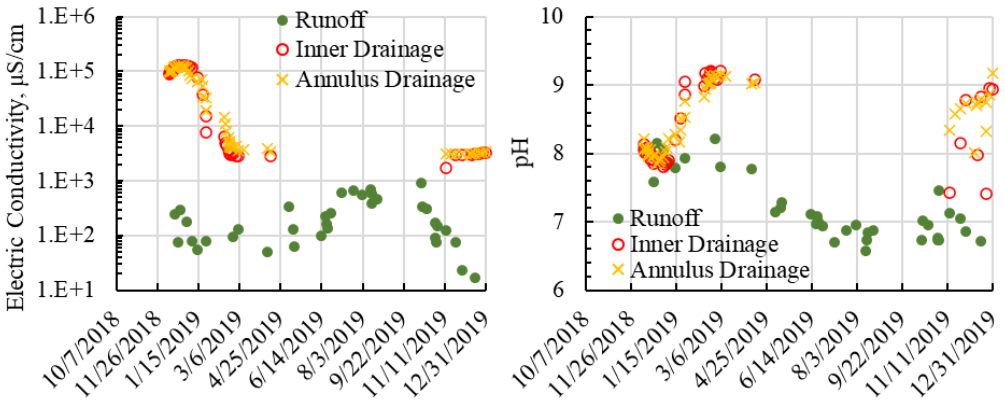

Figure 2.5. EC and pH of liquid samples from annulus, inner drainage, and surface runoff.

Figure 2.6 presents the electric conductivity (EC) and the total leachate to CFA ratio (L/S) of the testbed over the study period. Based on the previous discussion of the categorization of pore fluid into the initial, transition, and stable phases, the phases occurred at the L/S of approximately 0.2, 0.2 - 0.5, and greater than 0.5, respectively. At the L/S of 0.5, the EC value of the leachate had reduced from over 100,000 µS/cm to approximately 3,000 µS/cm, equivalent to the EC value of 100-times dilution level of the brine. The quantity of leachate with EC at the level of FGD brine released from the testbed was equivalent to the added brine at a mass ratio of 0.2. Since the EC was an indicator of the salinity, the release implies the majority of salinity in added brine as

removed from the testbed at L/S of 0.5. The analysis suggests the co-disposal of compacted CFA-FGD brine is ineffective in retaining the halides within the mixture in the weather and environmental conditions similar to Charlotte, NC.

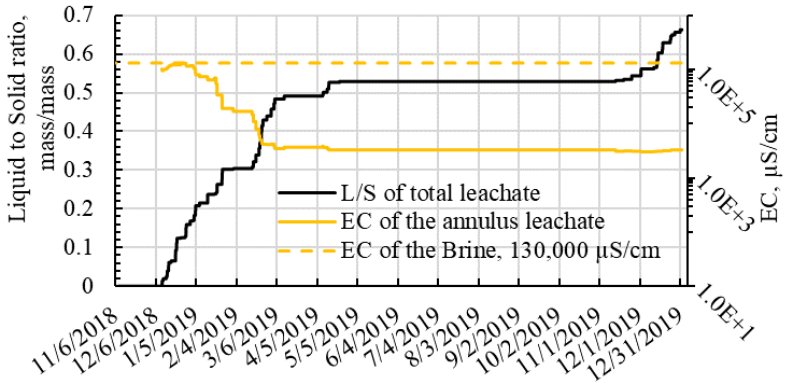

Figure 2.6. Total leachate to coal fly ash (L/S) ratio and EC of the annulus leachate.

2.5.2. Volumetric water content and temperature profile

For simplicity, the selection of $\varepsilon^{0.5}$ - VWC correlations for interpreting the field data is divided into initial, transition, and stable phases as the categories of salinity variation of the pore solution. As the initial phase assumes the salinity of pore solution equivalent to that of the undiluted brine, the transition phase assumes a 10-times dilution, and the stable phase assumes a 100-times dilution level. The selection of dilution curve used for each VWC sensor depended on the $\varepsilon^{0.5}$ trend, as shown in Figure 2.7. For the pore solution at a given salinity, $\varepsilon^{0.5}$ is expected to increase as the moisture content increases (Figure 2.3). If the $\varepsilon^{0.5}$ decreases significantly during or immediately after a precipitation event, it is reasonable to assume a reduction of pore solution salinity (Figure 2.3). The patterns identified as corresponding to the decrease in $\varepsilon^{0.5}$ with

precipitations are selected as the end of the initial phase or stage 1. The end of stage 1 for the sensors at locations 1, 2, 3 were observed on 11/15/2018, 12/9/2018, and 12/20/2018, respectively. While a distinct pattern can be observed for stage 1 due to the relatively significant magnitude of change, the shift from the transition to the stable phase was gradual. This study used one endpoint of stage 2, or transition phase, on 2/22/2019 for all sensors.

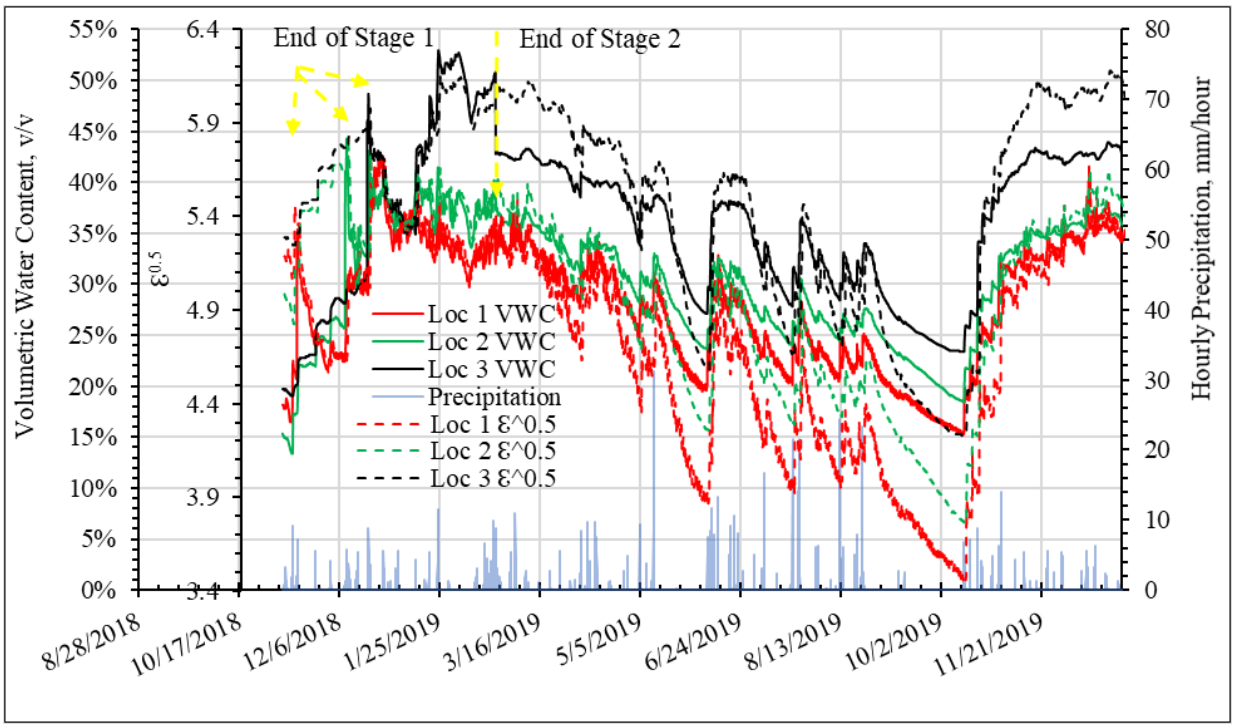

Figure 2.7. The spatial-temporal profile of permittivity ($\varepsilon^{0.5}$), volumetric water content, and precipitation in the testbed, (a) are the ends of the initial phase for sensors at different depths, (b) is the end of the transition phase for all sensors.

While the total area-normalized quantity of runoff and leachates was 776.78 mm, representing 47.8% of the total precipitation, the remaining infiltration partially became moisture storage and partially lost from the testbed through evaporation. Evaporation seems to be a

dominant factor throughout the testbed's entire depth, as evidenced by the continuous reduction of VWC in the absence of leachate generation. The rate of VWC reduction appeared to decrease when the volumetric water content was lower than 22%, as observed during the summer of 2019.The rate reduction can result from changing meteorological conditions and decreasing moisture content at the surface (Fredlund et al. 2016).

The spatial-temporal temperature profile is presented in Figure 2.8. In general, the range of diurnal temperature variation of the testbed falls within the range of atmospheric temperature. Exceptions were observed from 5/29/2019 to 6/6/2019 and 7/15/2019 to 7/20/2019 when values from loc 1 was higher than the ambient temperature. The higher temperature at loc 1 implies the surface temperature of the testbed could be significantly higher than the ambient temperature.

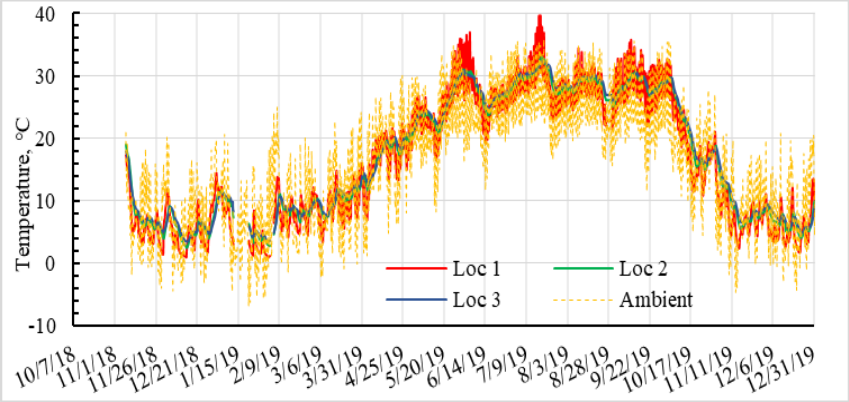

Figure 2.8. The spatial-temporal temperature profile of the testbed.

2.6.Conclusions

In this study, a testbed with surface runoff and leachate collection system instrumented with VWC and temperature sensors under field scenario in Charlotte area was used to investigate

the co-disposal of compacted CFA/FGD brine mixture. The testbed has been in operation since 11/7/2018 with weekly and severe rain event collections of leachate and runoffs, routine inspection, and vegetation removal. The analysis of the leachate collected from the annulus and inner LCS suggests no significant preferential flow or side leakage had occurred during this study period. The semi-quantitative analysis of EC and pH of the leachates suggests the testbed released most of the initial salinity within the added FGD brine after leachate to CFA mass ratio of 0.5. To address the complex relationship between VWC - $\varepsilon^{0.5}$ - EC, this study categorized the variation of pore fluid salinity within the testbed into initial, transition, and stable phases. The spatial-temporal VWC profile provides insights into the moisture storage within the testbed and will be critical in the hydraulic modeling and calculation of mass balance in subsequent studies. The spatial-temporal temperature profile indicates the surface temperature can sometimes be significantly higher than the ambient temperature (particularly in the summer months), which will be valuable in validating heat transfer modeling and ground heat flux estimation. While preliminary results show that compacted CFA and FGD brine is not an ideal co-disposal method for a ZLD strategy in the weather and environmental conditions in the Charlotte area, the performance of such as system is very likely to be site- and weather- dependent.

The ongoing research will continue to investigate hydraulic properties of the testbed, perform quantitative analysis on the halides retention, and develop models to simulate the performance of compacted CFA/FGD brine mixture under different weather scenarios. The spatial-temporal VWC data will be critical in the validation of hydraulic modeling, the mass balance of the testbed, and in computing estimated evaporation and its relationship to the estimated potential evaporation. The spatial-temporal temperature profile of the testbed will be used as the validation for heat transfer modeling and the estimation of the ground heat flux.

References

ACAA. (2019). *Coal Ash Recycling Rate Declines Amid Shifting Production and Use Patterns*.

Apak, R., Tütem, E., Hügül, M., and Hizal, J. (1998). "Heavy metal cation retention by unconventional sorbents (red muds and fly ashes)." *Water research*, Elsevier, 32(2), 430–440.

ASTM International. (2012). "ASTM D698 - 12e2 Standard Test Methods for Laboratory Compaction Characteristics of Soil Using Standard Effort (12 400 ft-lbf/ft3 (600 kN-m/m3))." (D. 0. S. and R. (Sponsoring Committee), ed.).

ASTM International. (2013). "ASTM D6349-13: Standard Test Method for Determination of Major and Minor Elements in Coal, Coke, and Solid Residues from Combustion of Coal and Coke by Inductively Coupled Plasma—Atomic Emission Spectrometry BT - Standard Test Method for Determinati."

ASTM International. (2014). "D854-14 Standard Test Methods for Specific Gravity of Soil Solids by Water Pycnometer."

Chen, Y., and Or, D. (2006a). "Effects of Maxwell-Wagner polarization on soil complex dielectric permittivity under variable temperature and electrical conductivity." *Water Resources Research*, Wiley Online Library, 42(6).

Chen, Y., and Or, D. (2006b). "Geometrical factors and interfacial processes affecting complex dielectric permittivity of partially saturated porous media." *Water resources research*, Wiley Online Library, 42(6).

Cho, H., Oh, D., and Kim, K. (2005). "A study on removal characteristics of heavy metals from aqueous solution by fly ash." *Journal of hazardous materials*, Elsevier, 127(1–3), 187–195.

Dumenu, L. (2019). *Water Repellency Effect on Unsaturated Properties of Compacted Coal Combustion Residuals* . ProQuest LLC, Ann Arbor, MI.

Fatoba, O. O., Petrik, L. F., Gitari, W. M., and Iwuoha, E. I. (2011). "Fly ash-brine interactions: Removal of major and trace elements from brine." *Journal of Environmental Science and*

Health, Part A, Taylor & Francis, 46(14), 1648–1666.

Fredlund, M. D., Tran, D., and Fredlund, D. G. (2016). "Methodologies for the Calculation of Actual Evaporation in Geotechnical Engineering." *International Journal of Geomechanics*, American Society of Civil Engineers, 16(6), D4016014.

John Rumble. (2018). *Handbook of Chemistry and Physics 99th Edition*. CRC Press.

Mohan, S., and Gandhimathi, R. (2009). "Removal of heavy metal ions from municipal solid waste leachate using coal fly ash as an adsorbent." *Journal of hazardous materials*, Elsevier, 169(1–3), 351–359.

Tong, T., and Elimelech, M. (2016). "The global rise of zero liquid discharge for wastewater management: drivers, technologies, and future directions." *Environmental science & technology*, ACS Publications, 50(13), 6846–6855.

Topp, G., Davis, J., and Annan, A. (1980). "Electromagnetic determination of soil water content: measurements in coaxial transmission lines." *Water Resources Research, Wash., D.C*, (G. Topp, ed.), 16(3), 574–582.

U.S. EPA. (2009). *Steam Electric Power Generating Point Source Category: Final Detailed Study Report*.

U.S. EPA. (2015). "Hazardous and Solid Waste Management System; Disposal of Coal Combustion Residuals From Electric Utilities; Final Rule." *The Federal Register*, Federal Information & News Dispatch, Inc., Washington.

U.S. EPA. (2019). "Coal Ash Basics." <https://www.epa.gov/coalash/coal-ash-basics#05> (Apr. 15, 2021).

U.S. EPA. (2020a). "Steam Electric Reconsideration Rule." 40 C.F.R. Part 423.

U.S. EPA. (2020b). "Supplemental Technical Development Document for Proposed Revisions to the Effluent Limitations Guidelines and Standards for the Steam Electric Power Generating Point Source Category." 40 C.F.R. 423.

CHAPTER 3 FIELD STUDY OF THE FLUE GAS DESULFURIZATION BRINE – COAL FLY ASH CO-DISPOSAL METHOD BY COMPACTION

Abstract

The co-disposal of coal fly ash (CFA) and the flue gas desulfurization (FGD) wastewater concentrate (brine) is a potential way to achieve the Zero Liquid Discharge (ZLD) strategy for waste management in coal-fired steam electric power plants to meet regulatory requirements. It is convenient for certain facilities to use the FGD brine as an alternative liquid source to serve as the moisture conditioner and dust control to dispose of the CFA by compaction. The preliminary result of the field study on a compacted class F CFA- FGD brine co-disposal mixture in an instrumented testbed under weather conditions in the Charlotte area showed the material failed to retain salinity due to the failure of the mixture to achieve stabilization/solidification (S/S). Chemical analysis of leachate and runoff showed the material released 79.1% of chloride and 88.6% of bromide during the experiment, and the major anion in leachate shifted from chloride to sulfate when EC reached the relatively stable level of 3,000 μS/cm. As the salinity of pore solutions varies with the leaching stage, an empirical equation accounting for the estimated electric conductivity (EC) was developed to translate the measured bulk dielectric permittivity to volumetric water content (VWC). Further investigation showed the high intensity but less frequent rainfalls during the summer led to significant runoff generation, while the low intensity but more frequent rains during the winter generated a significant amount of leachate. The extensive drying at the surface of material led to surface salting, which led to unexpected spikes in halide concentration, adding difficulties for runoff management. The elevated temperature of the bare surface above the ambient due to solar radiation signaled the need to consider the ground heat flux for evaporation estimation. Since the compacted material's hydraulic behaviors depend highly on the local climate, the use of this co-disposal method under different weather conditions requires further investigation. It is

recommended to apply hydraulic binders in the co-disposal of FGD - brine when using CFA of non-cementitious properties in weather conditions similar to that of this study.

3.1. Introduction

The coal-fired steam electric power plant generates coal combustion products and flue gas desulfurization (FGD) products. To address the environmental concerns of these products, the U.S. environmental protection agency (U.S. EPA) established the Coal Combustion Residuals (CCRs) rules (U.S. EPA 2015) and the Effluent Limitations Guidelines (ELGs) (U.S. EPA 2020) for the solid and liquid wastes, respectively. As the major component of the CCRs, coal fly ash (CFA) must be disposed of in an engineered landfill to protect groundwater. The landfilling of CFA by compaction requires the addition of moisture, which is typically water. It is convenient for certain facilities to use the FGD wastewater as an alternative liquid source to reduce water consumption, which was successfully used in South Africa for ash with lime content greater than 5% (Fatoba et al. 2011). Ideally, the co-disposed material will retain the elements of concern in the FGD wastewater, which typically has the value of total dissolved solids (TDS) ranging from 6,500 to 26,000 mg/L with high halide concentrations (Fatoba and Petrik 2015; U.S. EPA 2009). The co-disposal of CFA-FGD wastewater might be a method to achieve the zero-liquid-discharge (ZLD) strategy, which can be economical and be environmentally responsible for a facility. As the quantity of the ash to be disposed of is relatively limited compared to the FGD wastewater, the co-disposal is more appropriate for concentrates or brines generated from the volume reduction technologies such as membranes filtration or thermal evaporation. These FGD brines can contain TDS as high as 130,000 mg/L with 77,468 mg/L of chloride and elevated concentrations of heavy metals such as cadmium and mercury. While ash has long been used to sequestrate heavy metals for its negatively charged surface in an alkaline environment (Apak et al. 1998; Cho et al. 2005;

Mohan and Gandhimathi 2009), such surface chemistry cannot simultaneously stabilize the negatively charged halide ions. The highly mobile halide ions can escape from the co-disposal material and becomes contaminants in the leachate. The leachate generation depends on the local weather condition, which controls the infiltration and potential evaporation from the co-disposal material. If a dynamic balance is achieved between infiltration and evaporation, the compacted CFA-FGD brine can still sequester the elements of concerns by minimizing leachate generation. Thus, the ability of co-disposal material consisting of a class F CFA and high halide concentration brine method under any weather conditions requires thorough investigation.

To investigate the co-disposal method under the weather conditions in Charlotte, North Carolina, this study used an instrumented small-scale testbed to simulate an engineered landfill. The preliminary results (He et al. 2022) of the first 12 months of this study qualitatively found that the co-disposal of CFA – FGD brine by compaction failed to retain the salinity within the matrix and identified the challenges in the interpretation of the permittivity data from volumetric water content sensors due to spatial-temporal variation of the salinity level in the pore solution. The preliminary results also showed that leachate generation pauses with increased runoff are linked to precipitation patterns during the summer months. The monitored temperature suggested that the surface temperature of the testbed can be significantly higher than the atmospheric temperature, implying the ground heat flux should be considered for estimating the surface energy balance.

This study presents the correlation between EC, volumetric water content, and bulk permittivity for sensor calibration and proposes a method to address the variability in pore solution's salinity. With the correlation, this study was able to better evaluate the hydraulic performance of the co-disposal method in terms of moisture movement and identify the underlying principle of reoccurring patterns for leachate and runoff generation in 35 months of the experiment.

The chemical analysis of the leachate and runoff quantifies the halide sequestration efficiency and provides insights into the leaching processes of the co-disposal material. The study also investigates the magnitude and mechanism of surface heating during the summer and its potential impact on runoff quality. It is worth noting that the field performance relies significantly on the local weather conditions. Hence the performance of the compacted co-disposal material may depend on the prevailing local environment.

3.2.Materials and Methods

3.2.1. Coal fly ash

The coal fly ash was acquired from a steam electric power generation facility in the southeast U.S. The chemical compositional analysis followed ASTM D6349 (ASTM International 2013a), and the result is presented in Table 3.1. The concentration of arsenic (As), lead (Pb), chromium (Cr), and mercury (Hg) are 57.5, 66.7, 231, and 0.12 mg/L, respectively. Following the ASTM C1216 (ASTM International 2013b), the water-soluble concentrations of chloride (Cl), fluoride (F), and sulfate (SO_4) in the CFA were found to be 134, 31.8, and 4400 mg/L, respectively. Based on the chemical compositional analysis, the ash was categorized as class F according to ASTM C618 (ASTM International 2017). The quantitative mineralogical study was performed using the Rietveld refinement X-Ray diffraction (XRD) method with Cu-Kα radiation. The 2θ angle ranging from 5 to 90º was used in the XRD analysis. XRD analysis shows that 75% by mass of CFA is in amorphous form, with 16% of mullite, 5% of quartz, and 2% of magnetite. The specific gravity of ash was 2.322 at 20 ℃, acquired using ASTM D854-14 (ASTM International 2014) standard method. The particle size distribution analysis with a Horiba LA-910 laser diffraction particle size analyzer showed the value of D_{10}, D_{50}, and D_{90} equal 4.78 μm, 17.37 μm, and 54.57 μm, respectively.

Table 3.1. Chemical composition of the CFA

Oxides	Mass %	Oxides	Mass %
Al_2O_3	26.9	CaO	0.89
SiO_2	53.5	MgO	1.72
Fe_2O_3	8.66	Na_2O	0.35
T_iO_2	1.31	K_2O	2.45

3.2.2. Flue Gas Desulfurization (FGD) Brine

The FGD brine was acquired from a steam electric power generation facility in the southeast U.S. and has a density of 1.13 g/cm^3 at room temperature. The brine has 0.216 grams of total solids (TS) with 0.005 grams of total suspended solids (TSS) per gram of brine. The concentrations of major metals and anions in the brine, including the analytical methods used are presented in Table 3.2. As a widely used indicator for total dissolved solids (TDS) (Rhoades 1996), electrical conductivity (EC) is used in this study to assess the change of salinity in liquids. The EC, pH, and density of the brine at different dilution levels are shown in Table 3.A1 in the supplement material. The EC and the pH of the brine are 131,585 μS/cm and 8.11, respectively.

Table 3.2. Concentration of major metals and anions in the FGD brine

	Concentration, mg/L.	Method*		Concentration, mg/L.	Method*
Chloride	77468	1	Sodium	4220	2
Calcium	12200	2	Potassium	1060	2
Magnesium	11300	2	Boron	838	2
Sulfate	3075	2	Bromide	1106	1

*Method 1: EPA 9056 (U.S. EPA 2007), method 2: EPA 3005A (U.S. EPA 1992)

3.2.3. CFA-FGD brine mixture

The standard proctor compaction test was performed with deionized water (DI) and undiluted FGD brine following the ASTM D698 (ASTM International 2012). As the dry unit

weight, γ_d (kN/m^3) of the compacted material is determined from the oven-dried mass of solids, the mass of water-soluble solids from the TS in added brine can be erroneously included as the mass of CFA particles. The mass of the TS in the brine must be accounted to avoid underestimating the void in the compacted material. Consequently, the dry unit weights $\gamma_{d(CFA)}$ and $\gamma_{d(solids)}$ were determined and used to represent the dry unit weights of CFA molded with DI water and the CFA plus TS from using brine as the molding fluid, respectively. The maximum dry unit weights ($\gamma_{d(max)}$) and optimum moisture contents (OMC) of CFA prepared with DI and FGD brine were 22.7%, 13.11 kN/m^3, and 22.0%, 13.55 kN/m^3, respectively. While the target moisture for field compaction was 22%, the average moisture of in-place material was 21.9%. The calculated $\gamma_{d(solids)}$ and $\gamma_{d(CFA)}$ of the compacted field material were 12.17 kN/m^3 and 11.62 kN/m^3, respectively. The estimated CFA volume fraction of the field material was 48.96%, with a maximum potential porosity of 51.04%. The saturated hydraulic conductivity of the CFA-DI mixture prepared at the field dry unit weight was 4×10^{-4} cm/s, though higher than the value of 1×10^{-4} cm/s acquired at the maximum dry unit weight (Dumenu 2019) but still within the same order of magnitude. The saturated hydraulic conductivity of the CFA-DI mixtures falls within the typical range of values of silty sand soils.

3.2.4. Volumetric water content (VWC) sensor calibration

The ML3 sensor (by Delta-T Devices) used in this study measures the bulk dielectric permittivity, Ɛ, of the material, which is translated to volumetric water content (VWC) using a material-specific equation (Gaskin and Miller 1996). The sensor utilizes a 100MHz excitation frequency to minimize the influence of salinity on the measured bulk apparent dielectric permittivity (Gaskin and Miller 1996; Topp et al. 1980). The Ɛ of the compacted material is mainly controlled by the pore solution's properties and the VWC, temperature, soil properties, and the dry

unit weight of the material also influence the reading (Chen and Or 2006a; 2006b). Though the recorded temperatures within the testbed in this study ranged from 1 to 40 ℃, all the experiments to correlate measured permittivity ε to volumetric water content at different salinity levels were limited to room temperature and the field dry unit weight (11.62 kN/m^3) of the compacted material. Given the expected changes in the chemical compositions of the pore fluid of the compacted material over time resulting from leaching due to infiltration, the potential brine characteristics were simulated in the laboratory through monitoring of the EC values of the brine at different dilution levels. The EC, pH, and density of the FGD brine at different dilution (undiluted, 2-, 5-, 10-, 50-, and 100- times) levels are presented in Supplementary 3.A. Consequently, samples of compacted CFA were prepared with FGD brine diluted at the aforementioned levels and DI water to develop a correlation between measured $\varepsilon^{0.5}$ (by ML3 sensors) and the VWC for the pore solutions. The correlation between $\varepsilon^{0.5}$ and VWC for the CFA-DI mixture served as the reference. Sample preparation involved first mixing CFA with FGD brines or DI and allowed to mellow for 24 hours (to achieve equilibrium), then thoroughly remixing and compacting to the target γ_{CFA} (11.62 kN/m^3) in a 7.62 cm - diameter by 15.24 cm - height cylinder container. Triplicate specimens of each mixture were prepared, monitored for permittivity ε using ML3 and oven-dried to determine the VWC.

3.2.5. Instrumentation and field data collection

The instrumented testbed used in this study consists of the containment system, the leachate collection system (LCS), the surface runoff collection system (SRCS), and the data acquisition system (DAS). All accessories of the LCS, SRCS, and DAS are made of chemical-resistant materials. The containment system of the testbed includes the High-Density Polyethylene (HDPE) container and the thermal insulation layer. The thermal insulation layer of external HDPE walls

comprises a 15.88 cm thick R-19 fiberglass layer, while the bottom has double-layer insulation. A layer of UV-resistant HDPE liner is used to protect the insulation fiberglass from precipitation and degradation. The HDPE container has width, length, and height of 96.52 cm, 114.30 cm, and 111.76 cm, respectively. The top surface of the container is exposed to the atmosphere. Routine inspection and removal of any growth on the exposed surface were performed to eliminate potential evapotranspiration. The SRCS is located at the lower end of the 2% tilt of the container, which consists of the collection unit and the storage unit. The collection unit is an HDPE film-lined trench filled with gravel. The size of gravel used ranges from 5 to 10 mm. The unit's width, length, and depth are 7.62 cm, 96.52 cm, and 12.7 cm, respectively. The storage unit is two removable HDPE tanks connected to the collection unit via chemical-resistant plastic tubing. The LCS is divided into inner and annulus sections and has designated storage units for each section. The plan view of the LCS is shown in Figure 3.1 (a). LCS is a 17.78 cm sand layer with a saturated hydraulic conductivity of 0.180 cm/s. To assess potential side leakage, the inner section is separated from the annulus with HDPE walls extended 2.54 cm higher than the surface of the sand layer in the LCS. The areas of the inner and annulus sections are 1224 and 9808.2 cm^2, respectively. The storage unit for each section of the LCS also consists of two removable HDPE tanks connected to the collection unit via chemical-resistant plastic tubing. The DAS consists of embedded sensors and loggers to monitor changes in temperature and moisture along the depth profile of the testbed. A set of sensors was installed at a depth of 12.7 cm (Top), 38.1 cm (Middle), and 63.5 cm (Bottom) from the exposed surface. The set of sensors includes one ML3 ThetaProbe volumetric water content (VWC) sensor and one T108 temperature sensor. Hourly data are collected by the GP2 datalogger (Delta-T Devices) and CR800 dataloggers (Campbell Scientific Inc.) for ML3 and T108

sensors, respectively. A weather station located 5 meters from the testbed collects the hourly local weather data.

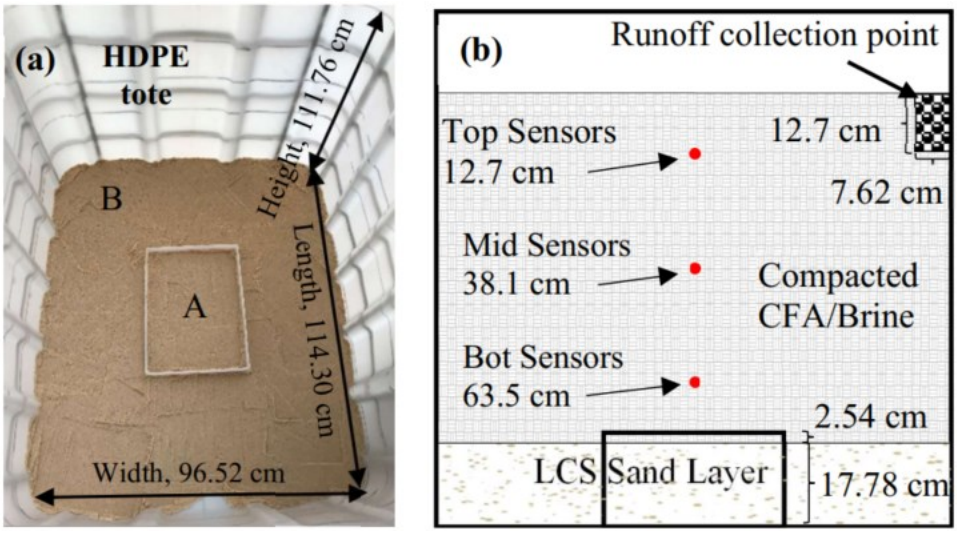

Figure 3.1. Plan view of the sand layer (a) and the vertical layout of the testbed (b) (He et al. 2022).

3.2.6. Chemical analysis of leachate and runoff

Over the experiment period, the total leachate collected from the inner and annulus sections of the LCS and the total runoff was 157.8 kg, 1063.65 kg, and 969.39 kg, respectively. The precipitation events, defined as the interval between two successive precipitations, occurred 211 times during the duration of the field experiment (November 06, 2018 – June 6, 2021). Of the precipitation events, 91, 150, and 155 measurements were taken for inner leachate, annulus leachate, and surface runoff, respectively. Among the measurements, 59, 78, and 99 counts were collected with an interval greater than or equal to 24 hours. Samples were collected after the mass measurements of the collected fluid, which could happen multiple times during a precipitation event. The total number of samples collected were 74, 115, and 106 for inner leachate, annulus leachate, and surface runoff, respectively. The collected samples cover every precipitation event

with multiple collections for events that last longer than 24 hours or generate large quantities of leachate/runoff.

While the EC and pH were measured for all leachate and runoff samples, selected samples were analyzed for cation and anion concentrations using inductively coupled plasma-optical emission spectrometry (ICP-OES) and ion chromatography (IC), respectively. The ICP-OES targeted sodium (Na), potassium (K), arsenic (As), lead (Pb), cadmium (Cd), iron (Fe), magnesium (Mg), and silicon (Si). The anion analysis was performed for chloride (Cl^-), bromide (Br^-), and sulfate (SO_4^{2-}). The collected samples were diluted with ultrapure deionized water with a conductivity of 18.2 MΩ·cm and filtered through a 0.45 μm polypropylene filter before testing. The Agilent 5100 was used for the ICP-OES analysis, and the IC analysis was performed with Dionex ICS-3000 for samples before June 2020, and a Metrohm IC system for later samples.

3.3.Results and Discussion

3.3.1. Relationships among electrical conductivity, permittivity, and volumetric water content

The widely used 3rd order polynomial relationship between the square root of permittivity ($\varepsilon^{0.5}$) and volumetric water content (VWC) was developed by Topp et al. (1980). A simplified linear relationship is proposed for "Mineral Soil" in the ML3 sensor's user manual (Delta-T Devices Ltd 2017), as demonstrated in Figure 3.2, to provide a generalized interpretation method. In this study, the measured volumetric water content versus the permittivity prepared at different FGD dilution levels are presented in Figure 3.2. Compared with the reference CFA-DI mixture, VWCs estimated by the "Mineral Soil" equation was on average 6% higher, indicating the need to develop a material-specific relationship. The effect of pore solution's salinity on the relationship

between $\varepsilon^{0.5}$ and VWC is evident for fluids with EC greater than 20,000 μS/cm (i.e., FGD brine with no more than ten times dilution levels). The permittivity value of the compacted CFA at the same volumetric water content increased with an increase in the EC value of the pore fluid. This difference in permittivity values between DI and saline water decreases as the volumetric water content increases and eventually reduces to zero at 40% VWC for fluid with EC less than 20,000 μS/cm (equivalent to at least ten times dilution of FGD brine). A similar pattern of difference in permittivity of the porous medium caused by the pore fluid salinity was also reported by other studies (Delta-T Devices Ltd 2017; Szypłowska et al. 2018).

In this study, the correlation between the salinity (represented by EC) and the $\varepsilon^{0.5}$ is not linear, as demonstrated in Figure 3.A1 in the supplementary section (Supplementary 3.A). The permittivity of the diluted brine decreases with the increase of EC in the range of 0 and 14,000 μS/cm. However, above that range, the permittivity of the solution increases with increasing EC of the solution. Nevertheless, the permittivity of FGD at any dilution level was less than the permittivity of DI. The change of bulk permittivity of a saturated porous medium with varying salinity of the pore solution should follow the same pattern as the pore solution's permittivity and salinity. Under unsaturated conditions, the interfacial polarization effect (Maxwell-Wagner, M-W effect) can also result in increased bulk dielectric permittivity with increasing salinity (Abidin and Hsai-Yang 1997; Oh et al. 2007). Chen and Or (2006a) suggested the migration of the relaxation of M-W effect towards a higher frequency with increasing pore solution's EC will lead to the increase of bulk dielectric permittivity measured with a fixed frequency, which explains the increasing bulk permittivity under the unsaturated condition with increasing EC observed in this study.

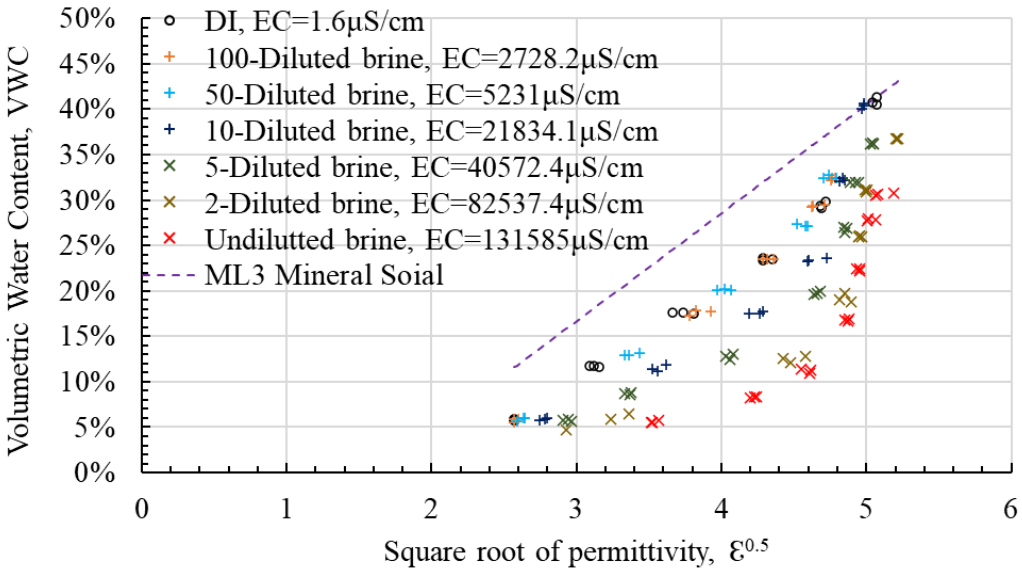

Figure 3.2. Measured relationships between volumetric water content and permittivity.

The reference function established for the CFA-DI mixtures used the 3rd order polynomial relationship between VWC and the squared root of permittivity. The fitting was performed with the ordinary least squares method, and the fitted equation for the volumetric water content of the CFA-DI mixtures, VWC_{DI}, is:

$$VWC_{DI} = -1.64090 + 1.39251\varepsilon^{0.5} - 0.37738(\varepsilon^{0.5})^2 + 0.03598(\varepsilon^{0.5})^3 \qquad \text{Eq. 3.1.}$$

After extensive investigation and trials, the best empirical function that captures EC variation in the volumetric water content of the pore solution (VWC_s) for the CFA-FGD Brine mixtures is of the form in equation 3.2:

$$VWC_s = VWC_{DI} \times a(exp\left(b(\varepsilon^{0.5} - c)\right) + d) \qquad \text{Eq. 3.2.}$$

Where a, b, c, and d, are fitting parameters, VWC_s is the volumetric water content of the pore solution. The data collected from VWC sensor calibration tests on undiluted and 2-, 5-, 10-

times dilution of the FGD brine were used to determine the fitting parameters of equation 3.2 and the results of the fitted plots are presented in Figure 3.3. The root mean squared error (RMSE) of the prediction using equation 3.2 for undiluted, 2-, 5-, and 10- times brine dilution are 2.1%, 2.2%, 1.4%, and 1.6%, respectively. The maximum range of the prediction error for all fitted VWC_s falls within the range of ±5.0%, with an overall RMSE of 1.85%.

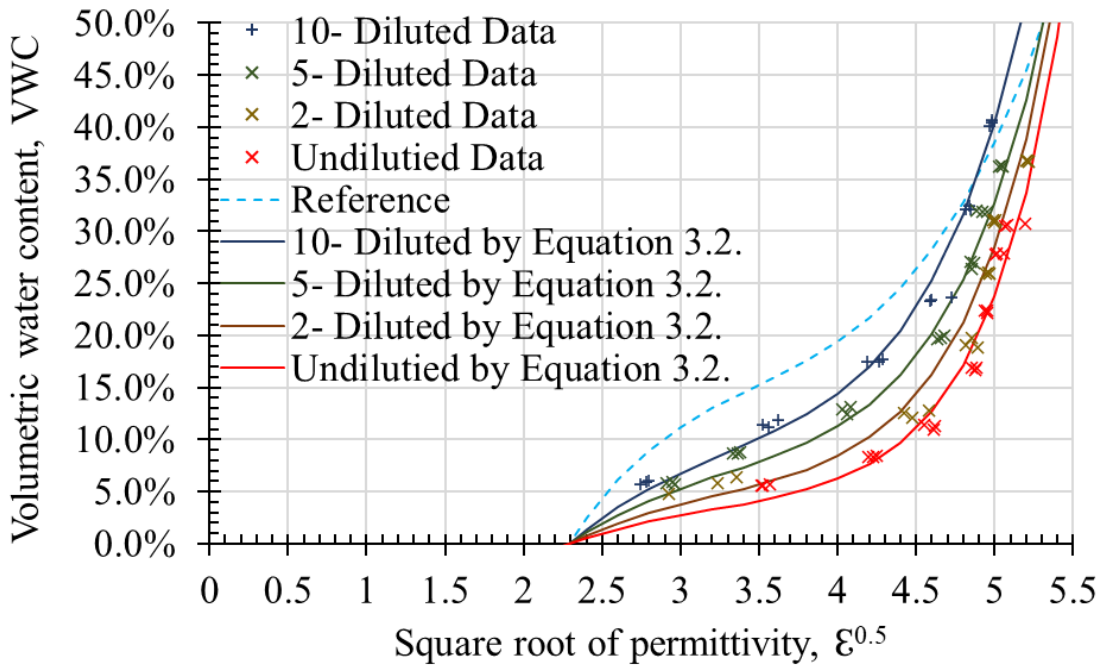

Figure 3.3. Plots of VWC using the calibration data as a function of the square root of permittivity.

Since calibration tests and data were only performed for a limited sample size with pore fluid at discrete and specific salinity levels of undiluted and 2-, 5-, 10- times dilution of the FGD brine corresponding to EC values of 131585, 82537.4, 40572.4, and 21834.1 µS/cm, respectively, they cannot adequately capture the more continuous and greater levels of salinity under field

scenario. To address the VWC-$\varepsilon^{0.5}$ for all the ranges of salinity levels considering in this study, the relationships of the fitting parameters a, b, c, and d as a function of EC values of the pore fluids were established and presented in Figure 3.4. The equations of the relationships between the fitting parameters and EC values are:

$$a = (-2.671 \times 10^{-3}) \times logEC + 1.501 \times 10^{-2} \quad \text{Eq. 3.3.}$$

$$b = (6.671 \times 10^{-1}) \times logEC - 2.126 \quad \text{Eq. 3.4.}$$

$$c = 2.519 \times logEC - 1.225 \times 10^{1} \quad \text{Eq. 3.5.}$$

$$d = (-3.627 \times 10^{-1}) \times logEC + 2.070 \quad \text{Eq. 3.6.}$$

Knowing the EC of the pore solution, the fitting parameters in equation 3.2 can be predicted using equations 3.3 to 3.6. Using the predicted fitting parameters, the volumetric water content of the pore solution (VWC_s) for the CFA-FGD brine mixture in the testbed can be estimated for the permittivity reading using equations 3.1 and 3.2. The estimated VWC_s for the predicted fitting parameters yield an error range between 5.8% to -7.3%, with an average error of -0.18%. The RMSE values of the predictions for undiluted, 2-, 5-, and 10- times dilution levels are 2.6%, 2.6%, 3.9%, and 2.7%, respectively. The estimated VWC_s values from the fitting parameters predicted using equations 3.3 – 3.6 and determined from the calibration data match well against the measured VWC_s values (Figure 3.5). While the preliminary results showed that the leachate reached a constant EC within the first six months of the study (He et al. 2022), the pore water migrating from an overlying layer will raise the salinity of the layer being infiltrated or leached in an engineered landfill operation for several years depending on the size/thickness of cells. Hence, it is recommended to run calibration tests at dilution levels at closer EC values from the undiluted to

100 times dilution levels of the FGD brine to establish more continuous EC relationships for field monitoring of VWC_s.

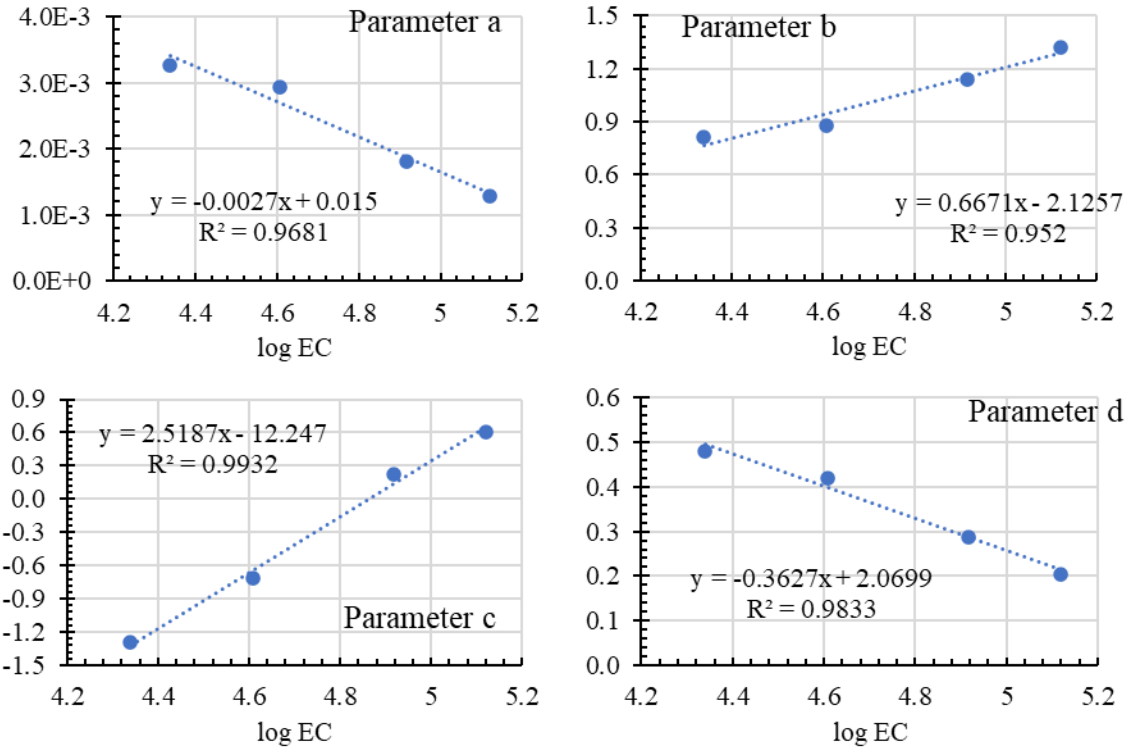

Figure 3.4. Relationships between the fitting parameters (a, b, c, and d) of equation 3.2 as a function of EC.

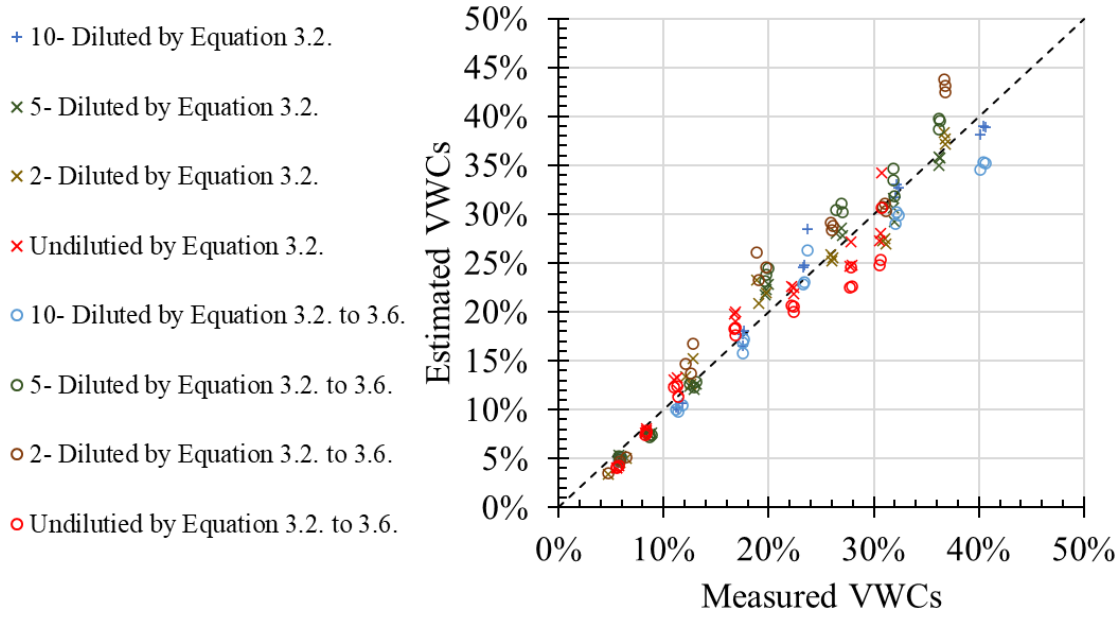

Figure 3.5. Comparison of estimated VWC_s using predicted and determined fitting parameters with the measured VMC_s.

3.3.2. EC, pH, and chemical compositions of leachates and runoff

While the precipitations are discrete events, the leaching process of the testbed is continuous in the study, albeit intermittent in reality. The mass ratio of leachate to CFA solids, L/S, is used to present the continuous change in leachate composition. As a reference, the mass ratio of FGD brine used to condition or mold the CFA in this study is 0.22. The masses of CFA above the inner and annulus sections, assuming 1-dimensional infiltration flow in the testbed, are 110.5 and 885.7 kg, respectively. The EC and pH of leachate samples collected from the testbed as a function of L/S are presented in Figure 3.6. The EC value of leachate for the first L/S of 0.22 is equivalent to that of the undiluted FGD brine and decreased to a value corresponding to the EC value of the 100 times brine dilution level at L/S of 0.5. The L/S of 0.22 for this study occurred on 1/7/2019, which was two months into the operation of the testbed. The matching trend and values of EC and

pH at the same L/S between inner and annulus leachate suggests the chemical composition of pore fluid is homogeneous across the cross-section of the testbed. As discussed in the preliminary result paper of this study (He et al. 2022), the trend of the generated leachate can be categorized into initial (leaching/washoff), transition, and leached/residual stages corresponding to EC values greater than 100,000 µS/cm, between 100,000 and 3,000 µS/cm, and less than 3,000 µS/cm, respectively. The EC value of the leachate generated during the initial stage is equivalent to the quantity and salinity of the undiluted brine suggesting wash off or complete release of the added brine in the mixture. The pH of the leachate increases from 8 to 9 with a decrease of pore solution's EC, which was likely the result of the dissolution of the CFA particle since potassium was detected in the leachate. However, it is different from the increase of pH during the dilution of the brine. The cause of pH increase in brine dilutions was likely due to the dissolution of the brine solids, which is 88.8% inyoite ($CaB_3O_3(OH)_5 \cdot 4H_2O$) by mass.

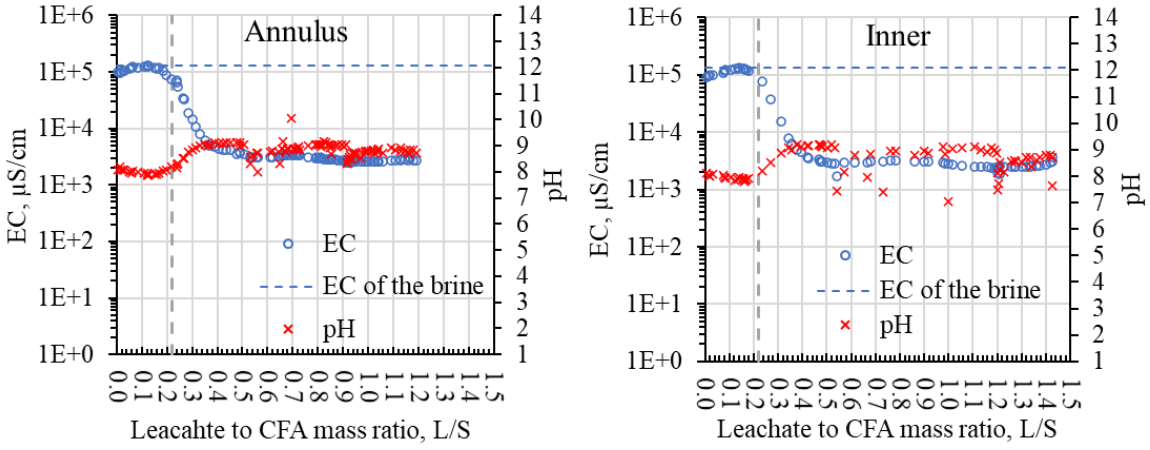

Figure 3.6. Electrical conductivity and pH of the annulus and inner leachate sections of LCS.

The cation and anion concentrations of the annulus leachate are presented in Figures 3.7a and 3.7b. The cumulative quantities of chloride and bromide in the collected leachate at the end of the transition stage were 78.8% and 88.6%, respectively. At the end of the experiment, the total chloride and bromide released from the testbed were 79.1% and 88.6%, respectively. Bromide in the leachate collected from the annulus section was below the detection limit of the IC machine after the initial stage. The consistent concentration and prominence of sulfate and calcium during the leached/residual stage suggest the dissolution of $CaSO_4$ precipitates. The precipitates were likely formed during the mixing of the materials from the FGD residues, as white precipitates were observed during the placement of the compacted CFA/FGD brine mixture. These precipitates could obstruct and shelter the brine from infiltration water, hence prolonging the release of highly mobile ions such as Cl^- and Na^+. The appearance of Si in the leachate after the initial stage indicated the potential dissolution of CFA particles had started. Considering the extensive dilutions during ICP and IC chemical analysis (10,000 level) used for the leachate from the initial stage, it is likely the trace elements such as lead and arsenic could be missed as the detection limits of the machine for them were 1.9 and 3.7 µg/L (19 and 37 mg/L before dilution), respectively. While lead was stable between the pH range of 7 and 9, studies have shown that arsenic is likely to be released from the material at this pH range (Izquierdo and Querol 2012; Wang et al. 2020). As the initial and transition stages suggest the wash off of the added FGD brine from the mixture, the leached/residual stage represents the leaching of the CFA particles. The long-term leachability of coal fly ash has been widely studied under laboratory and field environments, which implies the potential release of some other elements of concerns during the leached/residual stage (Daniels and Das 2018; Dudas 1981; Hjelmar 1990; Izquierdo and Querol 2012; Tiruta-Barna et al. 2006). While the relative ratio of cations did not appear to change with leaching, as shown in Figure 3.7a,

the dominant anion shifted from chloride to sulfate about L/S of 0.36, as shown in Figure 3.7b. For the leachate, the dominant anion determined the level of EC, as demonstrated in Figure 3.7b, which showed the EC no longer decreased with chloride after the sulfate became the dominant anion. Therefore, although the EC is a good indicator of salinity, the chemical composition of the solution could change significantly. It is recommended that landfill operators perform routine checks of leachate's chemical composition to avoid unexpected changes in solution chemical composition.

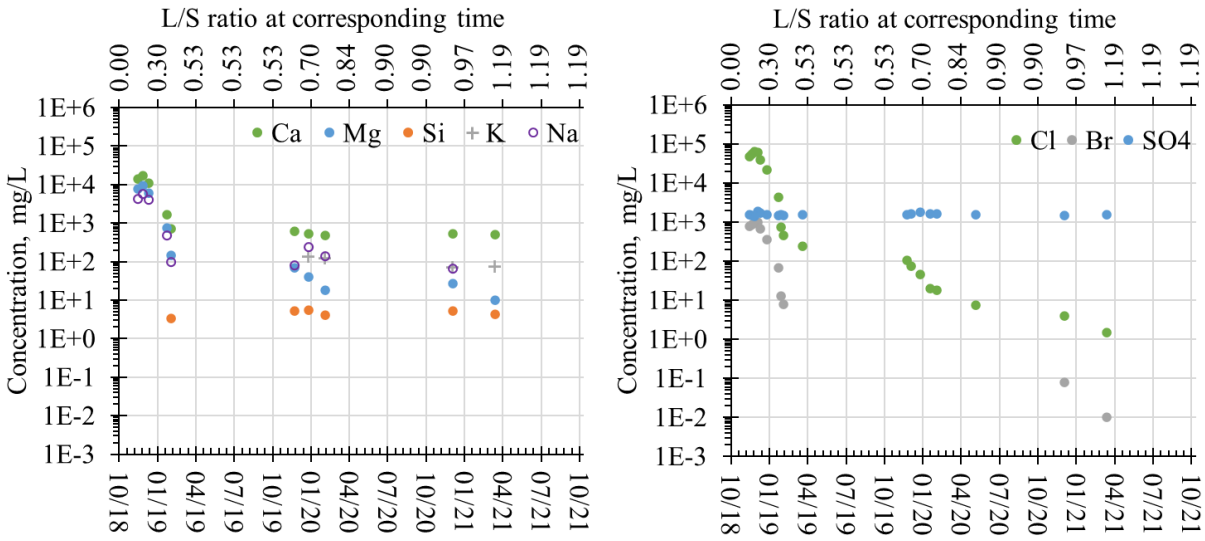

Figure 3.7 a. Chemical composition of leachate from the annulus section of the LCS.

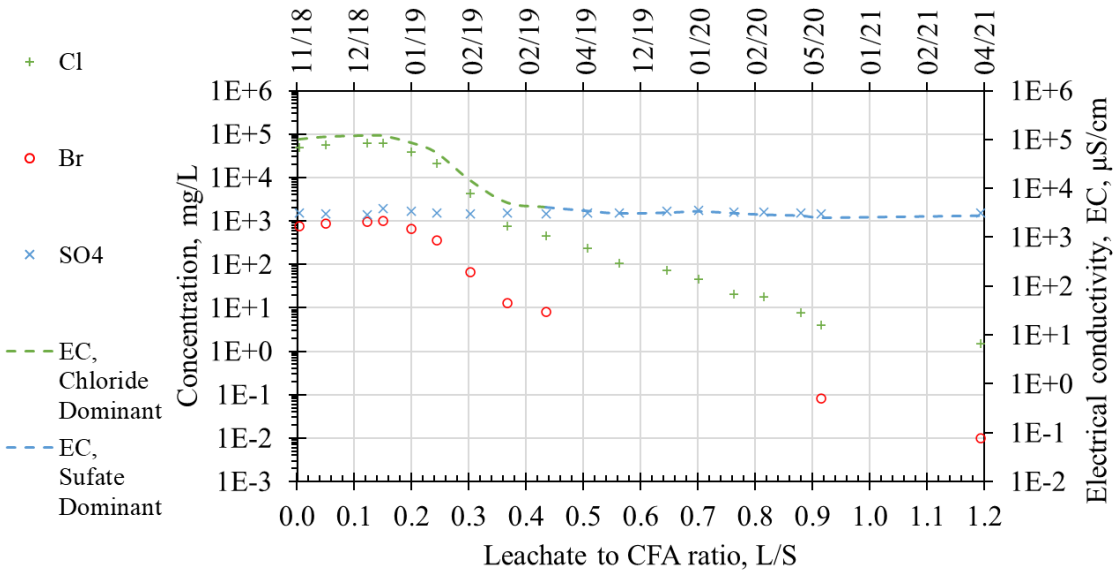

Figure 3.7 b. EC and anion concentration of annulus leachate as a function of L/S.

The results of the chemical analysis of runoff samples showed seasonal fluctuation within the range of 10 to 1,000 µS/cm, as shown in Figure 3.8. The higher EC values, as expected, occurred during the summer runoffs rather than in the winter rain events due to the wicking effect from intense evaporation, which also resulted in the increased concentration of the pore fluid within the top layer/surface of the testbed. Considering that no runoff was observed prior to cumulative precipitation of 204.72 mm of the operation, the relatively low chloride concentration in the runoff compared to the leachate during the initial period could be due to advective transport of the element via high infiltration. The detection of Si in the runoff suggests the potential dissolution of the coal fly ash particle as soon as the first runoff was collected. Among the analyzed samples, 0.188 mg/L of arsenic was observed on 7/10/2020, with the highest Na concentration of 65.5 mg/L. The reappearance of the highly mobile Na with the highest concentration suggests the arsenic in the runoff is likely to result from the concentration of the element at the surface due to evaporation similar to the crust formation (Dai et al. 2016; Nachshon et al. 2011). While no

significant salt crust was observed, the most observable salt precipitation was on 10/10/2020, as shown in Figure 3.9. The detection of arsenic in runoff combined with surface salting indicates the first few sets of runoffs collected after any prolonged period of dry season will require special attention from the landfill operator to prevent the potential surge of chemical concentrations in stormwater.

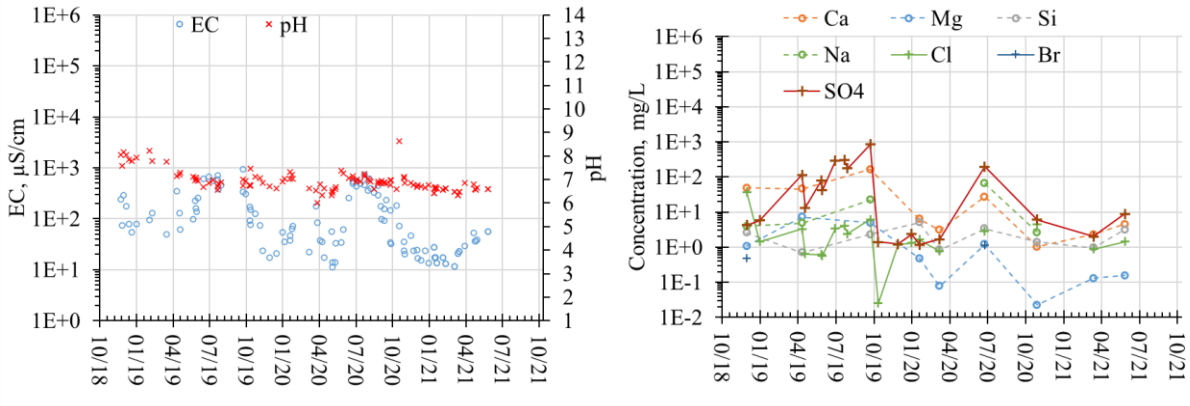

Figure 3.8. Electrical conductivity, pH, and chemical composition of runoff.

Figure 3.9. Surface salting observed on 10/10/2019.

3.3.3. Permittivity and volumetric water content profile

Since the testbed was not instrumented with EC sensors, this section attempts to estimate the salinity of the pore fluid and investigate its effect on permittivity data and volumetric water content values. The change in pore solution's EC at any depth of the testbed was assumed to be mainly due to the quantity of liquid percolating through the overburden materials during the initial and transient stages. The assumption was that the change in pore solution's EC at any depth of the testbed was mainly caused by the quantity of liquid percolated through the overburden materials during the initial and transient stages. In this case, the pore solution's EC for a given percolation to the overburden thickness (P/O) ratio at any depth would be the same as the leachate collected at the same P/O ratio. The overburden used for the leachate is the total thickness of the compacted testbed. For example, a total percolation of 127 mm passing through the top layer (127 mm thick)

will have a P/O of 1, which is equivalent to 762 of leachate generated from the bottom of compacted material (762 mm thick). This assumption was made based on the negligible runoff and evaporation compared to the precipitation during the initial and transition leaching stage, suggesting the advection is the dominant process in solute transport. A key limitation of this assumption involves neglecting the effect of salinity redistribution within the material by diffusion through concentration gradient and moisture variation due to evaporation. The depth from the top surface to locations of the top, middle, and bottom sensors are 12.7, 38.1, and 63.5 cm, which are 1/6, 1/2, and 5/6 of the 76.2 cm, the thickness in the compacted material in the testbed. Therefore, the increase of the P/O ratio at the top, the middle, and the bottom locations will be 6, 2, and 1.2 times faster than that of the leachate. The approximation is supported by the onset of the abrupt peak with an immediate decrease of permittivity with infiltration, which indicated either a decrease in the pore solution's salinity or an end of the initial stage (He et al. 2022). The estimated average EC values at the top, middle, and bottom layers plus the leachate relative to the measured permittivity values are presented in Figure 3.10. The marker arrows in Figure 3.10 identify the estimated end of the initial stage for each sensor matching the prescribed characteristics of the permittivity. It should be noted again that this assumption did not address the potential movement of liquid with hydrological processes and redistribution through diffusion and dispersion processes, which may lead to noticeable differences in the results.

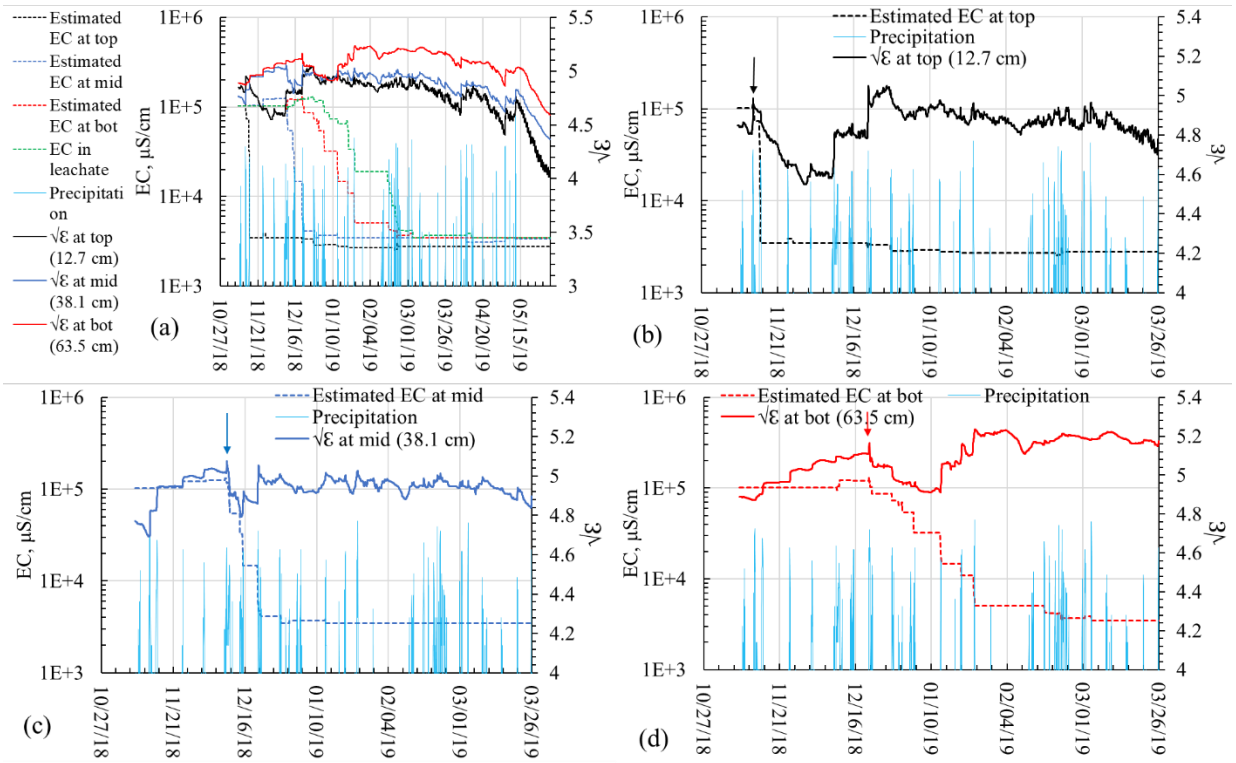

Figure 3.10. (a) Measured permittivity and estimated electrical conductivity profile, with the end of initial stage identified for (b) top, (c) middle, and (d) bottom sensor locations.

The estimated EC from the P/O ratio at different sensor locations was then used to translate the permittivity data into VWC using equations 3.1 to 3.6. The spatial-temporal profile of the squared root of permittivity (√ε) and the estimated volumetric water content (VWC) are presented in Figure 3.11. While the permittivity of the sensors shows similar trends as the VWC, the values generally increase with the depth (Figure 3.11). Seasonal fluctuation of the VWC was observed at all depths of the testbed, indicating the evaporative zone extended throughout the depth of the compacted material. The increases in the VWC in the top layer were observed within an hour of precipitation, with consequent infiltration observed in the middle and bottom layers later as expected. The rapid response of VWC to rainfall suggests the compacted material was susceptible

to infiltration considering its high hydraulic conductive of 4×10^{-4} cm/s, which was also reported by Raucci et al. (2019) as the decrease in matric suction of the material.

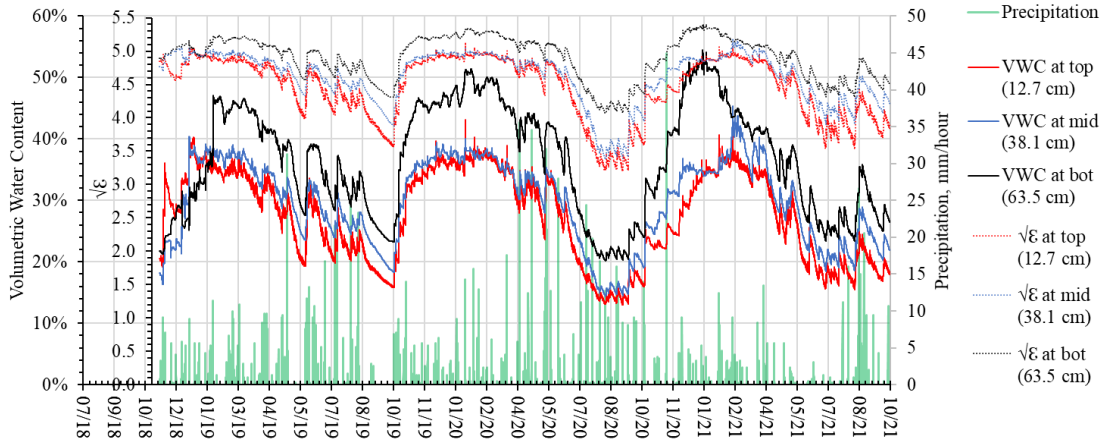

Figure 3.11. Permittivity and volumetric water content profiles with hourly precipitation.

3.3.4. Precipitation, runoff, and leachates generation patterns

Over the duration of the experiment, the total quantity of runoff, leachate from inner and annulus sections were 969.4 kg (0.969 m^3), 157.8 kg (0.158 m^3), and 1063.7 kg (1.064 m^3), respectively. The total precipitation, estimated from the weather station measurement, was 4215.05 kg (4.215 m^3), which indicates that the runoff and leachate collected amounts to 52.0% of the precipitation. The monthly quantities of the leachate and runoff per unit area of the testbed are presented in Figure 3.12. The variability between the quantities collected from inner and annulus sections was attributed to the random error associated with the large 8:1 area ratio of the sections. It is recommended for future studies to apply the 1:1 area ratio to investigate potential side leakage. Seasonal patterns of leachate and runoff generation cycles or periods were observed. The periods

when high leachate and negligible runoff volumes were generated generally coincide with the winter and spring precipitations, while the summer and early fall precipitations generated large runoff and little leachate volumes (Figure 3.12a). This leachate production period during winter was also observed in Hjelmar's study (1990) on the field leaching of class F coal fly ash. While the monthly rains could be perceived to be relatively constant, the summer rainfall was low frequency with high intensity, and the winter rainfall was high frequency with low intensity, as observed in Figure 3.12 (b). During the fall season, infiltrations from recorded precipitations appeared to be stored as the moisture in the testbed increasing the overall VWC profile from the minimum VWC recorded in August/September, as presented in Figure 3.11. Combined with low precipitation, evaporation was the dominant factor for the continued decrease of the overall VWC observed during August/September months. Since an actual engineered landfill will have a depth of the material much greater than the 76.2 cm testbed, it would provide greater storage capacity with the possibility of evapotranspiration, which was prevented through the removal of growth in this study. Considering the significant reduction of VWC due to evaporation and rapid response to infiltration at 63.5 cm below the surface, a deeper compacted material under current weather could prolong the duration for percolation through the material to become leachate during winter. One management option in an engineered landfill could be to store and recirculate the leachate during the dry months corresponding to August/September months in this study. The recirculation of leachate can also benefit from the evaporation process during the summer months. Carefully designed recirculation might also be beneficial to control the salting process due to extensive evaporation, as discussed in the runoff section. To further reduce leachate generation and improve salinity retention, hydraulic binders such as quicklime and cement are recommended (Batchelor 2006; Conner and Hoeffner 1998; Ellison 2015; Oza et al. 2015).

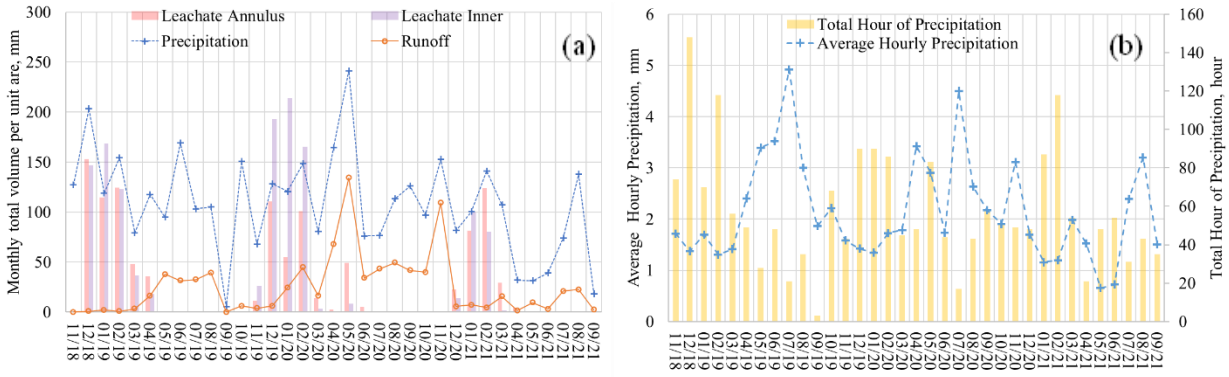

Figure 3.12. (a) Monthly precipitation, runoff, and leachates, (b) with precipitation patterns.

3.3.5. Temperature profile and surface temperature

The temperature profile of the testbed is presented in Figure 3.13. In general, the temperature profile of the testbed falls within the atmospheric temperature, with exceptions during the summer months of 2019. The temperature measurements at the top sensor location (12.7 cm below the surface) exceeded the atmospheric temperature by 5 ℃ an hour after the peak solar radiation of a day. Since the testbed is thermally insulated, heat flux in the testbed is 1-dimensional in the vertical direction. To understand the extent of heating at the surface, the surface temperature was monitored from 6/13/2021 to 7/13/2021. The surface temperature was higher than the ambient when the surface was exposed to sunlight and returned to the atmospheric ambient temperature when direct sunlight was sheltered, such as during rainfall, as demonstrated from 6/30/2021 and 7/3/2021. Evidently, a significant amount of solar radiation is used to heat the compacted material, generally referred to as the ground heat flux, G, which is an important factor in estimating surface evaporation. While the use of a constant to relate G and net solar radiation in models (Allen et al. 2006; Walter et al. 2000) usually depends on the vegetation state, the bare/unvegetated soil

constitutes a more complicated scenario. Studies have shown that G can be estimated from the water content at the surface of bare ground, and the correlation appeared to be soil-dependent (Sauer and Horton 2005). Therefore, it is suggested for future field studies to implement the ground heat flux sensor for more precise estimation of evaporation

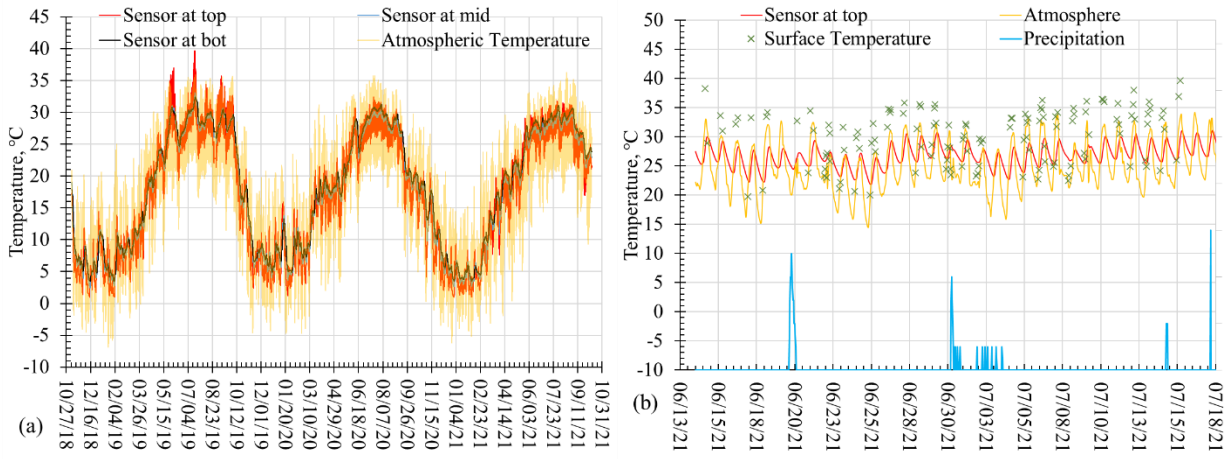

Figure 3.13. (a) Temperature profile and (b) surface temperature measurements of the testbed.

3.4. Conclusions

The co-disposal of a class F coal fly ash and FGD brine by compaction failed to retain halides within the compacted material. The lack of stabilization process in the management option and the permeable matrix led to the release of 79.1% and 88.8% of chloride and bromide in added brine over 35 months. An alternating leachate/runoff generation pattern was observed in this study due to shifting precipitation patterns and variations in evaporation. Observation of salting on the surface of the testbed and surge of chemical concentrations in runoff results from extensive evaporation. As the temperature on the surface of the compacted material was significantly

increased by solar radiation, to model a more realistic evaporation process from a coal fly ash landfill, ground heat flux sensors should be used to collect related data. This study also addressed the difficulties in volumetric water content measurement using a permittivity sensor in an environment with extremely high and variable salinity values by establishing an empirical function correlating the electrical conductivity of the pore solution, the permittivity reading, and the volumetric water content. The hourly VWC data is valuable for developing a physics-based model to evaluate the landfill behavior under different weather scenarios, especially the response of landfills to extreme precipitations for runoff controls and slope stability (Huvaj-Sarihan and Stark 2008; Koerner and Soong 2000). While the co-disposal method of CFA and FGD brine by compaction was unsuccessful in retaining the highly mobile constituents of concerns under the weather conditions in the Charlotte, NC area, it can be successful in weather conditions with higher evaporation and high-intensity but less frequent precipitations. To further control the leachate generation and immobilize salinity in co-disposal of CFA/FGD brine in weather conditions similar to Charlotte, NC, implementing a stabilization/solidification process by adding hydraulic binders is recommended.

Supplementary 3.A

Table 3.A1. EC, pH, and density of FGD brine at different dilution levels

Dilution Level	pH	EC (μS/cm)	Density, (g/ml)
None	8.11	1.316E+05	1.103
2	8.71	8.253E+04	1.051
4	9.09	4.625E+04	1.026
5	9.00	4.057E+04	1.023
8	9.36	2.587E+04	1.013
10	9.38	2.093E+04	1.011
20	9.48	1.154E+04	1.005
40	9.52	5.949E+03	1.001
50	9.53	5.231E+03	1.000
80	9.54	3.181E+03	1.001
100	9.51	2.607E+03	1.002

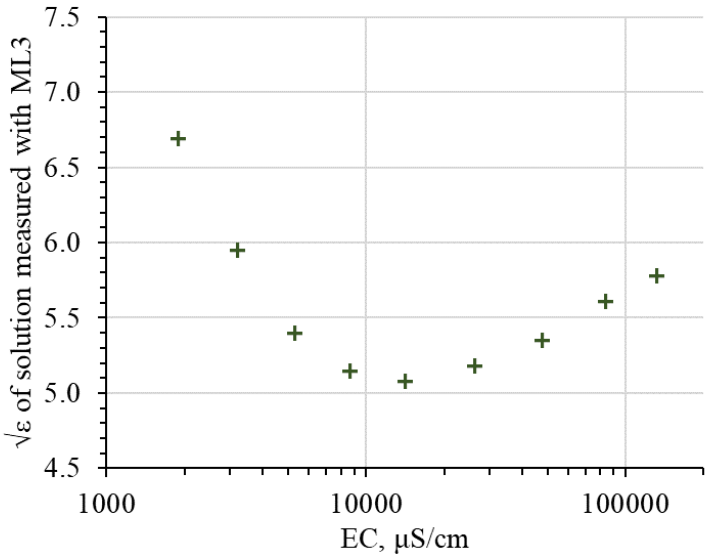

Figure 3.A1. The permittivity of the diluted FGD brine measured by the ML3 sensor as a function of the EC value

References

Abidin, K., and Hsai-Yang, F. (1997). "Identification of Contaminated Soils by Dielectric Constant and Electrical Conductivity." *Journal of Environmental Engineering*, American Society of Civil Engineers, 123(2), 169–177.

Allen, R. G., Pruitt, W. O., Wright, J. L., Howell, T. A., Ventura, F., Snyder, R., Itenfisu, D., Steduto, P., Berengena, J., Yrisarry, J. B., Smith, M., Pereira, L. S., Raes, D., Perrier, A., Alves, I., Walter, I., and Elliott, R. (2006). "A recommendation on standardized surface resistance for hourly calculation of reference ETo by the FAO56 Penman-Monteith method." *Agricultural Water Management*, 81(1), 1–22.

Apak, R., Tütem, E., Hügül, M., and Hizal, J. (1998). "Heavy metal cation retention by unconventional sorbents (red muds and fly ashes)." *Water research*, Elsevier, 32(2), 430–440.

ASTM International. (2012). "ASTM D698 - 12e2 Standard Test Methods for Laboratory Compaction Characteristics of Soil Using Standard Effort (12 400 ft-lbf/ft3 (600 kN-m/m3))." (D. 0. S. and R. (Sponsoring Committee), ed.).

ASTM International. (2013a). "ASTM D6349-13 Standard Test Method for Determination of Major and Minor Elements in Coal, Coke, and Solid Residues from Combustion of Coal and Coke by Inductively Coupled Plasma—Atomic Emission Spectrometry." (D. 2. C. and C. (Sponsoring Committee), ed.), West Conshohocken, PA.

ASTM International. (2013b). "ASTM C1216 / C1216M - 13 Standard Test Method for Adhesion and Cohesion of One-Part Elastomeric Solvent Release Sealants."

ASTM International. (2014). "D854-14 Standard Test Methods for Specific Gravity of Soil Solids by Water Pycnometer."

ASTM International. (2017). "ASTM C618-17a Standard Specification for Coal Fly Ash and Raw or Calcined Natural Pozzolan for Use in Concrete."

Batchelor, B. (2006). "Overview of waste stabilization with cement." *Waste Management*, Elsevier Ltd, 26(7), 689–698.

Chen, Y., and Or, D. (2006a). "Geometrical factors and interfacial processes affecting complex dielectric permittivity of partially saturated porous media." *Water resources research*, Wiley Online Library, 42(6).

Chen, Y., and Or, D. (2006b). "Effects of Maxwell-Wagner polarization on soil complex dielectric permittivity under variable temperature and electrical conductivity." *Water Resources Research*, Wiley Online Library, 42(6).

Cho, H., Oh, D., and Kim, K. (2005). "A study on removal characteristics of heavy metals from aqueous solution by fly ash." *Journal of hazardous materials*, Elsevier, 127(1–3), 187–195.

Conner, J. R., and Hoeffner, S. L. (1998). “A critical review of stabilization/solidification technology.” *Critical Reviews in Environmental Science and Technology*, Taylor & Francis, 28(4), 397–462.

Dai, S., Shin, H., and Santamarina, J. C. (2016). “Formation and development of salt crusts on soil surfaces.” *Acta Geotechnica*, Springer, 11(5), 1103–1109.

Daniels, J. L., and Das, G. P. (2018). “Influence of Flow Rate on Leachability.” *Coal Combustion and Gasification Products*, 10(3), 34–40.

Delta-T Devices Ltd. (2017). “User Manual for the ML3 ThetaProbe.”

Dudas, M. J. (1981). “Long-term leachability of selected elements from fly ash.” *Environmental Science and Technology*, 15(7), 840–843.

Dumenu, L. (2019). *Water Repellency Effect on Unsaturated Properties of Compacted Coal Combustion Residuals* . ProQuest LLC, Ann Arbor, MI.

Ellison, K. (2015). “Industry Perspectives on Integrating ELG and CCR Compliance through Wastewater Encapsulation: Challenges, Opportunities, and Technology Readiness.” *2015 World of Coal Ash Conference (www …*.

Fatoba, O. O., Petrik, L. F., Gitari, W. M., and Iwuoha, E. I. (2011). “Fly ash-brine interactions: Removal of major and trace elements from brine.” *Journal of Environmental Science and Health, Part A*, Taylor & Francis, 46(14), 1648–1666.

Fatoba, O., and Petrik, L. (2015). “Stability of brine components in co-disposed fly ash-brine solid residue.” *World of coal ash (WOCA) conference, WOCA, Nashville, Tennasee TN, USA*.

Gaskin, G. J., and Miller, J. D. (1996). “Measurement of soil water content using a simplified impedance measuring technique.” *Journal of agricultural engineering research*, Elsevier, 63(2), 153–159.

He, R., Ogunro;, V. O., and Ellison, K. M. (2022). “Preliminary Results of Compacted Coal Fly Ash/Flue Gas Desulfurization Brine Co-disposal in an Instrumented Testbed.” *Geo-Congress 2022*.

Hjelmar, O. (1990). “Leachate from land disposal of coal fly ash.” *Waste Management & Research*, 8(6), 429–449.

Huvaj-Sarihan, N., and Stark, T. D. (2008). “Back analyses of landfill slope failures.” *6th International Conference on Case Histories in Geotechnical Engineering and Symposium in Honor of Professor James K. Mitchell*.

Izquierdo, M., and Querol, X. (2012). “Leaching behaviour of elements from coal combustion fly ash: An overview.” *International Journal of Coal Geology*, 94, 54–66.

Koerner, R. M., and Soong, T.-Y. (2000). “Stability assessment of ten large landfill failures.”

Advances in transportation and geoenvironmental systems using geosynthetics, 1–38.

Mohan, S., and Gandhimathi, R. (2009). "Removal of heavy metal ions from municipal solid waste leachate using coal fly ash as an adsorbent." *Journal of hazardous materials*, Elsevier, 169(1–3), 351–359.

Nachshon, U., Weisbrod, N., Dragila, M. I., and Grader, A. (2011). "Combined evaporation and salt precipitation in homogeneous and heterogeneous porous media." *Water Resources Research*, Wiley Online Library, 47(3).

Oh, M., Kim, Y., and Park, J. (2007). "Factors affecting the complex permittivity spectrum of soil at a low frequency range of 1 kHz–10 MHz." *Environmental geology*, Springer, 51(5), 821–833.

Oza, S., Ogunro, V., Daniels, J., and Ellison, K. M. (2015). "Sequestration of Halides from FGD Wastewater through Lime Stabilization of Fly Ash." *2015 World of Coal Ash Conference. Retrieved from http://www. flyash. info/2015/064-ogunro-2015. pdf*.

Raucci, J. J., Samson, J., Ellison, K. M., Gallagher, B. J., Hines, J. S., and Kelsey, J. A. (2019). *Encapsulation of flue-gas desulfurization wastewater using coal combustion by-product mixtures: Field lysimeter investigations*.

Rhoades, J. D. (1996). "Salinity: Electrical conductivity and total dissolved solids." *Methods of soil analysis: Part 3 Chemical methods*, Wiley Online Library, 5, 417–435.

Sauer, T. J., and Horton, R. (2005). "Soil Heat Flux." *Micrometeorology in Agricultural Systems*, Agronomy Monographs.

Szypłowska, A., Szerement, J., Lewandowski, A., Kafarski, M., Wilczek, A., and Skierucha, W. (2018). "Impact of soil salinity on the relation between soil moisture and dielectric permittivity." *2018 12th International Conference on Electromagnetic Wave Interaction with Water and Moist Substances (ISEMA)*, IEEE, 1–3.

Tiruta-Barna, L., Rakotoarisoa, Z., and Méhu, J. (2006). "Assessment of the multi-scale leaching behaviour of compacted coal fly ash." *Journal of Hazardous Materials*, 137(3), 1466–1478.

Topp, G., Davis, J., and Annan, A. (1980). "Electromagnetic determination of soil water content: measurements in coaxial transmission lines." *Water Resources Research, Wash., D.C*, (G. Topp, ed.), 16(3), 574–582.

U.S. EPA. (1992). "SW-846 Test Method 3005A: Acid Digestion of Waters for Total Recoverable or Dissolved Metals for Analysis by Flame Atomic Absorption (FLAA) or Inductively Coupled Plasma (ICP) Spectroscopy."

U.S. EPA. (2007). "SW-846 Test Method 9056A: Determination of Inorganic Anions by Ion Chromatography."

U.S. EPA. (2009). *Steam Electric Power Generating Point Source Category: Final Detailed Study*

Report. United States Environmental Protection Agency, Washington, D.C.].

U.S. EPA. (2015). "Hazardous and Solid Waste Management System; Disposal of Coal Combustion Residuals From Electric Utilities; Final Rule." *The Federal Register*, Federal Information & News Dispatch, Inc., Washington.

U.S. EPA. (2020). "Steam Electric Reconsideration Rule." 40 C.F.R. Part 423.

Walter, I. A., Allen, R. G., Elliott, R., Jensen, M. E., Itenfisu, D., Mecham, B., Howell, T. A., Snyder, R., Brown, P., and Echings, S. (2000). "ASCE's standardized reference evapotranspiration equation." *Watershed management and operations management 2000*, 1–11.

Wang, N., Sun, X., Zhao, Q., Yang, Y., and Wang, P. (2020). "Leachability and adverse effects of coal fly ash: A review." *Journal of Hazardous Materials*, 396, 122725.

CHAPTER 4 EXPERIMENTAL STUDY OF CO-DISPOSAL OF COAL FLY ASH AND FLUE GAS DESULFURIZATION BRINE USING PASTE ENCAPSULATION TECHNOLOGY

Abstract

Coal-fired steam electricity plants are interested in finding efficient ways to manage by-products from the combustion process out of environmental and regulatory considerations. As a potential management strategy, the Zero Liquid Discharge (ZLD) targets eliminating the liquid waste from leaving the premises. One potential method to achieve ZLD is the co-disposal of solid and liquid by-products through solidification/stabilization (S/S). To address the problem of limited solid waste relative to liquid waste for some facilities, the paste encapsulation technology was proposed as a S/S method to co-dispose coal fly ash (CFA) and flue gas desulfurization (FGD) wastewater concentrate (brine) with the addition of a hydraulic agent (quicklime). The field test of the paste in an instrumented testbed showed on average 80% retention of chloride and bromide during the thirty-five months of the experiment, and on average a 97% halides retention if side leakage could be eliminated. While the chemical analysis found no heavy metals in the leachate and runoff from the testbed, the semi-dynamic leaching test in the laboratory showed the dominant mechanism for halide retention was solidification. The mineralogical analysis of different paste samples showed that minerals formed during the curing process were poorly structured, which posed difficulties for the interpretation of XRD results. The significant presence of magnesium in the FGD brine complicated validation of the hypothesis of the halide stabilization process through the precipitation of Friedel's salt and Kuzel's salt. The low saturated hydraulic conductivity on parallelly cured samples in the laboratory (1.44×10^{-8} m/s) explained the lack of responsiveness of the volumetric water content (VWC) sensors to rainfalls as infiltration in the paste material was minimal. The elevated temperature of the paste during the summer by solar radiation could

potentially impact the local microclimate as a heat source. With proper management of side leakage, the paste landfill will be effective in sequestering halides, but storm management should be designed on the expectation that runoff will be approximately equivalent to local precipitation at the facility.

Introduction

The by-products generated from the coal combustion process in a steam electric power plant are regulated under the Coal Combustion Residuals (CCRs) rules (U.S. EPA 2015) and the Effluent Limitations Guidelines (ELGs) (U.S. EPA 2020). As the major solid waste, coal fly ash (CFA) must be disposed of in the engineered landfill as stipulated in the CCR rules to prevent groundwater contamination. The ELG regulates the wastewaters from the combustion processes and disposal landfills. The main wastewater from the combustion processes is the flue gas desulfurization (FGD) purge water, often referred to as FGD wastewater or scrubber water. The reported values of total dissolved solids in typical FGD wastewaters ranged from 6,500 to 26,000 mg/L with high halide concentrations (EPA 2009). To reduce environmental impacts and promote the efficient use of water resources, the zero liquid discharge (ZLD) strategy is gaining interest from electricity generating facilities for FGD wastewater management (U.S. EPA 2020). While treatments used in the ZLD strategy, such as reversed osmosis, can reduce the wastewater stream, the liquid concentrate (brine) still requires further treatment (Tong and Elimelech 2016). A holistic ZLD strategy for coal-powered electric plants is to co-dispose the CFA and FGD brine in an engineered landfill, reducing water consumption by using the brine as the replacement for moisture conditioning. One of the co-disposal methods is through mixing and compaction, used in South Africa (Fatoba et al. 2011). The coal fly ash used in the study by Fatoba et al. (2011) has a lime content greater than 5%, which contributed to the stabilization/solidification (S/S) process. As the

stabilization process reduces the mobility of contaminants or transforms them into more geochemically stable or less harmful forms, the solidification process reduces contacts between water and potential constituents of concerns by reducing hydraulic permeability of the disposed material (Spence and Shi 2004; U.S. EPA 2000).

Since the lime content in the coal fly ash depends on the source of coal, ashes with lime content less than 5% require additional hydraulic binders such as quicklime and cement to solidify (Bhatt et al. 2019). The paste encapsulation technology for CFA-FGD brine co-disposal was proposed for discharge elimination and halide sequestration through the S/S of a cementitious paste (Oza et al. 2015; Ellison 2019; Raucci et al. 2019). Laboratory leaching studies showed that the cured paste materials could effectively encapsulate heavy metals, but failed to immobilize halides (Oza et al. 2015; Huang et al. 2017). While the leaching method typically employed (semi-dynamic leaching test, EPA Method 1315) presents the worst-case scenario for a continuously submerged sample, the contact between the material and the precipitation is limited to the exposed surface if appropriately managed.

This study investigated the co-disposal of a class F coal fly ash and FGD brine with the addition of the quicklime binder to produce a dense paste mixture in an instrumented testbed under the weather condition of the Charlotte area in North Carolina. While using the electrical conductivity (EC) as an indicator for total dissolved solids, selected leachate and runoff samples were also analyzed for the halides, heavy metals, and significant cations for quantitative evaluation of the performance of the disposal technique. The semi-dynamic leaching tests on the cured lab samples were performed to understand the effectiveness of the stabilization process. The in-situ permittivity and temperature sensors were used to understand the moisture, and heat flow and pattern within the material. Parallel paste samples cured under laboratory conditions were used to

investigate the strength and mineralogical changes. The lab cured samples were compared to the cored samples from the testbed at the end of the three-year experiment to understand the environmental impact on the curing process and field performance of the paste material.

4.2. Materials and Analysis Methods

4.2.1. Coal fly ash and quicklime

The coal fly ash used in this study was sourced from a coal-fired electric power plant in the southeast U.S. The chemical composition of the CFA expressed as oxides showed a 0.89% CaO by weight with 26.9% of Al_2O_3 and 53.5% of SiO_2 (ASTM International 2013a). The ash is categorized as class F based on its chemical composition (ASTM International 2017). The ash also contains 0.12 μg/g of mercury (Hg), 57.5 μg/g of arsenic (As), 66.7 μg/g of lead (Pb), and 231 μg/g of chromium (Cr). The water-soluble chloride (Cl), fluoride (F), and sulfate (SO_4) in the ash are 134, 31.8, and 4400 mg/L, respectively (ASTM International 2013b). The Rietveld refinement X-Ray diffraction (XRD) method showed that the ash consists of 75% amorphous glass with mullite, quartz, and magnetite contents at 16%, 5%, and 2% by weight, respectively. The Cu-Kα anode was used as the radiation source in the XRD analysis with the scanning 2θ angle ranging from 5 to 75º. The specific gravity of the ash at 20°C was 2.322 (ASTM International 2014). The quicklime was provided by a local supplier (Charlotte, North Carolina). The Rietveld XRD analysis showed the mass percentage of quicklime (CaO), calcium hydroxide ($Ca(OH)_2$), and calcite ($CaCO_3$) was 89.6%, 7%, and 1%, respectively.

4.2.2. Flue gas desulfurization brine

The flue gas desulfurization brine used in this study was sourced from a coal-fired electric power plant in the southeast U.S. The major halides in the FGD brine used were chloride and

bromide at 77,468 and 1,106 ppm, respectively (U.S. EPA 2007). Concentrations of other major elements were determined with the U.S. environmental protection agency (EPA) method 3005A (U.S. EPA 1992), and results are presented in Table 4.1. The EC and pH of the brine were 1.316×10^5 μS/cm and 8.11, respectively. The total solids (TS) and total suspended solids (TSS) in the brine were 0.005 and 0.216 grams per gram, respectively.

Table 4.1. Concentration of major metals and anions in the FGD brine

	Concentration, mg/L.		Concentration, mg/L.
Calcium	12200	Sodium	4220
Magnesium	11300	Potassium	1060
Sulfate	4230	Boron	838

4.2.3. Thermogravimetric analysis (TGA) and differential scanning calorimetry analysis (DSC)

The TGA and DSC were simultaneously performed with the Q600 SDT from TA Instruments. The material of the sample container and the reference cartridge were both alumina. The temperature range of the test was 50℃ – 1,000℃ with a heating rate of 20 ℃/min. High purity nitrogen was used as protective gas at a flow rate of 100 ml/min. Lab cured paste samples and coring samples from the field testbed were oven-dried at 60 ℃ and cooled to room temperature before analysis. The TGA provides the mineralogical compositions of the tested sample through characteristic weight loss behavior at different temperatures.

4.2.4. X-ray diffraction (XRD) analysis

The X-ray diffraction analysis was performed with a PANalytical's X'Pert PRO Materials Research Diffractometer. Scans were performed with the Cu-Kα radiation (λ = 1.542 Å) from 5 º to 75º at the step size of 0.02º and step time of 0.5 s. The XRD analysis was performed on lab

cured and field cored samples for mineralogical study. Compared to TGA, the XRD analysis was based on the diffraction profile of crystalline, which requires the knowledge of dominant elements to identify potential minerals in the material.

4.2.5. Semi-dynamic tank leaching for halides

The semi-dynamic tank leaching was performed following the guideline of the U.S. EPA method 1315 (U.S. EPA 2017). Samples cured under the laboratory condition for 856 days were used. Leachate from each leachant exchange/renewal was sampled and analyzed for EC, pH, and anions. The leached sample was oven-dried to determine the moisture content. The test was used as a long-term leaching test to investigate the potential chemical release from lab-cured samples. The method provides a worst-case scenario for leaching, which is the continuous submerge of the sample with routine water replacements.

4.2.6. Chemical analysis for liquids from lab leaching tests and field collect samples

The concentrations of the cations in the liquid samples were analyzed by the inductively coupled plasma-optical emission spectrometry (ICP-OES) using the Agilent 5100 instrument. The ion chromatography (IC) was used to quantify the anion concentrations using the Dionex ICS-3000 for samples collected prior to 6/2020, and a Metrohm IC system for later samples. Sample dilutions were prepared with ultrapure deionized water with a conductivity of 18.2 MΩ·cm. The samples were tested for sodium (Na), potassium (K), arsenic (As), lead (Pb), cadmium (Cd), iron (Fe), magnesium (Mg), silicon (Si), chloride (Cl^-), bromide (Br^-), fluoride (F^-), and sulfate (SO_4^{2-}) representing the major elements in the brines.

4.3. Instrumentation and Paste Material Testbed

The dimension of the High-Density Polyethylene (HDPE) used as the containment of the testbed was 96.52 cm × 114.30 cm × 111.76 cm, in width, length, and height, respectively. The testbed is located in the courtyard of the EPIC building in the University of North Carolina at Charlotte. A weather station recording hourly wind speed, solar radiation, atmospheric temperature, precipitation, and relative humidity was located six meters northeast of the testbed. A 17.78 cm sand layer for the leachate collection system was compacted at the bottom of the container to a saturated hydraulic conductivity of 0.180 cm/s. The leachate collection layer was divided into the annulus and the inner sections by HDPE walls extended 2.54 cm higher than the surface of compacted sand, as shown in Figure 4.1 (a). The area ratio of inner and annulus sections of the LCS was 1:8. The proportions of the paste mixture were 62.4% of CFA, 5.1% of quicklime, and 32.5% of FGD brine by weight. The paste was prepared with a grout mixer and pumped into the testbed to a height of 76.2 cm on top of the leachate collection layer. Sensors were installed at 12.7 cm (Top), 38.1 cm (Middle, Mid), and 63.5 cm (Bottom, Bot) below the exposed surface. A set of one ML3 ThetaProbe volumetric water content (VWC) sensor and one T108 temperature sensor was placed at each location. Dataloggers were used to collect and store hourly data from the sensors. The testbed was placed indoor and covered to allow the paste material to set for 33 days before moving it to the current location in the EPIC courtyard at UNC Charlotte and uncovered. The testbed was tilted to achieve a 2% slope, and a runoff collection system was installed at the lower end for the tilt. The runoff was directed into an HDPE film-lined trench with width, length, and depth of 7.62 cm, 96.52 cm, and 12.7 cm, respectively. Gravel with sizes ranging from 5 to 10 mm was used to fill the trench. Designated and chemically resistant tubing and storage tanks collected leachate from each leachate collection section and the surface runoff., Collected leachate

and runoff liquids were weighed and sampled for chemical analysis. The external walls except the exposed top surface were thermally insulated with a 15.88 cm thick R-19 fiberglass layer, and the testbed was routine inspection and repaired when necessary.

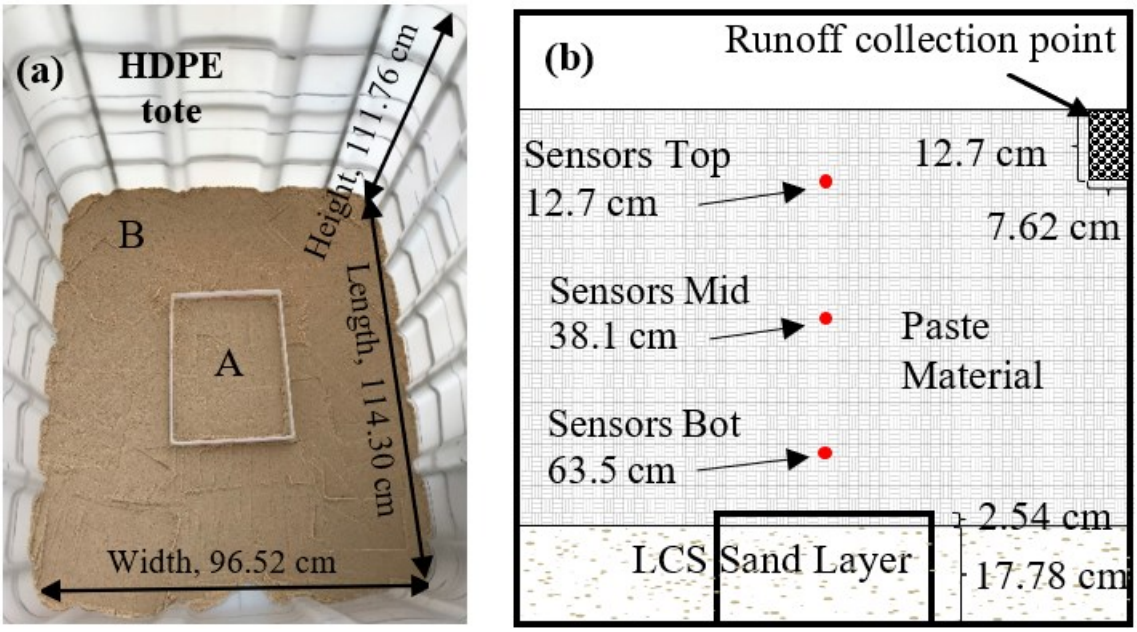

Figure 4.1. (a) Plan view of the sand drainage layer and (b) the cross-section alone the tilting direction (He et al. 2022).

4.4. Results and Discussion

4.4.1. Leachate and runoff generation

The total mass of runoff and leachate collected from the testbed over the duration of the experiment was 3701.2 kg and 570.4 kg, respectively. Compared to the 4215.1 kg precipitation estimated from the weather station data, representing 101.3% of the total estimated rainfall. The monthly quantities of collected runoff and leachate per unit of exposed surface area are presented

in Figure 4.2 with the monthly precipitation. Since in only four instances had any leachate been collected from the inner leachate collection section totaling a mass of 0.43 kg (3.53 mm), and a relatively substantial amount of leachate (580.79 in mm, 569.99 kg) was collected from the annulus section, a ratio of 1:1325.6 far larger area ratio of inner and annulus of 1:8, it is believed that leachate collected through this section was mainly generated from side leakage. The leak most likely occurred in narrow gaps between the container and the paste, which could have resulted from the shrinkage of the paste during curing and lack of adhesion to the HDPE container. Comparison of results from the chemical analysis of the leachate collected from the inner and annulus sections will be utilized to determine and conclude if the leachate from the annulus is generated through side leakage. No significant correlation was observed between the precipitation and the leachate generation for the paste testbed.

To investigate the water balance of the testbed, the recovery ratio was used to present the ratio of the monthly total leachate and runoff to monthly precipitation. The recovery ratio versus the monthly rainfall is shown in Figure 4.2. The average monthly rainfall from the weather station was 109.16 mm, with a standard deviation of 49.14 mm. The average recovery ratio was 1.07 with a standard deviation of 0.30, indicating the total recovery slightly exceeds the rainfall. Further analysis found no significant correlation between the weather conditions and the recovery rate. Since the testbed can be considered as a rain lysimeter located 27 cm below the level of the rain gauge, the observed variation of the recovery ratio could be the random error caused by the large area difference (exposed surface: opening of rain gauge = 84:1) and the height difference according to the study by Hoffmann et al. (2016). It is recommended that the precipitation gauge be installed at the same elevation for future field studies. Compared to an actual landfill, the testbed has a relatively high perimeter to area ratio, increasing the probability of side leakage and the quantity

of the side leakage as the runoff increases. Therefore, with proper side leakage management, the paste landfill will require a runoff control pond large enough to hold practically all the amount of the local precipitation.

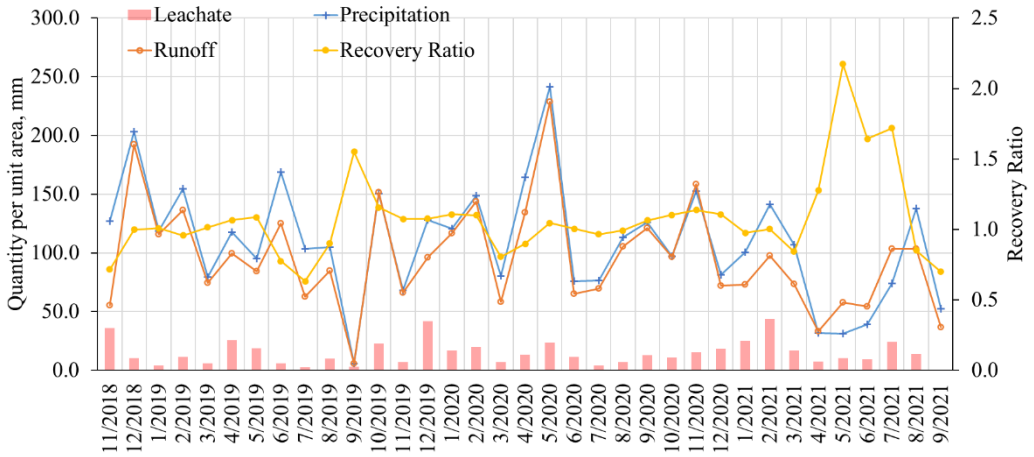

Figure 4.2. Monthly total leachate, runoff, and precipitation with the recovery ratio.

4.4.2. Permittivity and the free water content

The water content of the paste was monitored with the permittivity sensor. The bulk permittivity of a wetted granular porous medium is mainly controlled by the volumetric water content of the pore fluid, which is also affected by the pore solution's dielectric properties, the solid's dielectric properties, and the temperature (Chen and Or 2006a). Compared to the granular porous medium, the fresh paste mixture is a cementitious porous medium similar to concrete, but the chemical composition and pore structure changes with time as the solidification process progresses (Robert 1998). The bulk permittivity in the Portland cement concrete mix is immediately lowered as the free water in the matrix is rapidly consumed (Makul 2013). Compared

to the cementitious reactions in cement concrete mixes, the much slower pozzolanic reactions in the CFA paste, as ash particles slowly release water-soluble silica, would unlikely lead to a rapid change of the permittivity readings (Antiohos et al. 2006; Ma and Brown 1997). Even in a cement-CFA binary system with much higher alkalinity and calcium, unreacted CFA amorphous glass fraction was still found in samples after 4 years and 20 years (Luke and Lachowski 2008; Wang et al. 2012). Therefore, after the rapid hydration of the quicklime in the paste, the change in bulk permittivity should represent the change in free water content and temperature.

To investigate the influence of free water content on the bulk permittivity of the paste, duplicate samples of the paste were prepared using deionized water (DI). The maximum potential water content of 49.3% in the paste sample was the weight ratio of added DI in the total mass of mix, considering hydration processes take time. Since the degree of lime hydration was unknown during the process, the potential water content represents the remaining free water in the system. After the complete hydration of added quicklime, the potential free water content was expected to be 46.1%. The initial temperature increase shown in Figure 4.3 was due to quicklime hydration, which raised the temperature of the sample by 12℃ in about two hours after casting the paste samples then stabilizing back to room temperature of 21 ℃. The permittivity of the samples did not respond to the temperature change during this period. Theoretically, the correlation between permittivity and temperature depends on the water content of the porous medium (Or and Wraith 1999), the excitation frequency of the sensor (Chavanne and Frangi 2014), the dielectric properties of the pore solution, and potentially the measurement technique (Chen and Or 2006b). For the CFA-FGD brine co-disposal paste material measured at 100 MHz excitation frequency, the high salinity in the pore solution would enhance the Maxwell-Wegner polarization effect, which would lead to the increase of bulk permittivity with the rise in temperature (Chen and Or 2006b). The

reduction in free water content within the first 24 hours was due to the draining of the bleed water, which did not lead to the decline in Ɛ as the samples remained saturated, as demonstrated in Figure 4.3 (b). To further evaluate the relationship between moisture content and bulk permittivity, accelerated drying of the samples was performed by removing a portion of the container wall and oven drying at 40 °C. Figure 4.4 demonstrates the decrease in permittivity with free water content at a relatively constant temperature. In summary, the rise of permittivity in the testbed would indicate an increase in either or both temperature and free water content, and vice versa for a decrease in permittivity.

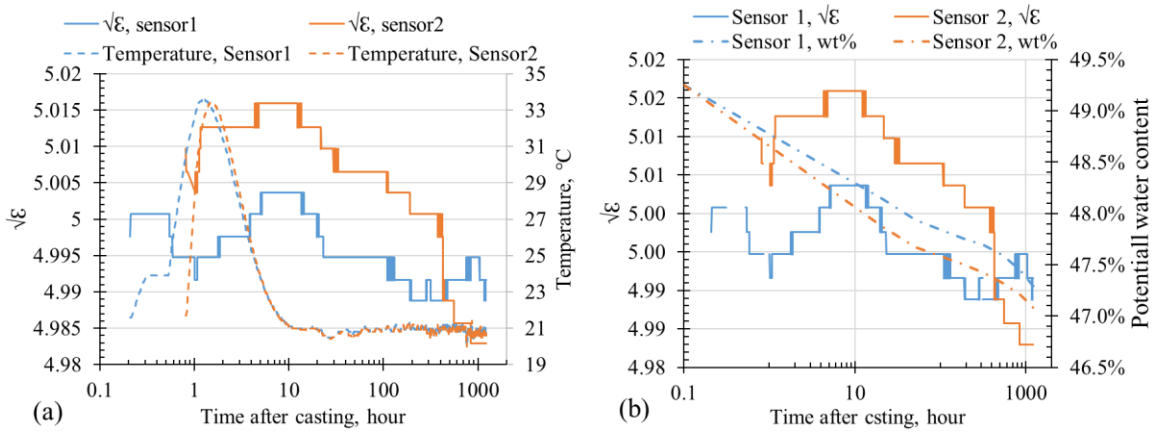

Figure 4.3. (a) Continuous monitoring of bulk permittivity and (b) potential water content during the paste curing process.

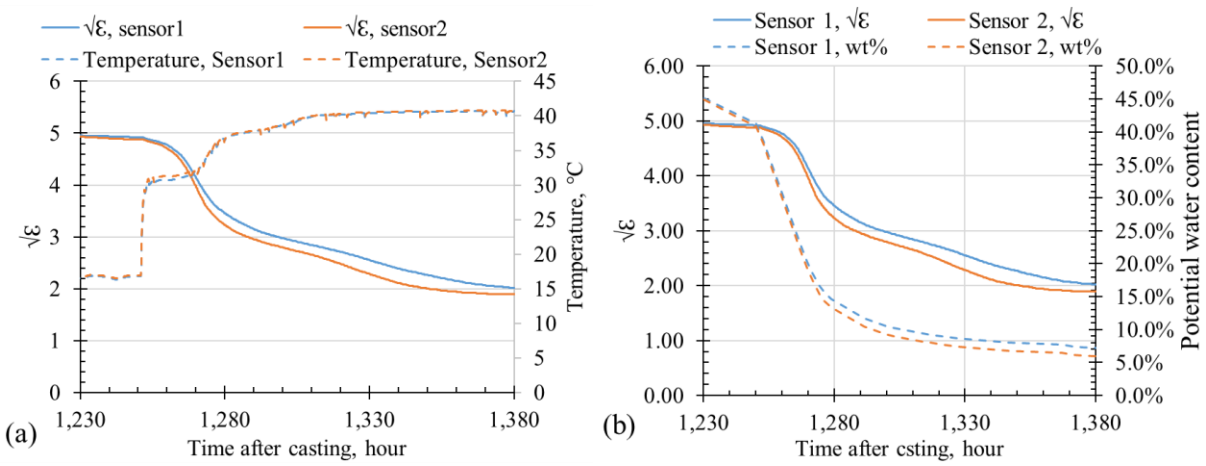

Figure 4.4. Relationship between permittivity and (a) temperature, (b) free water content in paste samples subjected to accelerated drying.

4.4.3. Permittivity and temperature profile of the testbed

The plot of the bulk apparent dielectric permittivity measured in the testbed in ($\varepsilon^{0.5}$) is shown in Figure 4.5, and the analysis of the permittivity data is presented in Table 4.2. As observed from Figure 4.5, the permittivity values did not vary significantly irrespective of the intensity and frequency of precipitation or the sensor locations in the testbed. Considering the quick response of the sensors to the change of water content as demonstrated in the previous section, the lack of variation in the responses of the sensors to precipitation indicates a lack of infiltration through the material because of its low saturated hydraulic conductivity of 1.44×10^{-8} m/s. The lowest variation of ±1.1 % from the mean value over the test duration of 3 years was observed at the center of the testbed, followed by ±1.8 % at the bottom and ±2.0 % at the top. As previously discussed, the permittivity was dominantly influenced by the paste material's temperature and free water content. To acquire the free water content, the cored samples from the testbed were dried at 60 °C to prevent the weight loss from trace minerals and the potential decomposition of ettringite (Antiohos and Tsimas 2004). The maximum potential free water content of the field paste mixture was 33.5%

when assuming complete hydration of quicklime without further water-consuming reactions. The theoretical maximum was greater than the free water content of 30% for lab cured samples under a sealed environment and 33% for samples after the leaching test. The higher free water content from the leached samples was attributed to the potential replacement of salt precipitates in pore spaces by water during leaching. The free water content obtained for the cored samples from the field was on average 32%, close to the theoretical maximum values, implying little change of water content during the field study period. Therefore, the cause of permittivity variation in the paste testbed was mainly attributed to temperature change.

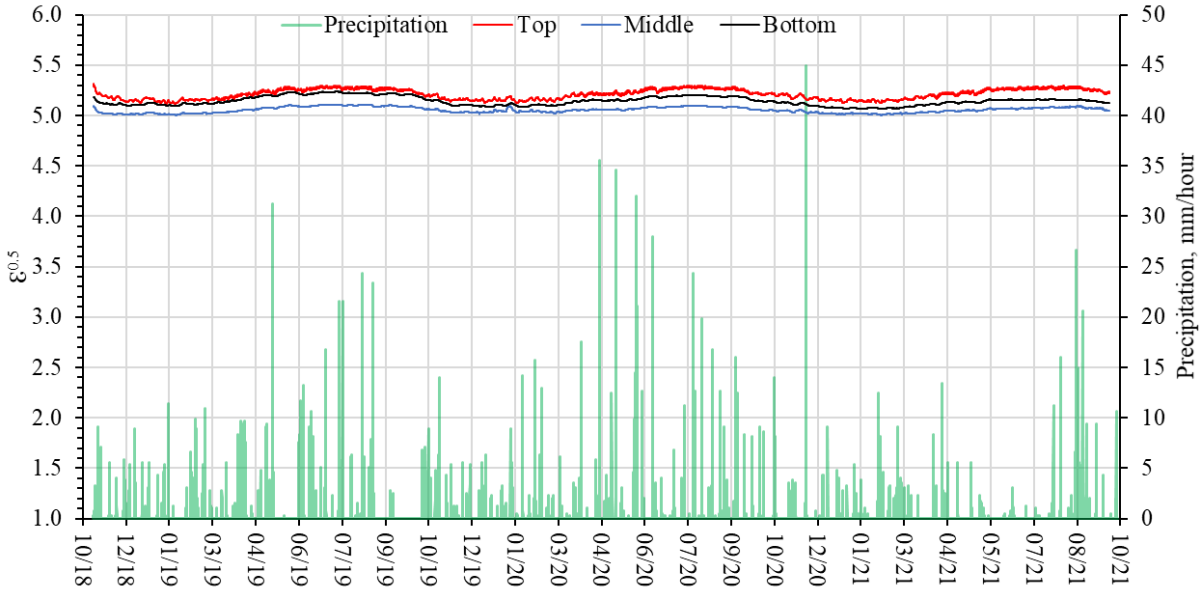

Figure 4.5. Permittivity profile in the testbed with hourly precipitation.

Table 4.2. Summary of $\varepsilon^{0.5}$ profile

Location (level)	Top	Middle	Bottom
Average $\varepsilon^{0.5}$	5.212	5.055	5.144
Std	0.0501	0.0282	0.0449
Max	5.315	5.109	5.236
Min	5.113	5.004	5.065
Max%	1.98%	1.07%	1.78%
min%	1.90%	1.02%	1.53%
Permittivity when coring	5.218	5.007	5.108
Free water content of cored samples	31.54%	32.02%	32.31%

The temperature and permittivity measurement from the sensors at the top, middle, and bottom locations are shown in Figure 4.6. The result demonstrated the permittivity change with the temperature, and the positive correlation agreed with the previous discussions. The correlations between the temperature and $\sqrt{\varepsilon}$ are 0.98, 0.93, and 0.89 for the top, middle, and bottom sensors, respectively. While no significant change was found for the temperature versus $\sqrt{\varepsilon}$ response at the top and the middle location with time, the bottom sensor showed a decrease in permittivity with time. The continuing decline of the permittivity at the bottom layers was likely attributed to the change of pore solution's dielectric properties (Chen and Or 2006a), considering the layer was least likely to experience a change of moisture. While the change of pore solution was most likely to be the result of the continuous dissolution of the CFA particles and quicklime hydration, the actual processes were not well known since the temporal profile of mineralogical analysis at the bottom of the testbed is lacking. Since the coring of the testbed could cause unexpected damage and stability issues, it is recommended that electrical conductivity (EC) sensors be installed in future studies at the sensor's location to provide information on the pore solution's salinity.

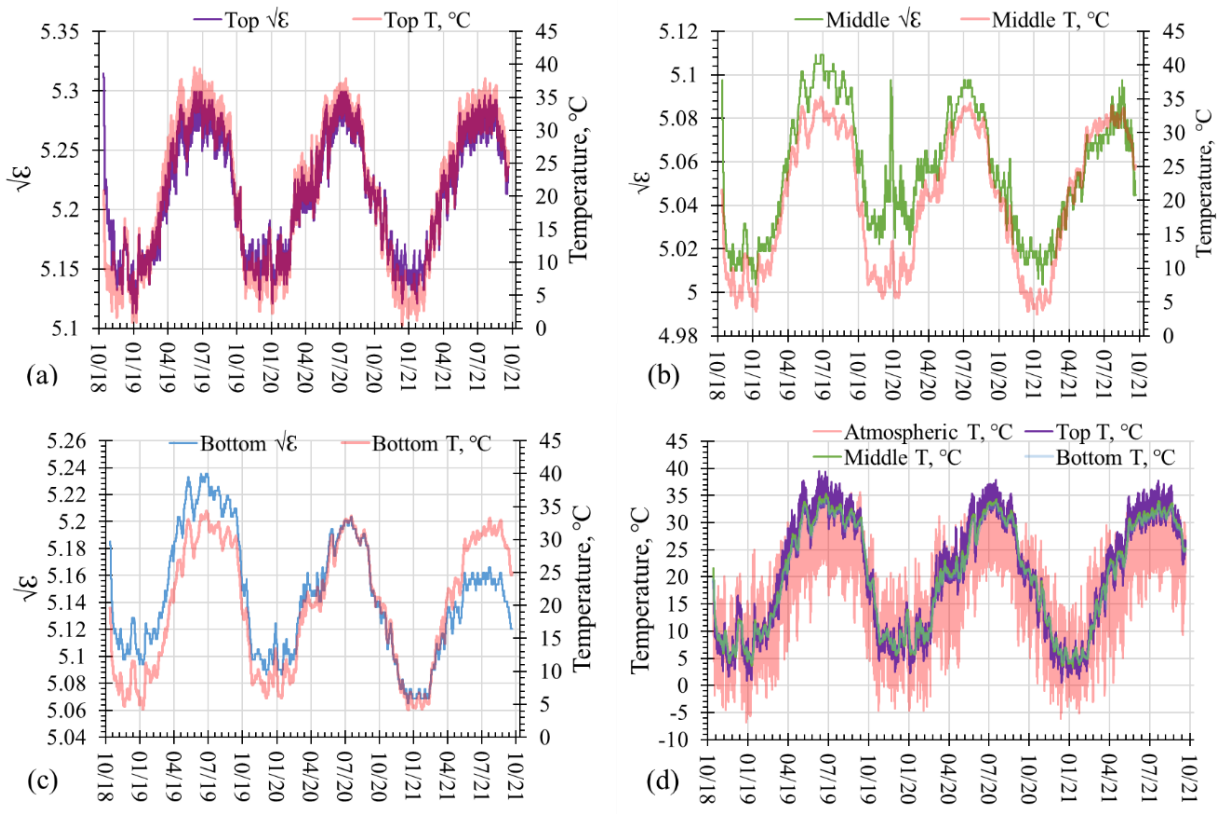

Figure 4.6. Relationship between permittivity and temperature readings at the (a) top, (b) middle, and (c) bottom in the testbed, and (d) the plot of the temperature profile in the testbed and atmospheric temperature.

Figure 4.6 shows that the temperature throughout the testbed generally stayed within the ambient temperature range except in the summer months. This higher overall temperature during the summer resulted from solar heating, demonstrated by the elevated surface temperature during the daytime, as shown in Figure 4.7. The average monthly solar radiation and the average hourly temperatures presented in Figure 4.7 further showed the elevated temperatures between March and November for 2019 and 2020. For half of a year, the higher temperature implies a paste landfill that can become a potential source of a heat island effect, capable of impacting air quality and creating a microclimate similar to a concrete parking lot (Huang et al. 2008; Onishi et al. 2010).

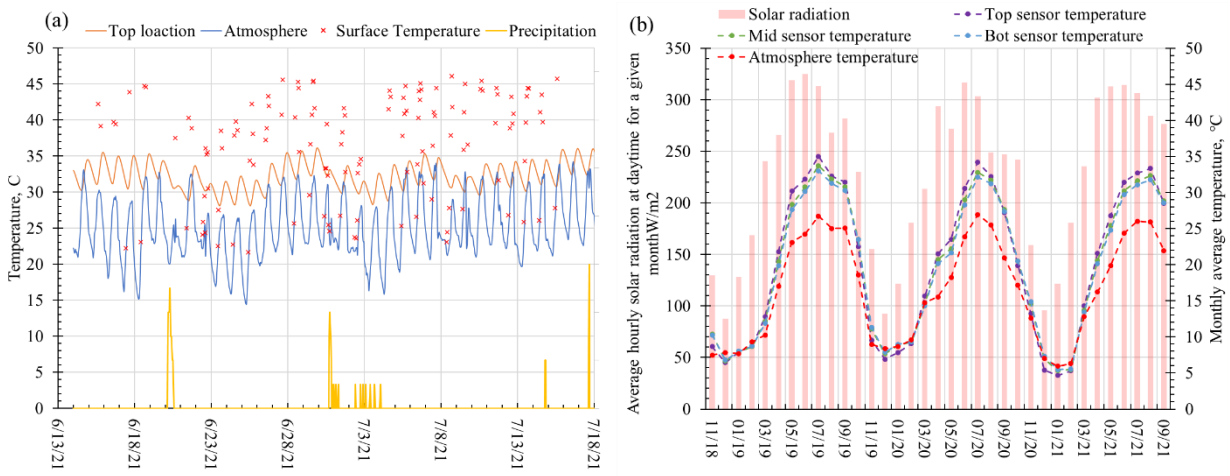

Figure 4.7. (a) Surface temperature measurement and (b) the average monthly temperature readings of the ambient condition and sensors with the average hourly solar radiation at daytime for the given month.

4.4.4. Chemical composition of the leachate and runoff samples

The runoff and leachate samples were tested for EC and pH to monitor the potential change in salinity, and the results are shown in Figure 4.8 (a). The EC of runoff varied randomly around an average of 1845 µS/cm with a standard deviation of 1647 µS/cm, while the pH remained practically constant around 7 for the study period.

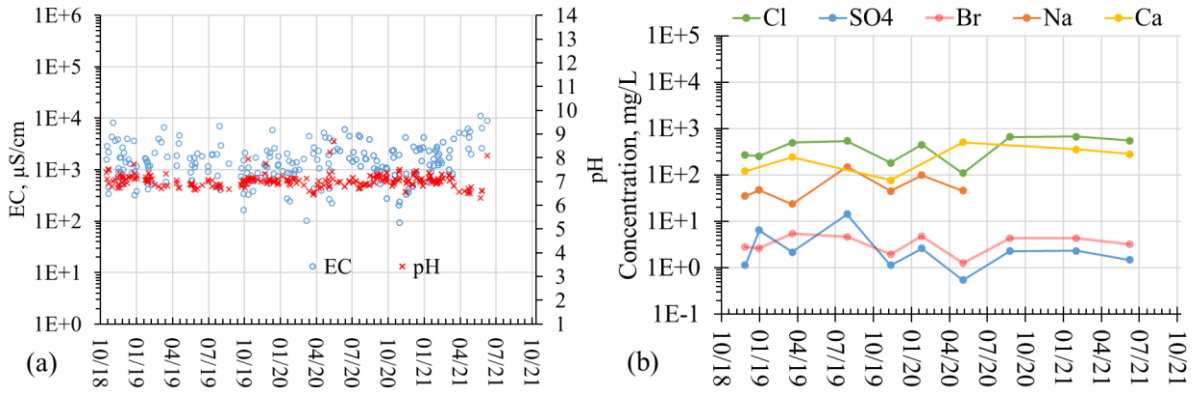

Figure 4.8. (a) Electrical conductivity (EC) and pH profile and (b) the chemical composition of runoff.

The chemical analysis for selected samples of the runoff presented in Figure 4.8 (b) showed the significant presence of chloride in the calcium and sodium salts. Since the main component of the surface scale was identified as calcium carbonate by XRD analysis, the lower pH of 7 in runoff compared to the pH above 8 in the leachate could be attributed to the carbonation reaction at the surface. The lowered salinity in the runoff originated from the dissolution/wash-off of the salts at the surface of the paste material could then be explained as the reduction of direct contact between the paste material and rainfall by the calcite scale. Considering the potential benefit of surface scaling, which forms at the surface of the paste material during curing, providing a cover material such as a sand layer to protect the precipitates from degradation and weathering could be one of the recommended operational and management practices for a paste landfill.

The EC of leachate rapidly decreased from 115,000 to 50,000 µS/cm over a cumulative mass of 51 kg, followed by a slow decrease to 20,000 µS/cm level as shown in Figure 4.9 (a). The pH of the leachate samples generally decreased from 11 to 8 during the study period compared to the lower pH at a relatively constant value of 7 for the runoff samples, as discussed previously.

The initial high ion concentration (salinity) was likely the release of residual brine through the consolidation process of the paste. With sodium and sulfate concentrations falling below the detection limits after 68.6 kg of leachate was collected, the main constituents of the leachate were calcium chloride and bromide, as shown in Figure 4.9 (b). A good correlation was obtained for the EC (μS/cm) and the concentration (mg/L) of collected samples of leachate and surface runoff, as shown in Figure 4.10, which resulted from chloride being the dominant anion (Corwin and Lesch 2003) throughout the study period. Since the EC of a solution can easily be monitored, the relationship suggests it can be used as an approximation tool for chloride concentration in the operation of paste landfills. Considering that the FGD brine has a substantial amount of magnesium concentration, the lack of such element in the leachate suggests the formation of magnesium hydroxide (brucite), which has a solubility of 6.9×10^{-3} g/L in water at 20 ℃ compared to the solubility value of 560 g/L of $MgCl_2$ at 25 ℃ (John Rumble 2018). While the hydration of quicklime produces concentrated calcium ions and alkalinity, the presence of brucite and gypsum precipitates can coat the quicklime particles and inhibit the hydration process (Ineich et al. 2017). The inhibition process could explain the existence of unreacted lime in the presence of abundant free water. The lack of evidence of brucite in the XRD analysis suggests the brucite precipitates might be amorphous, as reported by Kurdowski (2004). The approximate cumulative releases of the fraction of chloride and bromide added through the FGD brine were 22.2% and 18.6%, respectively. The chemical analysis showed the average chloride and bromide concentration in the inner leachate was 49,028 and 510 mg/L, respectively. The significantly lower halide average concentrations (9982 mg/L of chloride and 92 mg/L of bromide) in annulus leachate at the approximate time further suggest the side leakage was the dominant source of annulus leachate. Otherwise, the salinity level should be equivalent if leachates were generated from percolation.

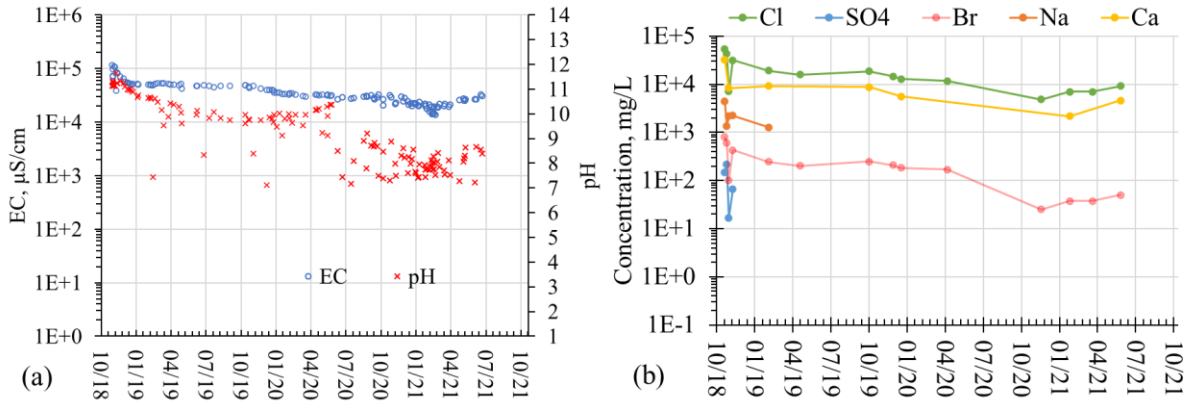

Figure 4.9. (a) Electrical conductivity (EC) and pH profile and (b) the chemical composition of leachate.

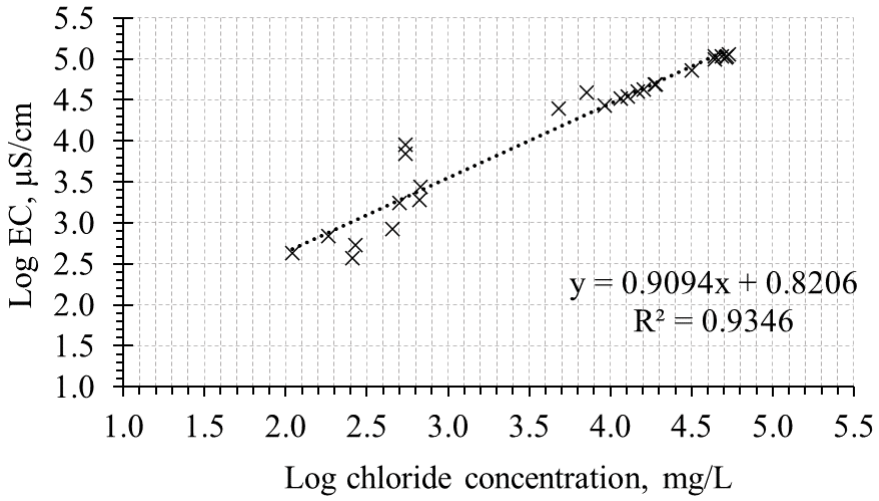

Figure 4.10. Correlation between electrical conductivity (EC) and concentration of chloride in liquids from paste co-disposal testbed.

While the inner section released 0.05% of chloride and 0.04% of bromide of the added FGD brine, the cumulative releases of chloride and bromide from surface runoff were only 3.3% and 2.0%, respectively. Therefore, if side leakage could be properly managed during this study,

the paste material would have been excellent for halide sequestration. It should be noted that during the implementation, 46.3 kg of consolidation water was collected after the implementation of the paste material, which was discounted from the salinity retention calculations. Such consolidation water could be managed by recycling into the paste production process. The paste encapsulation technology has potentially achieved an excellent halide retention efficiency in this field experiment, and paste landfill would be a key component of achieving zero liquid discharge in coal power plants.

4.4.5. Semi-dynamic tank leaching test for halides

The semi-dynamic tank leaching test using EPA method 1315 was performed to investigate the mechanism and effectiveness of the paste to immobilize and stabilize chloride and bromide. The sulfate was also monitored since it had a significant presence in the FGD brine. The test was performed on samples cured for 856 days under laboratory conditions. The intervals of the ten leachant exchanges were 0.08, 1, 1, 5, 7, 14, 14, 13, 15, and 7 days under an average room temperature of 22℃. The pH of the extraction liquid increased from 9 to 10.3 at 28 days, and remained a value higher than 9 afterward. The cumulative release of the chloride, bromide and sulfate per unit area of the exposed surface of the samples and the slopes of the curves between each interval are presented in Figure 4.11 (a). The slope of the log-log curve is used to interpret the leaching mechanism by method 1315 (Oza et al. 2015; Roessler et al. 2015). Generally, a slope greater than 0.65 represents release by washoff/dissolution, and a slope lower than 0.35 is considered leaching due to depletion at the surface. Between the 0.35 and 0.65, the dominant mechanism is attributed to diffusion from the monolith. During this experiment, chloride and bromide have highly similar slope values, indicating the same leaching mechanisms for these two halides. Both started with a slope of approximately 1, and the slope quickly dropped below 0.65

after the third exchange, indicating a fast dissolution of chloride and bromide from the monolith, as expected. The slope continued to fall below 0.35 after seven days and remained below the threshold, indicating the depletion was the dominant leaching mechanism and confirming the quantities of the elements in the samples are exhaustible. The sulfate experienced the same initial wash-off as halides, but the slope was maintained around 0.35 for the rest of the leaching experiment, indicating the anion was continuously diffused from the sample. At the end of the test, the cumulative releases of chloride, bromide, and sulfate from the added FGD brine were 80.4%, 75.5%, and 49.0%, respectively. While the retention of the sulfate was likely due to gypsum precipitation produced with added lime and the possible formation of ettringite, the halides were likely to be precipitated through the formation of Friedel's salts (Manikonda et al. 2019; Renew et al. 2016; Zhang et al. 2020). The XRD analysis in later discussion confirmed the existence of a trace amount of Ca-LDHs (Friedel's salt), but the weak intensity suggested the quantity was relatively small. The leaching test indicated a limited amount of halides were stabilized, and the halides were primarily released by dissolution and diffusion. Controlling water contact and infiltration would be the best management option to minimize halide release from a paste landfill of co-disposal of CFA and FGD brine with the addition of quicklime. Hence, the design and operation of a CFA-FGD brine co-disposal paste landfill should avoid continuous immersion scenarios such as surface ponding and should reduce the travel time of runoff water on the surface.

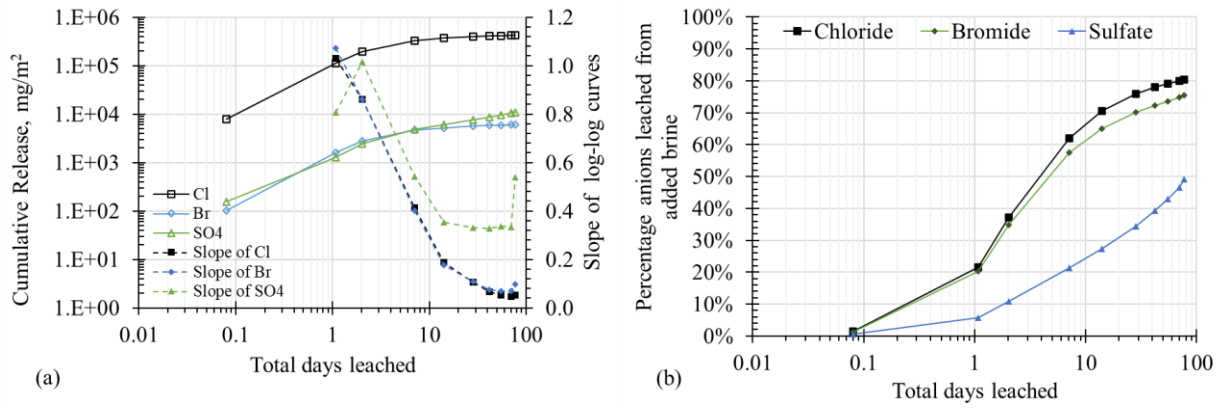

Figure 4.11. (a) The cumulative release per unit area and the slope of log-log curves, and (b) cumulative percentage release of anions from the lab cured paste samples.

4.4.6. Mineralogy study

As discussed in previous sections, the mineralogical studies were performed on samples dried at 60℃ to remove free water content. While the TGA was performed to quantify the quantity of hydration products in the samples, XRD was used to qualitatively understand the potential mineral compositions of the cured materials (Collin et al. 2021; Monteagudo et al. 2014). To better highlight the weight loss pattern from TGA tests, the differential thermogravimetric analysis (DTG) of the samples presented as the percentage weight loss per degree Celsius is discussed in the latter part of this section. The XRD analysis of the samples shown in Figure 4.12 suggested a minimal formation of layered double hydrates (LDHs) such as Friedel's salt (FS). Compared to other studies showing a significant formation of Friedel's salts and ettringite (Collin et al. 2021; Zhang et al. 2020), the weak LDHs signals could potentially result from limited aluminum or poorly structured precipitates. In terms of ettringite, studies have shown magnesium can inhibit the precipitation of ettringite and destabilize ettringite (Cody et al. 2004; Dou et al. 2017; Pajares et al. 2003). However, definitive conclusions cannot be drawn on whether the mineral was absent or in a very poorly

structured form such as woodfordite (Pajares et al. 2003). Considering aluminum was not readily available in this paste system as observed from its absence in leachates and runoffs, the competition from magnesium to form hydrotalcite type layered double hydroxide (Mg-LDH) will impact the formation of Friedel's salt (Ca-LDH). It should also be noted that Mg-LDH shares a very similar XRD pattern with Ca-LDH due to its highly similar crystalline structure (Grover et al. 2010), which can lead to errors in isolating the exact chloride binding minerals. In this research, the formation of FS was promoted by using quicklime as the hydrating reagent, which reduces the magnesium concentration while providing additional calcium sources (Farnam et al. 2015; Sutter et al. 2006). After the leaching schedule presented in the previous section, the samples were subjected to continued leaching for additional four water exchanges at the interval of 14 days to acquire a blank material, which represents a completely leached sample. The disappearance of the lime (CaO, L) phase in the leached sample suggests the lime content detected in paste samples was ready for reaction, which indicates the lime was prevented from further hydration when abundant free water was present. Per the previous discussion, the lime particles were likely coated with brucite and gypsum, which were released during the leaching experiment (Ineich et al. 2017).

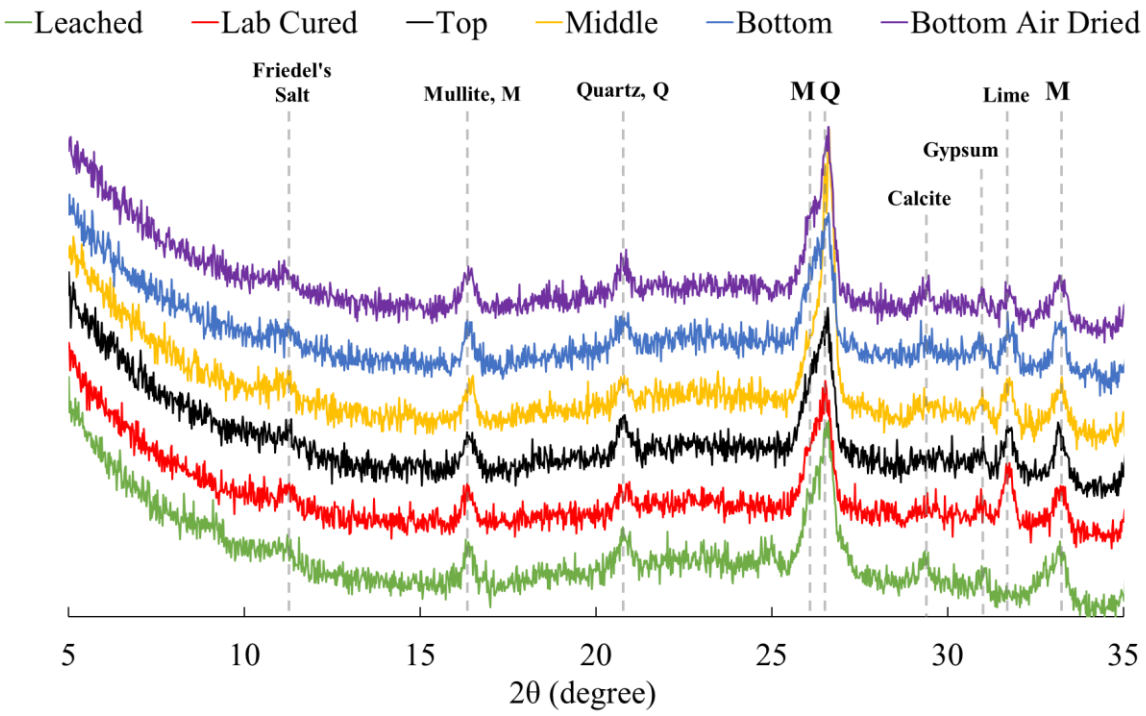

Figure 4.12. X-ray diffraction analysis of samples cured (lab cured), collected (Top, Middle, and Bottom layers of testbed), and treated under different conditions (oven-dried, air dried, or leached).

The DTG patterns of samples collected from different layers of testbed (top, middle, and bottom) cured samples, leached samples, the quicklime sample, and the fly ash sample for the range of 50 to 1000 ℃ are presented in Figure 4.13. Difficulties always exist in identifying the weight loss associated with the ettringite as the mineral decomposes at 60 ℃ (Ndiaye et al. 2017). The 60 ℃ decomposition temperature overlaps with the removal of adsorbed water (Földvári 2011), which accounted for a significant portion of weight loss. To identify the potential impact of the drying method on the TGA method, the samples from the bottom layer of the testbed were separated into dried at the laboratory ambient condition or room temperature (air-dried) and in the 60 ℃ oven followed with equilibrium at room conditions (oven-dried). The free water contents determined through the two drying methods were comparable at 28% for air-dried and 27% for

oven-dried samples. Considering the water content calculated for the oven-dried samples immediately after removal from the oven was 32%, the oven-dried samples absorbed the ambient humidity to reach the same state as the air-dried samples. Since the curing process of this paste system was directly related to the hydration of the lime, which provided the alkalinity in the system that led to further formation of other hydrates, the thermogravimetric analysis focused on the decomposition of the metal hydrates similar to the work of Alarcon-Ruiz et al. (2005). In general, the weight loss can be categorized in three phases in a cementitious or pozzolanic system as dehydration (Ldh), dehydroxylation (Ldx), and decarbonization (Ldc) that relate to the decomposition of metal-silicate-hydrates, metal hydroxides, and metal carbonates, respectively (Alarcon-Ruiz et al. 2005; Monteagudo et al. 2014; Pane and Hansen 2005). The significant presence of sulfate in the paste would increase the weight loss in the Ldh and Ldc zones through the dehydration and decomposition of metal sulfate salt, respectively (Földvári 2011).

Considering the starting temperature of the Ldh varies depending on the study or the investigators, the analysis using Ldh_{105} (105~350 ℃) from Monteagudo et al. (2014) and Ldh_{140} (140~350 ℃) from Pane and Hansen (2005) was presented for comparison. Below the 140 ℃, a significant weight loss peak was observed around 80 ℃ with a secondary peak around 110 ℃, indicating a different weight loss mechanism. As this secondary weight loss peak was also present in the analysis of the ash, it was most likely attributed to the loss of adsorbed water on the aluminosilicate surface of ash particles (Földvári 2011). While the weight loss between 105~430 ℃ also represents the dehydration of the calcium-silicate-hydrates (CSH) in the calcium cement system, the temperature range included the dehydration of magnesium-silicate-hydrates (MSH) system (Alarcon-Ruiz et al. 2005; Bernard et al. 2019; Jin and Al-Tabbaa 2013; Monteagudo et al. 2014). Furthermore, the dehydration study on MSH suggested weight loss between 105~430 ℃

overlapped with dehydroxylation of brucite ($Mg(OH)_2$) between 350~450 ℃ (Jin and Al-Tabbaa 2013). The characteristic peaks around 360 ℃ observed in Figure 4.13 were mainly attributed to the dehydroxylation of brucite, which could potentially overlap with the weight loss from dehydration of CSH and MSH. Acknowledging the potential underestimation of weight loss due to dehydration of the metal-silicate-hydrates content, the 140~350 ℃ was assigned to the Ldh process. Consequently, the temperature range of 350 to 530 ℃ was used to calculate the dehydroxylation of brucite and portlandite ($Ca(OH)_2$) zone.

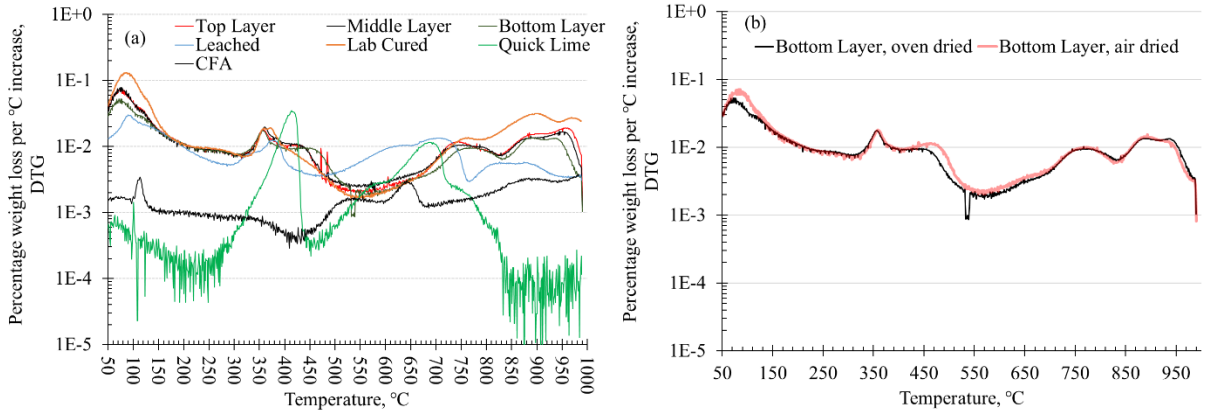

Figure 4.13. Differential thermogravimetric (DTG) analysis: (a) materials and samples, and (b) samples dried under different conditions.

The weight loss of each process and the stacked weight loss of each sample is illustrated in Figure 4.14. The weight loss from dehydration and the difference between each cured sample estimated from the Ldh_{105} method was significantly higher than the Ldh_{140} method. Compared to the cured samples, the weight loss of ash particles between 105 ℃ and 140 ℃ should represent the maximum potential weight loss due to water adsorption on the particles, which was relatively

small. The difference in weight loss suggests dehydration was the dominant process in cured samples. However, the TGA method cannot separate the weight loss contributed by CSH and MSH phases due to the highly overlapping decomposition temperature zones (Jin and Al-Tabbaa 2013; Monteagudo et al. 2014). While the Ldx represents the quantity of brucite and portlandite, the result showed a similar hydroxide content among the oven-dried top, middle, bottom, and lab cured samples with an average of 1.50%. Further analysis showed the dominant weight loss was due to dehydroxylation of brucite rather than the portlandite, as shown in Figure 4.15, which further supported the brucite coating assumption in the previous discussion as the leached sample presented a higher portlandite fraction than brucite.

The results from Ldc showed a significantly higher value for lab cured samples than other samples, and the top and middle samples had higher values than the bottom samples. While the Ldc was used to represent the broad weight loss due to the decomposition of carbonate and sulfuric compounds, a significantly different weight loss pattern was presented in the DTG curve between the leached and un-leached samples. The major weight loss in the Ldc of the leached samples happened between 550 ℃ and 770 ℃, while the unleached samples showed major weight loss beyond 670 ℃. The peak around 950 ℃ resembles the decomposition of calcite, which was evident in top, middle, and lab cured samples than the bottom samples. The comparison of the lab cured sample and the leached sample suggests a portion of the hydroxides responsible for Ldc could have been removed by the leaching process, which indicates the precipitates that contributed to the weight loss were likely to have an amorphous structure. The amorphous structure also explained the weak calcite peak in the XRD analysis for top and middle layers when a calcite crust was present on the paste surface of the testbed during the study period. The weight loss due to decarbonization was evidently higher in field samples taken closer to the surface of testbed, which

indicates carbonation potentially due to extensive carbon dioxide infiltration. Although CFA-FGD brine co-disposal paste is a relatively new subject, studies showed the addition of fly ash in the cement mix would increase the carbonation depth of the concrete (Khunthongkeaw et al. 2006; Šavija and Luković 2016). The carbonation of paste material can potentially be a disadvantage to the chloride binding capacity by the precipitation of metal carbonates from metal hydrate (Kayyali and Qasrawi 1992).

Overall, the lab cured sample showed a higher weight loss due to the decomposition of minerals than the field samples, suggesting a potential difference in the degree of curing between field and lab conditions. Due to the poorly structured minerals, the XRD analysis cannot provide definitive information on the mineral formations, suggesting other analytical methods such as Fourier-transform infrared spectroscopy (FTIR) and scanning electron microscopy with energy dispersive X-ray spectroscopy (SEM-EDS) would be needed to provide the element-based analysis (Durdziński et al. 2015; Madejová 2003). The significant presence of magnesium in the mixture suggests the magnesium-based cementing reactions need to be considered in addition to the calcium-based reactions, which could change the mechanism of the stabilization/solidification process in the lime-amended co-disposal system.

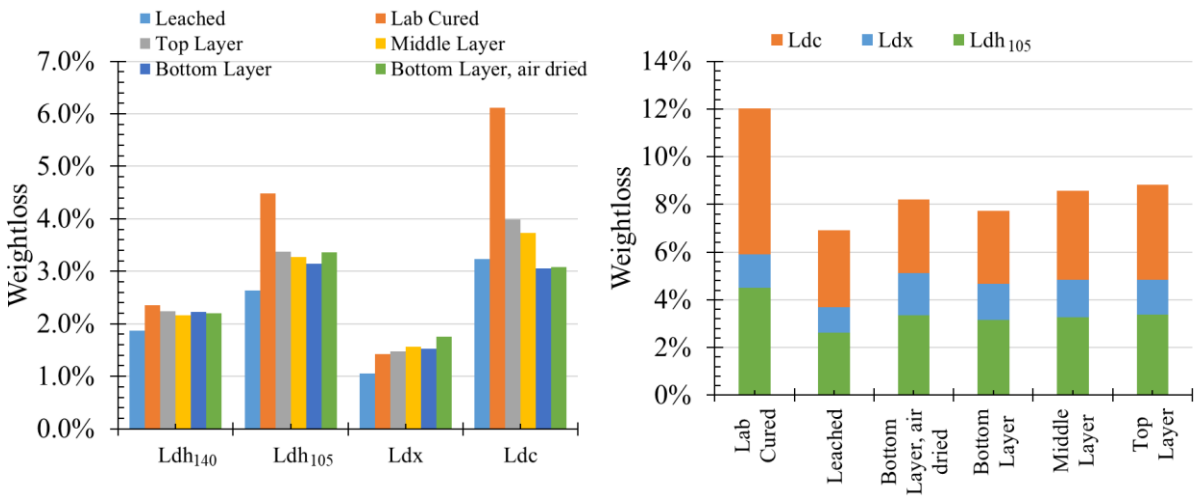

Figure 4.14. Weight loss attributed to each hydration process (left) and the stacked weight loss of each sample(right) (where Ldh_{105} is estimated between 105 and 350 ℃, and Ldh_{140} is estimated between 140 and 350 ℃).

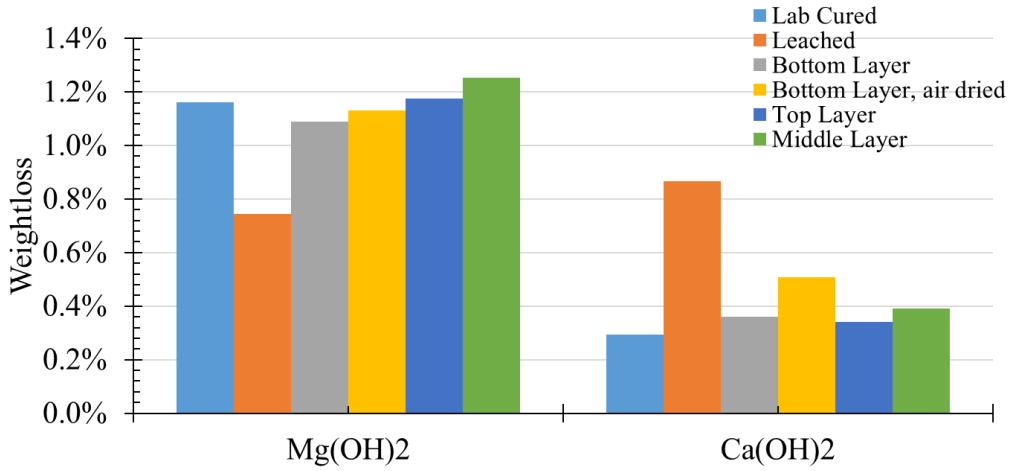

Figure 4.15. Weight loss attribute the dehydroxylation of $Mg(OH)_2$ (350~450℃) and $Ca(OH)_2$ (450~530 ℃)

4.5. Conclusions

The field experiment of the lime stabilized CFA-FGD brine co-disposal paste technology achieved good retention of halide for the three years of study. The in-situ monitoring of bulk

permittivity has a high correlation to the temperature. The analysis showed the testbed was significantly heated by solar radiation, making a paste landfill a potential heat island that may negatively impact the local climate if not mitigated with an appropriate cover soil. The semi-dynamic tank leaching test showed that the halide retention ability of the paste in the testbed was through solidification rather than stabilization, and the major leaching mechanism was the dissolution/wash off of the elements from the samples. The mineralogical analysis showed the formation of poorly structured precipitates, which poses significant challenges to using XRD analysis for mineral identification. The TGA analysis showed a significant presence of brucite compared to portlandite, suggesting the necessity to consider the magnesium-based cementing reactions in the lime-amended CFA-FGD brine mixture with a substantial magnesium presence. The decomposition of carbonated minerals near the surface of the testbed suggests potential carbon dioxide infiltration into the paste material, causing carbonation of the paste, which could lead to the reduction of the chloride binding capacity of the cured materials. It should also be noted that the mineral sequestration of halides through precipitation of layer double hydrates requires adequate aluminum in addition to the lime addition. Although the chemical composition of coal fly ash consists of a significant amount of aluminum, the element appears not to be readily available for reactions under the prevailing condition in the paste material. Paste landfills will be expected to generate large surface runoffs with an EC averaging 1845 μS/cm and a standard deviation of 1647 μS/cm. The relatively low EC in the runoff compared to the side leakage suggests the calcite scaling potentially reduced the direct contact between rainfall and the material, reducing salinity release through dissolution/wash-off. Therefore, it is recommended that surface protective covers such as a sand layer be implemented to prevent physical damages to the cured surface.

References

Alarcon-Ruiz, L., Platret, G., Massieu, E., and Ehrlacher, A. (2005). "The use of thermal analysis in assessing the effect of temperature on a cement paste." *Cement and Concrete research*, Elsevier, 35(3), 609–613.

Antiohos, S., Papageorgiou, A., and Tsimas, S. (2006). "Activation of fly ash cementitious systems in the presence of quicklime. Part II: Nature of hydration products, porosity and microstructure development." *Cement and Concrete Research*, 36(12), 2123–2131.

Antiohos, S., and Tsimas, S. (2004). "Activation of fly ash cementitious systems in the presence of quicklime: Part I. Compressive strength and pozzolanic reaction rate." *Cement and concrete research*, Elsevier, 34(5), 769–779.

ASTM International. (2013a). "ASTM D6349-13 Standard Test Method for Determination of Major and Minor Elements in Coal, Coke, and Solid Residues from Combustion of Coal and Coke by Inductively Coupled Plasma—Atomic Emission Spectrometry." (D. 2. C. and C. (Sponsoring Committee), ed.), West Conshohocken, PA.

ASTM International. (2013b). "ASTM C1216 / C1216M - 13 Standard Test Method for Adhesion and Cohesion of One-Part Elastomeric Solvent Release Sealants."

ASTM International. (2014). "D854-14 Standard Test Methods for Specific Gravity of Soil Solids by Water Pycnometer."

ASTM International. (2017). "ASTM C618-17a Standard Specification for Coal Fly Ash and Raw or Calcined Natural Pozzolan for Use in Concrete."

Bernard, E., Lothenbach, B., Chlique, C., Wyrzykowski, M., Dauzeres, A., Pochard, I., and Cau-Dit-Coumes, C. (2019). "Characterization of magnesium silicate hydrate (MSH)." *Cement and concrete research*, Elsevier, 116, 309–330.

Bhatt, A., Priyadarshini, S., Acharath Mohanakrishnan, A., Abri, A., Sattler, M., and Techapaphawit, S. (2019). "Physical, chemical, and geotechnical properties of coal fly ash: A global review." *Case Studies in Construction Materials*, 11, e00263.

Chavanne, X., and Frangi, J.-P. (2014). "Presentation of a complex permittivity-meter with applications for sensing the moisture and salinity of a porous media." *Sensors*, Multidisciplinary Digital Publishing Institute, 14(9), 15815–15835.

Chen, Y., and Or, D. (2006a). "Geometrical factors and interfacial processes affecting complex dielectric permittivity of partially saturated porous media." *Water resources research*, Wiley Online Library, 42(6).

Chen, Y., and Or, D. (2006b). "Effects of Maxwell-Wagner polarization on soil complex dielectric permittivity under variable temperature and electrical conductivity." *Water Resources Research*, Wiley Online Library, 42(6).

Cody, A. M., Lee, H., Cody, R. D., and Spry, P. G. (2004). "The effects of chemical environment on the nucleation, growth, and stability of ettringite [Ca3Al (OH) 6] 2 (SO4) 3· 26H2O." *Cement and Concrete Research*, Elsevier, 34(5), 869–881.

Collin, M., Prentice, D. P., Arnold, R. A., Ellison, K., Simonetti, D. A., and Sant, G. N. (2021). "Fly Ash–Ca(OH)2 Reactivity in Hypersaline NaCl and CaCl2 Brines." *ACS Sustainable Chemistry & Engineering*, American Chemical Society, 9(25), 8561–8571.

Corwin, D. L., and Lesch, S. M. (2003). "Application of soil electrical conductivity to precision agriculture: theory, principles, and guidelines." *Agronomy journal*, Wiley Online Library, 95(3), 455–471.

Dou, W., Zhou, Z., Jiang, L.-M., Jiang, A., Huang, R., Tian, X., Zhang, W., and Chen, D. (2017). "Sulfate removal from wastewater using ettringite precipitation: Magnesium ion inhibition and process optimization." *Journal of environmental management*, Elsevier, 196, 518–526.

Durdziński, P. T., Dunant, C. F., Haha, M. Ben, and Scrivener, K. L. (2015). "A new quantification method based on SEM-EDS to assess fly ash composition and study the reaction of its individual components in hydrating cement paste." *Cement and Concrete Research*, Elsevier, 73, 111–122.

Ellison, K. (2019). *Landfill Sequestration of Brine: Research Updates*. *World of Coal Ash*.

Farnam, Y., Wiese, A., Bentz, D., Davis, J., and Weiss, J. (2015). "Damage development in cementitious materials exposed to magnesium chloride deicing salt." *Construction and Building Materials*, Elsevier, 93, 384–392.

Fatoba, O. O., Petrik, L. F., Gitari, W. M., and Iwuoha, E. I. (2011). "Fly ash-brine interactions: Removal of major and trace elements from brine." *Journal of Environmental Science and Health, Part A*, Taylor & Francis, 46(14), 1648–1666.

Fatoba, O., and Petrik, L. (2015). "Stability of brine components in co-disposed fly ash-brine solid residue." *World of coal ash (WOCA) conference, WOCA, Nashville, Tennasee TN, USA*.

Földvári, M. (2011). *Handbook of Thermogravimetric System of Minerals and Its Use in Geological Practice*. Magyar Állami Földtani Intézet alkalmi kiadványa, Geological Institute of Hungary (=Magyar Állami Földtani Intézet).

Grover, K., Komarneni, S., and Katsuki, H. (2010). "Synthetic hydrotalcite-type and hydrocalumite-type layered double hydroxides for arsenate uptake." *Applied clay science*, Elsevier, 48(4), 631–637.

He, R., Ogunro;, V. O., and Ellison, K. M. (2022). "Preliminary Results of Compacted Coal Fly Ash/Flue Gas Desulfurization Brine Co-disposal in an Instrumented Testbed." *Geo-Congress 2022*.

Hoffmann, M., Schwartengräber, R., Wessolek, G., and Peters, A. (2016). "Comparison of simple rain gauge measurements with precision lysimeter data." *Atmospheric Research*, Elsevier,

174, 120–123.

Huang, C.-H., Renew, J. E., Engineering, C. and E., Burns, S., Yiacoumi, S., Chen, Y., and Tang, Y. (2017). “Immobilization of heavy metals in solidified/stabilized co-disposed bituminous coal fly ash and concentrated flue gas desulfurization wastewater.”

Huang, L., Li, J., Zhao, D., and Zhu, J. (2008). “A fieldwork study on the diurnal changes of urban microclimate in four types of ground cover and urban heat island of Nanjing, China.” *Building and environment*, Elsevier, 43(1), 7–17.

Ineich, T., Degreve, C., Karamoutsos, S., and du Plessis, C. (2017). “Utilization efficiency of lime consumption during magnesium sulfate precipitation.” *Hydrometallurgy*, Elsevier, 173, 241–249.

Jin, F., and Al-Tabbaa, A. (2013). “Thermogravimetric study on the hydration of reactive magnesia and silica mixture at room temperature.” *Thermochimica acta*, Elsevier, 566, 162–168.

John Rumble. (2018). *Handbook of Chemistry and Physics 99th Edition*. CRC Press.

Kayyali, O. A., and Qasrawi, M. S. (1992). “Chloride binding capacity in cement-fly-ash pastes.” *Journal of materials in civil engineering*, American Society of Civil Engineers, 4(1), 16–26.

Khunthongkeaw, J., Tangtermsirikul, S., and Leelawat, T. (2006). “A study on carbonation depth prediction for fly ash concrete.” *Construction and building materials*, Elsevier, 20(9), 744–753.

Kurdowski, W. (2004). “The protective layer and decalcification of CSH in the mechanism of chloride corrosion of cement paste.” *Cement and Concrete Research*, Elsevier, 34(9), 1555–1559.

Luke, K., and Lachowski, E. (2008). “Internal composition of 20-year-old fly ash and slag-blended ordinary Portland cement pastes.” *Journal of the American Ceramic Society*, Wiley Online Library, 91(12), 4084–4092.

Ma, W., and Brown, P. W. (1997). “Hydrothermal reactions of fly ash with Ca (OH) 2 and CaSO4· 2H2O.” *Cement and Concrete Research*, Elsevier, 27(8), 1237–1248.

Madejová, J. (2003). “FTIR techniques in clay mineral studies.” *Vibrational spectroscopy*, Elsevier, 31(1), 1–10.

Makul, N. (2013). “Dielectric permittivity of various cement-based materials during the first 24 hours hydration.” *Open Journal of Inorganic Non-metallic Materials*, Scientific Research Publishing, 2013.

Manikonda, A., Ogunro, V. O., Ellison, K. M., and Moo-Young, K. (2019). “Synthesis of Friedel’s Salt for Application in Halide Sequestration Using Paste Encapsulation Technology.” *Geo-Congress 2019: Geoenvironmental Engineering and Sustainability*, American Society of Civil Engineers Reston, VA, 167–176.

Monteagudo, S. M., Moragues, A., Gálvez, J. C., Casati, M. J., and Reyes, E. (2014). "The degree of hydration assessment of blended cement pastes by differential thermal and thermogravimetric analysis. Morphological evolution of the solid phases." *Thermochimica Acta*, Elsevier, 592, 37–51.

Ndiaye, K., Cyr, M., and Ginestet, S. (2017). "Durability and stability of an ettringite-based material for thermal energy storage at low temperature." *Cement and Concrete Research*, Elsevier, 99, 106–115.

Onishi, A., Cao, X., Ito, T., Shi, F., and Imura, H. (2010). "Evaluating the potential for urban heat-island mitigation by greening parking lots." *Urban forestry & Urban greening*, Elsevier, 9(4), 323–332.

Or, D., and Wraith, J. M. (1999). "Temperature effects on soil bulk dielectric permittivity measured by time domain reflectometry: A physical model." *Water Resources Research*, Wiley Online Library, 35(2), 371–383.

Oza, S., Ogunro, V., Daniels, J., and Ellison, K. M. (2015). "Sequestration of Halides from FGD Wastewater through Lime Stabilization of Fly Ash." *2015 World of Coal Ash Conference. Retrieved from http://www. flyash. info/2015/064-ogunro-2015. pdf*.

Pajares, I., Martínez-Ramírez, S., and Blanco-Varela, M. T. (2003). "Evolution of ettringite in presence of carbonate, and silicate ions." *Cement and Concrete Composites*, Elsevier, 25(8), 861–865.

Pane, I., and Hansen, W. (2005). "Investigation of blended cement hydration by isothermal calorimetry and thermal analysis." *Cement and concrete research*, Elsevier, 35(6), 1155–1164.

Raucci, J. J., Samson, J., Ellison, K. M., Gallagher, B. J., Hines, J. S., and Kelsey, J. A. (2019). *Encapsulation of flue-gas desulfurization wastewater using coal combustion by-product mixtures: Field lysimeter investigations*.

Renew, J. E., Huang, C.-H., Burns, S. E., Carrasquillo, M., Sun, W., and Ellison, K. M. (2016). "Immobilization of Heavy Metals by Solidification/Stabilization of Co-Disposed Flue Gas Desulfurization Brine and Coal Fly Ash." *Energy & Fuels*, 30(6), 5042–5051.

Robert, A. (1998). "Dielectric permittivity of concrete between 50 MHz and 1 GHz and GPR measurements for building materials evaluation." *Journal of applied geophysics*, Elsevier, 40(1–3), 89–94.

Roessler, J. G., Townsend, T. G., and Ferraro, C. C. (2015). "Use of leaching tests to quantify trace element release from waste to energy bottom ash amended pavements." *Journal of Hazardous Materials*, 300, 830–837.

Šavija, B., and Luković, M. (2016). "Carbonation of cement paste: Understanding, challenges, and opportunities." *Construction and Building Materials*, 117, 285–301.

Spence, R. D., and Shi, C. (2004). *Stabilization and solidification of hazardous, radioactive, and mixed wastes*. CRC press.

Sutter, L., Peterson, K., Touton, S., Van Dam, T., and Johnston, D. (2006). "Petrographic evidence of calcium oxychloride formation in mortars exposed to magnesium chloride solution." *Cement and Concrete Research*, 36(8), 1533–1541.

Tong, T., and Elimelech, M. (2016). "The global rise of zero liquid discharge for wastewater management: drivers, technologies, and future directions." *Environmental science & technology*, ACS Publications, 50(13), 6846–6855.

U.S. EPA. (1992). "SW-846 Test Method 3005A: Acid Digestion of Waters for Total Recoverable or Dissolved Metals for Analysis by Flame Atomic Absorption (FLAA) or Inductively Coupled Plasma (ICP) Spectroscopy."

U.S. EPA. (2000). *Solidification/Stabilization Use at Superfund Sites*.

U.S. EPA. (2007). "SW-846 Test Method 9056A: Determination of Inorganic Anions by Ion Chromatography."

U.S. EPA. (2009). *Steam Electric Power Generating Point Source Category: Final Detailed Study Report*. United States Environmental Protection Agency, Washington, D.C.].

U.S. EPA. (2015). "Hazardous and Solid Waste Management System; Disposal of Coal Combustion Residuals From Electric Utilities; Final Rule." *The Federal Register*, Federal Information & News Dispatch, Inc., Washington.

U.S. EPA. (2017). "SW-846 Test Method 1315: Mass Transfer Rates of Constituents in Monolithic or Compacted Granular Materials Using a Semi-Dynamic Tank Leaching Procedure."

U.S. EPA. (2020). "Steam Electric Reconsideration Rule." 40 C.F.R. Part 423.

Wang, Q., Feng, J., and Yan, P. (2012). "The microstructure of 4-year-old hardened cement-fly ash paste." *Construction and Building Materials*, Elsevier, 29, 114–119.

Zhang, W., Oswal, H., Renew, J. E., Gallagher, B., Ellison, K., and Huang, C.-H. (2020). "Solidification/stabilization of flue gas desulfurization brine and coal fly ash for heavy metals and chloride immobilization: Effects of S/S conditions and zero-valent-iron pretreatment." *Journal of Hazardous Materials*, 384, 121463.

CHAPTER 5 NUMERICAL MODELING OF COMPACTED COAL FLY ASH – FLUE GAS DESULFURIZATION BRINE CO-DISPOSAL TESTBED USING COMSOL WITH MATLAB

Abstract

The co-disposal of coal fly ash (CFA) and flue gas desulfurization (FGD) concentrates (brines) is gaining attention as a potential way to achieve the Zero Liquid Discharge (ZLD) waste management strategy for coal-fired steam electric power plants. While it is convenient for some facilities to use the hypersaline FGD brine as an alternative source for CFA compaction and dust control in the landfill, previous studies have shown the co-disposal material failed to retain salinity when the mixture lacks cementitious properties. The retention of salinity in such a co-disposal mixture highly depends on local weather conditions as the solutes are released with leachate and runoff. This study established a physics-based model simulating the heat transfer, solute transport, and moisture flow, aiming to reproduce observations from the field study over a 35-month period. While COMSOL Multiphysics was used as the platform for the finite element method modeling, the MATLAB-based modeling frame updates the boundary conditions for hourly simulation and shortens the runtime by storing COMSOL solutions externally. The COMSOL-MATLAB (CM) model evaluated runoff, evaporation, ground heat flux, and surface heating using weather conditions monitored by an adjacent weather station. The simulation results showed a sound reproduction of field observations, highlighted by the leachate/runoff generation pattern, moisture content variation, temperature profile, and the change of chloride and bromide concentration in leachates during the leaching/wash off stage. Further investigation suggested the simulation of hydraulic behaviors and temperature variation could be improved with a more accurate estimation of surface conditions. The validated CM model allowed the investigation of potential management methods for the co-disposal material under current weather conditions and explored the material's field behaviors under different weather conditions through numerical simulation.

5.1.Introduction

While the world is making progress in reducing fossil fuel consumption, the coal-fired steam power plant still generates 19% of the electricity in the U.S. in 2020, as reported by the U.S. energy information administration (U.S. EIA) (U.S. EIA 2021). Besides the carbon emissions, the by-products of the coal combustion process, such as coal fly ash (CFA) and flue gas desulfurization (FGD) wastewater, can still cause environmental concerns such as groundwater contamination. To address environmental concerns of these by-products, the U.S. environmental protection agency (U.S. EPA) established the Coal Combustion Residuals (CCRs) rules (U.S. EPA 2015) and the Effluent Limitations Guidelines (ELGs) (U.S. EPA 2020) for the solid and liquid wastes, respectively. According to the CCRs rules' requirements, the CFA needs to be disposed of in an engineered landfill, which requires the management of leachate and runoff with groundwater monitoring, while by-product from the FGD treatment often requires landfill or encapsulation. Studies have explored and proposed co-disposal of the CFA and FGD wastewater in the engineered ash landfill through compaction as a potential method for zero liquid discharge (ZLD) strategy (Fatoba et al. 2011; U.S. EPA 2020). As the goal of the ZLD strategy is eliminating contaminant liquids exiting the power plant, the leachate and runoff from the ash landfill, if not appropriately managed, could become potential sources of wastewater (He et al. 2022). Considering the hydraulic performance of a landfill is highly dependent on the local weather conditions, it is advantageous to conduct numerical models on the performance of the co-disposal under different weather scenarios.

This study proposed a COMSOL-MATLAB (CM) model to simulate the hydraulic performance, heat transfer, and solute transport in a testbed used to co-dispose CFA-FGD brine through compaction. The COMSOL Multiphysics is a well-known finite element analysis software

used for geotechnical and geoenvironmental research (Azad et al. 2016; Batini et al. 2015; COMSOL AB 2020; Halloran et al. 2019; Li et al. 2009; Nardi et al. 2014). The proposed 1-D model uses the solute transport module from the COMSOL while solving the partial differential equations (PDE) for unsaturated flow and heat transfer modeling. Since the estimation of some surface boundary conditions requires simulation results from the previous timestep, a MATLAB script was developed to extract needed information. The script calculates surface boundary conditions with the weather data and updates the COMSOL model for simulation of the next timestep. The estimated surface conditions include the surface temperature and the moisture flux (infiltration or evaporation) for heat transfer and unsaturated flow. This model did not consider the frozen soil condition and snow cover period. Since the previous study showed the majority of chloride and bromide were released within the first four months of the experiment through convective flow (Chapter 3), the simulation of solute transfer is limited to the same period. The unsaturated flow and heat transfer simulations were performed for the study period of 35 months, with outputs including infiltration, runoff, temperature profile, and moisture profile.

5.2.Structure and Workflow of the CM Model

The 1-D CM model encompasses three main components consisting of the unsaturated flow module (UF), the heat transfer module (HT), and the solute transport module (ST). These three modules were connected in the COMSOL model and solved simultaneously. The diagram of the module connection is presented in Figure 5.1. The unsaturated flow module provides the velocity field and moisture profile to the solute transport to estimate the change of pore solution's concentration. The heat transfer module simulates the changes in the temperature and the bulk thermal properties of the material. The heat transfer module is linked to the unsaturated flow and solute transport model through the temperature profile. While the fluid properties were assumed

to be constant to reduce the complexity of the model, the change in the pore solution's chemical compositions will not impact the heat transfer and unsaturated flow simulations. Therefore, the solute transport module does not provide the concentration profile to other modules.

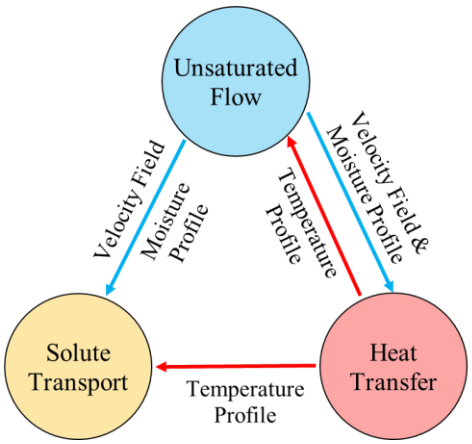

Figure 5.1. Diagram of the module connections in the COMSOL model

The CM model computes the hourly solution using the COMSOL solver and uses the previous hour's results as the initial conditions for the next hour. The MATLAB script extracts solutions from the last hour of the COMSOL model, combined with the weather data to estimate the surface boundary conditions for the next timestep. By storing the solutions in MATLAB, the runtime of the COMSOL model is accelerated. The stored data is compiled at the end of the simulation for further analysis. In this case, the size of the COMSOL model file was limited by only keeping solutions for current and two previous hours during the simulation. The workflow of the CM model is presented in Figure 5.2. A detailed description of the computations of the boundary conditions is discussed in the following sections.

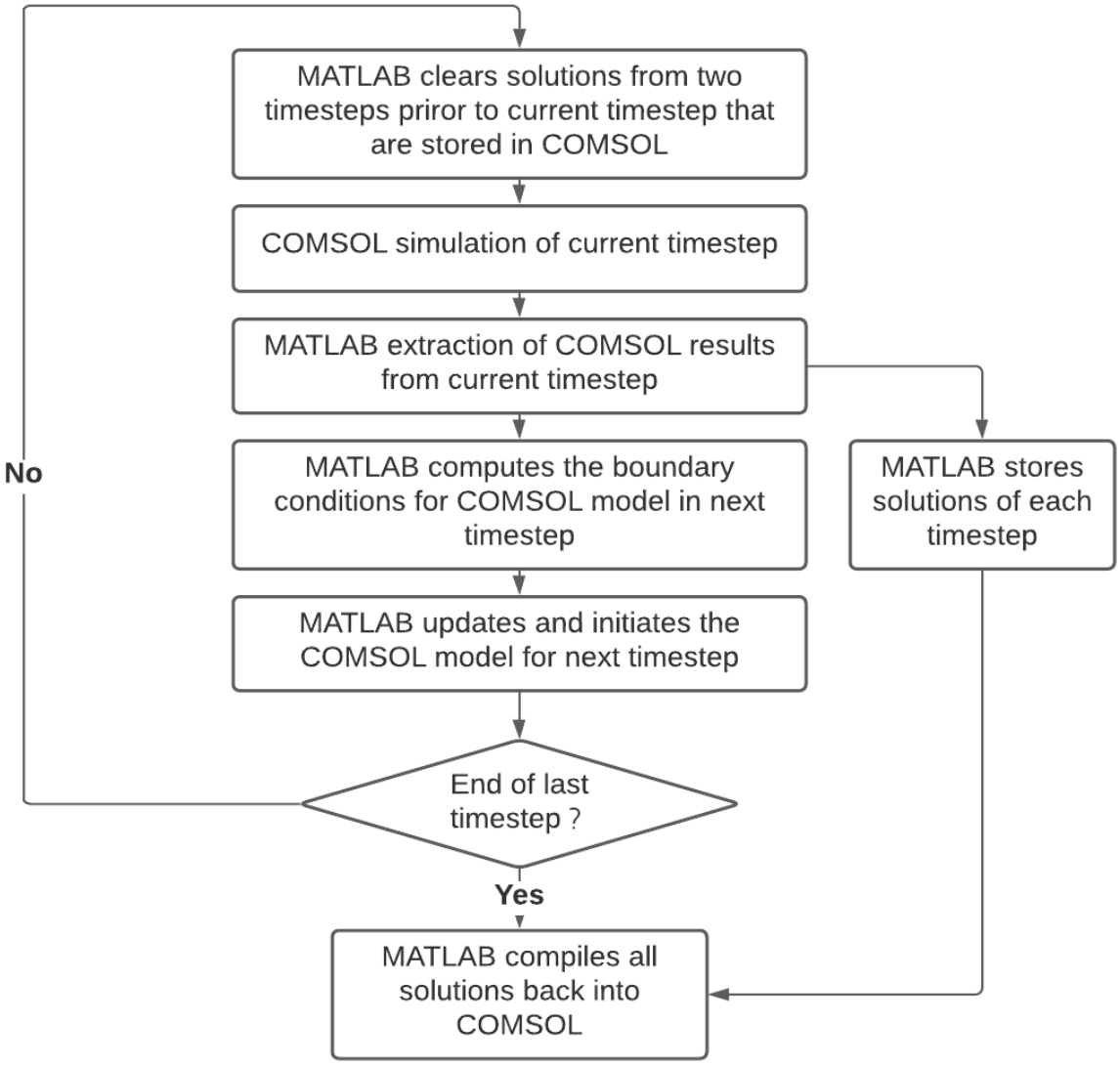

Figure 5.2. Diagram of the workflow in the CM model

5.3.Mathematical Description of the CM Model

While the testbed was carefully constructed and operated to maintain 1-D heat and moisture flow (Chapter 3), it also went through routine inspection to prevent vegetation growth and surface ponding. The 1-D domain of the model has a height of 0.762 meters with a maximum mesh size of 0.01 meters. The surface boundary is defined at 0.762 meters, and the bottom boundary is located at 0 meters. The direction of the gravity vector is downward from the surface of the testbed to the bottom boundary, as depicted in the schematic illustration of the domain in Figure 5.3. The model does not consider vaporization of the pore water and the transfer of pore vapor, as evaporation is assumed to occur only at the surface boundary of the testbed. The infiltration and evaporation at the surface boundary for the UF module are considered as the moisture flux in to and out of the surface, respectively. For the HT module, a temperature boundary is used to represent the surface temperature condition. The surface boundary of the ST model considered the concentration of species in the moisture entering or leaving the surface to be zero. The UF module was assigned a free drainage process at the bottom boundary, and the outflow of heat and solute was set for the HT and ST modules, respectively. The overall mass balance of the UF module for the closed system can be written as:

$$\text{Infiltration} - \text{Evaporation} - \text{Bottom drainage} = \text{change of moisture storage} \quad \text{Eq.5.1}$$

Where the evaporation and bottom drainage remove moisture from the testbed and infiltration supplies the moisture. The change of moisture storage is demonstrated by the change of the overall volumetric water content of the domain. While the temperature boundary drives the heating and cooling of the testbed at the surface (Gao et al. 2017; Liebethal and Foken 2007), the outflow boundary for the HT module at the bottom only allows heat to be removed with liquid.

Considering the rainfall and evaporation from the surface do not contain chloride, bromide, and sulfate, the surface boundary condition assigns a concentration of zero for all species in the infiltration and evaporation fluxes.

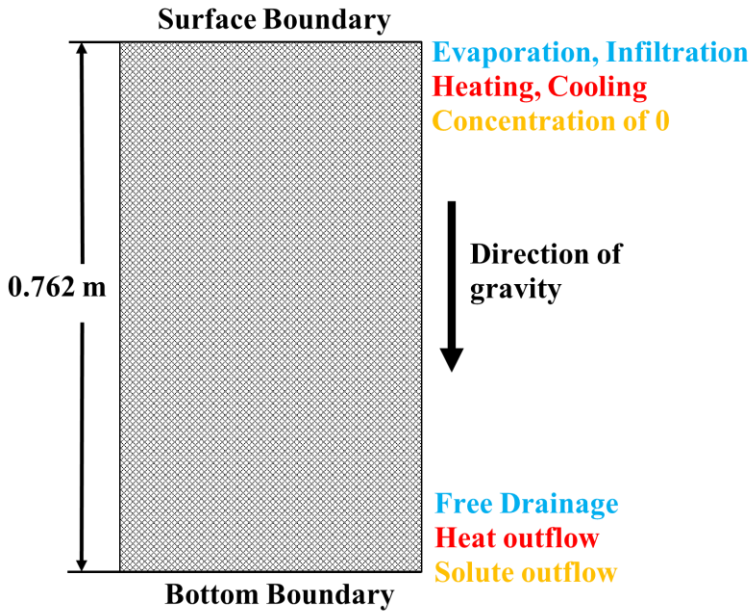

Figure 5.3. Schematic illustration of the 1-D domain

5.3.1. Unsaturated flow module (UF)

Richard's equation describes the transient mass balance of the unsaturated flow in the compacted material (Richards 1931; Whitaker 1986). The expressions of Richard's equation described in the COMSOL manual is as follows (COMSOL AB 2020):

$$\rho_{liq}\left(\frac{C_m}{\rho g}+SeS\right)\frac{\partial p}{\partial t}+\nabla\cdot\rho_{liq}\left(-K_sK_r\left(\nabla p+\rho_{liq}g\nabla D\right)\right)=Q_m \qquad \text{Eq.5.2}$$

$$Se=(\theta-\theta_r)/(\theta_s-\theta_r) \qquad \text{Eq.5.3}$$

$$\nabla=\frac{\partial}{\partial X} \qquad \text{Eq.5.4}$$

Where C_m is the specific moisture capacity, ρ_{liq} is the density of the pore fluid, Se is the degree of saturation, θ_s is the saturated volumetric water content, θ_r is the residual volumetric water content, S is the storage coefficient, Ks is the saturated hydraulic conductivity, p is the suction (negative pore pressure), K_r is the relative hydraulic conductivity, D is the elevation head, and the Q_m is the internal source, and ∇ is the divergence. The K_r is the unsaturated hydraulic conductivity normalized to the saturated hydraulic conductivity. The model assumes the single-phase flow of liquid in the compacted testbed. In this study, the storage coefficient was set as 0 as the material was not behaving as an aquifer, and Q_m was also appointed as zero since no internal liquid source or sink was presented. The van Genuchten equation was selected to represent the numerical relations between suction and the degree of saturation as written below (Van Genuchten 1980):

$$Se = [1/(1 + (\alpha h)^n)]^m \quad \text{Eq. 5.5.}$$

Where α, n, and m are the parameters experimentally determined by the soil-water characteristic curve (SWCC), and the h is the positive capillary suction. To estimate the unsaturated conductivity in the model, the van Genuchten – Mualem (vGM) equation was used to express the correlation between the suction and relative hydraulic as (Van Genuchten 1980; Mualem 1976):

$$K_r(h) = \frac{\{1-(\alpha h)^{n-1}[1+(\alpha h)^n]^{-m}\}^2}{[1+(\alpha h)^n]^{m/2}} \quad \text{Eq. 5.6.}$$

The incorporation of equations 5.5 and 5.6 into equation 5.2 is achieved through the following equations:

$$\theta_{H_p<0} = \theta_r + Se(\theta_s - \theta_r);\ \theta_{H_p\geq 0} = \theta_s \quad \text{Eq.5.7.}$$

$$Se_{H_p<0} = 1/(1 + |\alpha H_p|^n)^m;\ Se_{H_p\geq 0} = 1 \quad \text{Eq.5.8.}$$

$$C_{m,H_p<0} = \frac{\alpha m}{1-m}(\theta_s - \theta_r)Se^{\frac{1}{m}}(1 - Se^{\frac{1}{m}})^m;\ C_m = 0 \quad \text{Eq.5.9.}$$

$$K_{r,H_p<0} = Se^l[1 - (1 - Se^{1/m})^m]^2;\ K_{r,H_p\geq 0} = 1 \quad \text{Eq.5.10.}$$

Where H_p is the pore pressure expressed in the unit of meter-head of water. Once the pore pressure is greater than or equal to zero, Richard's equation reduces to a saturated flow following Darcy's law as

$$u = -K_s(\nabla p + \rho g \nabla D) \quad \text{Eq.5.11.}$$

Where u is the velocity vector, and the negative sign represents the direction of the flow. While the equations in this section described the internal moisture movement in the unsaturated porous medium, the boundary conditions are separately estimated for the runoff and evaporation. Considering the bottom of the compacted material is in contact with the sand drainage layer, the suction profile is assumed to be continuous as modeling layered soils (Huang et al. 2013; Romano et al. 1998). As the hydraulic conductivity of the sand layer is 0.18 cm/s, which is significantly higher than the 4×10^{-4} cm/s of the compacted CFA-FGD brine mixture, the bottleneck of the flow is controlled by the compacted material. Therefore, the flux across the boundary was estimated using the unsaturated hydraulic conductivity of the compacted material. The suction at the sand and compacted layer interface is assumed to be the suction representing the water hold capacity of the compacted material. The water holding capacity, θ_h, of 0.4 was experimentally determined by saturating the sample and allowing it to drain freely under lab conditions. The bottom boundary is defined as a free drainage boundary with the assumption that the flow through the boundary only occurs if the volumetric water content is greater than the θ_h with a unit gradient:

$$u_{\theta \geq \theta_h} = K_r K_s, u_{\theta < \theta_h} = 0 \quad \text{Eq.5.12.}$$

Where u (m/s) is the velocity of flow out of the domain, the outflow from the bottom boundary represents the leachate generation in the testbed under the assumption that the storage in the sand layer is negligible after the initial charging period.

5.3.2. Heat transfer module (HT)

The study models the heat transfer under the local equilibrium scenario, which assumes the same liquid, solid, and air temperature pointwise (Bejan 2013). The governing equation is modified from the "heat transfer in porous media" module in the COMSOL library to account for unsaturated conditions. While this study assumes the heat conduction in the solid and the fluid occurs parallelly, the governing equations are as follows (COMSOL AB 2020):

$$(\rho C_p)_{eff} \frac{\partial T}{\partial t} + (\rho C_p)_{eff} u \cdot \nabla T + \nabla q = \mathrm{Q} \quad \text{Eq.5.13.}$$

$$q = -k_{eff} \nabla T \quad \text{Eq.5.14.}$$

$$(\rho C_p)_{eff} = \rho_p C_{p,p} + \theta_w \rho_w C_{p,w} \quad \text{Eq.5.15.}$$

$$k_{eff} = k_p + \theta_w k_w \quad \text{Eq.5.16.}$$

Where $(\rho Cp)_{eff}$ ($J/m^3/K$) is the effective volumetric heat capacity at constant pressure, T (K) is the temperature, u (m/s) is the velocity field provided by the UT module, q (W/m^2) is the conductive heat flux, k_{eff} (W/m/K) is the effective thermal conductivity. The subscription p and w stand for particle and water, respectively. The ρ_w (kg/m^3) is the density of the pore fluid, ρ_p (kg/m^3) is the dry density of the compacted material, the θ is the volumetric fraction of each phase. The physical properties of the materials are assumed to be constant in the model. The outflow boundary is defined as:

$$q = 0 \qquad \text{Eq.5.17.}$$

Equation 5.17 suggests the heat transfer through the boundary is limited to the convection process. While the fluid transport modeled in this study is limited to water, the thermal contribution of air or pore vapor is ignored in this model.

5.3.3. Solute transport module (ST)

While the moisture transport in this model considered the density of the solution as a constant to avoid unnecessarily complicating the problem, in this case, the transport of diluted solution in partially saturated porous media interface in Chemical Engine module from COMSOL was used. This interface considered the solute transport mechanisms are diffusion and convection. This study focused on the rapid release of the halides at the early stages (leaching stage) of the experiment, which is evidently dominated by the convection process driven by rain events. Therefore, this model simulates the diffusion and the convection for the period of interest. The governing equation of the ST module is as follow (COMSOL AB 2020):

$$\frac{\partial}{\partial t}(\theta c_i) + u \cdot \nabla c_i = \nabla \cdot (D_{e,i} \nabla c_i) \qquad \text{Eq.5.18.}$$

$$D_e = \frac{\theta}{\tau_L} D_L \qquad \text{Eq.5.19.}$$

$$\tau_L = \theta^{-7/3} {\theta_s}^2 \qquad \text{Eq.5.20.}$$

Where the subscript i represents the modeled chemical species, θ is the volumetric water content, u (m/s) is the velocity field of the fluid flow, $D_{e,i}$ (m^2/s) is the effective diffusion coefficient, D_L (m^2/s) is the liquid diffusion coefficient, τ_L is the tortuosity factor, and θ_s is the volumetric fraction of solids. The species modeled in this study are chloride (Cl^-), bromide (Br^-), and sulfate (SO_4^{2-}). The tortuosity factor is calculated with the Millington and Quirk model

(Millington and Quirk 1961). The outflow boundary is set at the bottom of the domain for the ST module, which considered convection the sole mechanism of solute transport across the boundary:

$$-D\nabla c_i = 0 \qquad \text{Eq.5.21.}$$

The concentrations of the species in the outflow are the same as in the leachate. Since the dissolution of the particles was not modeled, the trend of the modeled concentrations will not include the shift of dominant species caused by the change of solute source (Chapter 3).

5.3.4. Surface boundary conditions

The surface boundary conditions for the CM model consist of the infiltration and evaporation for the unsaturated flow module, the temperature boundary for the heat transfer module, and the inflow boundary condition for the solute transport module. The evaporation and infiltration are both defined as flux boundary with limitation, which is commonly used in unsaturated flow models such as the hydrologic evaluation of landfill performance (HELP) model (Schroeder et al. 1984), unsaturated soil water and heat flow (UNSAT-H) model (Fayer 2000), and HYDRUS (Šimunek et al. 2012). In general, the potential evaporation is estimated through the energy balance at the soil's surface, which requires the knowledge of surface temperature. The net solar radiation received at the surface of a bare (unvegetated) surface is used to heat the soil (ground heat flux) and evaporate the moisture. The distribution of net solar radiation between these two components varies across soil types (Sauer and Horton 2005). This study uses the Idso et al. (1975) model to predict the ground heat flux from net solar radiation and the moisture content at the surface of bare loamy soils, which present similar characteristics as the compacted co-disposal material. The soil temperature estimated from ground heat flux is then used to evaluate the potential and actual evaporation from the soil surface. The surface temperature and the actual

evaporation estimations in this model are calculated in an uncoupled manner, suggesting the energy in the residual evaporation is not used to heat the soil, as shown in Figure 5.4 (Fredlund et al. 2011, 2016). The inflow boundary for the solute transport assigns zero to the concentration of the solutions either flowing into or out of the domain. In this case, the concentration of the species can either be enriched or lessened at the top boundary of the domain. This study does not consider the chemical process at the surface since no surface scaling was observed during the initial leaching stages, and the crystallization and dissolution process in pore space is not considered either.

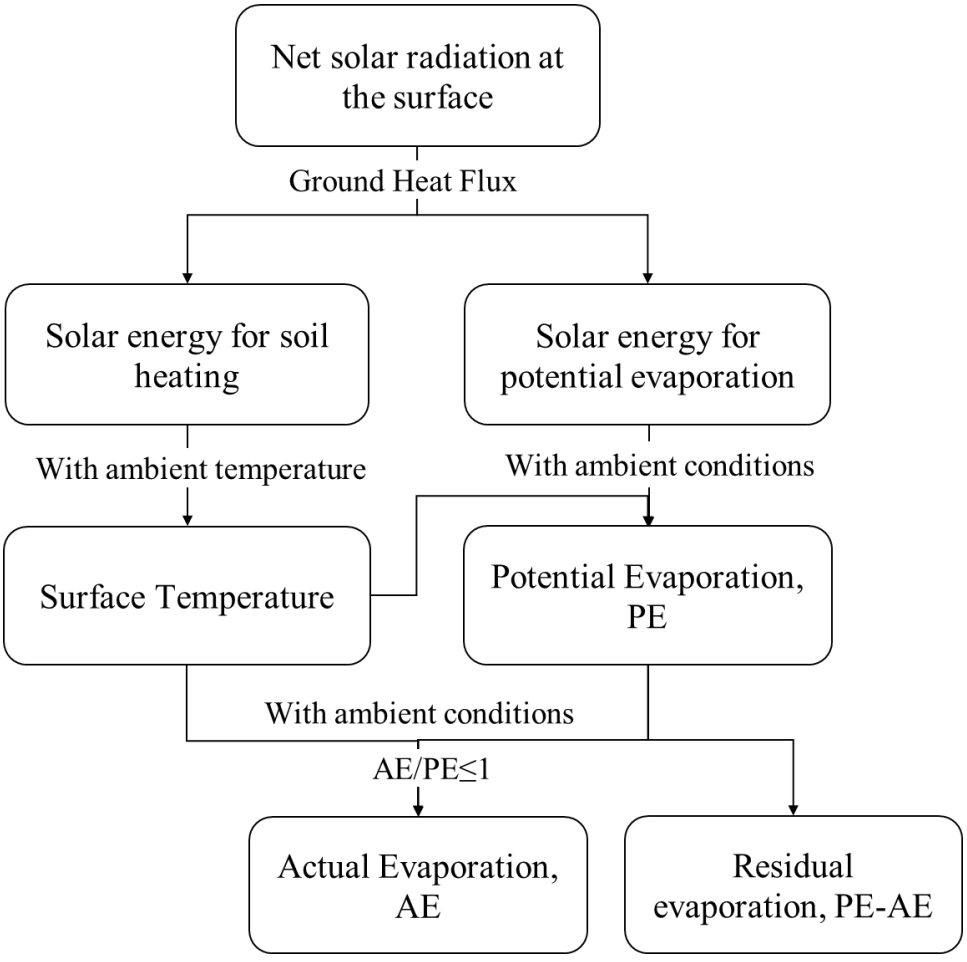

Figure 5.4. Workflow diagram of uncoupled surface temperature and evaporation model

5.3.4.1. Evaporation and ground heat flux estimation

In general, the potential evaporation, which is the maximum possible evaporation from a soil surface, was modeled following the methodology in the HELP model (Schroeder et al. 1994). The methodology uses a modified Penman method (Penman 1963), which categorized the available energy into the radiative and the aerodynamic components according to equation 22:

$$LE_i = PENR_i + PENA_i \quad \text{Eq.5.22}$$

Where the subscript i represents the current number of the timestep, LE is the available energy for evaporation, PENR is the radiative component of the LE, and PENA is the aerodynamic component of the LE. The calculation of hourly energy components is:

$$PENR_i = \frac{\Delta_i}{\Delta_i+\gamma} R_{ni} \ (Langley\ per\ hour) \quad \text{Eq.5.23}$$

$$PENA_i = \frac{15.36\gamma}{\Delta_i+\gamma}(1 + 0.1488u)(e_{oi} - e_{ai}) \ (Langley\ per\ hour) \quad \text{Eq.5.24}$$

$$PE_i = LE_i/L_v \quad \text{Eq.5.25}$$

Where R_n (Langley/hour) is the net solar radiation received at the surface of the soil, Δ (millibars/°C) is the slope of the saturation vapor pressure curve at mean air temperature, γ (millibars/°C) is the constant of wet and dry bulb psychrometer, u (kilometers/hour) is the wind speed at the height of 2 meters, e_o (millibars) is the saturated vapor pressure at the air temperature, e_a (millibars) is the vapor pressure of the atmosphere, the L_v (Langley/millimeter water) is the latent heat of evaporation for water, PE (mm/hour) is the potential evaporation flux. While the estimation of Rn in the HELP model was based on daily timestep, the hourly Rn was estimated

according to the method described by Walter et al. (2000). The surface albedo of 0.23 was used for the calculation as recommended in the reference. The ground heat flux is then estimated with the Idso model (Idso et al. 1975a) as:

$$G = (0.681 - 1.418\theta_{avg}) \times Rn \quad \text{Eq.5.26}$$

Where G is the ground heat flux with the same unit of Rn (W/m^2), and θ_{avg} is the average volumetric water content at the thermally active layer on top of the surface, which has the depth $d_{thermal}$ = 10 cm in this study. The average temperature within the hour is then calculated as:

$$T_{soil} = T_{air} + G \times \Delta t/(C_{p,eff} d_{thermal})/2, Rn > 0 \quad \text{Eq.5.27}$$

$$T_{soil} = T_{air}, Rn \leq 0 \quad \text{Eq.5.28}$$

Where Δt (s) is the timestep length, $C_{p,\,eff}$ is the effective volumetric heat capacity as in equation 5.15. Equation 5.27 is based on the common assumption made in evaporation modeling that the soil's surface temperature is the same as the atmospheric temperature, which can be interpreted as the elevated temperature at the surface of the co-disposal material due to the ground heat flux. Once the surface was no longer under sunlight, the soil temperature was maintained at atmospheric temperature, as reported in (Chapter 3). The soil surface temperature is then used to estimate the actual evaporation following the method proposed in the Fredlund et al. (2011) SVFlux model as:

$$\delta = log3000 - log\psi_{residual} \quad \text{Eq.5.29}$$

$$u_{soil} = u_{soil}^0 \exp\left(\frac{10^{\delta}\psi g \omega_v}{\gamma_w R(273.15+T_{soil})}\right) \quad \text{Eq.5.30}$$

$$AE/PE = [(u_{soil} - u_{air})/(u_{soil}^0 - u_{air})] \quad \text{Eq.5.31}$$

Where δ is the total suction adjustment factor, $\psi_{residual}$ (kPa) is the residual suction from the drying soil water retention curve, γ_w (=9.807 kN/m^3) is the unit mass of water, u_{soil} is the vapor pressure at the soil surface temperature, u^0_{soil} is the saturated vapor soil surface temperature, u_{air} is the ambient vapor pressure, and AE and PE are the actual and potential evaporations, respectively. The actual evaporation from a soil surface was related to the total suction at the surface rather than the moisture content, as Wilson (1990) suggested, which observed the reduction of evaporation beyond a suction of 3,000 kPa. The residual suction estimated from the SWCC of the compacted material was 120 kPa, which results in δ = 1.4 being used in this model. In addition to the SVFlux model, the evaporation is further limited by the minimum pressure head at the soil surface as described in HYDRU (Šimůnek et al. 2018) model as:

$$h_A = \frac{RT}{Mg} \ln (Hr) \qquad \text{Eq.5.32}$$

Where h_A (m) is the minimum pressure head allowed under atmospheric conditions, R (8.314 J /(mol K)) is the gas constant, g (9.81 m/s^2) is the gravitational acceleration, and M (0.018015 kg/mol) is the molecular weight of water, and Hr is the ambient relative humidity (%). The evaporation is set as zero if the suction at the surface exceeds h_A or during precipitation events.

5.3.4.2. Runoff and infiltration

The runoff and infiltration at the surface of the testbed are determined with the widely used Soil Conservation Service (SCS) Curve Number (CN) model (Mishra and Singh 2003). The method uses the curve number to estimate the distribution of precipitation into runoff and infiltration as:

$$S = \frac{25400}{CN} - 254 \qquad \text{Eq.5.33}$$

$$I_a = \lambda S \quad \text{Eq.5.34}$$

$$Q = \frac{(P-I_a)^2}{P-I_a+S}, P > I_a; Q = 0, P \leq I_a \quad \text{Eq.5.35}$$

Where S (mm) is the potential maximum retention, I_a (mm) is the initial abstraction, λ is the initial abstraction ratio, which is usually set at 0.2, P is the rainfall (mm), and Q (mm) is the runoff. The infiltration through the surface boundary is then calculated by subtracting the surface runoff from the precipitation. The maximum potential infiltration rate at the surface boundary is limited to the saturated hydraulic conductivity of the material, 4×10^{-6} m/s, under the assumption of no surface ponding. The no surface ponding assumption can be described as the surface being saturated without water accumulation. In this case, the zero surface ponding condition is enforced when the surface is saturated using an "if scenario" as:

$$Inf = P - Q, P - Q \leq K_s,\ h \geq 0; Inf = K_s, P - Q > K_s, h \geq 0 \quad \text{Eq.5.36}$$

Where Inf (mm/hour) is the infiltration flux, P (mm/hour) is the rainfall intensity, Q (mm/hour) is the calculated runoff, h (Pa) is the pore pressure at the surface boundary, and K_s (mm/hour) is the saturated hydraulic conductivity. The saturation is described as pore pressure greater than or equal to zero, as described in section 5.3.2. The condition was well maintained in the field experiment by routine inspection during precipitation events.

Since precipitation is the sole source of infiltration, the infiltration modeling significantly influences the water balance. In general, a higher λ with a lower CN number will lead to higher infiltration by increasing the runoff threshold. While the Table of CN for various soil can be found from various sources (Division 1986; Hawkins et al. 2008; Hjelmfelt Jr 1991; Mishra and Singh 2003), these values were based on a λ of 0.2. Although the debates around the of λ suggest it should

be considered a varying value rather than a constant (Ponce and Hawkins 1996; Rawls and Brakensiek 1986; Woodward et al. 2003), Schneider and McCuen (2005) showed the goodness of fit is less sensitive to λ with increased CN. The best fitted CN value targeting minimum percentage difference for the field data was 96 with λ=0.2. The best fitted CN value is close to the value of 94 used in the run-on and run-off control system for the ash disposal area in Texas (Luminant Generation Company 2016) as well as the CN value of 92 estimated by the HELP model for the bare ground condition of silt soil using the testbed configuration of the slope of 2% and the slope length of 1.143 m (Schroeder et al. 1984). The optimized λ of 0.0306 was acquired for the CN value of 92, which did not show a significant improvement of runoff prediction than using CN = 96 and λ = 0.2, as demonstrated in Figure 5.5. Since the λ = 0.2 is a commonly used assumption in most SCS-CN model applications, this model adopts CN = 96 and λ = 0.2 for simulation, which predicted an infiltration that is 5.4% higher than the field observation at the end of the modeling period. Considering the collection of the precipitation in the field was discrete, a more detailed investigation into the runoff/rainfall ratio was not probable. It should also be noted that the precipitation measurement using a rain gauge with significant differences in area and elevation can lead to random error (Haselow et al. 2019; Hoffmann et al. 2016; McGuinness 1966). In this case, the difference between the actual precipitation received at the surface of the testbed and the measurement by the rain gauge will inevitably add to the error in runoff estimations. Therefore, it is recommended that precision lysimeters be used to acquire better precipitation measurements for actual operations and future field studies.

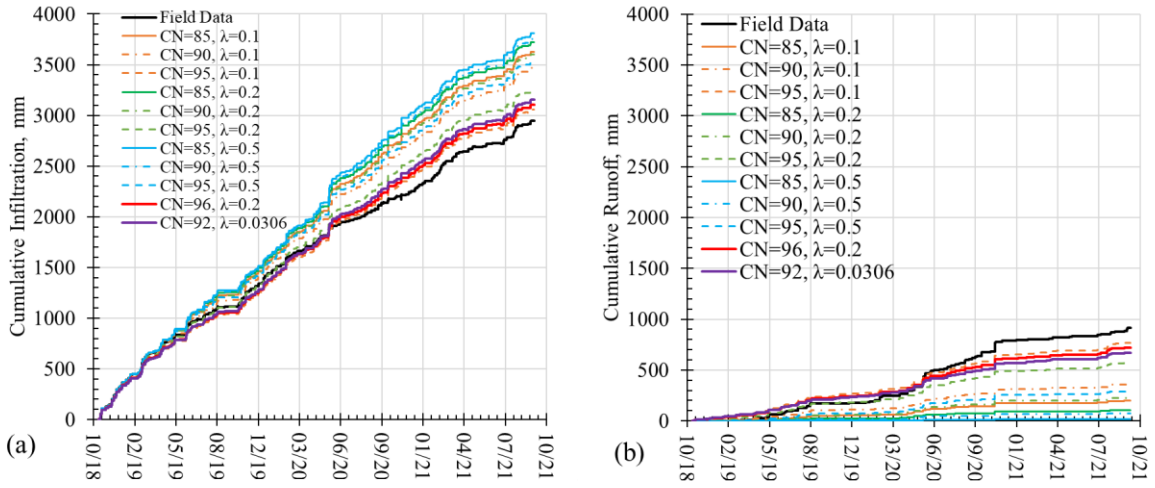

Figure 5.5. Estimated cumulative (a) infiltration and (b) runoff with varying curve numbers and initial abstraction ratios compared to filed data.

5.3.5. Summary of the CM model

In summary, the governing equations of the CW model consist of the unsaturated flow (Eq. 5.2), the heat transfer in an unsaturated porous medium (Eq. 5.13), and the solute transport in a partially saturated porous medium (Eq. 5.18). The workflow of the CM model demonstrated in Figure 5.2 showed the MATLAB script was used as the terminal to control the COMSOL solver and store the solutions. At the end of each timestep, the surface boundary conditions for the next timestep are estimated using the modeling result of the current step with the weather conditions as described in section 5.2. The MATLAB then stores the result of the current timestep and removes the solutions ion COMSOL except for the last two timesteps to allow a faster run time. The cycle continued till the final timestep of the simulation, which compiles the previous solutions into the COMSOL for storage and utilization of the COMSOL graphing tool. The reported results include but are not limited to the boundary fluxes of moisture and species, the temperature at the surface boundary, the spatial profile of moisture, heat, and solute distribution at each timestep. The summary of parameters and variables used in the COMSOL modeling are listed in Table 5.1.

Table 5.1. Summary of parameters and variables

Parameter	Reference	Value if applicable	Unit
Geometry			
Length	Depth of the modeled domain	0.762	m
Slope	Slope of the surface of the testbed	2	%
Slope length	Length of the surface slope	1.143	m
Top	Depth of the top sensor's location from the surface of the testbed	0.127	m
Mid	Depth of the middle sensor's location from the surface of the testbed	0.381	m
Bot	Depth of the bottom sensor's location from the surface of the testbed	0.635	m
Mesh size	Size of the elements of the modeled domain	0.01	m
Timestep	Interval of update for boundary condition	1	hour
Latitude	Latitude of the testbed location	35.3 N	degree
Longitude	Longitude of the testbed location	80.74 W	degree
Elevation	Elevation of the testbed location above sea level	203	m
Modeling Parameters			
g	Gravity acceleration	9.81	m/s^2
R	Gas constant	8.314	J/mol/K
ρ_{liq}	Density of pore fluid	1000	kg/m^3
ρ_p	Dry density of compacted material	1185	kg/m^3
α	van Genuchten parameter	0.303	m^{-1}
n	van Genuchten parameter	2.551	1
m	van Genuchten parameter	0.608	1
ψ_{res}	Residual suction	102	kPa

Ks	Saturated hydraulic conductivity	4×10^{-4}	cm/s
θs	Saturated volumetric water content	0.4635	1
θr	Residual volumetric water content	0.0008	1
Q_m	Mass source of liquid	0	1
S	Storage capacity	0	1
$C_{p,p}$	Specific heat capacity of compacted material	863	J/(kg·K)
kp	Thermal conductivity of compacted material	0.1753	W/(m·K)
$C_{p,w}$	Specific heat capacity of pore fluid	4184	J/(kg·K)
kw	Thermal conductivity of pore fluid	0.6	W/(m·K)
$D_{L, Cl}$	Diffusion coefficient of chloride in water	2.032×10^{-9}	m^2/s
$D_{L, Br}$	Diffusion coefficient of bromide in water	2.080×10^{-9}	m^2/s
$D_{L, SO4}$	Diffusion coefficient of sulfate in water	1.065×10^{-9}	m^2/s
M, ω_v	Molecular weight of water	0.018015	kg/mol
M_{Cl}	Molar mass of chloride	0.0355	kg/mol
M_{Br}	Molar mass of bromide	0.0799	kg/mol
M_{SO4}	Molar mass of sulfate	0.0960	kg/mol
CN	Curve Number	96	1
λ	Initial abstraction ratio	0.2	1
δ	Total suction adjustment factor	1.4	1
$d_{thermal}$	Depth of thermal active layer	10	cm
γ_w	Unit mass of water	9.807	kN/m^3

Variables

Unsaturated Flow, UF

p	Pore pressure, the dependent variable		Pa
Cm	Moisture capacity		1
Se	Degree of saturation		1
Kr	Relative hydraulic conductivity		1

θ	Volumetric water content	1
u	Fluid velocity	m/s

Heat Transfer, HT

T	Temperature, the dependent variable	K
$(\rho Cp)_{eff}$	Effective volumetric heat capacity	$J/(m^3 \cdot K)$
k_{eff}	Effective thermal conductivity	$W/(m \cdot K)$
q	Conductive heat flux	W/m^2
θp	Volumetric content of solid	1
θw	Volumetric content of pore fluid	1

Solute Transport, ST

c_i	Concentration of species	mol/L
$D_{e,i}$	Effective diffusion coefficient of species in water	m^2/s
τ_L	Tortuosity factor	1

Evaporation and surface temperature estimation

LE	Available energy for evaporation	langley/hr
PENR	Radiation component of LE	langley/hr
PENA	Aerodynamic component of LE	Langley/hr
Rn	Net solar radiation	langley/hr
Δ	Slope of saturation vapor pressure curve	millibar/°C
γ	Constant of wet and dry bulb psychrometer	millibar/°C
L_v	Latent heat of evaporation for water	langleys/mm water
e_a	Vapor pressure of the atmosphere	millibar
e_o	Saturate vapor pressure at the air temperature	millibar
u	Windspeed at 2 meters above the ground	km/hour
G	Ground heat flux	W/m2
u_{soil}	Vapor pressure at soil surface temperature	kPa

u^0_{soil}	Saturated vapor pressure at soil surface temperature	kPa
u_{air}	Ambient vapor pressure	kPa
AE/PE	Actual evaporation factor	1
Hr	Ambient relative humidity	1
h_A	Minimum pressure head allowed at the surface	Pa
Runoff estimation		
Ia	Initial abstraction value	mm/hr
S	Potential maximum retention	mm/hr
Q	Runoff flux	mm/hr
P	Rainfall intensity	mm/hr

5.4.Modeling Scenarios

The driving potential for the 1-dimension CM model developed in this was applied at the surface boundary through infiltration, evaporation, and ground heat flux module. While the infiltration with the SCS-CN model could be independently evaluated, the investigation of highly correlated evaporation and the ground heat flux could only be based on the results of simulations. The dependence on preceding moisture content added more complexity to analyzing the effects of ground heat flux and actual evaporation on the simulations. To better understand the impact of implementing the ground heat flux and actual evaporation on the simulation, modeling scenarios were designed, as shown in Table 5.2.

Table 5.2. Scenario labels and design

Scenario Label	Ground Heat Flux, G	Actual Evaporation, AE	Value of δ
G0S0	Off	Off	N/A
G1S0	On	Off	N/A
G0S1Sig14	Off	On	1.4
G1S1Sig14	On	On	1.4
G0S1Sig24	Off	On	2.4
G1S1Sig24	On	On	2.4

The G1S1Sig14 was the baseline scenario that used parameters in the modeling statement representing the field conditions. By turning off the ground heat flux and actual evaporation module, the G0S0 described the scenario of maximum potential evaporation controlled by the ambient humidity. Since turning off the actual evaporation would lead to overestimating evaporation, the δ of 2.4 was used to investigate the potential impact of underestimating evaporation. The physical meaning of δ =2.4 represents a material with residual suction of 10 kPa, which suggests that evaporation reduction started at around 95% degree of saturation (volumetric water content of 44.3%).

The evaluation of the simulations was based on the predicted volumetric water content, temperature, and runoff/leachate production. While the sensors were installed at 12.7 cm (top), 38.1 cm (middle), and 63.5 cm (bottom) below the testbed surface, the sensor data were considered to represent the average values of volumetric water content and temperature of the layers. Therefore, the average moisture contents and temperature within the top layer from 0~25.4 cm, middle layer from 25.4 cm ~ 50.8 cm, and bottom layer from 50.8 cm ~ 76.2 cm were acquired from simulations for evaluation.

Based on 35 months of data collection, the cumulative volume of leachate, runoff, and the residual (precipitation minus leachate and runoff) per unit area from the testbed is presented in

Figure 5.6 (a), and their percentages of the total rainfall are shown in Figure 5.6 (b). The percentages appeared to stabilize after a year of operation in the field to ratios of residual:leachate:runoff = 48:29:23. The simulated outflow from the bottom boundary was considered as the leachate, the quantity of which was impacted by the evaporation and the infiltration. It should be noted that although a fixed potential maximum retention (S) value was used in the CM model, which indicates the relation between runoff and precipitation was independent of the material's moisture content, the infiltration was also limited by the saturated hydraulic conductivity at the surface boundary when the surface was saturated. Therefore, the potential difference between the runoff estimated from the SCS-CN model alone and simulation results would suggest the existence of saturated surface conditions during rainfalls. The anion concentrations at the bottom boundaries were considered the same as the outflow or leachate. The simulated average solute concentration in the layers will be compared to the temporal profile of the bulk dielectric permittivity during the leaching stage, which exhibited a unique pattern of change due to variations of the pore solution's salinity.

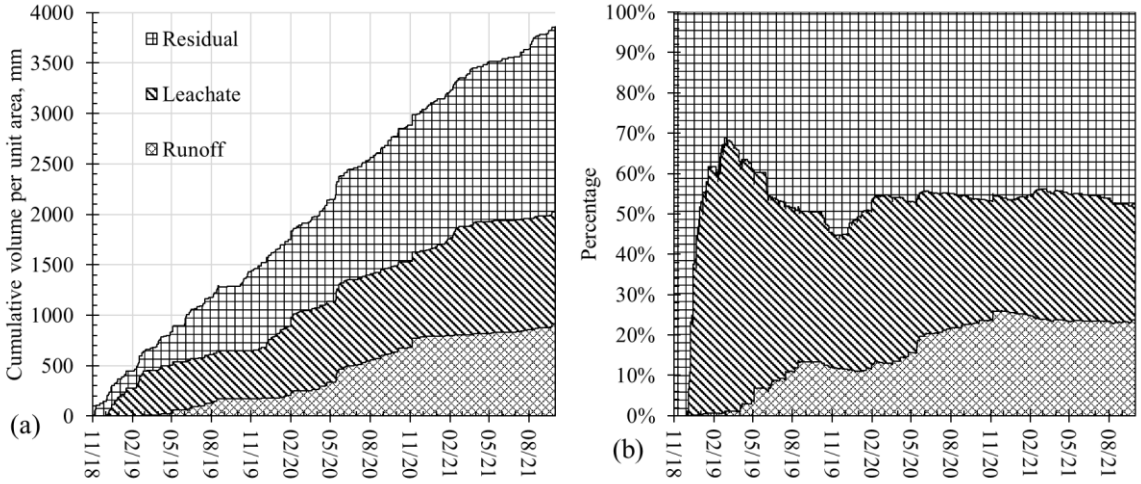

Figure 5.6. From field data collection, (a): the cumulative volume of leachate, runoff, and the residual (precipitation minus leachate and runoff) per unit area and (b): the percentage of each component relative to the total rainfall.

For all scenarios, the unsaturated flow and heat transfer model was simulated from 11/7/2018 18:00 to 10/1/2021 18:00, with a timestep of one hour, resulting in a total of 25416 modeled hours or modeling hours. The coupled solute transport simulation was performed for the baseline scenario between 1/7/2018 18:00 and 7/1/2019 18:00, covering the period of rapid salinity release through convective processes (He et al. 2022).

5.5.Results and Discussion

5.5.1. Baseline simulation

5.5.1.1. Simulated heat transfer

The CM model could accurately reproduce the temperature distribution in the testbed, as shown in Figure 5.7. The R^2 values the correlation of the values from simulation versus the field measurements for the top, middle, and bottom layers simulation are 0.93, 0.95, and 0.97, respectively. As the temperature was measured directly, the field data represented the actual temperature at the location. Since the thicker the overburdened material, the greater the potential to buffer the effect of temperature variation. Thus, the top layer was most significantly impacted by the variation in atmospheric conditions, as evident in the lower R^2 value. Nevertheless, further investigation of the simulation data showed that the temperature values of the middle and bottom layers were underestimated even if the values for the surface layer were overestimated. The deviation of the simulation values from field observations became more evident as the conductive heat transfer became the dominant process, particularly during March to September, when little or no infiltration was able to reach deeper depths of the testbed. Therefore, in this simulation, the

underestimation of the values in the middle and bottom layers was mainly attributed to the low predicted value of the conductive heat transfer. It should be noted that a constant thermal conductivity and heat capacity was used to reduce the complexity of the model, which could contribute to the potential errors as the thermal properties of the material could vary with temperature.

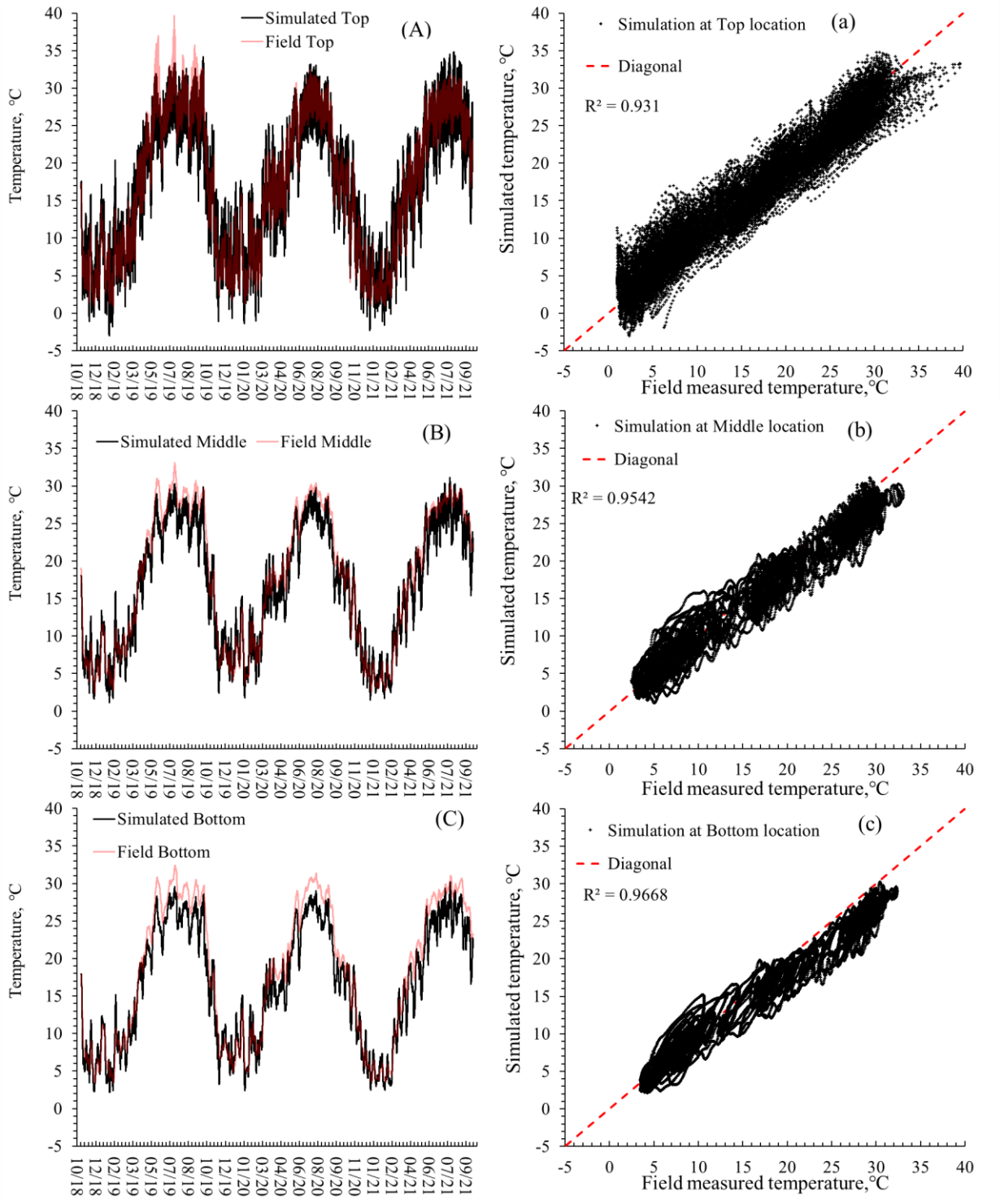

Figure 5.7. Simulated average temperature within: (A) the top, (B) the middle, and (C) the bottom layers; and the correlation of the values of the simulation versus field measurements for (a) the top, (b) the middle, and (c) the bottom layers.

Since the surface temperature can only be heated above ambient temperature by ground heat flux, Figure 5.8 (a) showed the increase of ground heat flux with higher atmospheric temperature. The simulated surface temperature versus the surface temperature measure from 6/14 to 7/15 2021 is presented in Figure 5.8 (b) with an R^2 of 0.53, suggesting factors beyond the surface moisture content is required to better predict the surface temperature. Improvements on surface temperature simulation could be achieved by coupled actual evaporation estimation and heat transfer (Fredlund et al. 2011), associating surface albedo with soil conditions (Idso et al. 1975b) and developing the material-specific correlation between the ground heat flux and soil moisture content. While the precise simulation of the ground heat flux or surface temperature often requires knowledge of either temperature near the surface or heat flux monitoring (Liebethal and Foken 2007; Yang and Wang 2008), instrumenting the surface with appropriate sensors to capture moisture, temperature, and heat capacity in future studies. As for field operations, remote sensing techniques could efficiently monitor surface temperature and moisture over a large field (Njoku and Entekhabi 1996; Schmugge 1978; Wang and Choudhury 1981).

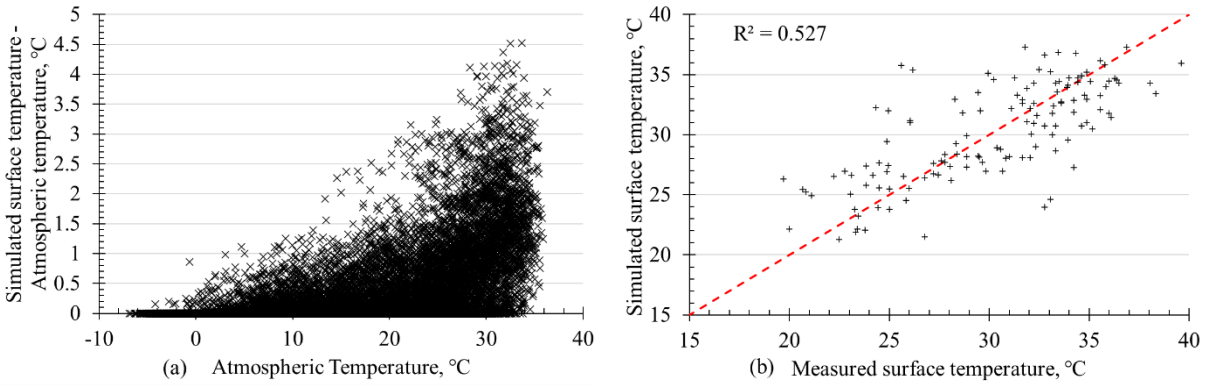

Figure 5.8. (a) Difference between simulated surface temperature and atmospheric temperature and (b) correlation between simulated surface temperature versus measured surface temperature from 6/14 to 7/15 2021.

5.5.1.2. Simulated hydraulic performance

The hourly simulation was continuously performed over 25416 timesteps with surface boundary conditions updated for each hour. The volumetric water content (VWC) pattern is shown in Figure 5.9. The simulation accurately reproduced the trends of average volumetric water content in the top, the middle, and the bottom layers of the field data, as demonstrated by Figure 5.9. These patterns were highlighted by the start and end of each leachate production cycle, the reduction of evaporation, and the response to precipitations. The average difference in VWC between the field data and simulation was -0.71%, -0.19%, and 5.08% for top, middle, and bottom layers, respectively. The overall R^2 of the prediction was 0.67, 0.61, and 0.54 for top, middle, and bottom layers, respectively. It should be noted that the actual property measured in the field was the bulk dielectric permittivity, which was translated to volumetric water content with an established correlation (chapter 3). While the estimated VWC was reasonable for the top and middle layer, the simulated VWC in the bottom layer was significantly lower than the field observation. This deviation could result from the inconsistent parameterization of SWCC as the maximum potential porosity estimated for the field material was 0.52, which was higher than the estimated θs of 0.46 from the samples used to acquire SWCC parameters. While the capillary barrier effect is expected from silty material sitting on the sand layer, it could increase the moisture storage in the compacted layer before drainage, potentially leading to the higher VWC observation in the field data (Stormont and Anderson 1999).

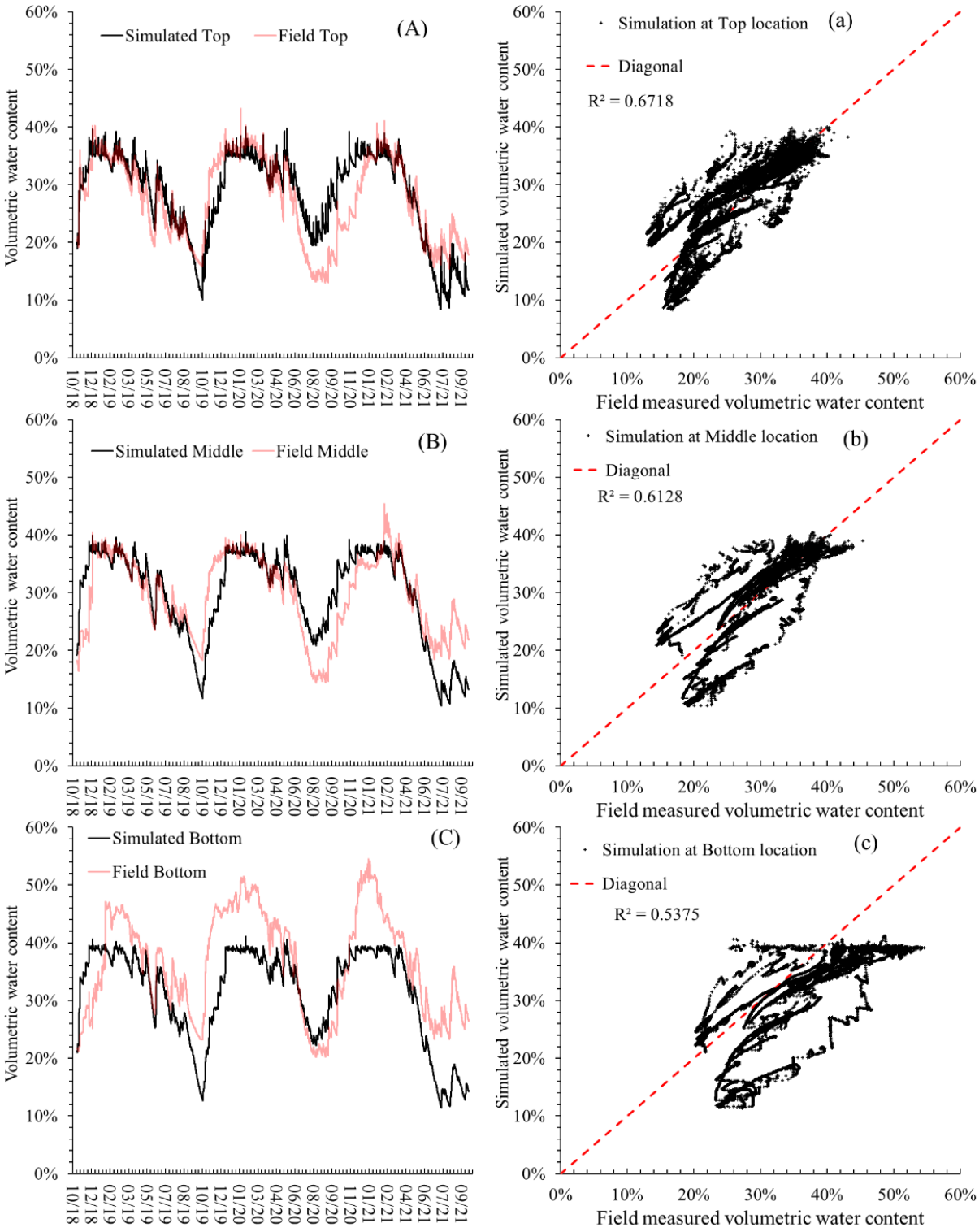

Figure 5.9. Simulated average volumetric water contents: (A) at the top, (B) middle, and (C) bottom layers and the simulation versus field measurements of VWC: (a) at the top, (b) middle, and (c) bottom layers.

The hydraulic performance of the testbed was evaluated based on the leachate and runoff production shown in Figure 5.10. While the simulation captured the daily and seasonal moisture fluctuations within the testbed, Figure 5.10 showed that the estimated runoff and leachate production matched the field data. The simulation predicted the start of the first leachate generation in 12/10/2018 that matched the field observation, and the underestimated leachate quantity from 1/19 to 4/19 was attributed to the overestimated runoff by the SCS-CN model. Since the simulated end date of the first leachate generating period also matched the field observation on 4/13/2019, it can be reasonably be concluded that the model could reproduce the leachate generation process in the field. While the ends of the second and third leachate generating periods were also accurately predicted, the mismatch of the start of the leachate production period was the result of errors in runoff prediction, as demonstrated in Figure 5.11. Though the monthly average of hourly actual evaporation energy did not show a significant difference between summers, underestimating runoff quantities in the summer of 2019 resulted in higher VWC in the testbed. In contrast, the overestimation of runoff value in 10/2019 led to the lower VWC in simulation, leading to a longer recharging time in the late fall of 2019. The lower VWC from simulation compared to the field observation in 7/2021 was attributed to potentially unrecorded rainfalls or unexpected water supply, indicated by a significant increase of VWC without rain, as shown in Figure 5.8.

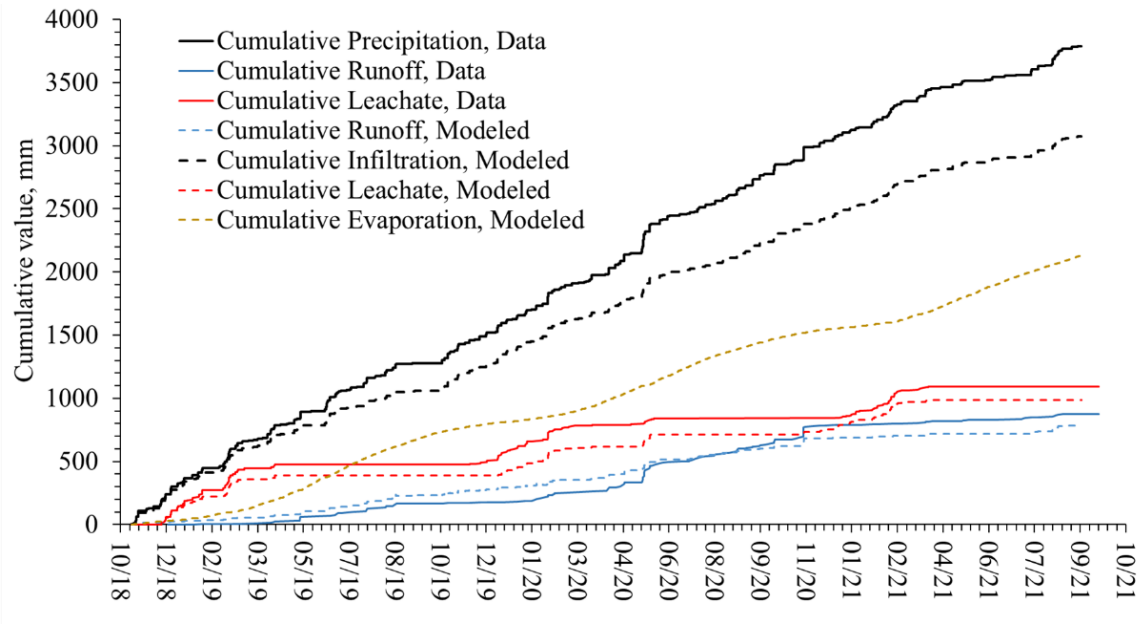

Figure 5.10. Simulated quantities of infiltration, runoff, leachate, and evaporation by baseline scenario compared to the field data.

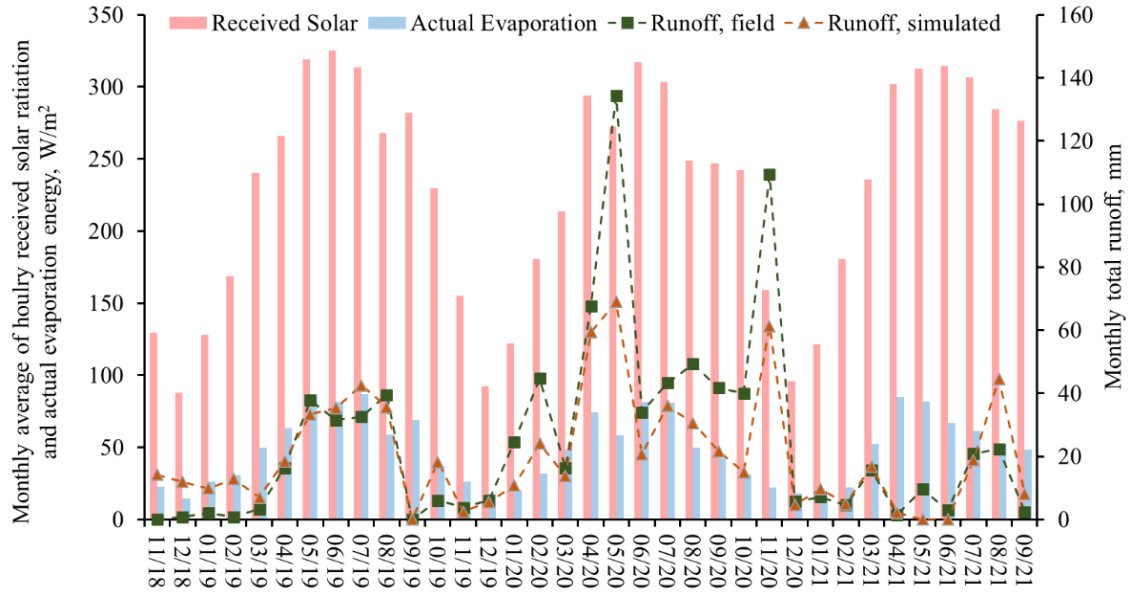

Figure 5.11. Monthly average hourly solar radiation and actual evaporation energy, and monthly runoff values from field data and simulation.

The total volume of leachate, runoff, and difference (precipitation minus leachate and runoff) per unit area is presented in Figure 5.12 (a), and the percentage of each item from the simulation is shown in Figure 5.12 (b). The total quantities of runoff and leachate throughout the simulation were 791.4 mm and 987.6 mm, respectively. With the simulated residual of 2041.6 mm shown in Figure 5.12 (a), the difference:leachate:runoff ratio was 53:26:21 for the simulation. Compared to the 48:29:23 ratio determined from the field data, the simulation underestimated the quantity of leachate and runoff. Considering the overall volumetric water content from the simulation was lower than the field data, the underestimated leachate and runoff were attributed to overestimated evaporation quantity. In conclusion, while the CM model could correctly reproduce the hydraulic behaviors within the testbed, a more accurate prediction could be achieved by improving the runoff estimation method.

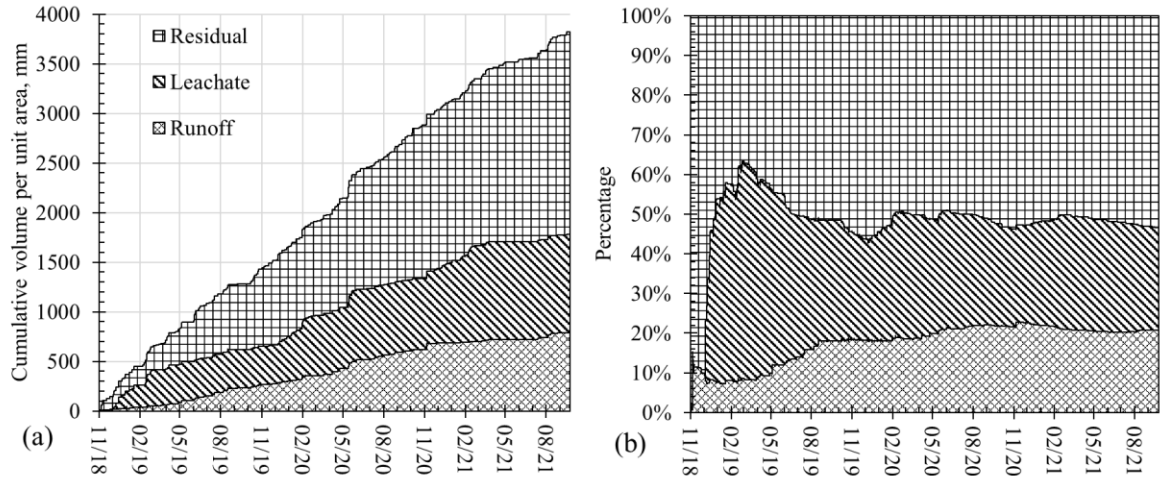

Figure 5.12. From CM simulation, (a): the cumulative volume of leachate, runoff, and the residual (Precipitation – leachate – runoff) per unit area and (b): the percentage of each component relative to the total rainfall.

5.5.1.3. *Simulated solute transport*

The simulation results of the chloride and bromide in the outflow from the bottom boundary presented in Figure 5.13 showed sound reproduction of field measurements in the inner and annulus leachate collection sections. Compared to the poorly simulated sulfate concentrations, the release of which was controlled by the dissolution of sulfate precipitates such as gypsum, the good simulation of the chloride and bromide concentration was attributed to the conduction and diffusion dominated transfer mechanism during the leaching stage. However, once the sulfate became the dominant anion in the leachate, the primary source of solute shifted to the dissolution of sulfate precipitates and weathering of the coal fly ash particles, which requires the modeling of geochemistry simulation to reproduce the field observations more accurately.

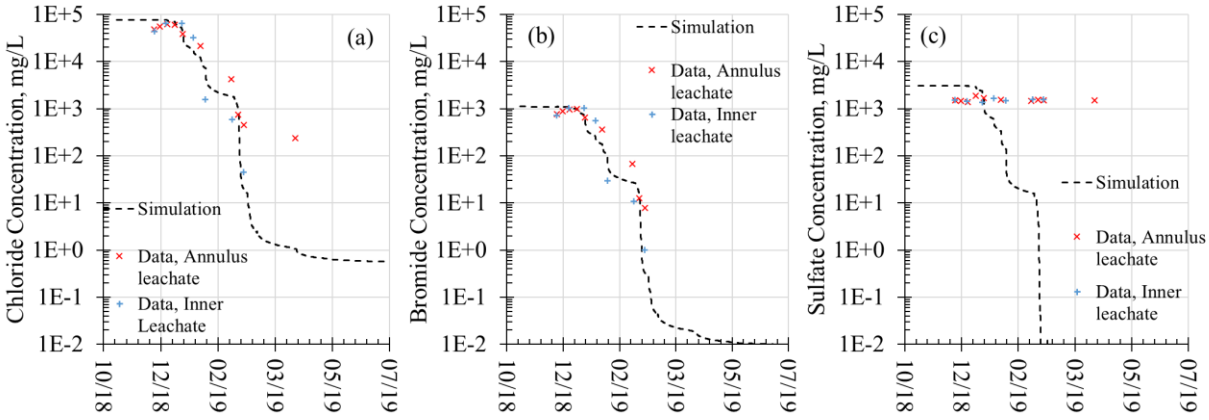

Figure 5.13. Simulation of (a) chloride, (b) bromide, and (c) sulfate concentrations in the outflow from the bottom layer boundary versus the measured concentrations of leachate samples collected from the inner and annulus sections of the testbed.

The previous study (Chapter 3) showed that the translation of the bulk dielectric conductivity (ε) to volumetric water content was influenced by the electrical conductivity (EC), or

salinity, of the pore solution. Further investigation showed the EC was highly correlated to the chloride concentration when it was the dominant anion. Therefore, it was reasonable to use EC as the surrogate of the chloride concentration. While sampling pore fluids at different depths for anion concentrations analysis was also challenging in the field study, the simulated average chloride concentrations at the top, middle, and bottom layers would provide insights into the salinity movement and Ɛ behavior in the testbed as demonstrated in Figure 5.14. The marker arrows identified the example of decreases in Ɛ with infiltration, which matched the predicted significant reduction of the chloride concentration. Further analysis showed increased chloride concentration due to evaporation, which was prominent in the top and middle layers but not in the bottom layer. It should be noted that the simulation did not consider precipitations resulting from salt saturation, which could have led to surface scaling and reduction of solute mobility. In this case, the simulation presents the worst-case scenario for the solute transfer with the flow of the simulated fluid when convection and diffusion were the dominant transport mechanisms.

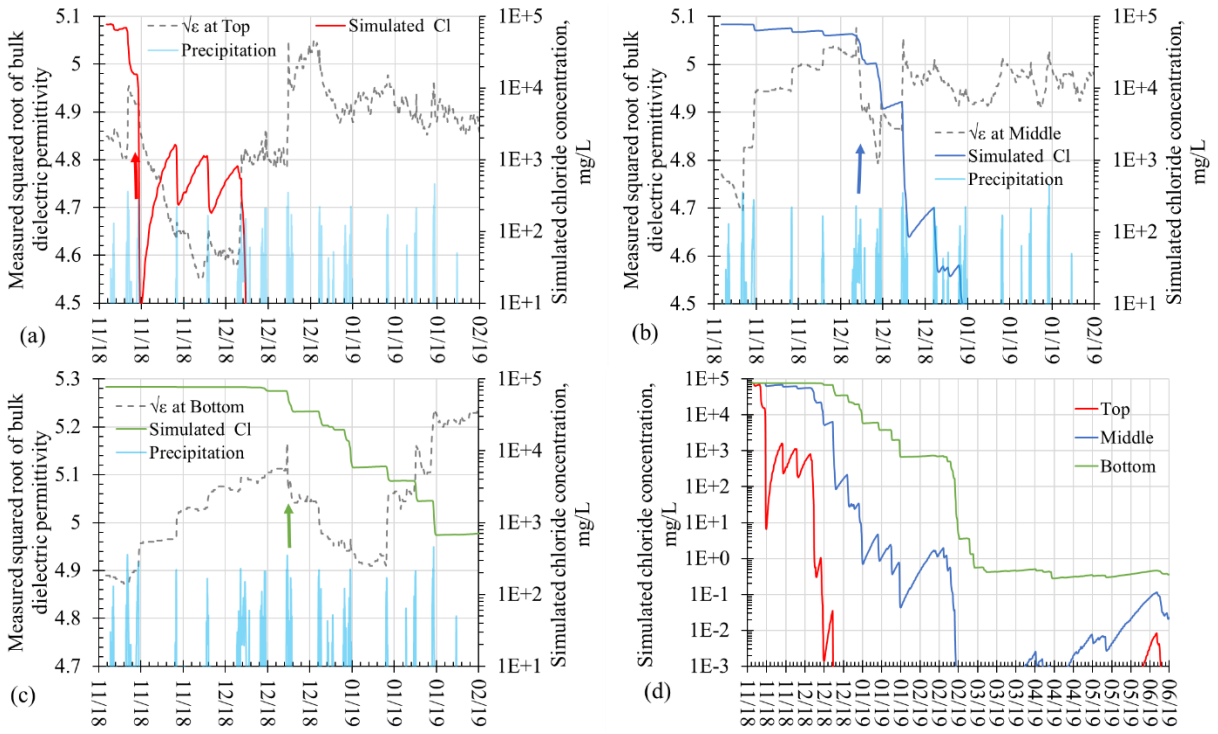

Figure 5.14. Simulation chloride concentration from November 2018 – February 2019 in the (a) top, (b) middle, (c), and bottom layers with the measured bulk dielectric permittivity as $\varepsilon^{0.5}$ and (d) the chloride profile for an extended period of November 2018 – June 2019.

5.5.2. Comparative analysis of scenarios

While the baseline scenario (G1S14) accurately reproduced the field observations, comparisons were made between different modeling scenarios based on the simulated volumetric water content at different layers, the simulated leachate and evaporation, and the statistical analysis of temperature predictions at different layers. While no significant difference in runoff was observed, scenarios with ground heat flux module disabled (G0) showed lower leachate production than their counterparts (G1) due to higher evaporation, as demonstrated in Figure 5.15. Figure 5.16 showed that the overestimation of evaporation occurred during the summer months and can be attributed to the higher solar radiation and atmospheric temperature in this study. The difference between two extreme evaporation scenarios, i.e., G0S0 with no evaporation limit due to material

properties, and G1S24, where material limitation was extrapolated, was 430.7 mm, about 60% of the 712.6 mm from G0S0. The difference in estimated evaporation was negligible between simulation without the actual evaporation module and the module using $\delta = 1.4$. However, a significant difference was observed when δ was increased to 2.4, representing a porous medium with residual suction of 12 kPa, typically characteristic of sandy materials. The improved simulation results from the G1S24 scenario suggested that further investigation into actual evaporation prediction may yield a better simulation of the hydraulic behaviors in the testbed.

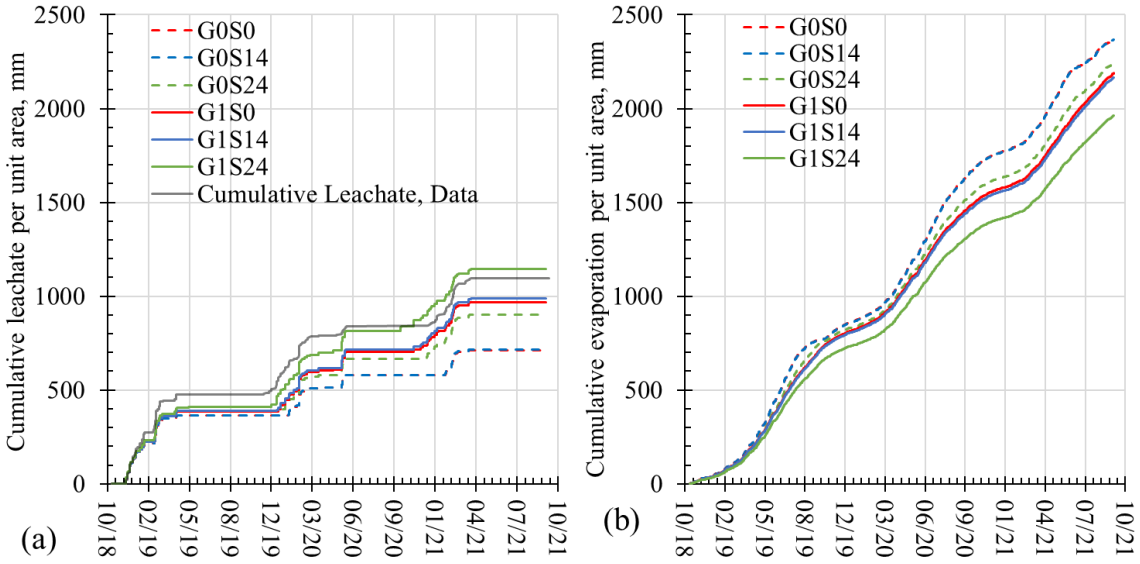

Figure 5.15. Simulated (a) leachate and (b) evaporation under different modeling scenarios.

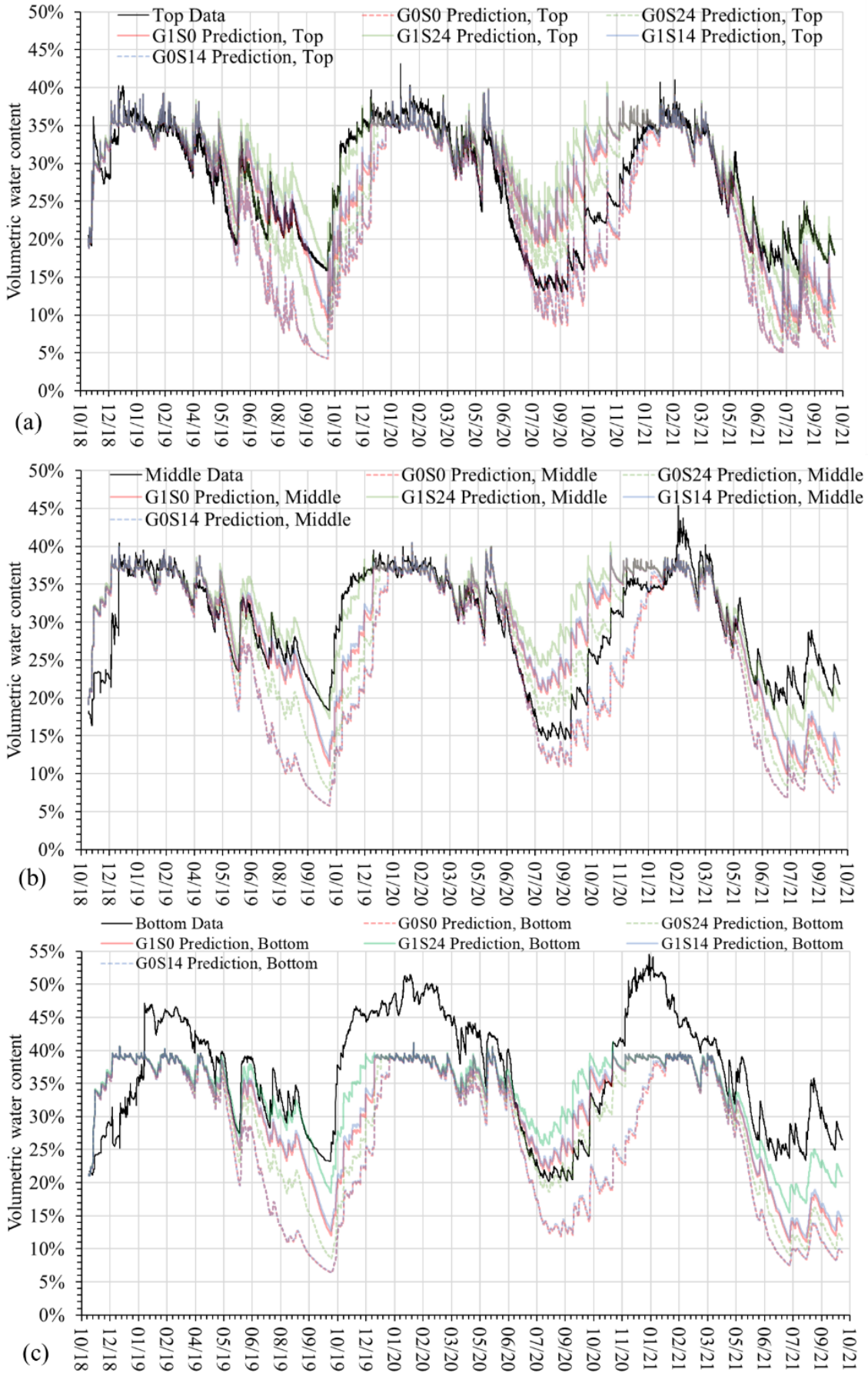
Top Data
G0S0 Prediction, Top
G0S24 Prediction, Top
G1S0 Prediction, Top
G1S24 Prediction, Top
G1S14 Prediction, Top
G0S14 Prediction, Top
Volumetric water content
(a)
Middle Data
G0S0 Prediction, Middle
G0S24 Prediction, Middle
G1S0 Prediction, Middle
G1S24 Prediction, Middle
G1S14 Prediction, Middle
G0S14 Prediction, Middle
Volumetric water content
(b)
Bottom Data
G0S0 Prediction, Bottom
G0S24 Prediction, Bottom
G1S0 Prediction, Bottom
G1S24 Prediction, Bottom
G1S14 Prediction, Bottom
G0S14 Prediction, Bottom
Volumetric water content
(c)

Figure 5.16. Simulated average volumetric water content in the (a) top, (b) the middle, and (c) the bottom layers under different scenarios.

The simulation results of heat transfer modeling were compared with field observations using different statistical parameters, including the goodness of fit (R^2), the average difference (AD), and the mean absolute error (MAE). A positive MAE suggests the simulated temperature was on average higher than the field observation. The goodness of fit for temperature simulations did not exhibit a significant difference between scenarios, as shown in Table 5.3. Further analysis showed a minor difference between the distribution of prediction errors, as shown in Figure 5.17. Although incorporating the ground heat flux estimation impacted the hydrological simulation significantly, its negligible effect on heat transfer simulation suggests other factors may be needed to improve the heat transfer simulation, as discussed for the baseline scenario.

Table 5.3. Summary of R^2 and MAE for temperature predictions in different layers under scenarios

	Layer	Scenarios					
		G0S0	G0S14	G0S24	G1S0	G1S14	G1S24
R2	Top	0.88	0.88	0.87	0.87	0.87	0.87
	Middle	0.94	0.94	0.95	0.95	0.95	0.96
	Bottom	0.95	0.97	0.96	0.97	0.95	0.97
AD	Top	0.05	0.04	0.26	0.23	0.26	0.04
℃	Middle	-1.31	-1.31	-1.09	-1.11	-1.09	-1.32
	Bottom	-1.86	-1.85	-1.63	-1.65	-1.87	-1.63
MAE	Top	2.37	2.46	2.45	2.50	2.45	2.26
℃	Middle	2.14	2.08	1.90	1.90	1.91	2.15
	Bottom	2.36	2.31	2.09	2.10	2.37	2.10

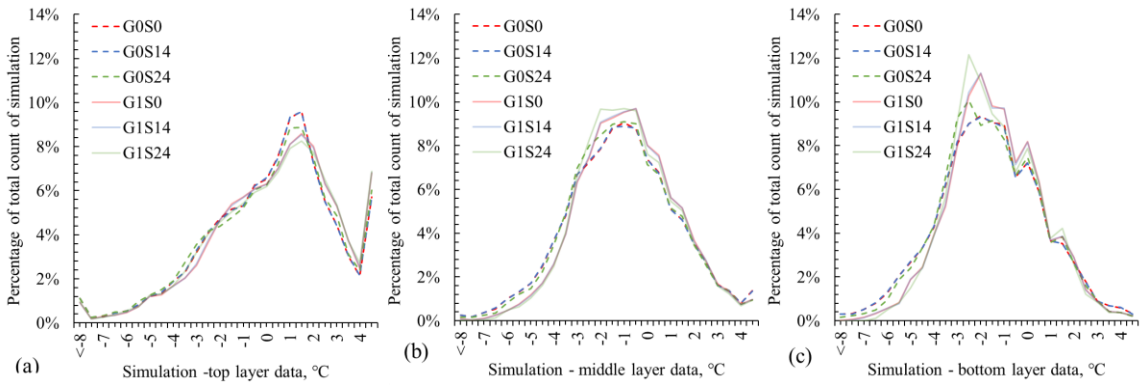

Figure 5.17. Percentage histogram of the difference between the field data and the simulation in the (a) top, (b) middle, and (c) bottom layers.

5.6.Conclusions

This study presented a COMSOL-MATLAB (CM) model that simulates the unsaturated flow, heat transfer, and solute transport in a field study performed in an instrumented testbed containing compacted CFA-FGD brine co-disposal material. The ability of the CM model to incorporate custom boundary conditions to include the ground heat flux estimation, actual evaporation estimation, runoff estimation, and surface temperature estimation expanded the simulation capacity. The MATLAB-based model allowed the continuous hourly simulation for 35 months with surface boundary conditions updated every hour.

The results from the baseline scenario showed sound reproduction of field observations in terms of the hydraulic performance, heat transfer, and halides transport. The baseline scenario failed to adequately reproduce the sulfate concentration in the leachate as the release of the anion was potentially controlled by the dissolution process rather than the convection and diffusion simulated in this model. Since the rainfall was the only source of moisture in this model, the accuracy of runoff simulation directly affects the hydraulic performance, including the change of

moisture content and the leachate generation in the testbed. More accurate runoff simulation may be acquired with models considering antecedent soil moisture, such as the SCS-CN model based on material moisture (Schroeder et al. 1994) and the Green-Ampt model (Chen and Young 2006). Scenario studies showed that the simulation of hydraulic behaviors might be improved by further investigating the actual evaporation estimation. The validated CM model can be used to investigate potential management methods for leachate reduction and explore the compacted material's performance under different weather conditions.

References

Azad, V. J., Li, C., Verba, C., Ideker, J. H., and Isgor, O. B. (2016). "A COMSOL–GEMS interface for modeling coupled reactive-transport geochemical processes." *Computers & Geosciences*, 92, 79–89.

Batini, N., Loria, A. F. R., Conti, P., Testi, D., Grassi, W., and Laloui, L. (2015). "Energy and geotechnical behaviour of energy piles for different design solutions." *Applied Thermal Engineering*, Elsevier, 86, 199–213.

Bejan, A. (2013). *Convection heat transfer*. John wiley & sons.

Chen, L., and Young, M. H. (2006). "Green-Ampt infiltration model for sloping surfaces." *Water Resources Research*, John Wiley & Sons, Ltd, 42(7).

COMSOL AB. (2020). "COMSOL Multiphysics® v. 5.5." Stockholm, Sweden.

Division, U. S. S. C. S. E. (1986). *Urban hydrology for small watersheds*. Engineering Division, Soil Conservation Service, US Department of Agriculture.

Fatoba, O. O., Petrik, L. F., Gitari, W. M., and Iwuoha, E. I. (2011). "Fly ash-brine interactions: Removal of major and trace elements from brine." *Journal of Environmental Science and Health, Part A*, Taylor & Francis, 46(14), 1648–1666.

Fayer, M. J. (2000). *UNSAT-H version 3.0: Unsaturated soil water and heat flow model theory, user manual, and examples*. Pacific Northwest National Lab., Richland, WA (US).

Fredlund, M. D., Tran, D., and Fredlund, D. G. (2016). "Methodologies for the Calculation of Actual Evaporation in Geotechnical Engineering." *International Journal of Geomechanics*, American Society of Civil Engineers, 16(6), D4016014.

Fredlund, M. D., Zhang, J. M., Tran, D., and Fredlund, D. G. (2011). "Coupling heat and moisture flow for the computation of actual evaporation." *Proceedings of the Canadian Geotechnical Conference and Fifth Pan-American Conference, Toronto, Ont*, 2–6.

Gao, Z., Russell, E. S., Missik, J. E. C., Huang, M., Chen, X., Strickland, C. E., Clayton, R., Arntzen, E., Ma, Y., and Liu, H. (2017). "A novel approach to evaluate soil heat flux calculation: An analytical review of nine methods." *Journal of Geophysical Research: Atmospheres*, John Wiley & Sons, Ltd, 122(13), 6934–6949.

Van Genuchten, M. T. (1980). "A closed-form equation for predicting the hydraulic conductivity of unsaturated soils." *Soil science society of America journal*, Soil Science Society of America, 44(5), 892–898.

Halloran, L. J. S., Brunner, P., and Hunkeler, D. (2019). "COMPEST, a PEST-COMSOL interface for inverse multiphysics modelling: Development and application to isotopic fractionation of groundwater contaminants." *Computers & Geosciences*, Elsevier, 126, 107–119.

Haselow, L., Meissner, R., Rupp, H., and Miegel, K. (2019). "Evaluation of precipitation measurements methods under field conditions during a summer season: A comparison of the standard rain gauge with a weighable lysimeter and a piezoelectric precipitation sensor." *Journal of Hydrology*, Elsevier, 575, 537–543.

Hawkins, R. H., Ward, T. J., Woodward, D. E., and Van Mullem, J. A. (2008). "Curve number hydrology: State of the practice." American Society of Civil Engineers.

He, R., Ogunro;, V. O., and Ellison, K. M. (2022). "Preliminary Results of Compacted Coal Fly Ash/Flue Gas Desulfurization Brine Co-disposal in an Instrumented Testbed." *Geo-Congress 2022*.

Hjelmfelt Jr, A. T. (1991). "Investigation of curve number procedure." *Journal of Hydraulic Engineering*, American Society of Civil Engineers, 117(6), 725–737.

Hoffmann, M., Schwartengräber, R., Wessolek, G., and Peters, A. (2016). "Comparison of simple rain gauge measurements with precision lysimeter data." *Atmospheric Research*, Elsevier, 174, 120–123.

Huang, M., Bruch, P. G., and Barbour, S. L. (2013). "Evaporation and water redistribution in layered unsaturated soil profiles." *Vadose Zone Journal*, The Soil Science Society of America, Inc., 12(1), vzj2012-0108.

Idso, S. B., Aase, J. K., and Jackson, R. D. (1975a). "Net radiation — soil heat flux relations as influenced by soil water content variations." *Boundary-Layer Meteorology*, 9(1), 113–122.

Idso, S. B., Jackson, R. D., Reginato, R. J., Kimball, B. A., and Nakayama, F. S. (1975b). "The dependence of bare soil albedo on soil water content." *Journal of Applied Meteorology and Climatology*, 14(1), 109–113.

Li, Q., Ito, K., Wu, Z., Lowry, C. S., and Loheide II, S. P. (2009). "COMSOL Multiphysics: A novel approach to ground water modeling." *Groundwater*, Blackwell Publishing Ltd Oxford, UK, 47(4), 480–487.

Liebethal, C., and Foken, T. (2007). "Evaluation of six parameterization approaches for the ground heat flux." *Theoretical and Applied Climatology*, Springer, 88(1), 43–56.

Luminant Generation Company, L. (2016). *Run-on and run-off control system plan big brown steam electric station ash disposal area II*.

McGuinness, J. L. (1966). *Comparison of Lysimeter Catch and Rain Gage Catch*. Agricultural Research Service, US Department of Agriculture.

Millington, R. J., and Quirk, J. P. (1961). "Permeability of porous solids." *Transactions of the Faraday Society*, Royal Society of Chemistry, 57, 1200–1207.

Mishra, S. K., and Singh, V. (2003). *Soil conservation service curve number (SCS-CN) methodology*. Springer Science & Business Media.

Mualem, Y. (1976). “A new model for predicting the hydraulic conductivity of unsaturated porous media.” *Water resources research*, Wiley Online Library, 12(3), 513–522.

Nardi, A., Idiart, A., Trinchero, P., de Vries, L. M., and Molinero, J. (2014). “Interface COMSOL-PHREEQC (iCP), an efficient numerical framework for the solution of coupled multiphysics and geochemistry.” *Computers & Geosciences*, 69, 10–21.

Njoku, E. G., and Entekhabi, D. (1996). “Passive microwave remote sensing of soil moisture.” *Journal of hydrology*, Elsevier, 184(1–2), 101–129.

Penman, H. L. (1963). “Vegetation and hydrology.” *Soil Science*, LWW, 96(5), 357.

Ponce, V. M., and Hawkins, R. H. (1996). “Runoff curve number: Has it reached maturity?” *Journal of hydrologic engineering*, American Society of Civil Engineers, 1(1), 11–19.

Rawls, W. J., and Brakensiek, D. L. (1986). “Comparison between Green-Ampt and curve number runoff predictions.” *Transactions of the ASAE*, American Society of Agricultural and Biological Engineers, 29(6), 1597–1599.

Richards, L. A. (1931). “Capillary conduction of liquids through porous mediums.” *Physics*, American Institute of Physics, 1(5), 318–333.

Romano, N., Brunone, B., and Santini, A. (1998). “Numerical analysis of one-dimensional unsaturated flow in layered soils.” *Advances in Water Resources*, Elsevier, 21(4), 315–324.

Sauer, T. J., and Horton, R. (2005). “Soil Heat Flux.” *Micrometeorology in Agricultural Systems*, Agronomy Monographs.

Schmugge, T. (1978). “Remote sensing of surface soil moisture.” *Journal of Applied Meteorology*, 17(10), 1549–1557.

Schneider, L. E., and McCuen, R. H. (2005). “Statistical guidelines for curve number generation.” *Journal of Irrigation and Drainage Engineering*, American Society of Civil Engineers, 131(3), 282–290.

Schroeder, P. R., Dozier, T. S., Zappi, P. A., McEnroe, B. M., Sjostrom, J. W., and Peyton, R. L. (1994). “The hydrologic evaluation of landfill performance (HELP) model: Engineering documentation for version 3.” Citeseer.

Schroeder, P. R., Gibson, A. C., and Smolen, M. D. (1984). *The hydrologic evaluation of landfill performance (HELP) model*. Municipal Environmental Research Laboratory, Office of Research and ….

Šimunek, J., Van Genuchten, M. T., and Šejna, M. (2012). “HYDRUS: Model use, calibration, and validation.” *Transactions of the ASABE*, American Society of Agricultural and Biological Engineers, 55(4), 1263–1274.

Šimůnek, J., Šejna, M., Saito, H., Sakai, M., and Genuchten, M. T. van. (2018). “The HYDRUS-

1D Software Package for Simulating the One-Dimensional Movement of Water, Heat, and Multiple Solutes in Variably-Saturated Media."

Stormont, J. C., and Anderson, C. E. (1999). "Capillary barrier effect from underlying coarser soil layer." *Journal of Geotechnical and Geoenvironmental Engineering*, American Society of Civil Engineers, 125(8), 641–648.

U.S. EIA. (2021). "Electricity explained - Electricity in the United States." <https://www.eia.gov/energyexplained/electricity/electricity-in-the-us.php> (Dec. 11, 2021).

U.S. EPA. (2015). "Hazardous and Solid Waste Management System; Disposal of Coal Combustion Residuals From Electric Utilities; Final Rule." *The Federal Register*, Federal Information & News Dispatch, Inc., Washington.

U.S. EPA. (2020). "Steam Electric Reconsideration Rule." 40 C.F.R. Part 423.

Walter, I. A., Allen, R. G., Elliott, R., Jensen, M. E., Itenfisu, D., Mecham, B., Howell, T. A., Snyder, R., Brown, P., and Echings, S. (2000). "ASCE's standardized reference evapotranspiration equation." *Watershed management and operations management 2000*, 1–11.

Wang, J. R., and Choudhury, B. J. (1981). "Remote sensing of soil moisture content, over bare field at 1.4 GHz frequency." *Journal of Geophysical Research: Oceans*, Wiley Online Library, 86(C6), 5277–5282.

Whitaker, S. (1986). "Flow in porous media I: A theoretical derivation of Darcy's law." *Transport in porous media*, Springer, 1(1), 3–25.

Wilson, G. W. (1990). "Soil evaporative fluxes for geotechnical engineering problems." University of Saskatchewan Saskatoon.

Woodward, D. E., Hawkins, R. H., Jiang, R., Hjelmfelt Allen T, J., Van Mullem, J. A., and Quan, Q. D. (2003). "Runoff curve number method: Examination of the initial abstraction ratio." *World water & environmental resources congress 2003*, 1–10.

Yang, K., and Wang, J. (2008). "A temperature prediction-correction method for estimating surface soil heat flux from soil temperature and moisture data." *Science in China Series D: Earth Sciences*, 51(5), 721–729.

CHAPTER 6 DATA-DRIVEN MODELING OF BULK DIELECTRIC PERMITTIVITY PROFILE OF A COAL FLY ASH – FLUE GAS DESULFURIZATION BRINE CO-DISPOSAL TESTBED FOR USE IN PREDICTING WATER CONTENT

Abstract

The advancement in technology has allowed the collection of a large quantity of real-time in-situ field data, promoting the development and use of data-driven models to predict properties of interest. Data-driven models do not require extensive knowledge of the potential physics processes that drive the targeted properties compared to the physics-based model. In this study, a data-driven model was established to predict the change in the bulk dielectric permittivity of the compacted co-disposal mixture consisting of class F coal fly ash (CFA) and hypersaline flue gas desulfurization (FGD) concentrate (brine) in an instrumented testbed under field environment. The in-situ sensors measure the bulk dielectric permittivity, which is widely used to estimate the volumetric water content of a porous medium when the electrical conductivity of the pore solution is known. For this study, the testbed was segmented into three individual layers with the change in permittivity at the top layer driven by ambient conditions, while the permittivity of the preceding layer drove those in the middle and bottom layers. While each layer was trained separately with the Neural Network (NN) Fitting function in MATLAB, models were connected using predictions from the preceding layer as inputs for the current layer in each timestep. The prediction with a forecast interval of 24 hours over the three years of the experiment using a model trained with the first-year data showed an average goodness fitting (R^2) of 97.6%, and the average R^2 increased to 99.5% when trained with the data of the first two years. The scenario studies demonstrated that the model could only accurately predict values with features and characteristics used for the training, which demands special considerations when unprecedented and variabilities are observed during operation. Further investigation revealed the prediction made by pattern recognition could simulate

processes that conventionally required additional information, only if such patterns were covered in the training dataset. Although the model in this study utilized a layer stacking structure, which was designed to address the common operation of implementing new layers on top of existing materials during landfill operation, the transfer of knowledge between layers at the same spatial order would require further investigation. Prediction accuracy ultimately depends on the quality and quantity of the training data, which demands proper instrumentation and careful maintenance of the data collection system for a sufficient duration to capture all the features and characteristics to produce good pattern recognition.

6.1. Introduction

The monitoring of in-situ dielectric properties of compacted material is made affordable and feasible with advancements in technologies, which allows researchers and operators to collect a large quantity of high-quality data (Cardell-Oliver et al. 2004; Flammini et al. 2007; Li et al. 2014; Scudiero et al. 2012; Young et al. 2014). While these in-situ real-time measurements allow a better understanding of the physic process in the material and better oversight over a large field, the real-time data also empowered the data-driven modeling to provide another perspective into the field behaviors (Hong et al. 2016; Kim and Singh 2014; Kornelsen and Coulibaly 2014). While physics-based modeling tools such as HYDRUS and COMSOL are familiar to researchers (COMSOL AB 2020; Radcliffe and Simunek 2018), the data-driven modeling tools are also commercially available at low cost or free on platforms such as MATLAB and Python (MathWorks 2021; Pedregosa et al. 2011). Compared to the physics-based model, the data-driven model does not require extensive knowledge of the physical processes governing the apparent observations, which can risk leading to empiricism due to the lack of mechanistic governing relationships. In other words, the trained data-driven model might not be transferred to other

applications as weather conditions and soil properties may vary (Wadoux et al. 2020). It should also be noted that although the data-driven model is free of theory, it does not prevent the use of theoretical concepts to select the factors for the model. For example, following the water balance concept of the soil, one would include factors such as temperature, humidity to represent evaporation, and rainfall for infiltration. In this case, using such factors in the data-driven modeling provides some level of physics principle without providing the correlation values to make predictions. Therefore, the transferable knowledge between data-driven modeling for field conditions is the structure of the model, selection of factors, and the validation of the factor selections for different materials.

In this study, a field experiment using instrumented testbed housing compacted co-disposed coal fly ash (CFA) and flue gas desulfurization (FGD) brine was conducted in climatic conditions in Charlotte, North Carolina. The co-disposal of CFA and FGD brine in the engineered CFA landfill through compaction provides a potential management option for coal-fired steam power electric plants to comply with regulation requirements (U.S. EPA 2015, 2017) (Chapter 3). The in-situ sensors gathered the hourly data for bulk dielectric permittivity, ε, and temperature, T (°C), at 12.7 cm (5 inches, top location), 38.1 cm (15 inches, middle location), and 63.5 cm (25 inches, bottom location) below the exposed surface of the testbed. An adjacently located weather station monitored the hourly atmospheric conditions, including the wind speed, solar radiation, atmospheric temperature, rainfall, and relative humidity. Although the squared root of bulk permittivity, $\sqrt{\varepsilon}$, could be translated to volumetric water content with soil-specific calibration, this study will model the $\sqrt{\varepsilon}$ since it was the measured property (Topp et al. 1980). This study utilized the Neural Network (NN) Fitting function in the Statistics and Machine Learning Toolbox in MATLAB to train the NN model for sensors at each location with datasets representing different

scenarios. This study aims to develop a modeling structure for $\sqrt{\varepsilon}$ prediction at different depths and investigate the potential challenges through scenario studies.

6.2. Instrumentation and Data Acquisition

The testbed was configured to simulate an engineered landfill with surface runoff and a leachate collection system. The operation started on11/7/2018, with the routine collection of leachate, runoff, and sensor data (temperature and bulk dielectric permittivity). Since the measurements of the collected liquids were not hourly, the information was not used in this model. The surface was under routine inspection and vegetation removal to prevent significant evapotranspiration, with details of the testbed available in He et al. (2022). The ML3 Theta Probe coupled with the GP2 datalogger from Delta-T. Inc was used to gather the bulk dielectric permittivity for volumetric water content measurement. The temperature at each location was monitored with a T108 thermal couple connected to a CR800 datalogger from Campbell Scientific. A set of one ML3 sensor and one T108 sensor was located at the top (12.7 cm), middle (38.1 cm), and bottom (63.5 cm) locations along the center of the testbed. The permittivity data collected during the experiment study period and the volumetric water content (VWC) estimated from the permittivity are shown in Figure 6.1, and Figure 6.2 demonstrates the temperature profile within the testbed. It should be noted that the salinity of the pore solution also influences the permittivity, which had a significant impact on the $\sqrt{\varepsilon}$ measurements before 3/1/2019. The moisture movement was considered the dominant factor for $\sqrt{\varepsilon}$ change after that date (He et al. 2022).

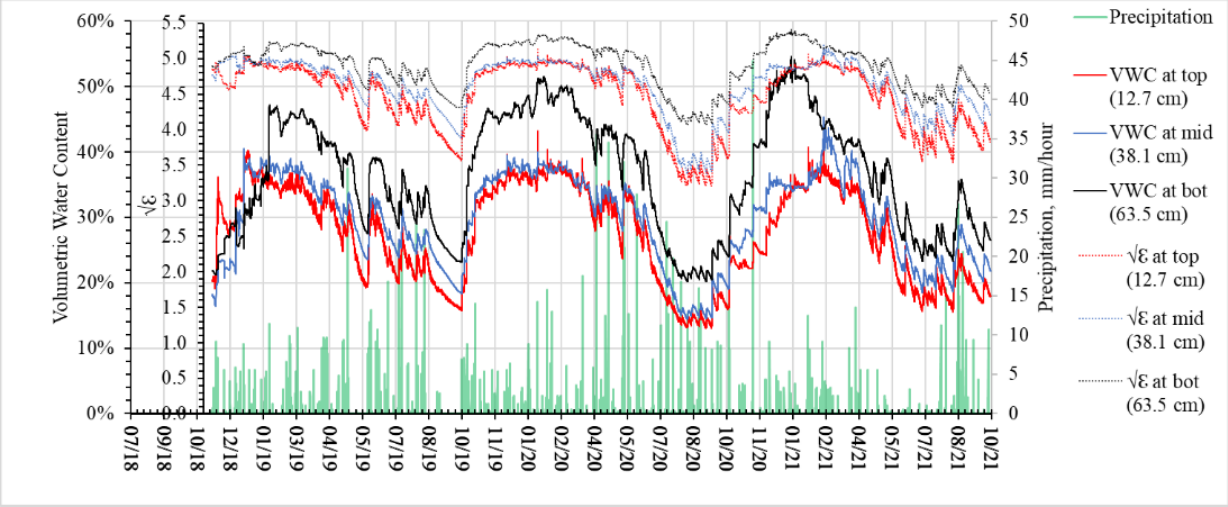

Figure 6.1. The hourly rainfalls, the permittivity (√ε), and the estimated volumetric water content (VWC) at the top (12.7 cm), the middle (38.1 cm), and the bottom (63.5 cm) locations of the testbed. (Chapter 3)

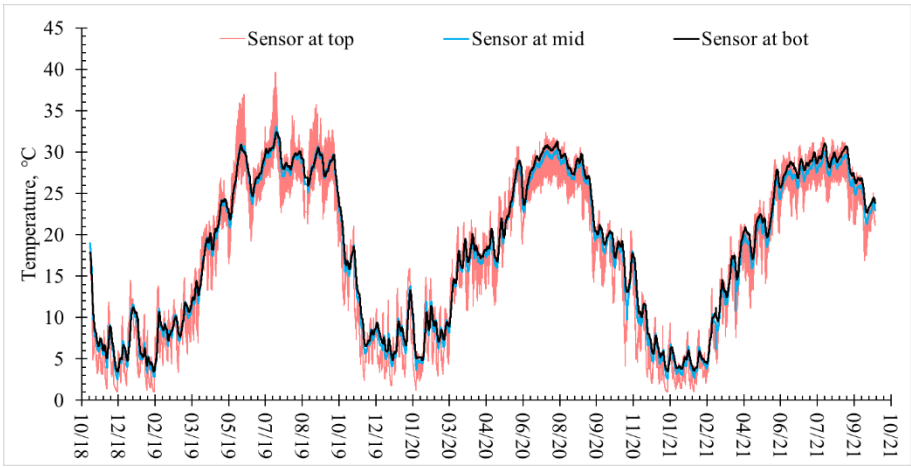

Figure 6.2. The temperature at the top, the middle, and the bottom locations of the testbed, modified from Chapter 3

6.3. Characteristic Behavior of Solute Transport in the Testbed

The bulk dielectric permittivity of the compacted CFA-FGD co-disposal material measured by the ML3 ThetaProbe was mainly a function of the volumetric water content (VWC) and the pore

solution's dielectric constant, which depends on the salinity of pore fluid as discussed in chapter 3. The permittivity of the compacted medium increases with an increase in VWC when the pore solution's salinity remains at the same value, as demonstrated in chapter 3. If the VWC of the material is maintained constant, the bulk permittivity decreases with the decreasing salinity in the pore solution.

In the field experiment, the VWC was expected to increase with water infiltration during a rain event, which would lead to an increase in permittivity. However, rainfall containing negligible salinity will inevitably washoff the initial hypersaline pore solution, decreasing permittivity during precipitation. Using the electric conductivity (EC) as an indicator of salinity (Rhoades 1996), the salinity washoff was shown by the rapid decrease of EC in leachate between Nov 2018 and Mar 2019 (He et al. 2022). Once the washoff process becomes insignificant, as demonstrated by a relatively constant EC and chemical composition in the pore solution, the variation of permittivity was dominated by the change of VWC as shown in chapter 3. In this case, the counteracting effects of increasing VWC and decreasing salinity would create the unique permittivity variation pattern, which is characterized by the decrease of permittivity with rainfall. Since the EC or salinity of pore solution at each layer was not measured in this study, there was no direct information of the pore solution's salinity. Therefore, the unique behavior could be used to identify the start and end of the major washoff period, predicting permittivity during the period requires assumptions on the EC of pore solution, which could bring additional errors.

6.4. Model Structure

As discussed in the introduction section, physics principles such as mass balance and energy balance will be incorporated into factors used in the data-driven model in this study.

Therefore, the role of the data-driven model in this study is to identify the correlations between the factors that would minimize the overall prediction error to best represent the multi-physics principles. For this study, the instrumented testbed was divided into three layers of 25.4 cm thickness. The weather conditions are input data used to model the top layer, as the evaporation and infiltration occur only through the exposed surface of the testbed. The input consists of weather station data (rainfall, surface temperature, atmospheric relative humidity, received solar radiation, wind speed), and the saturated vapor pressure, which was estimated according to the Hydrologic Evaluation of Landfill Performance (HELP) model (NEPIS 1994). These conditions are often used to predict the infiltration, evaporation, and temperature at the surface in physics-based models (Gao et al. 2017; Or et al. 2013; Penman and Keen 1948; Sauer and Horton 2005). The driving potential exerted on the top surface was then applied downward into the testbed, which means the immediate overlying layer influences the changes or supplies the inputs for the current layer. While atmospheric conditions are the driving potential and inputs for the top layer, the shift in permittivity (water content) at the middle and the bottom layers were assumed to be caused by the top and the middle layers, respectively. In this case, the legacy information (conditions and modeled data from previous timestep, i-1) and current information (condition at timestep, i) are used to predict the current permittivity in $\sqrt{\varepsilon}$, as demonstrated in Figure 6.3.

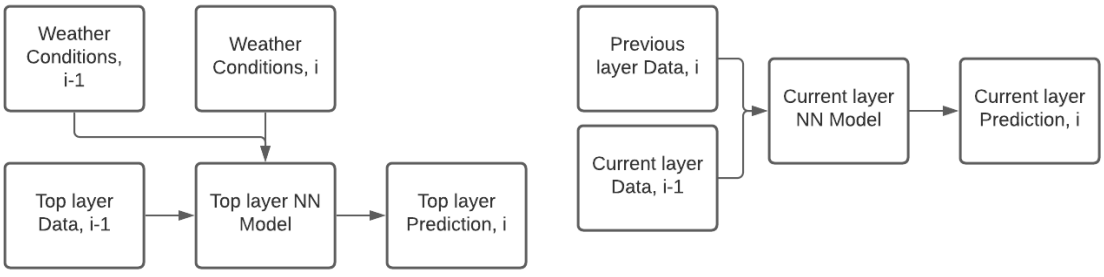

Figure 6.3. Diagram of data-driven model for individual layers, i is the timestep.

After models were individually trained, they were connected using predicted value as the input for the next layer. The structure of the integrated model for the continuous timestep simulation is demonstrated in Figure 6.4, where i represents the i^{th} timestep. The integrated model could then simulate the spatial-temporal profile of permittivity, and the stackable structure of the model allows further expansion to incorporate additional layers. The expansion ability was designed for use in an operating landfill since the stacking of new layers is expected. The Levenberg-Marquardt backpropagation method was used for the training model, and the summary of training configuration is presented in Table 6.1.

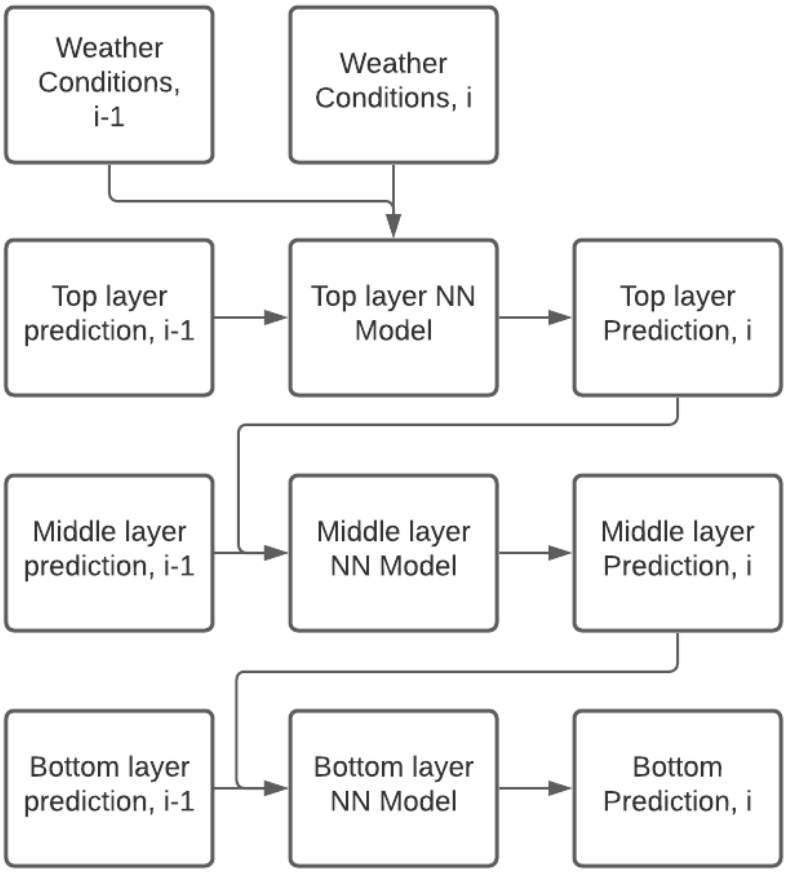

Figure 6.4. The integrated model for continuous timestep simulation.

Table 6.1. Configuration summary of NN model structure and training.

	Input layer size	Hidden layer size	Output layer size	Training set ratio	Validation set ratio	Test set ratio
Top	13	20	1	0.70	0.15	0.15
Mid	2	4	1	0.70	0.15	0.15
Bot	2	4	1	0.70	0.15	0.15

6.5. Training Scenarios and Forecast Intervals

Unlike the physics model, which utilizes the theoretical equations validated under different scenarios, the data-driven model represents what had been included in the dataset. To develop the data-driven model, a pre-existing set of data is required to first train the model, and future predictions are made based on the scenarios included in the training data set. Therefore, the dataset's limited scope becomes the trained model's limitation, or the model can only predict correlation that could be identified from the dataset. Three main scenarios of dataset limitations are proposed to better understand the limitations resulting from the dataset on the proposed integrated model (Table 6.2).

Scenario 1 (S1) examined the use of the data during the washoff/leaching process (11/7/2018 to 3/1/2019). In scenario 1, three models were trained with the 3-year dataset excluding the washoff fraction (S11), with the full 3-year dataset including the washoff fraction (S12), and with only the washoff data fraction (S13). S13 tested whether the model can predict the $\sqrt{\varepsilon}$ when lacking the direct knowledge of a significant factor (in this case, the pore solution's salinity). The goal of S11 and S13 was to investigate whether the data-driven model could predict the change of permittivity without direct knowledge of salinity. Though the salinity influenced the permittivity,

patterns reflecting the change in permittivity due to salinity variation may be recognized by S13. The S11 then provided the blank comparison for S13, showing whether the model could predict the change with zero knowledge on salinity change. The S12 then explored whether a model trained with a full dataset could accurately predict the washoff and leached period, which is essential in the actual operation due to the difficulties associated with identifying the end of washoff stages.

In scenario 2 (S2), the model was trained with 1 (S21), 2 (S22), and 3 (S23) years of data to investigate whether increasing the dataset will lead to more accurate predictions. Considering that the range of $\sqrt{\varepsilon}$ value continued to expand during the three years of the experiment, each year presented some new phenomena not encountered in previous years. Although expanding the training dataset was set to increase the overall accuracy, the increase in the degree of prediction accuracy can be used to quantify the improvement of the model.

Scenario 3 (S3) limited the conditions used to train the model by restricting the dataset to only the first and second six months of data. The first six months (S31) of the experiment did not include the significant summer drying (Figure 6.1), and the second six months (S32) did not experience the relatively constant $\sqrt{\varepsilon}$ value during the winter. S3 investigated the model's performance for uncharacteristic situations, which will help understand the criteria for selecting the minimum dataset size for model training.

The trained models were expected to forecast the $\sqrt{\varepsilon}$ based on future weather conditions and the accuracy of the integrated model, but as shown in Figure 6.4, the accuracy would decrease as errors accumulate with each timestep. While the ability to predict hourly weather conditions is also limited, different forecast intervals are investigated to identify the best forecasting practices.

The forecast intervals studied are 1-, 3-, 7-, 14-, 30-days, and 3-years. Different forecast intervals were implemented using the data instead of the prediction as inputs in the integrated model, as demonstrated in Figure 6.5. The summary of the dataset sizes and the time range of each dataset are presented in Table 6.2. The activation function, loss function, and the summary of performance can be found in supplementary materials.

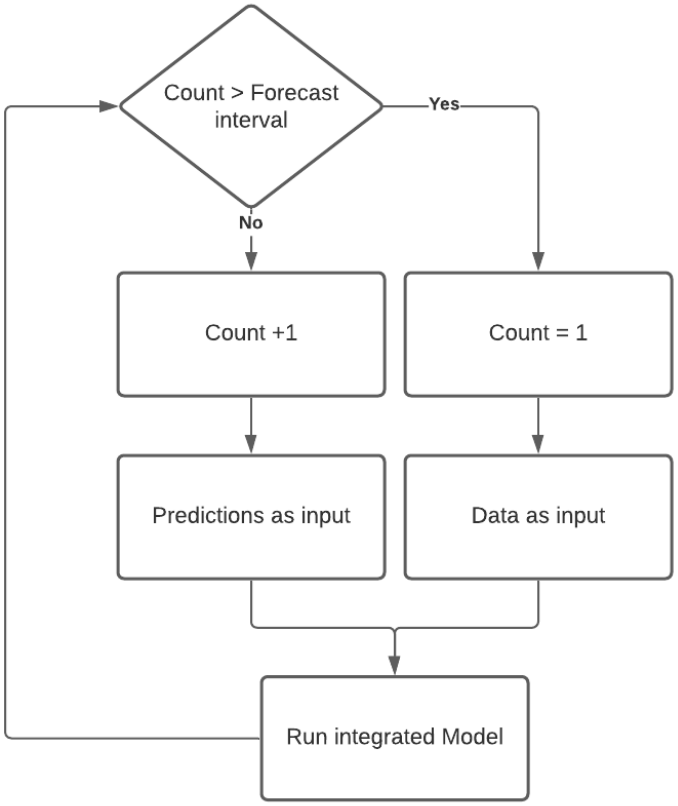

Figure 6.5. Diagram of the periodic forecasting process

Table 6.2. Summary of scenarios and prediction periods

Scenario Label	Section	Dataset size	Data range	Model Label	Evaluation Range
S11	Washoff data included	25604	11/7/2018 - 10/1/2021	M3YF	11/7/2018 - 3/1/2019
S12	Washoff data excluded	22885	3/1/2019 - 10/1/2021	M3Y	11/7/2018 - 3/1/2019
S13	Only washoff data	2719	11/7/2018 - 3/1/2019	M3YFL	11/7/2018 - 3/1/2019
S21	1 Year data	8759	11/7/2018 - 11/7/2019	M1YF	11/7/2018 - 10/1/2021
S22	2 Years data	17519	11/7/2018 - 11/6/2020	M2YF	11/7/2018 - 10/1/2021
S23	3 Years data	25604	11/7/2018 - 10/1/2021	M3YF	11/7/2018 - 10/1/2021
S31	Winter	4319	11/7/2018 - 5/6/2019	M6MFS	11/7/2018 - 10/1/2021
S32	Summer	4320	5/6/2019 - 11/2/2019	M6MFW	11/7/2018 - 10/1/2021

6.6. Results and Discussions

6.6.1. Evaluation methods and effect of forecast intervals

The models were evaluated based on the correlation coefficient (R^2), the mean squared error (MSE), and the mean absolute error (MAE). A better prediction will have the R^2 closer to 1 and a smaller MSE and MAE. While the evaluation results for all periods are presented in tabulated form, the prediction plots of 1-, 7-, 30-days, and 3-years are presented for demonstration. The heat mappings of R^2, MSE, and MAE summaries are presented in tables 3, 4, and 5, respectively. It should be noted that the weather conditions used in this study were collected from a nearby weather station, which better represents the atmospheric conditions experienced at the surface of the testbed

compared to weather forecasts. The use of forecasted weather conditions may add additional uncertainties to the prediction.

Table 6.3. Summary and heat mapping of R^2 for all forecast intervals under all scenarios.

SL	FI	Scenario Label							
		S11	S12	S13	S21	S22	S23	S31	S32
Top	1-D	93.9%	93.6%	96.3%	98.2%	99.5%	99.4%	80.2%	96.9%
Mid	1-D	85.0%	34.2%	89.1%	96.2%	99.5%	99.5%	68.9%	37.1%
Bot	1-D	97.7%	95.7%	97.9%	98.3%	99.5%	99.5%	80.5%	87.9%
Top	3-D	83.2%	85.3%	90.3%	95.4%	98.9%	98.4%	70.2%	91.4%
Mid	3-D	61.6%	19.7%	74.9%	85.0%	48.7%	98.7%	65.5%	36.6%
Bot	3-D	87.9%	81.8%	91.7%	95.8%	94.0%	98.8%	76.0%	63.2%
Top	7-D	68.0%	65.2%	76.2%	81.2%	96.5%	95.4%	63.1%	83.0%
Mid	7-D	39.2%	18.9%	66.9%	25.4%	1.1%	94.3%	62.4%	37.2%
Bot	7-D	83.4%	69.5%	79.3%	87.2%	91.8%	87.2%	72.3%	57.3%
Top	14-D	28.9%	47.1%	65.7%	59.4%	93.0%	91.0%	59.4%	73.6%
Mid	14-D	38.5%	15.7%	11.1%	11.2%	0.9%	87.0%	58.2%	23.8%
Bot	14-D	68.3%	53.5%	68.1%	73.7%	84.6%	92.8%	60.7%	27.9%
Top	30-D	27.2%	36.3%	18.4%	32.4%	85.1%	85.2%	55.3%	58.7%
Mid	30-D	9.4%	11.7%	37.3%	6.4%	1.3%	77.6%	56.3%	26.7%
Bot	30-D	54.1%	52.1%	32.6%	64.6%	61.8%	87.2%	47.2%	42.8%
Top	3-Y	2.5%	12.2%	2.8%	0.3%	73.5%	54.2%	53.7%	40.8%
Mid	3-Y	12.9%	30.2%	52.1%	0.0%	54.8%	44.0%	31.3%	9.0%
Bot	3-Y	32.8%	20.1%	40.6%	0.1%	1.1%	87.2%	24.8%	3.3%

*SL: Simulated Layer, FI: Forecast Interval

Table 6.4. Summary and heat mapping of MSE for all forecast intervals under all scenarios.

SL	FI	Scenario Label							
		S11	S12	S13	S21	S22	S23	S31	S32
Top	1-D	0.0008	0.0008	0.0005	0.0043	0.0010	0.0014	0.0904	0.0086
Mid	1-D	0.0006	0.0188	0.0004	0.0074	0.0007	0.0007	0.0888	0.9461
Bot	1-D	0.0003	0.0008	0.0002	0.0020	0.0005	0.0005	0.0466	0.0130
Top	3-D	0.0023	0.0021	0.0013	0.0108	0.0024	0.0034	0.1267	0.0217
Mid	3-D	0.0016	0.1040	0.0010	0.0240	0.1176	0.0020	0.0983	1.9712
Bot	3-D	0.0020	0.0031	0.0009	0.0049	0.0083	0.0013	0.0568	0.0435

Top	7-D	0.0046	0.0052	0.0031	0.0432	0.0079	0.0099	0.1478	0.0392
Mid	7-D	0.0028	0.1320	0.0014	0.1551	0.7762	0.0087	0.1048	2.7905
Bot	7-D	0.0019	0.0051	0.0026	0.0160	0.0089	0.0169	0.0646	0.0546
Top	14-D	0.0114	0.0074	0.0044	0.1193	0.0173	0.0203	0.1587	0.0587
Mid	14-D	0.0028	0.0336	0.0343	0.2166	1.5095	0.0224	0.1095	3.6142
Bot	14-D	0.0036	0.0075	0.0048	0.0319	0.0181	0.0080	0.0727	0.1074
Top	30-D	0.0114	0.0088	0.0132	0.4053	0.0356	0.0340	0.1673	0.0919
Mid	30-D	0.0048	0.0372	0.0033	0.2193	2.0082	0.0398	0.1129	4.0598
Bot	30-D	0.0058	0.0123	0.0136	0.0470	0.0536	0.0145	0.0816	0.0824
Top	3-Y	0.0168	0.0127	0.0166	8.8945	0.1420	0.1320	0.1737	0.1444
Mid	3-Y	0.0048	0.0035	0.0021	0.1697	5.4721	0.1401	0.3667	7.6256
Bot	3-Y	0.0106	0.0096	0.0128	0.1078	0.3648	0.0145	0.2717	0.2123

*SL: Simulated Layer, FI: Forecast Interval

Table 6.5. Summary and heat mapping of MAE for all forecast intervals under all scenarios.

SL	FI	Scenario Label							
		S11	S12	S13	S21	S22	S23	S31	S32
Top	1-D	0.0186	0.0202	0.0153	0.0313	0.0167	0.0216	0.1611	0.0597
Mid	1-D	0.0143	0.0500	0.0112	0.0309	0.0132	0.0143	0.1480	0.4470
Bot	1-D	0.0091	0.0199	0.0082	0.0233	0.0115	0.0118	0.1184	0.0572
Top	3-D	0.0347	0.0341	0.0260	0.0571	0.0302	0.0406	0.2057	0.1036
Mid	3-D	0.0274	0.1244	0.0206	0.0568	0.0569	0.0294	0.1646	0.8519
Bot	3-D	0.0297	0.0405	0.0176	0.0413	0.0479	0.0232	0.1405	0.0981
Top	7-D	0.0457	0.0506	0.0398	0.1042	0.0544	0.0688	0.2344	0.1438
Mid	7-D	0.0386	0.1500	0.0270	0.1451	0.2452	0.0602	0.1785	1.1749
Bot	7-D	0.0302	0.0564	0.0336	0.0741	0.0468	0.0474	0.1587	0.1246
Top	14-D	0.0707	0.0598	0.0490	0.1645	0.0841	0.0985	0.2515	0.1735
Mid	14-D	0.0409	0.0850	0.1550	0.1990	0.4512	0.0967	0.1887	1.4837
Bot	14-D	0.0454	0.0658	0.0471	0.1130	0.0719	0.0633	0.1782	0.1917
Top	30-D	0.0721	0.0690	0.0766	0.3028	0.1239	0.1319	0.2659	0.2076
Mid	30-D	0.0558	0.0975	0.0417	0.2254	0.6106	0.1320	0.1954	1.6472
Bot	30-D	0.0615	0.1004	0.0931	0.1375	0.1219	0.0867	0.1927	0.1782
Top	3-Y	0.0883	0.0802	0.0938	2.9151	0.2721	0.2515	0.2772	0.2742
Mid	3-Y	0.0582	0.0473	0.0367	0.2937	1.5526	0.2709	0.4216	2.7061
Bot	3-Y	0.0858	0.0835	0.0974	0.2678	0.4316	0.0867	0.3857	0.3567

*SL: Simulated Layer, FI: Forecast Interval

The general trend of evaluation criteria showed the accuracy decreases with a longer forecast interval or time or interval, which was attributed to the accumulation of the errors from each forecasting timestep. Regarding the variation of prediction accuracy at different depths, the most accurate predictions were on the measurements at the bottom location despite the worse prediction for the middle location. Considering the integrated model used the prediction from the overlying layer at the current timestep to estimate the values of the current layer, a good forecast from poor input dataset, in this case, suggests the moisture content at the bottom layer may be successfully predicted from the prior permittivity data from the current layer alone. Therefore, a model (Bot2H) based on permittivity $\sqrt{\varepsilon}$ data of the previous two hours at the bottom location was trained with two years of data. The 1-day forecast of the Bot2H model achieved an R^2 of 60.9%, as shown in Table 6.6. Examination of the prediction presented in Figure 6.6 shows that the Bot2H achieved good accuracy during the fall and winter months but not in the spring and summer months, suggesting that the influence from previous layers was more evident during the later periods. The periods when the prediction failed matched the observation in chapter 3, which identified these months as the moisture recharging stage occurring during late fall and extensive evaporation stage corresponding to late spring and early fall. Although the top and middle layers buffered atmospheric effects on the bottom layer, atmospheric conditions still significantly influenced the bottom layer through the change of conditions in the middle layer.

Table 6.6. Summary of evaluations for Bot2H model

	Bot2H-1-Day	Bot2H-3-Day	Bot2H-7-Day	Bot2H-30-Day
R^2	62.9%	63.7%	40.3%	27.6%
MSE	5.723E-02	5.336E-02	1.084E-01	1.596E-01
MAE	1.395E-01	1.416E-01	1.842E-01	2.517E-01

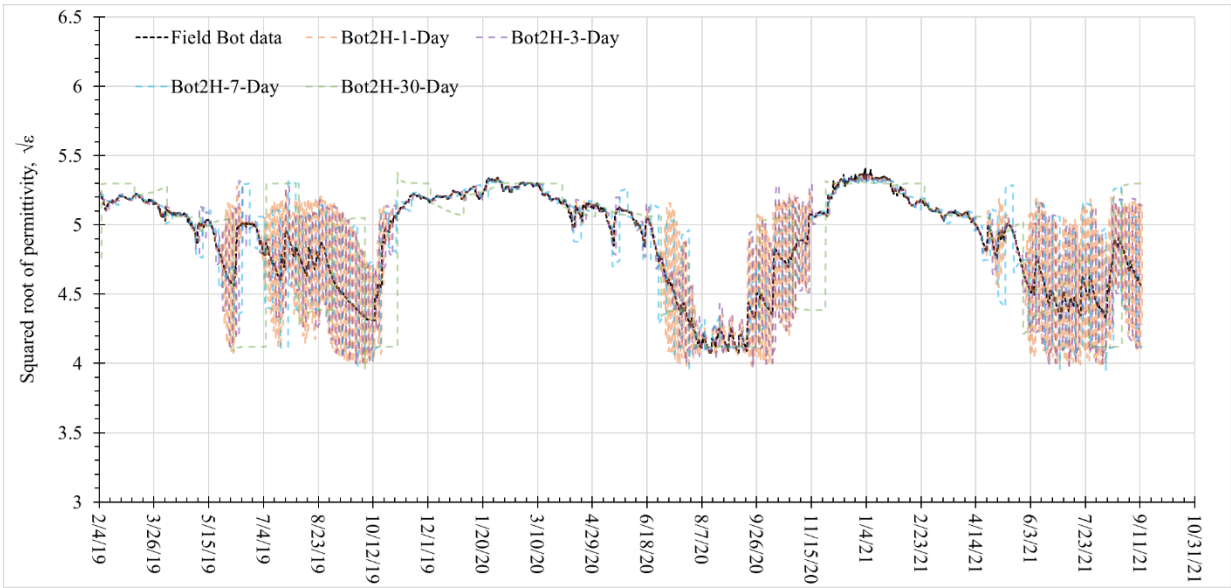

Figure 6.6. Prediction from Bot2H model for the bottom location based on the previous timestep data.

6.6.2. Scenario 1: Prediction with data lacking significant factor

The S13 showed the data-driven model could accurately predict the change of permittivity ($\sqrt{\varepsilon}$) with the 1-Day forecast interval despite lacking the information on pore solution salinity, as demonstrated in Figure 6.9. Based on the discussion on the characteristic behavior of solute transport in the testbed section, although the pore solution's salinity influences the bulk permittivity, EC was still required to predict the change of permittivity with VWC. By successfully predicting the permittivity change in the current layer using only the permittivity ($\sqrt{\varepsilon}$) data from the preceding layer and prior timestep data, without any complementary data on pore fluid's salinity, the NN model can interpret the intrinsic information through pattern recognizing. Considering the duration of the salinity on a layer increases with depth (chapter 3), the top layer should experience the least duration of the effect of salinity. At the same time, the middle and bottom locations were under high salinity conditions for roughly 30% of the time modeled. While

the S11 model was trained to recognize both the washoff-dominant and VWC-dominant permittivity patterns, the S12 model was trained to recognize only the VWC-dominant pattern, and the S13 model was trained to recognize only the washoff-dominant pattern.

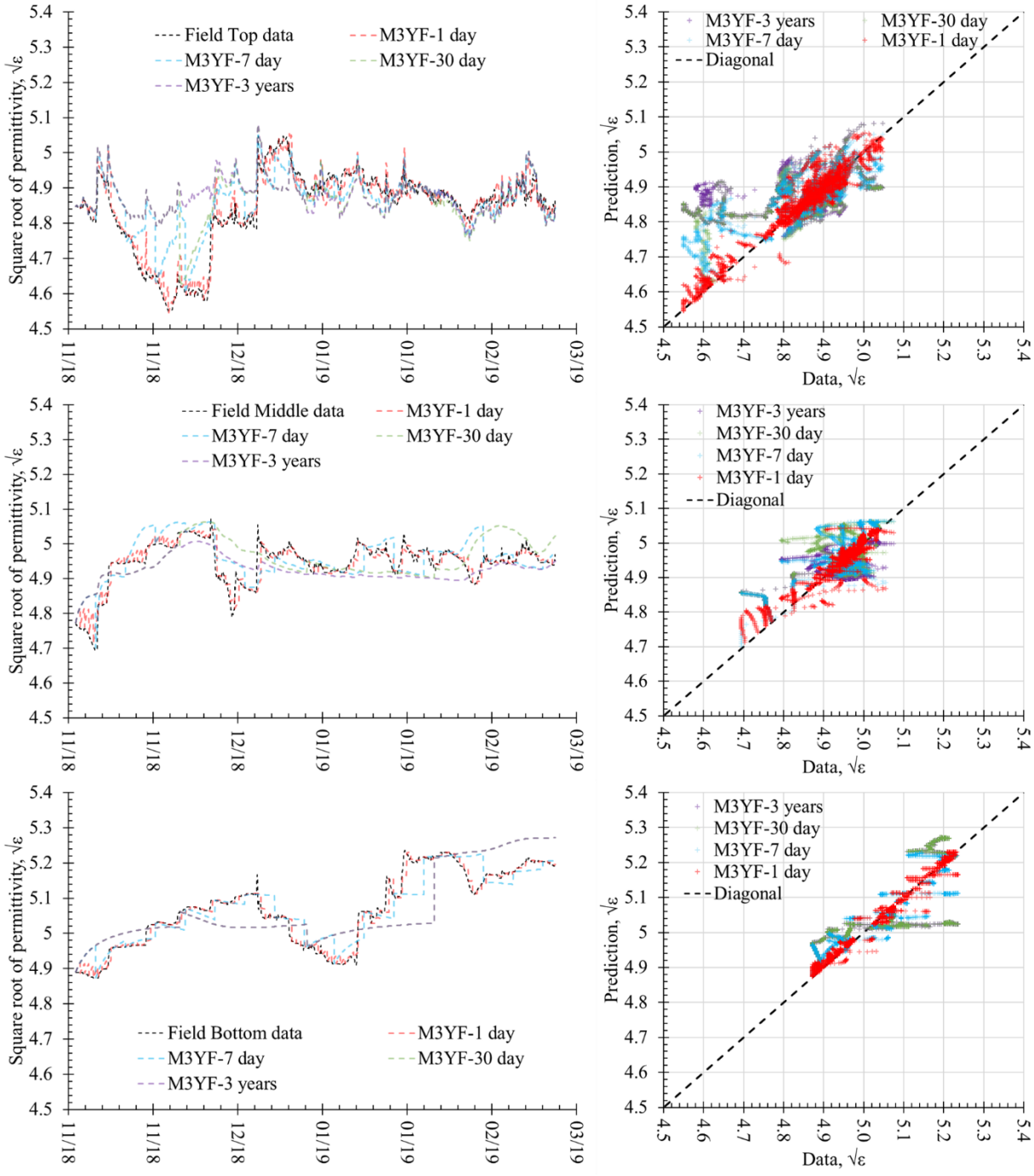

Figure 6.7. Prediction of Scenario 1 condition 1 (S11), model trained with three years of data including the washoff period.

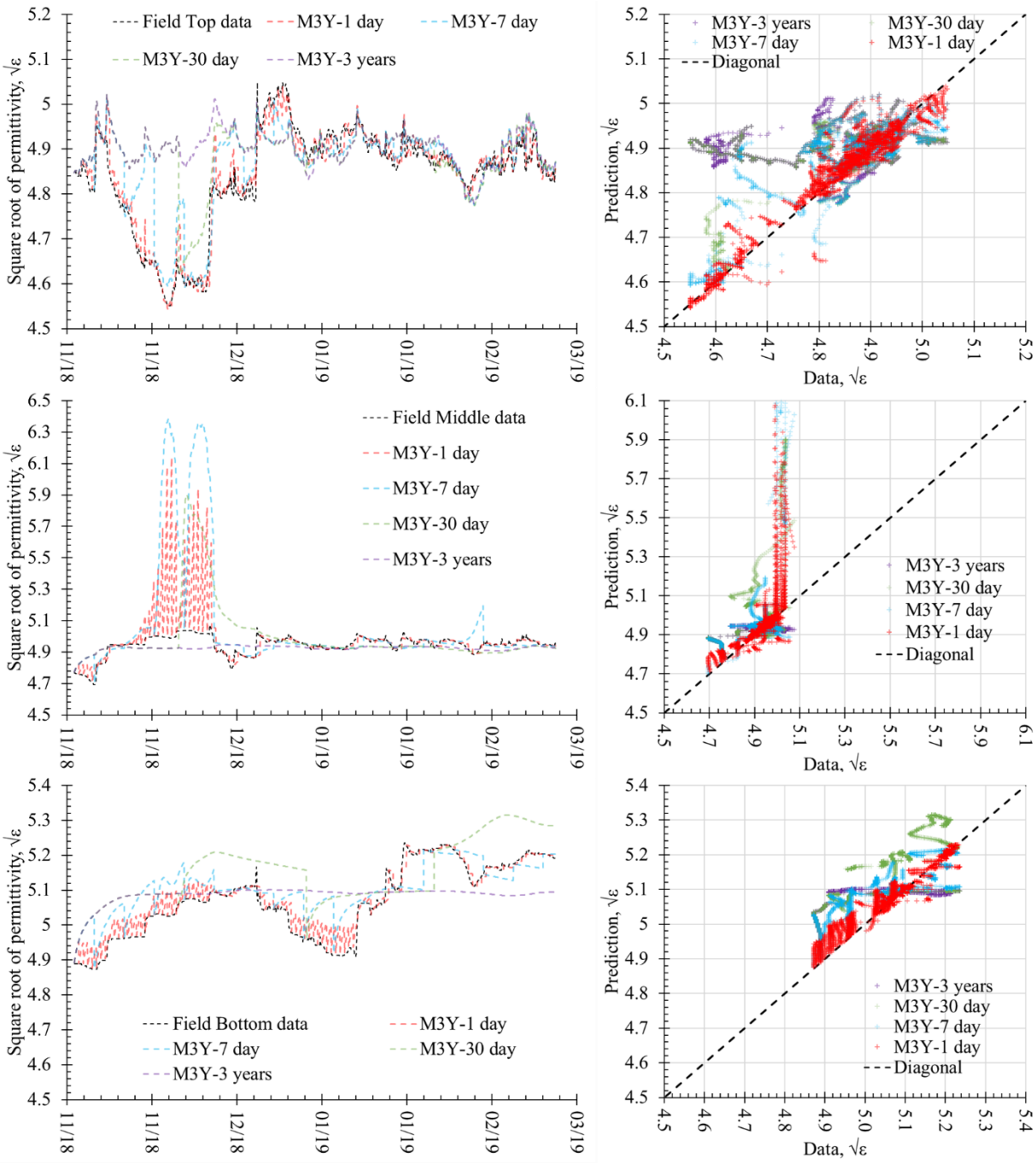

Figure 6.8. Prediction of Scenario 1 condition 2 (S12), model trained with three years of data excluding the washoff period.

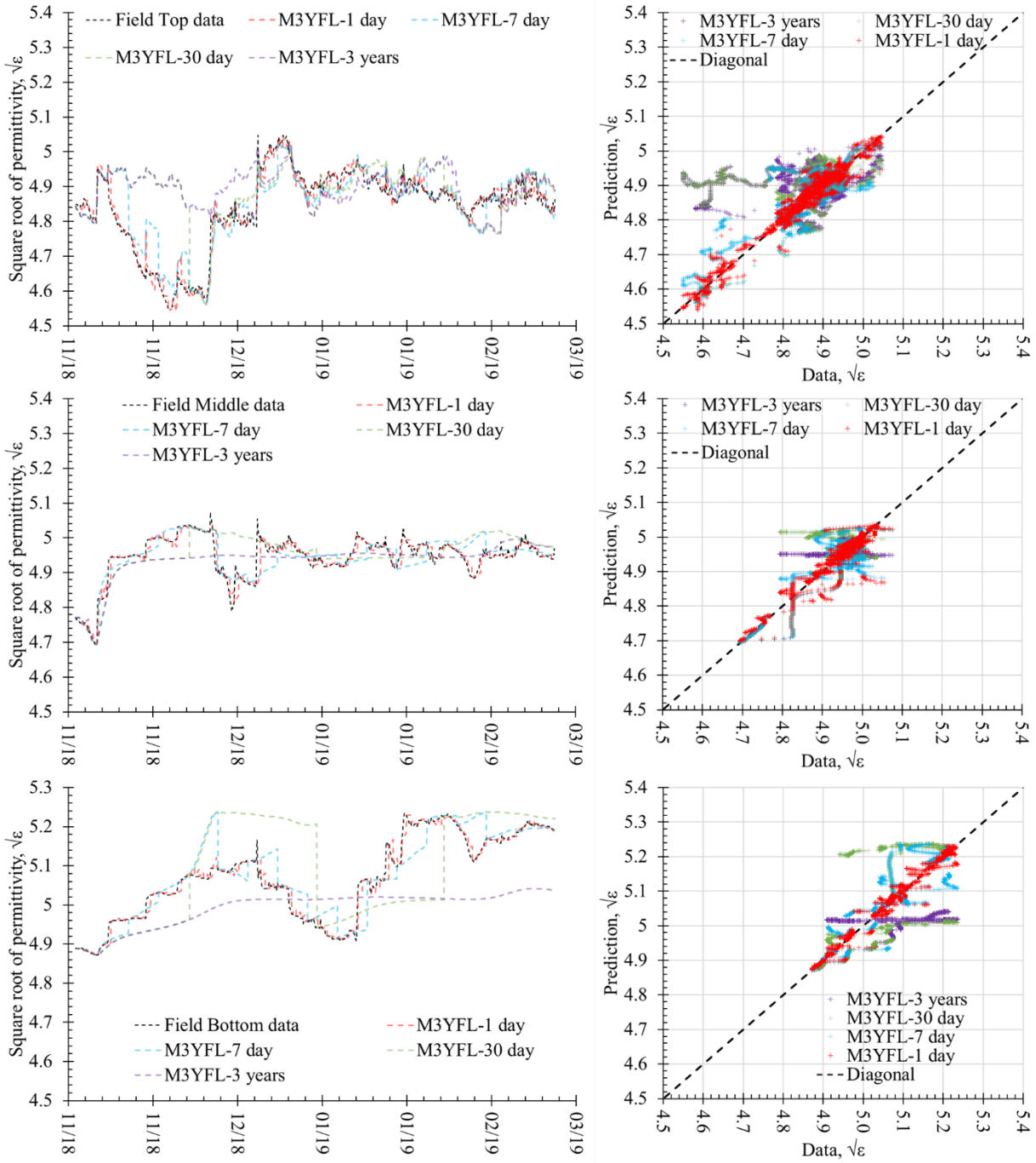

Figure 6.9. Prediction of Scenario 1 condition 3 (S13), model trained with only the washoff period data.

Excluding the washoff period from the model's training resulted in overestimating the permittivity when the location is still under the influence of high salinity, as observed by

comparing Figures 6.7 and 6.8. The dramatic error observed in Figure 6.8 between 11/2018 and 12/2018 can be explained by the influence of the varying salinity level on permittivity, as explained in Chapter 3. After the washoff stage, when the change in moisture content solely controlled the change in permittivity of the material, the rapid reduction in $\sqrt{\varepsilon}$ followed by a sudden spike was often associated with precipitation events, as shown in Figure 6.1. However, during the washoff stage, the abrupt reduction in $\sqrt{\varepsilon}$ could result from a decrease in the salinity front of the pore fluid unassociated with a potential increase in moisture content of the material. The abrupt reduction in $\sqrt{\varepsilon}$ from the preceding layer during the washoff stage could lead a model not trained with the dataset with washoff information (i.e., M3Y) to misinterpret such change as inflow, erroneously resulting in a spike of $\sqrt{\varepsilon}$ representing an increase in water content.

Using the full dataset that includes the post washoff stage in the training of the washoff stage decreased the R^2 of 1-Day prediction for the top and the middle locations by 2.4% and 4.15%, respectively. The prediction accuracy for the bottom location was relatively unchanged. The result suggests that incorporating data with two distinct characteristics of uneven dataset sizes (2719 for the washoff stage and 22805 for the post washoff stage) for model training can still accurately predict the $\sqrt{\varepsilon}$ during and after the washoff stage. However, the S11 model trained with the full dataset predicted less accurately than the S13 model explicitly trained for the pattern with fewer data, as demonstrated by Figures 6.7 and 6.9. Therefore, if a specific situation was targeted for investigation using a data-driven model, a model trained only with data specific to the period will make a better prediction.

6.6.3. Scenario 2: Effect of dataset size on prediction performance

Compared to the model trained with one year of data, increasing the dataset to include the 2nd year's data increased the R^2 of 1-Day forecast interval performance by 1.3%, 3.3%, and 1.2% at the top, the middle, and the bottom locations, respectively. Similarly, the MAE was reduced by 47%, 57%, and 51% at the top, the middle, and the bottom layers. The M3YF model trained with three years of data showed a limited performance difference compared to the M2YF at the forecast interval of 24 hours. Further analysis of prediction results revealed the better performance of the M3YF model for longer forecast intervals than other models, showing an average R^2 of 90.3% for 14 days interval. The average R^2 for M1YF and M2YF models over 14 days interval was 48.1% and 59.5%, respectively. Detailed examination on the prediction results showed the M1FT failed to predict the permittivity values not presented in the dataset for its training, such as low permittivity during the summer of 2020 presented in Figure 6.10. This failure to predict the unprecedented values indicates potential errors and the significance of retraining the model with a new, more inclusive dataset.

Since the integrated model used the prediction from the preceding layer as input, the prediction error accumulates with time and depth, implying that the accumulation of errors due to the carryover effect would most significantly impact the bottom layer. However, as discussed in the Bot2H scenario, the insensitivity of the bottom layer to the inputs from overlaying layer during the winter months allowed the simulation to maintain its prediction accuracy for half of a year. Therefore, the forecast for the middle location had the least prediction accuracy and stability, as demonstrated in Figures 6.10 and 6.11, which further confirmed the transfer of prediction errors from the top location. Given the integrated model in this study only consists of three layers,

implementing the stacked model for multiple layers for an engineered landfill in the field may encounter a more significant effect of stacked error in the intermediate layers.

To further explore the possibility of using existing data to improve the accuracy of the predicted permittivity, a neural network with three hidden layers was used to simulate the complex process of the top layer using the Deep Learning Toolbox. The loss function of the training was Mean Squared Error (MSE) with Root Mean Squared Error (RMSE) performance of 0.0095, and the details of the model and results are summarized in the supplementary section. While the simulation of the next hour showed a reproduction of values that were not in the training dataset, the simulation did relatively poorly compared to the shallow network in 24 hours forecast interval. Since this study focused on the shallow neural network as a proof of concept and the performances of models were quite good, future studies may explore the notion of using more sophisticated NN structure to simulate the complex processes at the surface of the domain.

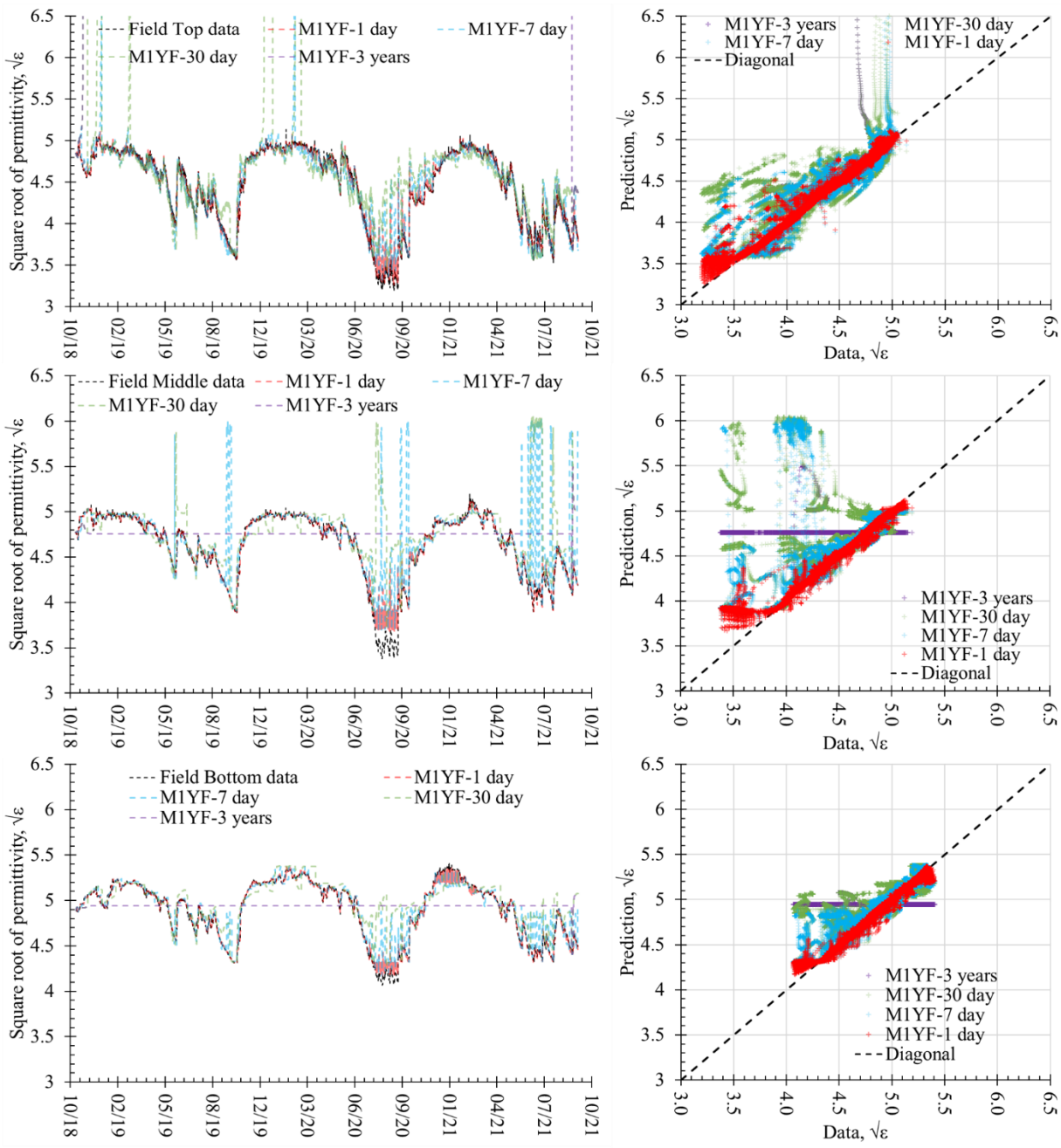

Figure 6.10. Prediction of Scenario 2 condition 1 (S21), model (M1YF) trained with 1-year of data.

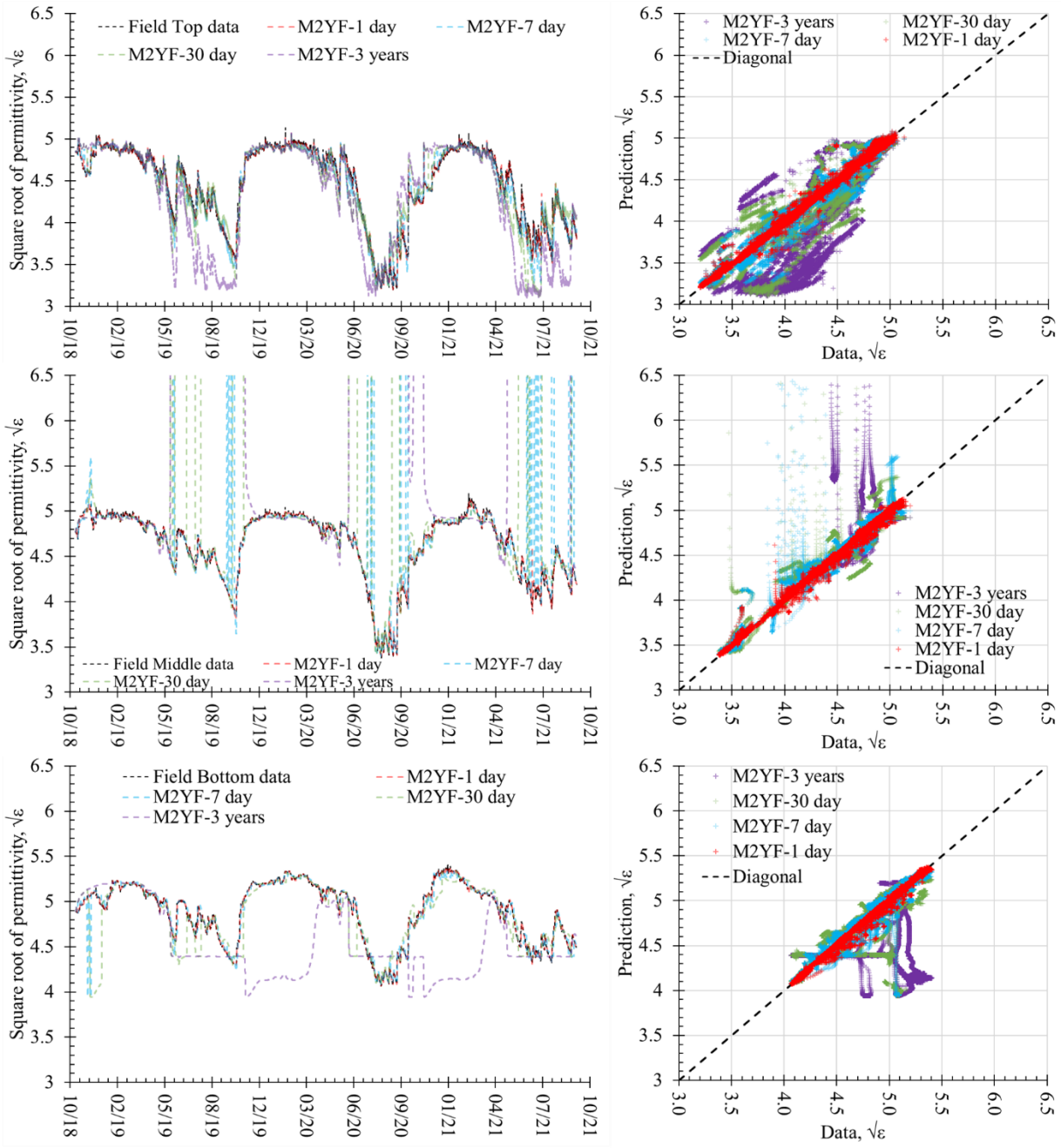

Figure 6.11. Prediction of Scenario 2 condition 2 (S22), model (M2YF) trained with 2-years of data.

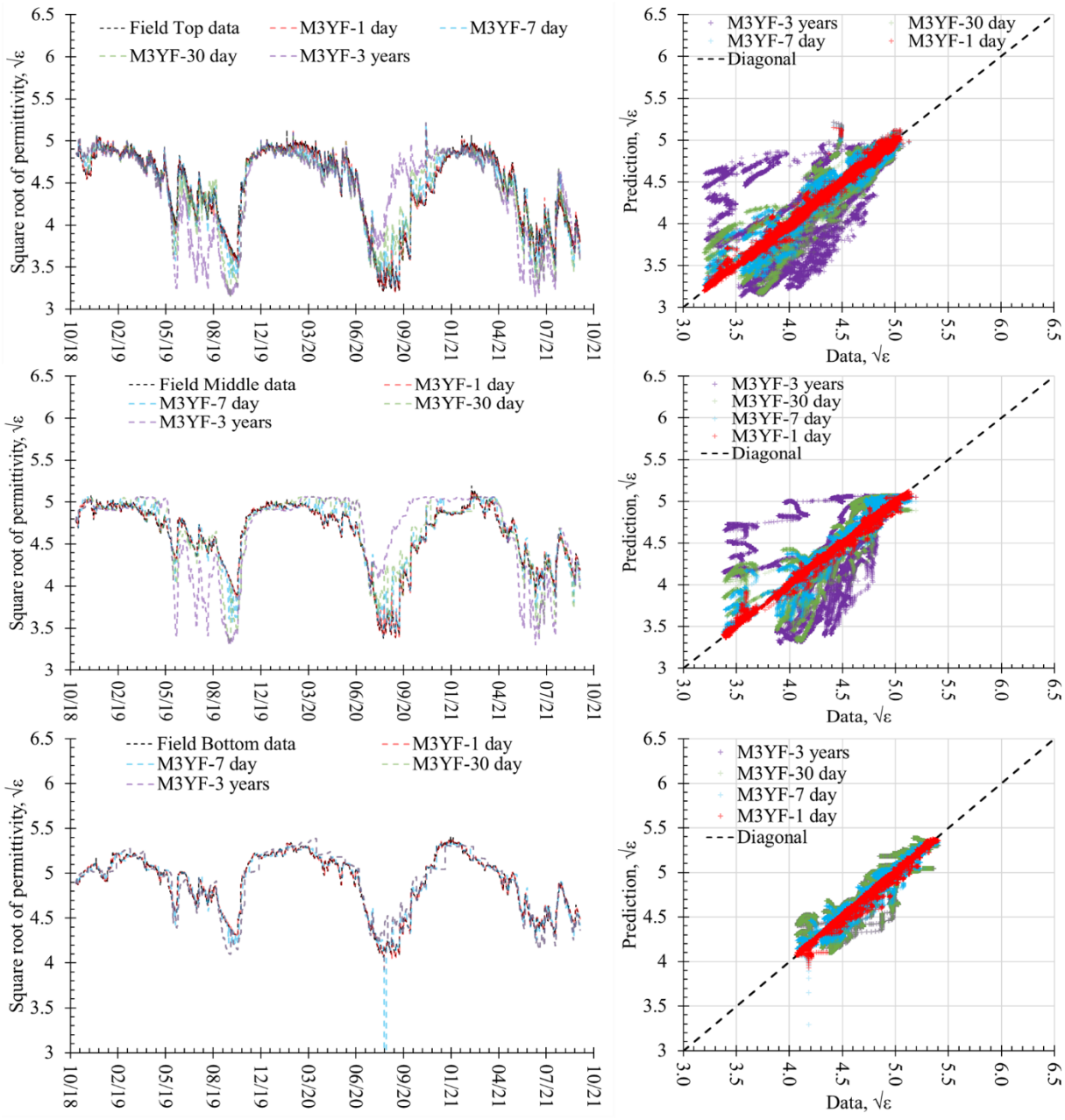

Figure 6.12. Prediction of Scenario 2 condition 3 (S23), model (M3YF) trained with 3-year2 data.

Other considerations when using the layered model presented in this study for other geomaterials are the hydraulic properties of the material and the thicknesses of the layers or spacings of the VWC monitoring sensors, which ultimately control the response time of each layer

to situations in the preceding layers. The response time lag to rainfall between different layers in this study was generally an hour, which allows the model structure to make an accurate prediction based on the lag 1-hour structure as presented in Figure 6.3. Therefore, it is suggested to investigate the general response pattern of sensors in the field to identify the response time lag between adjacent sensors for structuring the model.

6.6.4. Scenario 3: The effect of limiting the situations used in model training

The model trained with only summer data (M6MFS) or with only winter data (M6MFW) of the first year further demonstrated that the model could only make accurate predictions for $\sqrt{\varepsilon}$ included in the training dataset, as shown in Figure 6.13 and 6.14. The summer period can be described as the phase of reduction in $\sqrt{\varepsilon}$ due to high evaporation with occasion spikes in $\sqrt{\varepsilon}$ resulting in limited infiltration from rainfalls. In contrast, the $\sqrt{\varepsilon}$ during the winter period remained relatively high with limited increases caused by rain events. Significant errors were only observed from the predictions made on permittivity values not included in the training dataset for M6MFW and M6MFS as shown in Figures 6.13 and 6.14. It is worth noting that the apparent fluctuation in winter and summer precipitation patterns during the study period led to distinct winter and summer periods, which might not be observed under other weather conditions. Therefore, it is recommended to train the model with a dataset containing at least one complete weather cycle or covering all the seasons in a weather system to establish the general pattern and routinely retrain the data-driven model with the latest dataset to cover a broader range of $\sqrt{\varepsilon}$ values.

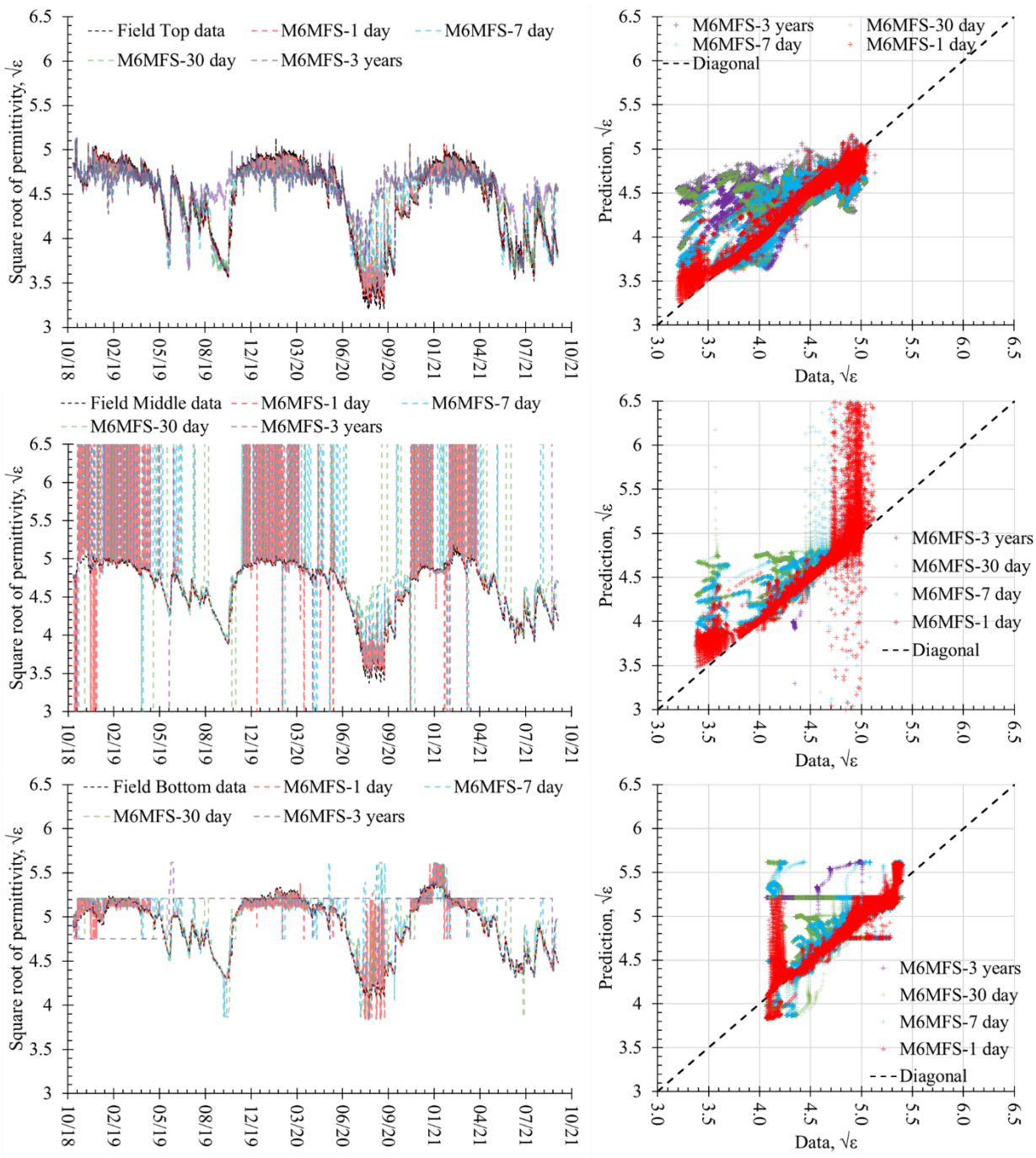

Figure 6.13. Prediction of Scenario 3 condition 1 (S31), model (M6MFS) trained with first year's summer data.

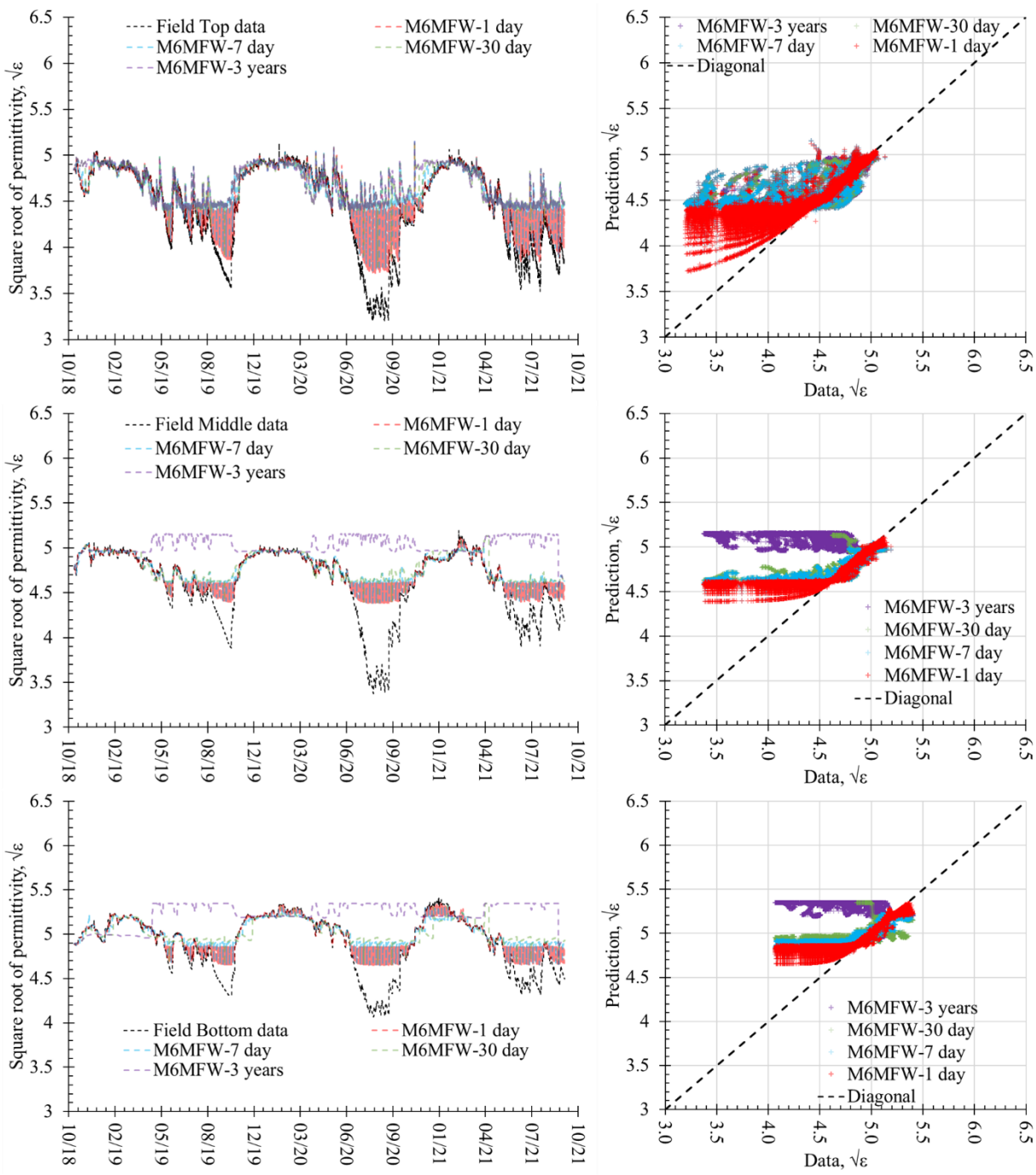

Figure 6.14. Prediction of Scenario 3 condition 2 (S32), model (M6MFW) trained with first year's winter data.

6.7. Conclusions

This paper presented the integration of individually trained data-driven models to predict the permittivity ($\sqrt{\varepsilon}$) profile in a testbed, which can be used to estimate the volumetric water content of a porous material. The hourly data from instrumented testbed under the field conditions were used to train individual models under different scenarios. The results from scenario 1 showed that the data-driven model could accurately predict the change in $\sqrt{\varepsilon}$ even if essential physics-relevant information is omitted. Despite lacking the important information, the successful predictions suggest the model can interpret the information of volumetric water content and salinity embedded in the $\sqrt{\varepsilon}$ data through the unique pattern recognition of decrease of permittivity with rainfall on the arrival infiltration fronts. Although the model could predict the $\sqrt{\varepsilon}$ accurately, one would still need the information on the salinity of the pore fluid to convert the $\sqrt{\varepsilon}$ to volumetric water content, which is the actual physical property of interest.

The analysis of the results from scenario 2 showed the proposed modeling structure trained with data over two years could make accurate predictions for observations over three years at the forecast interval of 1-Day (24 hours). Although the expansion of the training dataset to include the third year's data did not improve the 1-Day prediction, it allowed the model to maintain a good prediction accuracy ($R^2 > 90\%$) for a forecast interval of 14 days. The use of the previous hour's conditions as inputs for the model was based on the field observation, allowing the model to accurately reflect the moisture flow between layers. Considering the response time lag of the sensors was impacted by the hydraulic properties of the porous medium and the spacing of the sensors, assessment of sensors' responses during and after rainfalls is recommended before structuring the model inputs. Although developing a data-driven model does not require theoretical

equations, prediction accuracy depends on precedent data. Further investigation into the unique lines of data suggested that the model made predictions based on correlations extracted from limited input conditions rather than referencing pre-existing input conditions, even though the prediction was only accurate when the targeted value was presented in the dataset used for training. Considering the variation of $\sqrt{\varepsilon}$ during the leached/residual stage in this study was driven by infiltration and evaporation, which are highly dependent on the weather conditions, it is recommended the model be trained with a dataset containing at least one full cycle of weather seasons. In addition, attention should be paid to when unprecedented values are observed, indicating that the existing model is unlikely to make accurate predictions. Therefore, it is vital to routinely retrain the model with the latest dataset to cover a broader range of observations.

It should be noted that during the landfill operation, the stacking of the new layers on top of old layers would change the relative locations of layers in the integrated model structure. Further studies are necessary to understand the limitations of knowledge transfer. While a nearby weather station recorded the weather conditions used in this study, the use of weather forecasts as inputs will affect the accuracy of prediction. The data-driven model proposed in this study is more efficient for a spatially layered structure such as cover systems and earthen dams, which allows prolonged data accumulation at given locations. The prediction failure by the data-driven model trained with precedent conditions may indicate a significant change in behavior patterns, which can be viewed as warning signs of potential damage. Since the accuracy of the data-driven model eventually is based on the quality and quantity of data, proper instrumentation and careful maintenance of a data collection system are equally crucial to the success of a data-driven model.

Supplementary Materials

Table 6.S1. Summary of unique input conditions and unique lines of data in datasets

Data range	Model Label	Dataset size	Unique inputs			Unique lines of data		
			Top	Middle	Bottom	Top	Middle	Bottom
11/7/2018 - 10/1/2021	M3YF	25604	25604	6986	5299	25604	10734	8550
3/1/2019 - 10/1/2021	M3Y	22885	22885	6387	4675	22885	9622	7670
11/7/2018 - 3/1/2019	M3YL	2719	2719	1102	790	2719	1515	1047
11/7/2018 - 11/7/2019	M1YF	8759	8759	3297	2122	8759	4442	3201
11/7/2018 - 11/6/2020	M2YF	17519	17519	5345	3836	17519	7856	6238
11/7/2018 - 10/1/2021	M3YF	25604	25604	6986	5299	25604	10734	8550
11/7/2018 - 5/6/2019	M6MFS	4319	4319	1735	1197	4319	2378	1670
5/6/2019 - 11/2/2019	M6MFW	4320	4320	1644	928	4320	2085	1847

Table 6.S2. Summary of activation functions, loss functions, and performances of each model

Scenario	Model	Layer	Activation Function		Loss function / Performance
			Hidden	Output	Performance, Mean Squared Error
11	M3YF	Top	Sigmoid	Linear	1.05E-04
		Middle	Sigmoid	Linear	2.38E-05
		Bottom	Sigmoid	Linear	1.22E-05
12	M3Y	Top	Sigmoid	Linear	1.01E-04
		Middle	Sigmoid	Linear	2.43E-05
		Bottom	Sigmoid	Linear	1.26E-05
13	M3YFL	Top	Sigmoid	Linear	1.81E-05
		Middle	Sigmoid	Linear	1.21E-05
		Bottom	Sigmoid	Linear	6.67E-06
21	M1YF	Top	Sigmoid	Linear	4.22E-05
		Middle	Sigmoid	Linear	2.21E-05
		Bottom	Sigmoid	Linear	1.25E-05
22	M2YF	Top	Sigmoid	Linear	5.25E-05
		Middle	Sigmoid	Linear	1.88E-05
		Bottom	Sigmoid	Linear	1.10E-05
31	M6MFS	Top	Sigmoid	Linear	6.33E-05
		Middle	Sigmoid	Linear	2.73E-05
		Bottom	Sigmoid	Linear	1.73E-05
32	M6MFW	Top	Sigmoid	Linear	1.80E-05
		Middle	Sigmoid	Linear	1.32E-05
		Bottom	Sigmoid	Linear	6.88E-06
		Bottom	Sigmoid	Linear	8.09E-06

Table 6.S3. Summary of layer type, activation functions, and layer sizes of each model

Layer	Activation Function	Input Size	Output Size
Hidden	Sigmoid	13	37
Hidden	Sigmoid	37	29
Hidden	Sigmoid	29	19
Output	Linear	19	1

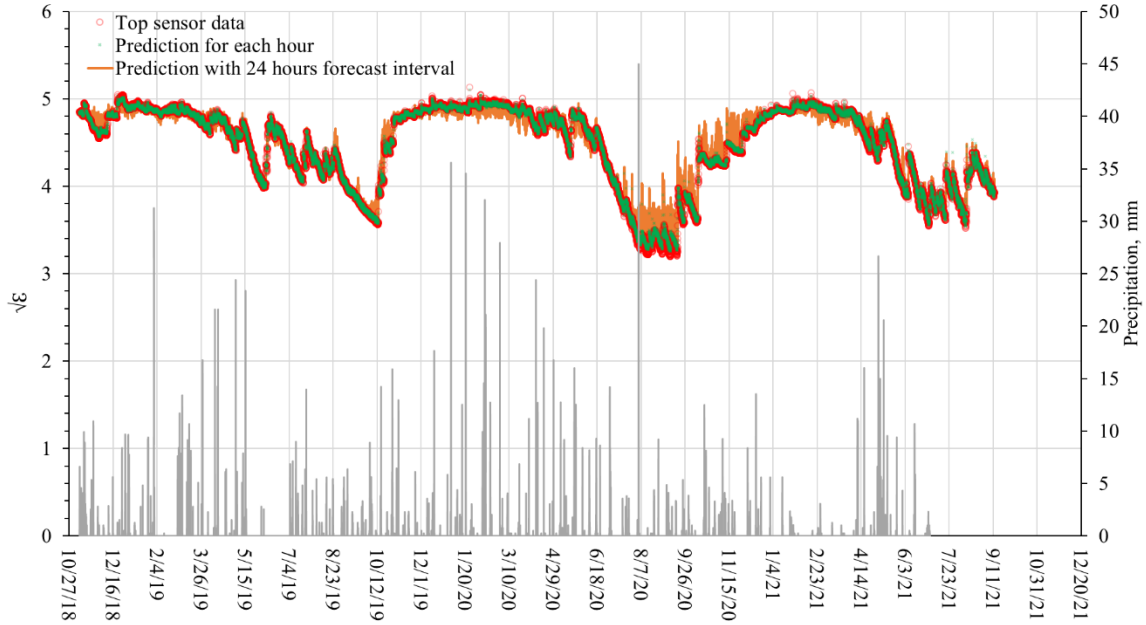

Figure 6.S1. Prediction and experimental data of permittivity at top layer using deep neural network plotted against time.

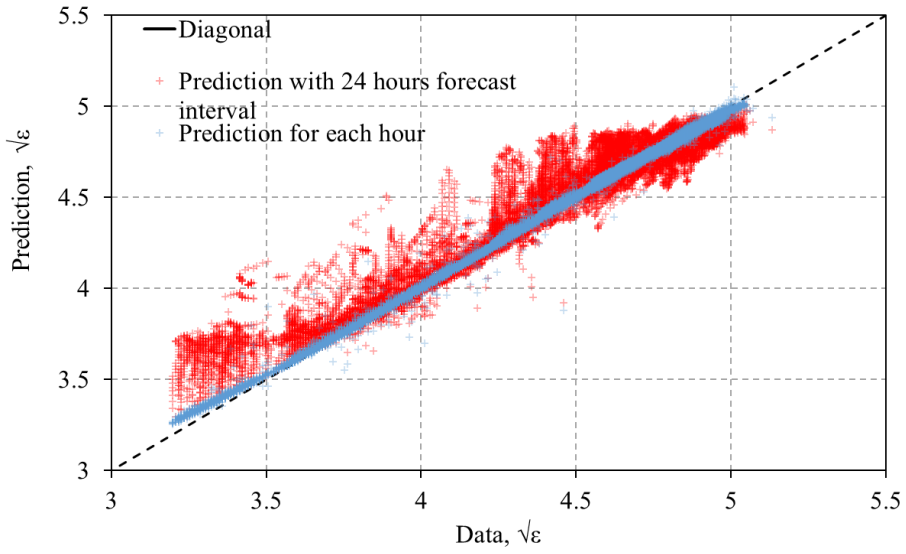

Figure 6.S2. Prediction of permittivity at top layer using deep neural network versus experimental data.

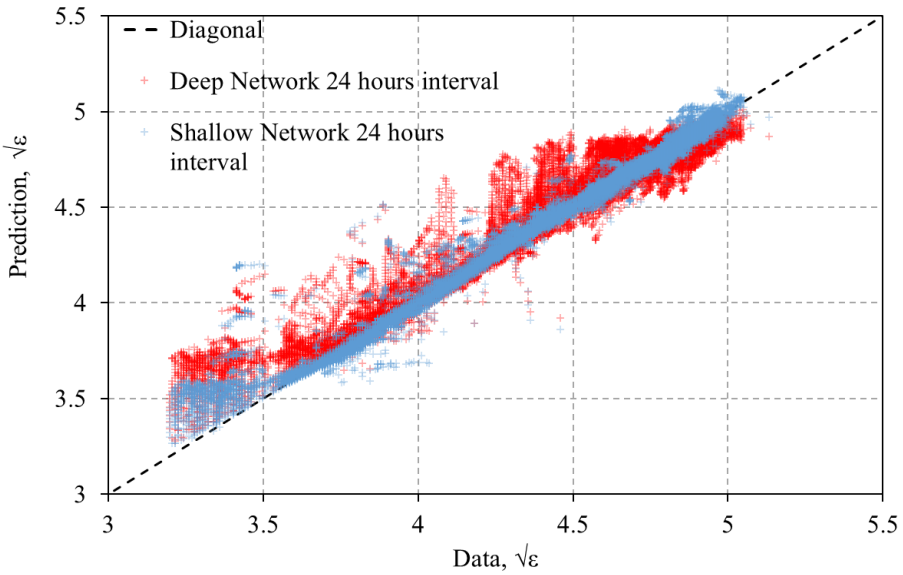

Figure 6.S3. Prediction of permittivity at the top layer using deep neural network and shallow neural network versus experimental data.

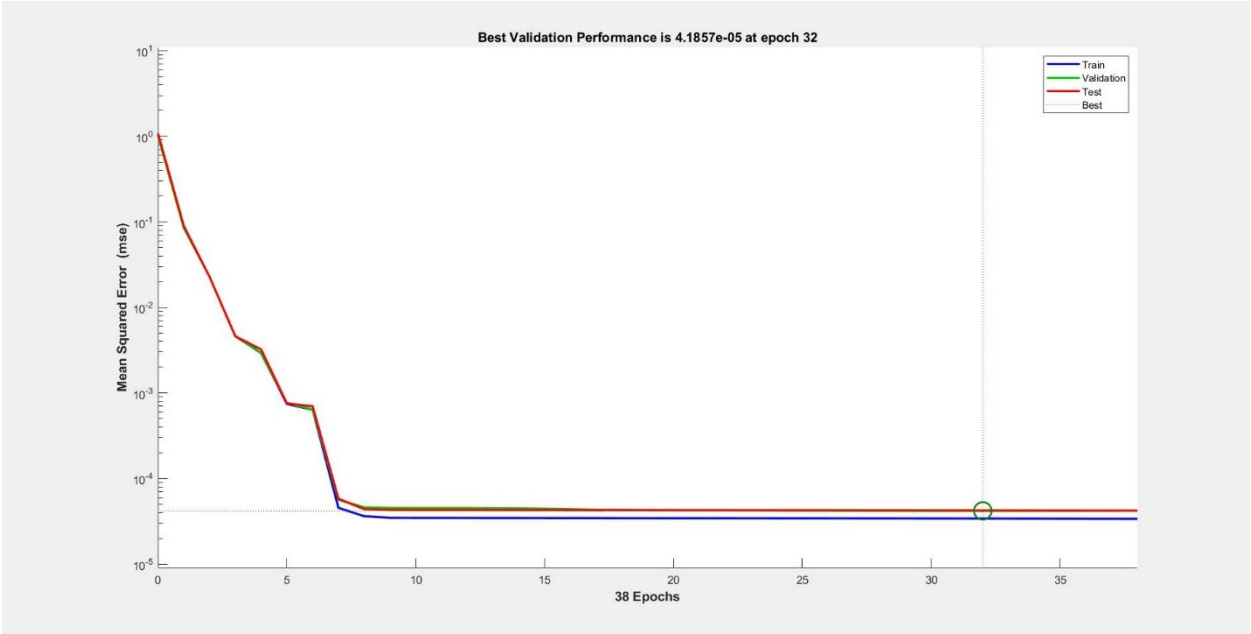

Figure 6.S4. Example of loss function performance for top layer in M1YF model.

References

Cardell-Oliver, R., Smettem, K., Kranz, M., and Mayer, K. (2004). "Field testing a wireless sensor network for reactive environmental monitoring [soil." *Proceedings of the 2004 Intelligent Sensors, Sensor Networks and Information Processing Conference, 2004.*, IEEE, 7–12.

Chen, Y., and Or, D. (2006). "Geometrical factors and interfacial processes affecting complex dielectric permittivity of partially saturated porous media." *Water resources research*, Wiley Online Library, 42(6).

COMSOL AB. (2020). "COMSOL Multiphysics® v. 5.5." Stockholm, Sweden.

Flammini, A., Marioli, D., Sisinni, E., and Taroni, A. (2007). "A real-time Wireless Sensor Network for temperature monitoring - IEEE Conference Publication." *2007 IEEE International Symposium on Industrial Electronics*, IEEE, Vigo, Spain.

Gao, Z., Russell, E. S., Missik, J. E. C., Huang, M., Chen, X., Strickland, C. E., Clayton, R., Arntzen, E., Ma, Y., and Liu, H. (2017). "A novel approach to evaluate soil heat flux calculation: An analytical review of nine methods." *Journal of Geophysical Research: Atmospheres*, John Wiley & Sons, Ltd, 122(13), 6934–6949.

He, R., Ogunro, V. O., and Ellison, K. M. (2022). "Preliminary Results of Compacted Coal Fly Ash/Flue Gas Desulfurization Brine Co-disposal in an Instrumented Testbed." *Geo-Congress 2022*.

Hong, Z., Kalbarczyk, Z., and Iyer, R. K. (2016). "A data-driven approach to soil moisture collection and prediction." *2016 IEEE International Conference on Smart Computing (SMARTCOMP)*, IEEE, 1–6.

Kim, S., and Singh, V. P. (2014). "Modeling daily soil temperature using data-driven models and spatial distribution." *Theoretical and applied climatology*, Springer, 118(3), 465–479.

Kornelsen, K. C., and Coulibaly, P. (2014). "Root-zone soil moisture estimation using data-driven methods." *Water Resources Research*, Wiley Online Library, 50(4), 2946–2962.

Li, Z., Wang, N., Franzen, A., Taher, P., Godsey, C., Zhang, H., and Li, X. (2014). "Practical deployment of an in-field soil property wireless sensor network." *Computer Standards & Interfaces*, Elsevier, 36(2), 278–287.

MathWorks, I. (2021). "Statistics and Machine Learning Toolbox."

NEPIS. (1994). "Hydrologic Evaluation of Landfill Performance (HELP) Model B (Set Includes, A- User's Guide for Version 3 w/disks, B-Engineering Documentation for Version 3."

Or, D., Lehmann, P., Shahraeeni, E., and Shokri, N. (2013). "Advances in soil evaporation physics—A review." *Vadose Zone Journal*, Wiley Online Library, 12(4), 1–16.

Pedregosa, F., Varoquaux, G., Gramfort, A., Michel, V., Thirion, B., Grisel, O., Blondel, M., Prettenhofer, P., Weiss, R., and Dubourg, V. (2011). "Scikit-learn: Machine learning in Python." *the Journal of machine Learning research*, JMLR. org, 12, 2825–2830.

Penman, H. L., and Keen, B. A. (1948). "Natural evaporation from open water, bare soil and grass." *Proceedings of the Royal Society of London. Series A. Mathematical and Physical Sciences*, Royal Society, 193(1032), 120–145.

Radcliffe, D. E., and Simunek, J. (2018). *Soil physics with HYDRUS: Modeling and applications*. CRC press.

Rhoades, J. D. (1996). "Salinity: Electrical conductivity and total dissolved solids." *Methods of soil analysis: Part 3 Chemical methods*, Wiley Online Library, 5, 417–435.

Sauer, T. J., and Horton, R. (2005). "Soil Heat Flux." *Micrometeorology in Agricultural Systems*, Agronomy Monographs.

Scudiero, E., Berti, A., Teatini, P., and Morari, F. (2012). "Simultaneous monitoring of soil water content and salinity with a low-cost capacitance-resistance probe." *Sensors (Basel, Switzerland)*, Molecular Diversity Preservation International (MDPI), 12(12), 17588–17607.

Topp, G., Davis, J., and Annan, A. (1980). "Electromagnetic determination of soil water content: measurements in coaxial transmission lines." *Water Resources Research, Wash., D.C*, (G. Topp, ed.), 16(3), 574–582.

U.S. EPA. (2015). "Hazardous and Solid Waste Management System; Disposal of Coal Combustion Residuals From Electric Utilities; Final Rule." *The Federal Register*, Federal Information & News Dispatch, Inc., Washington.

U.S. EPA. (2017). *Steam Electric Power Generating Effluent Guidelines - 2015 Final Rule*.

Wadoux, A. M., Román-Dobarco, M., and McBratney, A. B. (2020). "Perspectives on data-driven soil research." *European Journal of Soil Science*, Wiley Online Library.

Young, D. T., Chapman, L., Muller, C. L., Cai, X.-M., Grimmond, C. S. B., Young, D. T., Chapman, L., Muller, C. L., Cai, X.-M., and Grimmond, C. S. B. (2014). "A Low-Cost Wireless Temperature Sensor: Evaluation for Use in Environmental Monitoring Applications." *http://dx.doi.org/10.1175/JTECH-D-13-00217.1*.

CHAPTER 7 CONCLUSIONS AND RECOMMENDATIONS

7.1. Research Conclusions

This research dissertation investigated the halide retention and hydraulic performance of CFA-FGD brine co-disposal by compaction and paste encapsulation methods in instrumented testbeds simulating an engineered landfill under the weather conditions of the Charlotte area. Three years of the experiment showed that the paste encapsulation method could retain 96.7% of chloride and 98.0% of bromide if side leakages could be prevented. Investigations of halide retention mechanisms in paste material demonstrated the sequestration was mainly achieved through solidification of the mixture rather than stabilization resulting from the formation of halide-binding minerals. The mineralogy study revealed that the minerals formed in the paste during the curing process in both laboratory and field conditions were poorly structured, causing difficulties in identifying minerals with XRD analysis. Through solidification, the paste material achieved a low hydraulic conductivity of 1.44×10^{-8} m/s, implying the runoff production from a paste landfill will be equivalent to the quantity of rainfalls, as observed in the field experiment. Analysis of the paste testbed's temperature profile showed a significantly higher temperature of the material than the ambient due to solar heating, which indicates the paste landfill could be a significant heat source causing microclimate impacts.

On the other hand, the co-disposal by compaction method rapidly released 78.8% of chloride and 88.6% of bromide within the first four months of the experiment. The total release of chloride and bromide over the three years of the experiment was 79.1% and 88.6%, respectively. The failure to retain the halides was attributed to the lack of self-cementitious properties of the CFA-FGD brine mixture due to the negligible lime content of the ash. While the electric conductivity (EC) of liquids was commonly used as an indicator for salinity, which correlates with

chloride concentration when chloride was the domain anion, chemical analysis of the leachate showed the dominant anion shifted from chloride to sulfate after the rapid release period. The shift in major anion required the landfill operator to routinely perform chemical analysis on liquids to avoid misinterpretation of halide concentrations in the solution. While the high-frequency, low-intensity rains during winter periods lead to high infiltration and low runoff, the low-frequency, high-intensity precipitations during summers result in low infiltration and high runoff. With high evaporations, the leachate production paused during the summer months. The temperature profile in the testbed showed extensive solar heating of the compacted material, which suggests the ground heat flux should be considered for the evaporation estimations. Since compacted material's halide retention and hydraulic performance depend heavily on local weather conditions, the failure in the Charlotte area did not necessarily disqualify the use of this method in different locations.

The physics-based model was then developed to simulate the heat transfer, moisture transfer, and solute transport within the testbed. The weather conditions were used to estimate the runoff, infiltration, evaporation, and surface temperatures, which drove the changes in the testbed. While the model used COMSOL Multiphysics to perform numerical simulation, the modeling processes were controlled by a MATLAB script, which estimated and updated the surface boundary conditions. The COMSOL-MATLAB (CM) model could accurately reproduce the field observations regarding moisture and temperature profiles and leachate/runoff generation over the field experiment period, and variation of halide concentrations in the leachate during the rapid salinity release (washoff) period. Further investigation showed that the model could be improved by improving runoff estimation, evaporation estimation, and surface temperature estimation. The CM model validated by the field data provided a digitized testbed, which could be used to

investigate different management methods and explore the material's behaviors under different weather conditions.

While the physics-based model could soundly reproduce field observation, the large quantity of high-quality data acquired from the instrumented testbed for the compacted material spurs the interest in exploring the data-driven modeling, which could provide another perspective into the testbed's behaviors. The data-driven model simulating the change of bulk dielectric permittivity, which was the property directly measured by the moisture sensor, was then developed. The data-driven model accurately reproduced the permittivity changes dominated by salinity variation and moisture movement with a forecast interval of 24 hours. The prediction for the period when the permittivity changes were dominated by salinity variation with inputs lacking direct knowledge of the pore solution's salinity indicated the model could recognize the unique patterns of permittivity change during the period. Results showed the model's accuracy reduced when the targeted permittivity was not included in the dataset used to train the model. To avoid erroneous forecasts, the training dataset should cover the patterns and fluctuations in the properties. It should be noted that the accuracy of the data-driven model eventually depends on the quality of data, which requires proper instrumentation design and its careful maintenance during the operation.

7.2. Recommendations for Landfill Operations

7.2.1. Co-disposal of CFA-FGD brine through compaction method

1. For the CFA with no self-cementitious properties, addition of hydraulic binder(s) in appropriate quantity to promote the stabilization/solidification reactions is recommended.
2. Since major salinity will most likely be released in the leachate, it is recommended that infiltration control and measures be implemented to minimize leachate generations.

3. The extensive drying of the material during the summer months suggests the facility in the Charlotte area and similar weather conditions could store the winter leachate and recirculate the leachate in the landfill to take advantage of the benefits from intense evaporations.
4. Considering the pore fluid's salinity for the whole thickness of an actual landfill may never reach a leaching/residual stage during the period of active disposition of the materials as new layers will be placed on old layers, it is recommended to install sensors that measure the salinity, such as electric conductivity, and moisture content.
5. It is recommended to routinely analyze the chemical compositions of the leachate to avoid misinterpretation of the chemical compositions of the leachate or runoff based on EC measurement of the salinity values.
6. It is recommended to install ground heat flux sensors or temperature sensors close to the landfill's surface to better understand the evaporation processes.
7. In case a data-driven model is used to provide a timely forecast for daily operations, it is recommended to routinely retrain the model with the dataset that includes the latest measurements.

7.2.2. Co-disposal of CFA-FGD brine through paste encapsulation technology

1. It is recommended to protect the surface of the newly placed paste layer from rainfall and moisture prior to the final setting of the material to prevent halide washoff before the material is solidified.
2. Since the cured paste material has a low hydraulic conductivity, the runoff control pond should expect to receive a quantity of runoff equivalent to the rainfall.

3. While the primary halide retention mechanism for the current material was solidification, applying surface protection measures such as a sand layer is recommended to prevent mechanical damages or scour.
4. Applying a solar sheltering layer is also recommended to prevent extensive solar heating of paste material, which could influence local microclimate and serve as a heat source.
5. Reducing magnesium in the FGD brines is recommended if a significant concentration is presented, which could compromise the expected halide stabilization pathway by forming Friedel's salts and Kuzel's salts.

7.3. Future Research Opportunities

7.3.1. Co-disposal of CFA-FGD brine through compaction method

1. Investigate the S/S of compacted co-disposal material with hydraulic binders for halide sequestration.
2. Investigate the potential rainfall management strategies to reduce leachate generation through infiltration.
3. Investigate the potential leachate volume reduction by natural evaporation in the material through storage and recirculation.
4. Investigate the freeze and thaw effects on the compaction material.
5. Investigate the ground heat flux at the base material surface and its correlation to material properties such as surface albedo and moisture content.
6. Investigate the surface salting due to extensive evaporation and its influence on the runoff quality.

7. Investigate the precipitates dissolution mechanisms in the compacted material and its impact on the leachate quality.

7.3.2. Co-disposal of CFA-FGD brine through paste encapsulation technology

1. Investigate the halide sequestration through the formation of magnesium-based layered double hydrate minerals.
2. Investigate the mineral formation in a cementitious system with a significant presence of calcium and magnesium.
3. Investigate the impacts of the paste landfill on the local microclimates.
4. Investigate the carbonation processes in the paste material and its impact on the halide sequestration ability.
5. Investigate the methods to improve crystalline structures of minerals formed during the curing process and the enhancement of aluminum sources in the mixture.
6. Investigate the conditions to promote the formation of halide sequestering minerals in the co-disposal mixtures.
7. Investigate the mechanical properties at the interface between cured and fresh paste material.

7.3.3. Physics-based model of compacted material

1. Investigate methods to simulate runoff/infiltration of the bare compacted surface based on antecedent moisture content.
2. Coupling geochemical simulation with the solute transfer, heat transfer, and moisture flow to address potential salt precipitation and dissolution in the pore space.
3. Coupling actual evaporation and surface temperature estimation to improve simulation accuracy.

4. Investigate infiltration control strategies through model simulation and laboratory testing.
5. Investigate the compacted co-disposal method under different weather conditions by simulation and field/pilot testing.

7.3.4. Data-driven model of compacted material

1. Investigate the possibility of transferring knowledge in the trained data-driven model for general applications.
2. Investigate the feature engineering for data-driven models based on known physical principles and correlations.
3. Investigate the knowledge transfer and performance of the layer-stacking model structure during the expansion of the simulated domain.
4. Predict temperature variation in the compacted and paste material using data-driven models.
5. Predict permittivity variation in the paste material using data-driven models.
6. Study and compare the forecast accuracies of data-driven models using the volumetric water content and permittivity datasets.